AFWAL-TR-88-2046

AD-A202 426

HIGH DENSITY FUEL EFFECTS

N. K. Rizk, V. L. Oechsle, P. T. Ross, and H. C. Mongia
Allison Gas Turbine Division
General Motors Corporation
P. O. Box 420
Indianapolis, IN 46206-0420

18 August 1988

Final Report for
Period September 1985 – April 1988

DTIC
ELECTE
JAN 11 1989
H

89   1   09 '151

REPORT DOCUMENTATION PAGE	Form Approved OMB No. 0704-0188

1a. REPORT SECURITY CLASSIFICATION UNCLASSIFIED	1b. RESTRICTIVE MARKINGS
2a. SECURITY CLASSIFICATION AUTHORITY	3. DISTRIBUTION/AVAILABILITY OF REPORT
2b. DECLASSIFICATION/DOWNGRADING SCHEDULE	Approved for public release; distribution unlimited.

4. PERFORMING ORGANIZATION REPORT NUMBER(S) ALLISON EDR 13471	5. MONITORING ORGANIZATION REPORT NUMBER(S) AFWAL-TR-88-2046

6a. NAME OF PERFORMING ORGANIZATION ALLISON GAS TURBINE DIVISION General Motors Corp.	6b. OFFICE SYMBOL (If applicable)	7a. NAME OF MONITORING ORGANIZATION Air Force Wright Aeronautical Laboratories Aeropropulsion Laboratory (AFWAL/POSF)
6c. ADDRESS (City, State, and ZIP Code) P.O. Box 420, Indianapolis, IN 46206-0420		7b. ADDRESS (City, State, and ZIP Code) Wright-Patterson AFB, Ohio 45433-6563
8a. NAME OF FUNDING/SPONSORING ORGANIZATION	8b. OFFICE SYMBOL (If applicable)	9. PROCUREMENT INSTRUMENT IDENTIFICATION NUMBER F33615-86-C-2604

8c. ADDRESS (City, State, and ZIP Code)	10. SOURCE OF FUNDING NUMBERS			
	PROGRAM ELEMENT NO 63216F	PROJECT NO. 2480	TASK NO 05	WORK UNIT ACCESSION NO. 01

11. TITLE (Include Security Classification)

High Density Fuel Effects

12. PERSONAL AUTHOR(S)
N.K. Rizk, V.L. Oechsle, P.T. Ross, and H.C. Mongia

13a. TYPE OF REPORT Final	13b. TIME COVERED FROM 9/85 TO 4/88	14. DATE OF REPORT (Year, Month, Day) 18 August 1988	15. PAGE COUNT 173

16. SUPPLEMENTARY NOTATION

17. COSATI CODES			18. SUBJECT TERMS (Continue on reverse if necessary and identify by block number)
FIELD	GROUP	SUB-GROUP	High Density Fuel, Gas Turbine Combustion, Fuel Atomization, Combustor Durability, Emissions, Lean Blowout, Ignition
21	02		
21	05		

19. ABSTRACT (Continue on reverse if necessary and identify by block number)

The purpose of this program was to determine, by combustor rig tests and data evaluation, the effects of the high density fuel properties on the performance and durability of the Allison T56-A-15 combustion system. Four high density fuels in addition to baseline JP4 were evaluated in the effort. The rig test program included: nozzle flow bench testing, aerothermal performance and wall temperature, flame stability and ignition, injector coking and plugging, and flow transient effect.

The data evaluation effort involved the utilization of empirical correlations in addition to analytical multidimensional tools to analyze the performance of the combustor. The modifications required to optimize the performance with high density fuels were suggested and the expected improvement in performance was evaluated.

20. DISTRIBUTION/AVAILABILITY OF ABSTRACT ☐ UNCLASSIFIED/UNLIMITED ☐ SAME AS RPT. ☒ DTIC USERS	21. ABSTRACT SECURITY CLASSIFICATION UNCLASSIFIED
22a. NAME OF RESPONSIBLE INDIVIDUAL Curtis M. Reeves	22b. TELEPHONE (Include Area Code) 513 255-3524 — 22c. OFFICE SYMBOL AFWAL/POSF

DD Form 1473, JUN 86 — Previous editions are obsolete. — SECURITY CLASSIFICATION OF THIS PAGE

(3) this document shall be referred to AFWAL/POSF, WPAFB OH 45433-6563

DTID
COPY
INSPECTED
4

Accession For

NTIS GRA&I	☑	
DTIC TAB	☐	
Unannounced	☐	
Justification		

By *per telecon*

Distribution/

Availability Codes

	Avail and/or	
Dist	Special	
A-1		

Delete the Export Control statement in
Block 16 of the DD Form 1473
Per Ms. Wilma Hall, AFWAL/IST (STINFO)

SUMMARY

The purpose of this program was to determine, by combustor rig tests and data evaluation, the effects of property variations of high density fuels on the performance and durability of Allison Gas Turbine's T56-A-15 combustion system. In addition to baseline JP4 fuel, four high density fuels were evaluated in the effort. The largest increase of volumetric heating value reported for these fuels, above that of JP4, was about 11 percent. The hydrogen content of these fuels varied from 12.38 to 14.47 percent, and the aromatic content covered a range between 9.1 and 32.3 percent. The initial to end boiling point ranges were 296-577 K for JP4, and 373-683 K for the highest density fuel studied. The viscosity of the highest density fuel was almost three times higher than the JP4. The fuel surface tension also varied over a wide range.

The rig test program included nozzle flow bench testing, aerothermal performance and wall temperature, flame stability and ignition, injector coking and plugging, and fuel flow transient effect. The tests were conducted at idle, cruise, maximum cruise, and takeoff, in addition to altitude relight conditions.

Wall temperature measurements and analysis indicated that the highest temperatures occurred in the transition section and in regions away from cooling slots. The fuel with the lowest hydrogen content produced the hottest temperatures on liner walls and dome. An increase of up to 80 K was observed in some locations over those of JP4. For this fuel, the stress analysis showed that the liner would have considerably less low cycle fatigue life compared to JP4. Turbine vane oxidation penetration, and blade stress rupture characteristics were also dependent on fuel type with varying degrees.

At low power modes the emissions of carbon monoxide (CO) and unburned hydrocarbon (UHC) were found to be dependent on the fuel properties relevant to atomization and evaporation. The nitrogen oxide (NO_x) data analysis at high power showed less dependency on fuel physical properties. Smoke presence in exhaust gases was affected by fuel chemical properties such as smoke point,

aromatic, naphthalene, and hydrogen content. It was also found that inadequate mixing in the combustion zone was a significant factor in the high smoke levels observed for the combustor.

The fuel properties had little effect on combustion efficiency and combustor exit temperature profile. Sea level and altitude ignition, however, showed strong dependence on such parameters as vapor pressure and boiling temperatures, in addition to atomization quality. Similar trends were observed for flame stability data.

Fuel flow transient test, nozzle fouling, and combustor system coking results all showed minor effects due to fuel type. However, some variation in the circumferential fuel distribution was observed after using the nozzle in the fouling test of the high density fuels.

The data analysis included the use of the correlations presented in the report AFWAL-TR-84-2104 with some modifications to extend their applicability to the high density fuels. The prediction capability of the correlations was enhanced by incorporating detailed spray and evaporation calculation approaches, and the appropriate modifications to address the high density fuels properties. In addition, a combustor performance model that combines multidimensional combustor codes with proven correlations was utilized in an effort to provide insight into the combustor flow field and to aid in defining the changes needed in the system to eliminate unfavorable characteristics attributed to the high density fuels.

Modifications to the liner were proposed to improve the combustion characteristics and liner life when operating with high density fuels. The analysis, based on a combustor performance model, confirmed the importance of these changes to the combustor performance and durability.

FOREWORD

TABLE OF CONTENTS

TABLE OF CONTENTS (concluded)

LIST OF ILLUSTRATIONS

LIST OF ILLUSTRATIONS (cont)

LIST OF ILLUSTRATIONS (cont)

LIST OF ILLUSTRATIONS (cont)

LIST OF ILLUSTRATIONS (concluded)

LIST OF TABLES

I. INTRODUCTION

The main objective of the effort to design and develop a gas turbine combustion system has been always to achieve the required performance goals and structural durability. The combustor, thus, should perform satisfactorily at low power conditions and demonstrate acceptable ignition, lean blowout performance, and exit temperature profile. It is equally important to minimize exhaust emissions and nozzle and liner wall carboning. To formulate a combustor design approach that can be followed to satisfy the conflicting design requirements, a more thorough understanding of the flows within the system and the important processes of fuel injection and combustion is needed. For conventional aviation fuels, both empirical and analytical design methods are currently being employed with varying degrees of success to predict the performance of existing combustors and develop new concepts.

The trend toward the use of heavier fuels is largely a question of availability of lighter feedstocks as the next century approaches. The competition for the light petroleum feedstocks will continue from the automotive and petrochemical industries, forcing refineries to use heavier petroleum fractions. Alternative sources of energy, such as oil shale, tar sands, and coal also produce higher boiling, heavier synthetic crudes having similar properties. In addition to the availability issue, a strategic benefit arising from the use of high density fuels is the increased aircraft range that is possible due to the increased volumetric energy of the fuel.

The high density fuels are characterized by being more viscous, naphthenic and aromatic. These properties have been shown to affect the gas turbine combustion process in varying degrees, depending to a large extent on the design configuration baseline combustor and the quantity of the sensitive properties. The degree of impact on performance of burning such a high density fuel may, therefore, depend upon the particular combustor under test.

1

In general, the high aromatic content of the high density fuels would be expected to increase flame soot formation due to the stable high carbon-to-hydrogen (C/H) ratio of the benzene ring present in aromatic compounds. Flame sooting would significantly affect flame radiation, which, in turn, may affect liner temperature and durability. On the other hand, the higher viscosity and surface tension of these fuels would result in larger drop sizes in spray with attendant effects on ignition and flame stability. These would also be influenced by the distillation ranges of the high density fuels that are characterized by higher boiling points. Fuel nozzle fouling, combustor elements carboning, and turbine guide vane and blade life are some of the other parameters that may be affected by the fuel properties.

A typical empirical approach to analyze the alternative fuel results involves the efficient use of empirical correlations that are based on a wide experimental data base. Such an approach was successful in correlating the combustion data of 12 test fuels that included a baseline JP4, JP8, 5 blends of JP4, and 5 blends of JP8, in addition to a diesel fuel that approximated the Experimental Reference Broadened Specification (ERBS) aviation fuel. The results of this effort were presented in the technical report AFWAL-TR-84-2104 (Reference 1).

Extensive application of the analytical models has been used as a design aid in the development phases of combustors. These models account for the various physical and chemical processes occurring within the flow field, including turbulence and scalar transport, spray dynamics, evaporation and mixing, and hydrocarbon combustion chemistry (Reference 2). Significant advances are needed, however, in physical submodels and in the mathematical simulation of practical gas turbine hardware. This is to enhance the model capability to accurately predict the complex reacting flows encountered in gas turbine combustors. By combining these analytical models with the predictive tool of the proven empirical correlations, the applicability of these correlations would be extended to cover a wider range of fuel properties and would sense the impact of systematic modifications to the details of the combustor on its performance.

2

The Allison T56 engine combustion system was selected for evaluation since this engine has operated for a very large number of Air Force flight hours and will continue to operate as a transport aircraft engine for many more years. This engine has a well-documented test and operating statistical data base.

In order to accomplish the overall program objective of evaluating the effects of broadened property fuels on the T56-A-15 combustor performance and durability, extensive testing on a single-burner combustor rig was carried out (Reference 3). The data evaluation phase included the utilization of the empirical correlations and the analytical tools to describe the observed performance trends. Finally, the modifications required to optimize the combustion performance with high density fuels were suggested, and the expected improvement in performance was evaluated.

II. HIGH DENSITY FUEL PROPERTIES

The current Air Force requirements dictate the use of a low flashpoint, high volatility, low viscosity fuel designated JP4 and described by MIL-T-5724M. It is a petroleum distillate produced from relatively light high paraffin content feedstocks. Since these light petroleum feedstocks are becoming scarce, the Air Force is investigating the feasibility of developing a higher density fuels alternative for JP4.

The basic differences in chemical and physical properties of the high density fuels over JP4 is derived from their origination in heavier feedstocks. These feedstocks tend to be more viscous and dense and have a higher naphthenic and aromatic content. Near term sources of high density fuels are found in refinery byproduct streams such as light pyrolysis fuel oil and light cycle oil stock. Longer term sources are found in heavy oils, tar sands, and coal liquids.

The increased density of these fuels over JP4 is the result of the greatly increased volumetric concentrations of aromatic and cycloparaffinic (naphthenic) compounds, which have a higher carbon-to-hydrogen (C/H) ratio than the predominately paraffinic JP4. As a result of the higher C/H ratio, volumetric energy is increased and volatility decreased. Volumetric energy increase could be translated into range increases up to 15 percent for some volume limited aircraft.

Most property changes associated with high density fuels require investigation to determine the system performance changes due to the nonspecification fuels. Lower hydrogen content and smoke point, decreased volatility, and increased low temperature viscosity and surface tension may have detrimental effects on the overall combustor performance.

TABLE 1 compares the important chemical and physical properties of the baseline JP4 fuel and four high density fuels, which simulate fuels that could be produced from heavy crudes. These high density fuels produced by Sun Oil are special blends resembling JP8.

4

TABLE 1. Test fuel properties.

Property	JP4 POSF-2415	HDF-1 POSF-2383	HDF-2 POSF-2398	HDF-3 POSF-2414	HDF-4 POSF-2429
Lower heating value					
kJ/m^3	3.287×10^7	3.626×10^7	3.645×10^7	3.669×10^7	3.653×10^7
kJ/kg	43,687	42,661	42,526	42,305	42,240
Density, Kg/m^3					
at 313 K	733	838	845	855	875
at 243 K	782	889	897	907	920
Kinematic viscosity, m^2/s					
at 313 K	0.73×10^{-6}	1.76×10^{-6}	1.77×10^{-6}	1.75×10^{-6}	2.01×10^{-6}
at 253 K	1.64×10^{-6}	7.29×10^{-6}	7.57×10^{-6}	7.60×10^{-6}	8.85×10^{-6}
Surface tension, N/m					
at 313 K	0.0181	0.024	0.0242	0.0244	0.0251
at 263 K	0.0227	0.0281	0.0286	0.0288	0.0292
Distillation, K					
Initial boiling point	296	355	361	383	373
10% recovery	343	433	438	441	456
20% recovery	366	455	457	460	465
50% recovery	410	487	489	493	489
90% recovery	505	554	555	560	534
End point	577	682	666	684	683
Flash point, K	256	326	328	329	335
Freeze point, K	215	235	<235	237	<200
True vapor pressure, kPa					
243 K	0.73	0.0053	0.006	0.0059	0.0053
273 K	2.70	0.056	0.047	0.056	0.049
313 K	16.0	0.560	0.47	0.530	0.49
348 K	51.0	2.70	2.30	2.50	2.30
Thermal conductivity					
W/mK at 323 K	0.118	0.112	0.113	0.113	0.107
at 273 K	0.124	0.118	0.119	0.116	0.111
Specific heat, kJ/kgK					
at 333 K	2.29	1.27	1.48	1.46	1.84
at 273 K	1.95	1.09	1.23	1.26	1.57
Dielectric constant					
at 323 K	1.99	2.14	2.16	2.20	2.20
at 273 K	2.06	2.19	2.23	2.27	2.27

TABLE 1 (concluded).

Property	JP4 POSF-2415	HDF-1 POSF-2383	HDF-2 POSF-2398	HDF-3 POSF-2414	HDF-4 POSF-2429
Hydrocarbon type, vol %					
Paraffins	64.0	14.5	14.2	14.2	1.3
Monocycloparaffins	23.6	35.9	30.6	26.3	20.8
Dicycloparaffins	2.7	35.6	34.3	26.6	56.0
Alkylbenzenes	7.3	8.2	10.8	15.3	7.2
Indans and Tetralins	1.0	4.7	8.4	14.5	13.1
Naphthalenes	0.8	0.6	0.9	2.3	0.9
Olefins	0.7	0.4	0.8	0.7	0.7
Hydrogen content, wt %	14.47	13.31	12.93	12.38	12.47
Sulfur, wt %	0.026	0.006	0.007	0.022	0.004
Smoke point, mm	28.0	15.0	13.0	10.0	12.0
Corrosion Cu strip 2 hr at 373 K	1A	4A	4A	4A	4A

III. TEST AND DATA EQUIPMENT

3.1 T56-A-15 TURBOPROP ENGINE AND COMBUSTOR DESCRIPTION

The T56-A-15 engine consists of an internal combustion gas turbine power sec-
tion connected to a single reduction gear assembly having a single propeller
shaft offset above the power section centerline. The power section has 6 com-
bustion chambers of the through-flow type assembled within a single annular
chamber, and incorporates a 14-stage axial flow compressor directly coupled to
a 4-stage air cooled turbine.

The currently produced T56-A-15 engine is rated at 3609 kW shaft power. Its
power section, shown in Figure 1, is an axial flow unit of 9.6:1 compression
ratio and about 15.0 kg/s airflow at sea level takeoff conditions. The burner
outlet temperature is controlled to 1350 K. The flight start limits are
10,675 m for JP4, and 7,625 m for JP5, and maximum altitude is 16,775 m.

The combustion system of the T56-A-15 engine is shown in Figure 2. The radial
position of each can is set, at the inlet end, by a fuel nozzle centered within
a flared fitting in the dome, and in the exhaust end by the combustor transi-
tion engaging the turbine inlet vane assemblies. Axial positioning is accom-
plished by the igniter plugs in two cans, and dummy igniter plugs in the re-
maining four cans. Six cross-over tubes interconnect the cans and provide
flame transfer for starting. The six fuel nozzles are connected to a fuel
manifold attached to the external surface of the outer case.

The conventional design features of the combustor are as follows:

o dome air entry holes backed by baffles to induce a circular flow pattern
   across the hot face of the dome
o film cooling slots formed by overlapped wall segments
o dome-center-mounted fuel nozzle
o three rows of primary orifices
o nonuniform dilution hole spacing for gas temperature pattern control

7
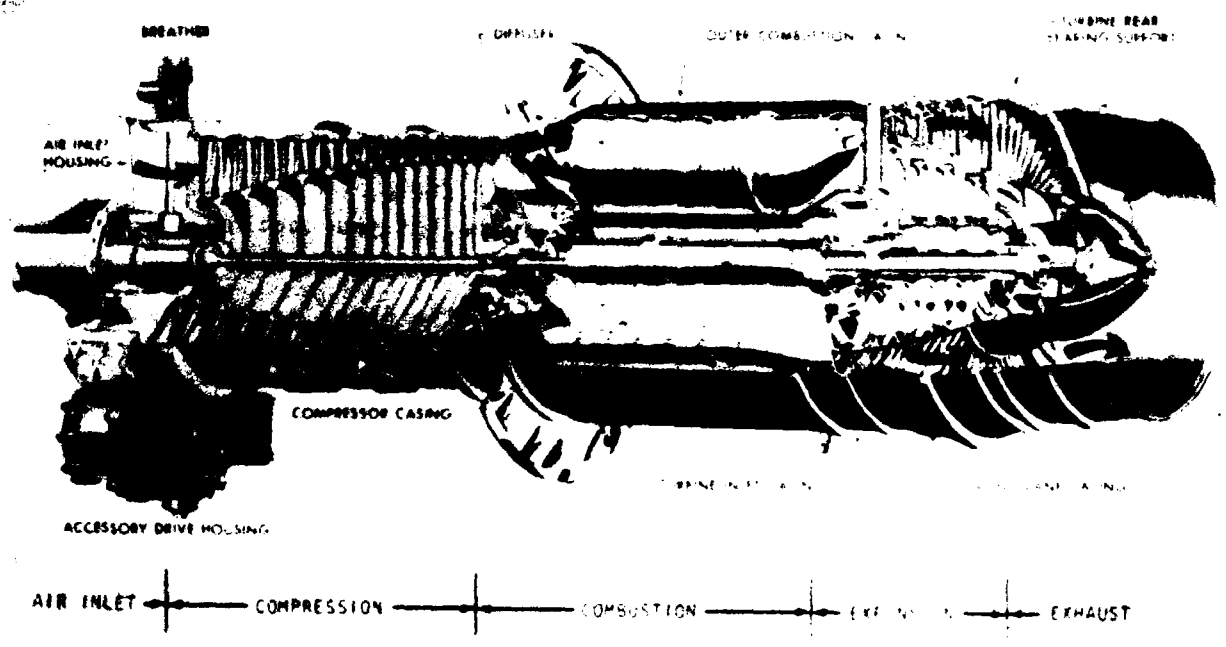
Figure 1. T56-A-15 engine airflow and combustion sections.
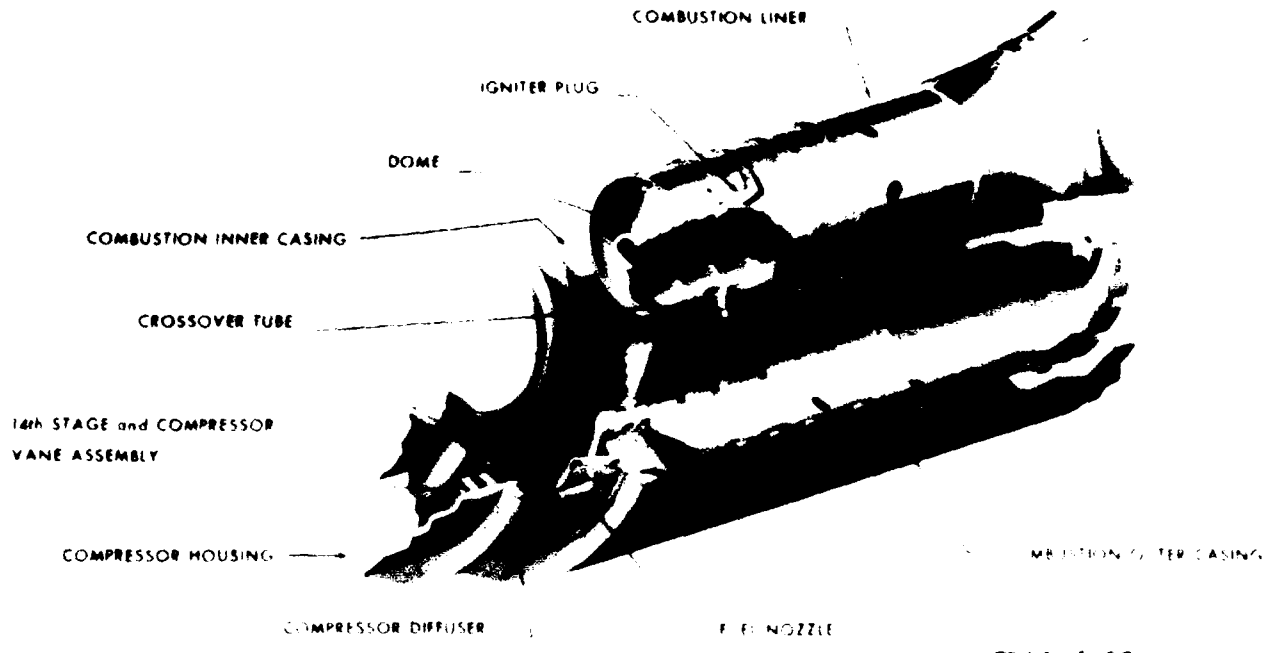
Figure 2. Combustion chamber details.

8

The design features of the combustor liner, along with the predicted airflow distribution, are shown in Figure 3. The film-cooled corrugated stacked ring combustor is 0.6 m long and 0.14 m in diameter.

The fuel injector used with the production liner is an air-assist dual-orifice, pressure atomizing type with an internal switching valve that opens the small pilot orifice for low fuel flows. For high flows, the main fuel section of the nozzle is operational in addition to the pilot. The liner pressure drop is utilized to provide airflow through the atomizer to assist in atomization at start and low power operation. The details of the fuel injector design and flow capacity are presented in the data evaluation section.

3.2 T56-A-15 SINGLE-COMBUSTOR RIG

The Allison T56-A-15 single-burner rig is fabricated from heavy duty stainless steel, and the hot sections are water-cooled for operation at climbout and takeoff conditions. The rig has a flow path that simulates the engine. The rig axial cross-section is designed to the exact dimensions of a 60-degree engine segment, including the compressor discharge passage, diffuser air passage, outer and inner cases, and the turbine inlet passage.

The instrumentation and measuring equipment used in the combustor rig are given in TABLES 2 and 3.

TABLE 2. T56-A-15 single-burner rig instrumentation.

	No. of rakes	Elements/rake
Inlet		
Rig inlet total pressure	2	1
Diffuser inlet total pressure	1	5
Rig inlet temperature	2	1
Fuel inlet	1	1
Outlet		
Burner out	10	3
Exhaust emissions (probes also provide outlet total pressure)	5	4

TABLE 3. T56-A-15 combustor rig instruments.

Measurement	Instrument
Airflow	
Rig inlet	Standard thin plate orifice
Rig bleed	Standard thin plate orifice
Fuel flow	
Rig fuel	Flotron
Exhaust emissions	
Carbon monoxide (CO)	Beckman Model 865-NDIR
Unburned hydrocarbons (UHC)	Beckman Model 402-heated FID
Total nitrogen oxides (NO_x)	TECO Model 10A-CL
Carbon dioxide (CO_2)	Beckman Model 864-NDIR
Smoke	ARP 1179 procedure
Infrared radiation	
Primary zone	Leeds & Borthurp thin film Rayotube—Model 8890 series

The T56 combustor rig is instrumented for radiation measurements as shown in Figure 4. The primary combustion zone is viewed through the liner flame cross-over ferrule at a plane 0.09 m downstream from the combustor dome plane. Gaseous emissions of CO, CO_2, NO_x, and UHC from the combustor rigs were determined by methods consistent with ARP 1256 using the Allison emission instrument system arrangement shown in Figure 5. Smoke emissions were measured by ARP 1179 procedure using the smoke sampling system shown in Figure 6.

The T56-A-15 combustion liner was coated with the following two thermal paints: TP-8 (low temperature resolution) around the cylindrical portion, and TP-6 (high temperature resolution) around the transition. After the liner paint test, the combustor was instrumented with 30 C/A type thermocouples. The location and identification of each thermocouple is given in Figures 7 and 8.

The Allison combustion test facility is shown in the block diagram of Figure 9. Figure 10 is a schematic diagram showing the air supply system which includes air heaters, airflow control, and measurement and pressure controls. Air can be supplied to this facility at 2069 kPa and 54 kg/s. A portable fuel supply system was used for the high density fuel testing and shown in Figure 11. The fuel
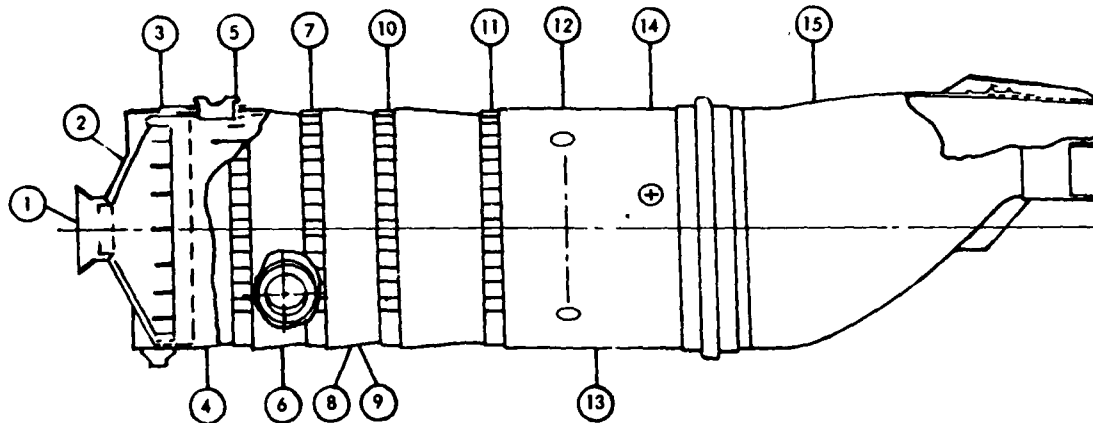
Station		Airflow--%
1.	Fuel nozzle	1.70
2.	Dome	7.53
3.	Cooling corrugation	17.62
4.	Primary holes	3.04
5.	Cooling corrugation	8.81
6.	Primary holes	3.58
7.	Cooling corrugation	8.66
8.	Cooling baffles	2.13
9.	Primary holes	5.72
10.	Cooling corrugation	7.72
11.	Cooling corrugation	7.72
12.	Dilution holes	11.83
13.	Cooling baffles	2.21
14.	Dilution holes	7.75
15.	Cooling baffle	1.10
16.	Exit gap	2.90

Summary	
Combustion	24.21%
Dilution	19.58%
Cooling	59.79%

TE83-2815A

Figure 3. T56-A-15 combustor air distributions.

system was drained and purged before each test by adding 0.11 m^3 (30 gal) of the next test fuel into the supply tank and recirculating the fuel through the system. All of the fuel in the system was then drained and the process repeated. Finally, the fuel supply tank was filled with the test fuel. A similar purging procedure was used for the fuel nozzle before installation in the combustor rig.

The compositional integrity of each test fuel was maintained by following established Allison procedures for testing of experimental fuels in combustor test rigs. Tee fittings were installed in the fuel supply lines just prior to the fuel nozzle inlet fittings to facilitate taking the required fuel samples.
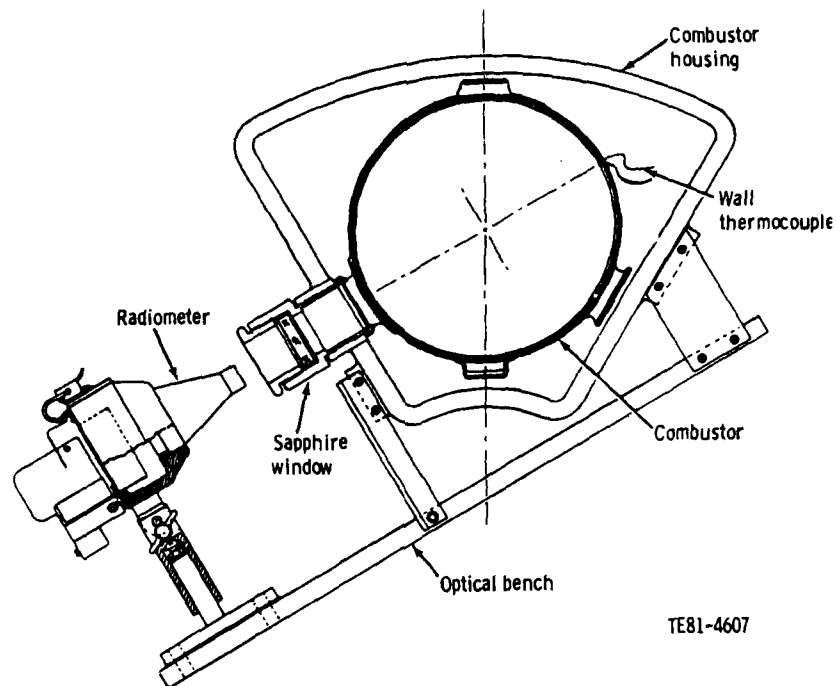
Figure 4. Configuration of flame radiation instrumentation.
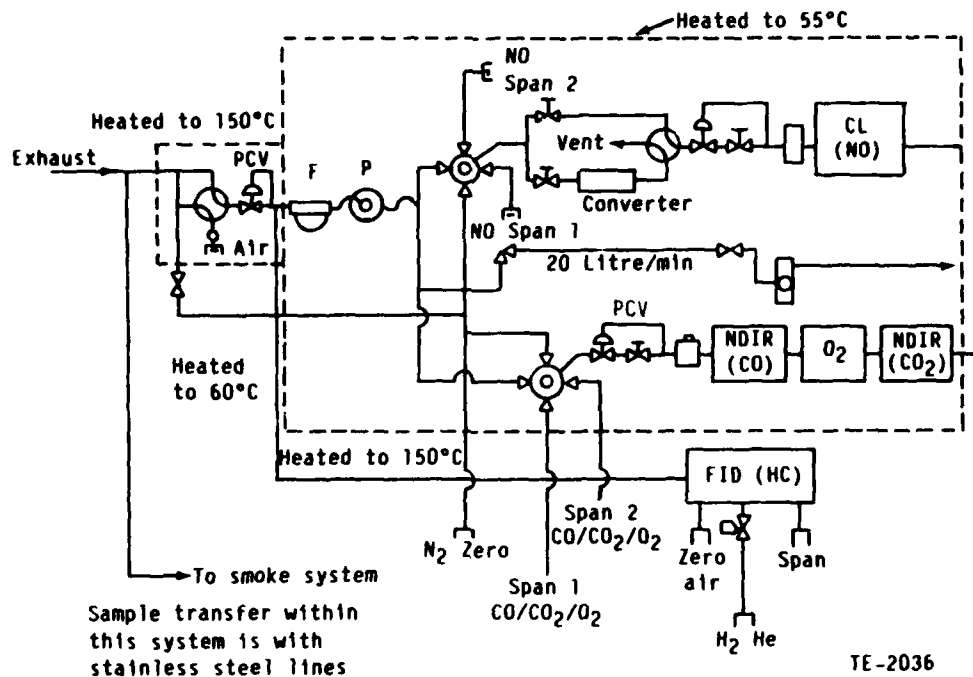
Figure 5. Emission instrument system arrangement (EPA aircraft system).
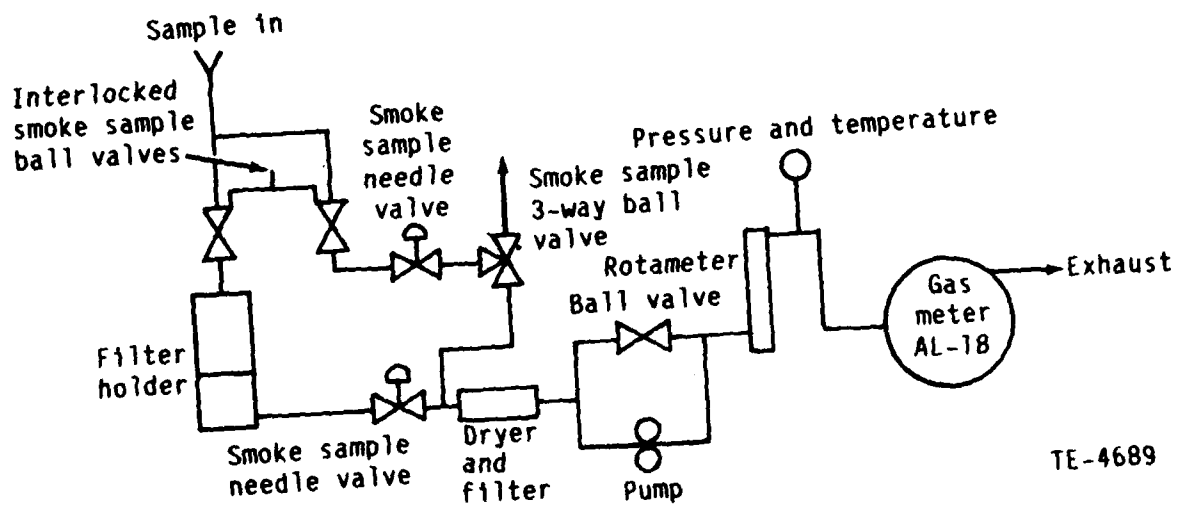
Figure 6.   Smoke sampling system schematic.
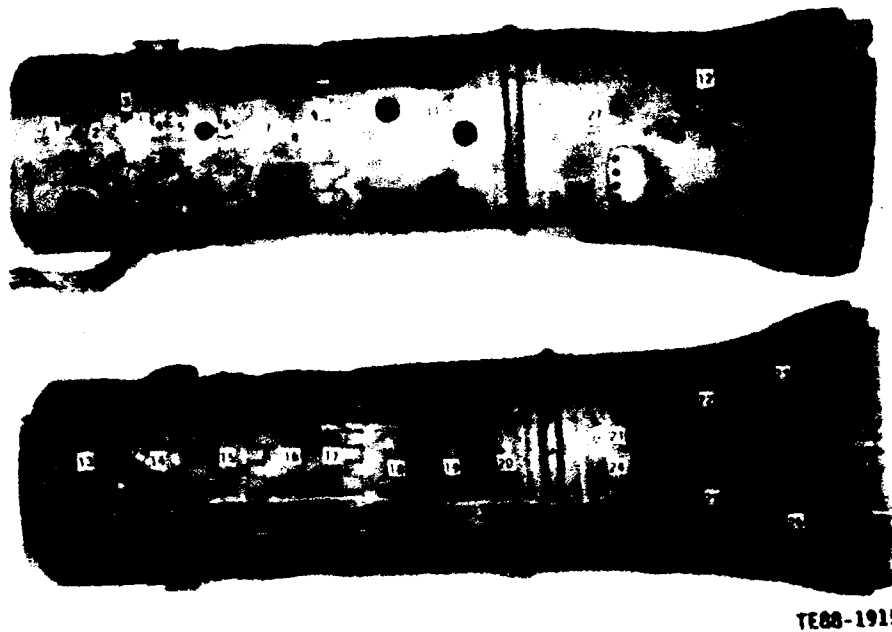
Figure 7.   Thermocouple locations on liner and transition walls.
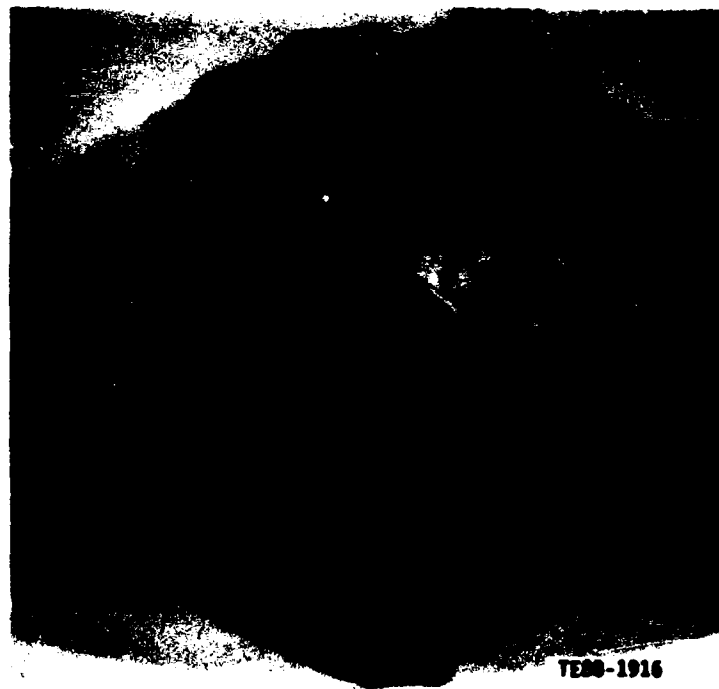
Figure 8. Thermocouple locations on combustor dome.

1E87-2593
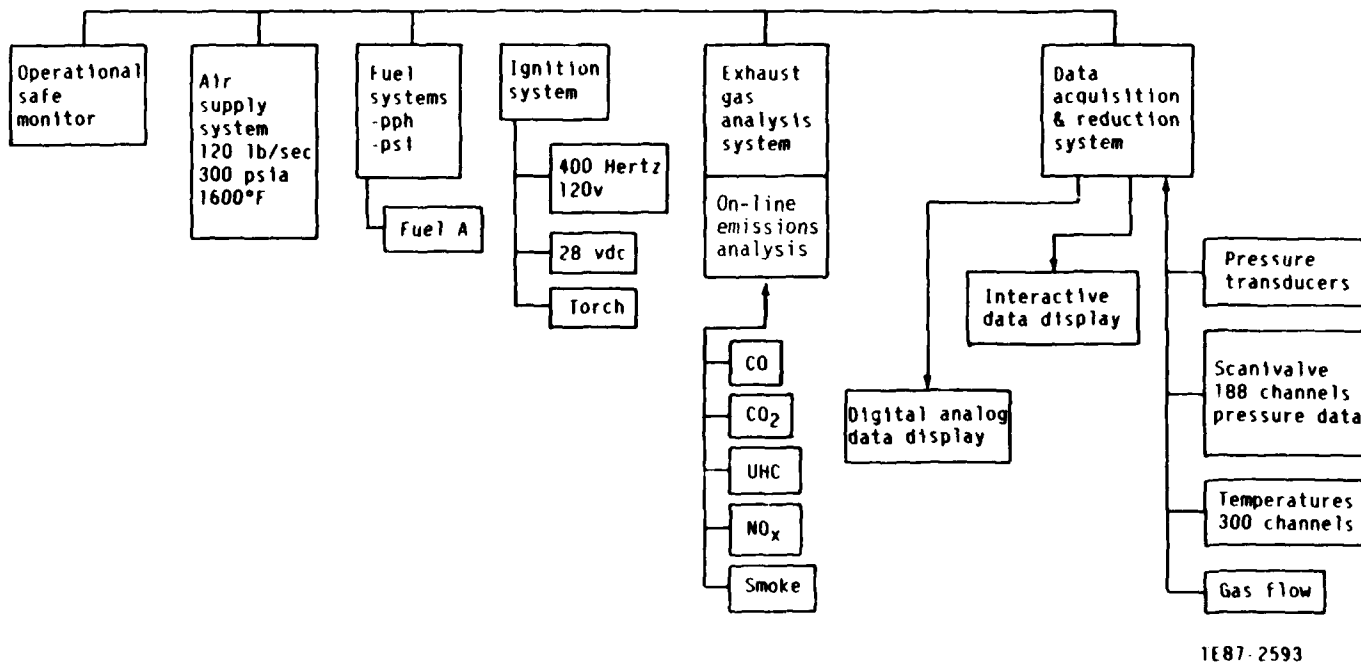
Figure 9. Combustion test facility block diagram.
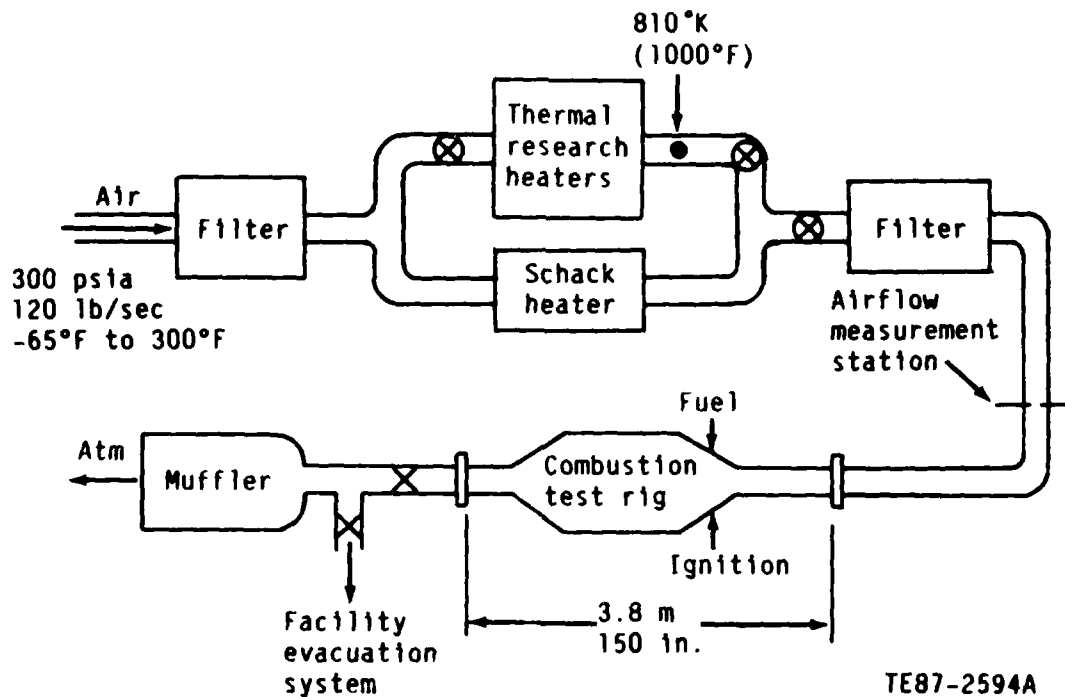
Figure 10. Combustion test facility schematic.
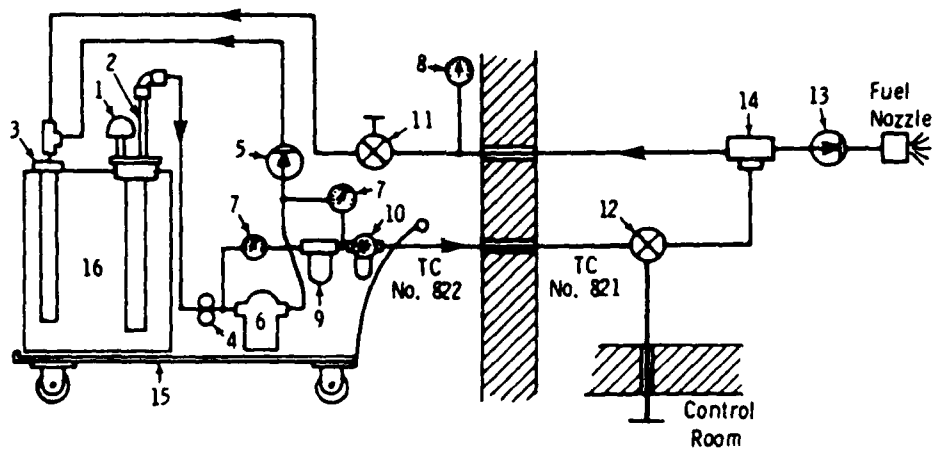
1 Flame Arrester-Vent	7 Gage, Filter ΔP	13 Check Valve
2 Suction Tube	8 Gage, Pump Discharge Pressure (600 psig)	14 Three-Way Valve
3 By-Pass Return	9 Filter, J71—10 micron	15 Cart
4 Pump	10 Flow Meter—Potter	16 Fuel Drum
5 Pressure Relief Valve	11 Needle Valve	
6 Skinner Filter	12 Needle Valve	TE-2019

Figure 11. Schematic of portable supply rig for experimental fuels.

15

Fuel samples were taken and sent to the Allison fuels laboratory before each series of tests for analysis.

The combustor rig data acquisition and reduction system used in the current program have the following features:

o direct display pressure gages, manometers, and temperature readout equipment

o SEL 840 computerized static data acquisition system

o capability of measuring and recording up to 200 channels of temperature data

o quick look (Silvertone) data display of test data including various routines for calculation of flows, temperature rise, etc

o centralized dynamic monitor and recording system stress and vibration magnetic tape recording and on-line diagnostic signal analysis

The SEL 840 system is linked with an IBM 370/168 computer that was used for data storage and processing.

3.3 FUEL SPRAY ANALYSIS FACILITY

The fuel spray characteristics were measured in the Combustion Laboratory at Purdue University, School of Mechanical Engineering. The apparatus used for studying spray characteristics is shown schematically in Figure 12. The atomizer under test was located at the top of the cylindrical pressure vessel and sprayed downward into the vessel. The vessel was pressurized to the desired level of primary-zone gas density using gaseous nitrogen tapped from a liquid nitrogen storage/evaporator system. Nitrogen was used instead of air to avoid the risk of explosion at high pressures.

The droplets produced by atomization gravitated into a collection tank at the bottom of the chamber, from where the fuel was returned to the fuel storage tank. The chamber is fitted with several pairs of diametrically opposed quartz windows in order to provide optical access at several distances downstream of

16
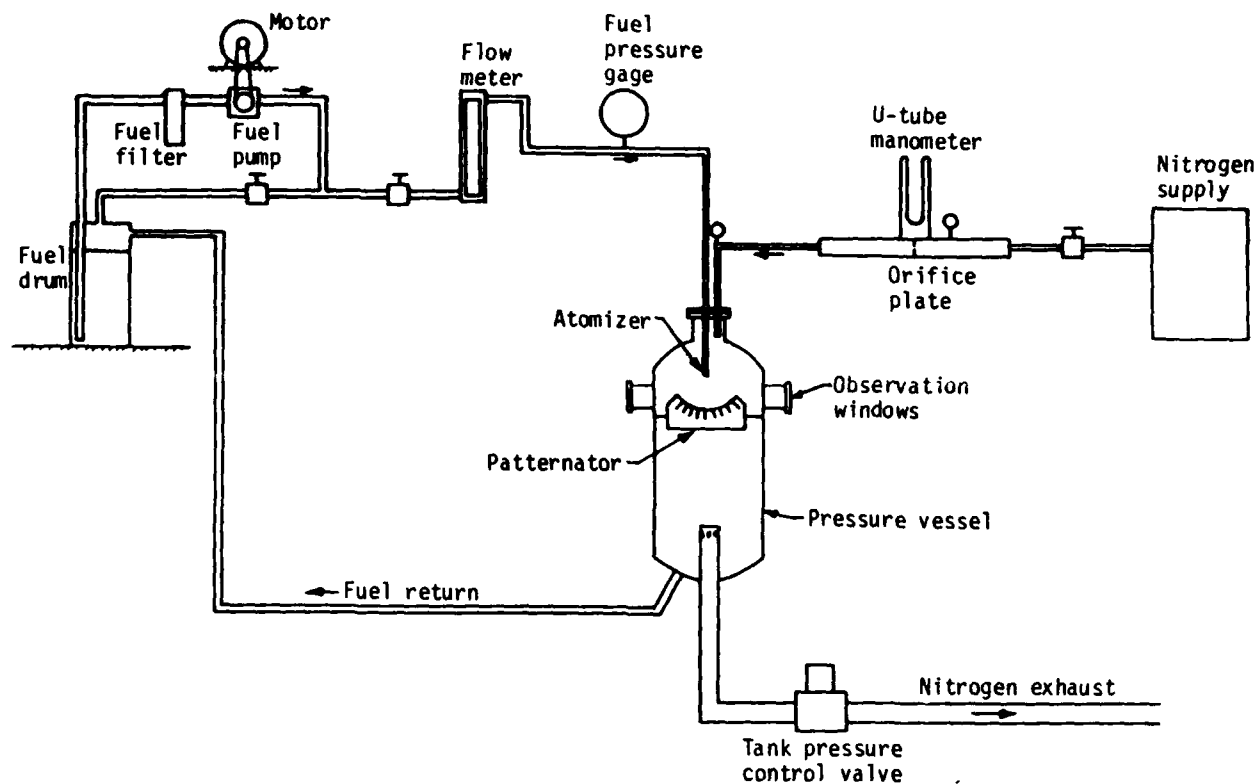
TE85-3137

Figure 12. Basic test facility for measurement of spray characteristics.

the atomizer. Measurements of drop sizes in spray utilized a Malvern spray analyzer, Model 2600D. Spray angle and radial fuel distribution were measured using a patternator of the type illustrated in Figure 13. This patternator is made of steel and consists of 29 sampling tubes spaced 4.3 deg apart on a 0.10 m radius. The volume of fuel in each tube was measured by visually locating the meniscus between lines scribed into the surface of the patternator. Provision was made for each nozzle to be "clocked" on its axis at intervals of 90 degrees to detect the asymmetry in spray.

Circumferential fuel distribution was measured at Allison using a patternator consisting of a round container divided into 12 equal sectors. The fuel

17
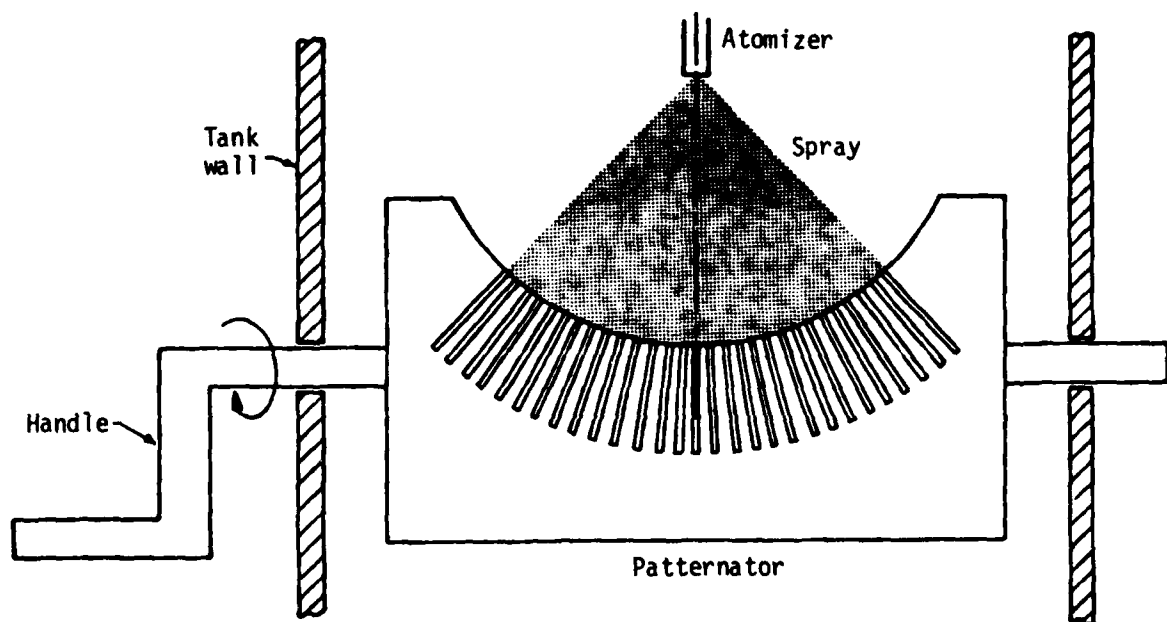
TE85-3138

Figure 13. Schematic diagram of patternator for measuring radial fuel
distribution.

collected in these sectors gives the circumferential fuel distribution. These
measurements were part of the nozzle fouling tests to determine the influence
of burning the high density fuels on the flow characteristics of the nozzles.

18

IV. COMBUSTION AND SPRAY TESTING

4.1 GENERAL TEST PLAN

The rig test program of the JP4 and the four high density fuels included the following:

o nozzle flow bench testing

o aerothermal performance and wall temperature characteristics at the sea level static (SLS) ground idle, altitude cruise, maximum cruise, and take-off conditions

o lean flame extinction characteristics at sea level idle and subidle flow conditions

o sea level ignition and altitude relight characteristics

o combustor cyclic testing

o injector coking/plugging testing at simulated altitude maximum cruise conditions

The nominal test conditions for the single can rig are given in TABLE 4. The ignition tests were conducted over a range of inlet pressure P_3 and combustor flow rate W_{a3} to simulate engine flow conditions during start and acceleration to the steady state sea level idle speed. The cyclic testing included steady-state operation at the 7,625 m altitude maximum cruise flow conditions, but the fuel flow was varied as a step function from 0.0266 kg/s (at maximum cruise) to 0.011 kg/s (corresponding to SLS idle fuel/air ratio).

4.2 AEROTHERMAL PERFORMANCE RESULTS

The aerothermal performance test data is given in TABLES 5 through 8 for the four operating modes.

The data for altitude ignition at 7,625 m test are given in TABLE 9, and the results of sea level ignition and lean flame extinction tests are given in TABLE 10.

TABLE 4. Single can rig test conditions.

	P_3 kPa	$W_{a3.1}$ kg/s	W_F kg/s	T_3 K	T_4 K	F/A
Aerothermal performance						
SLS ground idle	365	1.08	0.011	442	827	0.0099
Takeoff	999	2.34	0.053	605	1391	0.0226
7,625 m altitude cruise	464	1.17	0.021	554	1198	0.0179
7,625 m altitude maximum cruise	494	1.17	0.027	563	1359	0.0227
Lean flame extinction						
SLS idle--subidle	131	0.60	--	306	--	--
Ignition						
SL ignition	108-133	0.22-0.48	--	306	--	--
7,625 m relight	44	0.09-0.24	--	296	--	--
Cyclic testing						
7,625 m altitude max cruise	494	1.17	0.027	563	1359	0.0227

TABLE 5. Combustor rig test--idle.

		JP4 Nozzle 1	HDF-1 Nozzle 1	HDF-2 Nozzle 2	HDF-3 Nozzle 3	HDF-4 Nozzle 4
BIP	kPa	360	363	368	357	363
P_3	kPa	353	356	360	355	355
T_3	K	431	416	431	437	457
W_{a3}	kg/s	1.13	1.13	1.16	1.15	1.16
$W_{a3.1}$	kg/s	1.07	1.06	1.10	1.08	1.11
W_F	kg/s	0.0104	0.0109	0.0108	0.0107	0.0106
F/A mechanical		0.0097	0.0103	0.0099	0.0099	0.0096
BOT average	°K	820	794	794	803	807
BOT maximum	°K	894	869	866	874	871
BOT minimum	°K	744	697	714	726	737
PF		0.19	0.198	0.198	0.194	0.179
CO	g/kg fuel	26.9	39.3	38.3	39.0	38.1
UHC	g/kg fuel	13.6	14.9	15.4	15.3	6.4
NO_x	g/kg fuel	3.9	3.9	3.7	3.7	3.6
CO_2	%	2.3	2.3	2.2	2.2	2.2
Smoke	SAE No.	27.0	48.1	52.6	56.5	53.3
Combustion efficiency %		98.06	97.60	97.60	97.60	98.51
Burner pressure loss %		5.22	4.87	5.16	5.58	5.72

20

TABLE 6. Combustor rig test--cruise.

		JP4 Nozzle 1	HDF-1 Nozzle 1	HDF-2 Nozzle 2	HDF-3 Nozzle 3	HDF-4 Nozzle 4
BIP	kPa	463	468	470	463	463
P_3	kPa	454	459	461	455	455
T_3	K	552	554	552	551	551
Wa_3	kg/s	1.23	1.25	1.26	1.23	1.22
$Wa_{3.1}$	kg/s	1.17	1.18	1.19	1.17	1.15
W_F	kg/s	0.0207	0.0210	0.0214	0.0213	0.0209
F/A		0.0177	0.0178	0.018	0.0183	0.0182
BOT average	K	1196	1177	1183	1188	1192
BOT maximum	K	1331	1284	1288	1304	1301
BOT minimum	K	1033	1056	1038	1047	1058
PF		0.21	0.171	0.168	0.181	0.171
CO	g/kg fuel	6.7	10.5	10.7	10.4	13.0
UHC	g/kg fuel	0.8	2.3	3.0	2.6	3.5
NO_x	g/kg fuel	6.3	5.9	6.3	6.2	6.5
CO_2	%	4.0	4.0	4.0	4.2	4.0
Smoke	SAE No.	23.4	40.3	48.7	53.3	48.1
Combustion efficiency %		99.74	99.50	99.43	99.48	99.32
Burner pressure loss %		4.77	4.81	4.78	4.91	4.64

The thermocouple readings of the liner wall temperatures are given in TABLES 11 and 12 for the four power modes.

Primary zone radiation results are available in TABLE 13.

4.3 NOZZLE FOULING RESULTS

The results of the fuel nozzle flow calibration test before and after the nozzle fouling test are given in TABLE 14. The test involved running the combustor continuously for two hours at maximum cruise conditions for each fuel, then the nozzle was removed and flow calibrated using a standard test fluid. Circumferential patternation was also measured for all nozzles. Examples of these measurements are given in the data evaluation section.

TABLE 7. Combustor rig test--maximum cruise.

		JP4 Nozzle 1	HDF-1 Nozzle 1	HDF-2 Nozzle 2	HDF-3 Nozzle 3	HDF-4 Nozzle 4
BIP	kPa	490	499	492	491	496
P_3	kPa	482	491	484	495	488
T_3	K	564	563	559	561	561
Wa_3	kg/s	1.24	1.23	1.24	1.22	1.24
$Wa_{3.1}$	kg/s	1.18	1.18	1.18	1.16	1.17
W_F	kg/s	0.0263	0.0265	0.0267	0.0229	0.0261
F/A		0.0224	0.0225	0.0227	0.0229	0.0222
BOT average	K	1351	1326	1329	1338	1323
BOT maximum	K	1528	1473	1481	1496	1467
BOT minimum	K	1123	1146	1120	1133	1142
PF		0.227	0.191	0.197	0.204	0.189
CO	g/kg fuel	4.5	6.6	6.9	7.1	7.9
UHC	g/kg fuel	0.4	0.9	1.0	0.5	1.3
NO_x	g/kg fuel	6.3	6.3	6.7	6.9	7.3
CO_2	%	5.1	5.2	5.2	5.4	5.0
Smoke	SAE No.	23.4	38.3	47.4	53.3	48.7
Combustion efficiency %		99.84	99.73	99.71	99.75	99.65
Burner pressure loss %		4.51	4.30	4.42	4.26	4.30

4.4 SPRAY CHARACTERISTICS RESULTS

The radial fuel distribution of all nozzles was measured using a radial patternator. The nozzle under test was rotated at 90-degree intervals to examine the symmetry of the spray. The calculated equivalent spray angle is given in TABLE 15. This angle is the sum of two angles, $\phi = \phi_L + \phi_R$, where ϕ_L and ϕ_R represent the positions of the center of mass material of left and right lobes of the fuel distribution curve, respectively.

The data obtained for the drop sizes in spray are presented and discussed in the data evaluation section of this report.

TABLE 8. Combustor rig test--takeoff.

		JP4 Nozzle 1	HDF-1 Nozzle 1	HDF-2 Nozzle 2	HDF-3 Nozzle 3	HDF-4 Nozzle 4
BIP	kPa	1000	1000	993	1000	1000
P_3	kPa	986	986	979	986	979
T_3	K	606	606	603	606	602
Wa_3	kg/s	2.49	2.46	2.48	2.46	2.49
$Wa_{3.1}$	kg/s	2.36	2.36	2.34	2.33	2.37
W_F	kg/s	0.0530	0.0529	0.0533	0.0533	0.0532
F/A		0.0225	0.0226	0.0227	0.0228	0.0224
BOT average	°K	1407	1396	1402	1396	1379
BOT maximum	°K	1592	1561	1567	1556	1532
BOT minimum	°K	1210	1204	1195	1204	1187
PF		0.232	0.209	0.207	0.204	0.197
CO	g/kg fuel	1.2	1.4	3.1	2.5	1.6
UHC	g/kg fuel	0.1	0.4	0.4	0.1	0.9
NO_x	g/kg fuel	10.3	11.0	12.3	12.2	11.9
CO_2	%	5.3	5.3	5.6	5.5	5.3
Smoke	SAE No.	37.0	40.3	48.1	53.3	52.0
Combustion efficiency %		99.92	99.89	99.84	99.88	99.82
Burner pressure loss %		4.39	4.30	4.15	4.19	4.36

TABLE 9. Altitude ignition test at 7,625 m.

Fuel	P_3 kPa	T_3 °K	$Wa_{3.1}$ kg/s	F/A mechanical fired	F/A mechanical no fire
JP4	42.3	297	0.090	0.0097	
	43.9	297	0.160	0.0088	0.0081
	42.7	296	0.204	0.0121	0.0117
	42.6	296	0.234		0.038
HDF-1	43.1	296	0.092	0.0140	0.0129
	43.4	296	0.154	0.0139	0.0132
	42.4	295	0.206	0.0174	0.0162
	42.0	294	0.237		0.0356
HDF-2	42.4	296	0.083	0.0210	0.0193
	43.1	296	0.159	0.0161	0.0154
	41.0	297	0.206	0.0197	0.0184
	42.7	296	0.232		0.0387
HDF-3	42.1	298	0.093	0.0253	0.0239
	42.4	298	0.157	0.0156	0.0146
	42.8	298	0.207	0.0210	0.0202
	42.5	297	0.238		0.0361
HDF-4	42.7	297	0.093	0.0229	0.0215
	42.5	297	0.161	0.0171	0.0153
	41.5	296	0.200	0.0209	0.0198
	42.3	296	0.232		0.0396

TABLE 10. Ignition and lean blowout characteristics at sea level.

Fuel	P_3 kPa	T_3 °K	$Wa_{3.1}$ kg/s	F/A fire	F/A no fire	F/A LBO
JP4	105.9	296	0.241	0.01003	0.00916	
	106.6	296	0.328	0.00946	0.00910	
	111.6	296	0.398	0.00893	0.00850	
	114.8	296	0.459	0.00872	0.00838	
	125.8	296	0.609	0.00748	0.00727	0.00207
HDF-1	106.8	308	0.223	0.01711	0.01611	
	108.3	320	0.327	0.01475	0.01407	
	111.8	312	0.403	0.01561	0.01523	
	115.8	318	0.458	0.01353	0.01292	
	132.1	316	0.591	0.01511	0.01500	0.00336
HDF-2	107.8	303	0.222	0.01511	0.01489	
	107.4	303	0.309	0.01440	0.01364	
	112.5	302	0.399	0.01577	0.01507	
	118.2	302	0.482	0.02045	0.02037	
	133.5	302	0.609	0.02112	0.02068	0.00471
HDF-3	107.8	308	0.213	0.0176	0.01594	
	107.6	308	0.305	0.01428	0.01377	
	112.1	308	0.397	0.01515	0.01486	
	119.2	307	0.487	0.01665	0.01636	
	132.7	305	0.602	0.01907	0.01873	0.00472
DHF-4	108.1	306	0.218	0.02162	0.02037	
	107.6	306	0.308	0.01824	0.01783	
	112.4	306	0.397	0.02042	0.01984	
	118.2	306	0.483	0.02311	0.02258	
	133.1	305	0.604	0.02266	0.02216	0.00477

TABLE 11. Combustor liner wall temperature-- K.

T/C No.	Ground idle					Altitude cruise				
	JP4	HDF-1	HDF-2	HDF-3	HDF-4	JP4	HDF-1	HDF-2	HDF-3	HDF-4
1	492	518	543	566	564	621	657	664	669	664
2	443	434	453	461	475	566	574	576	574	576
3	518	563	596	627	626	675	751	766	779	772
4	445	436	457	464	473	576	590	597	600	598
5	401	406	540	428	538	501	529	547	546	537
6	443	433	451	458	467	576	589	596	600	596
7	497	517	538	543	538	684	742	784	797	776
8	510	521	522	540	540	711	754	768	807	791
9	444	432	447	455	464	581	592	598	602	596
10	472	473	487	493	497	646	696	717	703	687
11	512	506	518	533	540	691	724	742	758	742
12	686	660	672	683	690	949	937	948	960	952
13	496	511	560	578	574	629	689	705	711	710
14	501	526	548	558	561	650	700	726	724	718
15	481	518	523	538	541	647	703	732	729	722
16	460	469	478	485	491	622	669	682	678	669
17	483	503	506	517	519	666	704	731	748	733
18	466	463	477	482	488	641	680	707	698	684
19	479	480	489	498	503	670	696	729	726	714
20	493	491	498	511	516	692	716	736	744	737
21	513	504	511	525	532	712	728	737	744	739
22	553	538	556	564	572	791	791	794	812	805
23	594	578	601	603	607	843	844	854	862	854
24	528	518	523	539	544	738	751	754	768	762
25	611	587	576	600	606	863	853	833	858	862
26	657	635	633	648	651	934	914	899	918	922
27	625	608	617	638	642	866	863	868	889	879
28	551	556	696	613	627	702	722	731	744	746
29	531	548	577	592	605	667	691	701	711	713
30	542	559	591	621	609	702	747	749	763	760

26

TABLE 12. Combustor liner wall temperature-- K

T/C No.	Altitude maximum cruise					Ground takeoff				
	JP4	HDF-1	HDF-2	HDF-3	HDF-4	JP4	HDF-1	HDF-2	HDF-3	HDF-4
1	631	663	668	669	668	682	694	698	707	698
2	577	583	583	586	587	617	618	619	620	617
3	682	760	762	779	782	743	774	778	792	783
4	590	604	607	613	614	628	632	635	637	632
5	514	544	556	570	552	561	585	593	599	632
6	594	609	616	621	617	633	637	642	644	638
7	730	794	843	863	837	793	816	857	863	835
8	777	833	853	905	877	833	854	844	871	854
9	606	619	631	638	627	642	646	651	653	644
10	692	727	762	775	747	751	771	796	797	770
11	754	793	827	848	816	805	834	855	860	834
12	1046	1030	1049	1056	1034	1083	1076	1086	1094	1075
13	627	676	684	699	697	673	667	683	702	690
14	655	728	736	745	734	708	720	744	748	739
15	673	726	758	764	755	724	737	772	773	761
16	658	694	713	728	713	701	718	733	739	727
17	724	770	811	833	803	784	815	849	856	832
18	697	729	761	777	749	756	788	802	809	781
19	743	777	808	831	801	802	838	847	-	827
20	777	813	834	864	835	838	881	875	-	863
21	794	816	823	847	828	842	874	861	-	850
22	888	894	902	923	904	837	950	944	-	921
23	938	941	953	960	945	1010	1013	1012	-	981
24	824	847	853	878	853	878	906	898	-	884
25	967	973	954	986	968	1017	1021	1001	-	997
26	1048	1037	1022	1043	1030	1103	1084	1081	-	1076
27	958	961	973	988	964	985	992	994	-	992
28	725	731	735	745	747	799	793	790	-	790
29	679	692	698	708	713	720	736	724	-	733
30	701	754	766	774	768	773	763	756	-	758

TABLE 13. Primary zone radiative heat loading/radiometer results.

	Emittance W/(cm^2-SR)				
	JP4	HDF-1	HDF-2	HDF-3	HDF-4
Ground idle	4.79	10.46	12.99	10.18	9.45
Cruise	8.44	11.41	15.82	16.08	16.71
Maximum cruise	12.53	13.88	13.13	15.67	17.16
Takeoff	13.46	15.54	14.27	17.58	18.55

27

TABLE 14. Nozzle flow calibration test.
Test fluid: MIL-C-7024 B II

Test point	ΔP_a m H$_2$O	ΔP_f kPa	Fuel flow rate--kg/s					
			Before test nozzle 1	JP nozzle 1	HDF-1 nozzle 1	HDF-2 nozzle 2	HDF-3 nozzle 3	HDF-4 nozzle 4
1	0.11	210	0.0033	0.0033	0.0034	0.0032	0.00328	0.0034
2	0.11	345	0.0043	0.00435	0.00432	0.00415	0.00423	0.00429
3	0.11	414	0.005	0.0049	0.005	0.0046	0.00465	0.00474
4	0.11	485	0.010	0.0103	0.0104	0.0087	0.00845	0.00733
5	0.11	521	0.0125	0.0125	0.01257	0.0111	0.01109	0.0101
6	0.75	695	0.0208	0.0206	0.0209	0.0197	0.0199	0.0194
7	0.75	1038	0.0315	0.0315	0.03155	0.0304	0.0307	0.031
8	0.75	1380	0.0390	0.0386	0.0392	0.0381	0.0387	0.0386
9	0.75	1727	0.0458	0.0452	0.0456	0.0442	0.0455	0.0453
10	0.75	2418	0.0563	0.0562	0.0564	0.0547	0.0559	0.0566
11	0.11	521	0.0123	0.0122	0.01265	0.0113	0.0113	0.0102
12	0.11	414	0.00513	0.0053	0.00529	0.0047·	0.0047	0.0047

TABLE 15. Radial patternation test-angles in degrees.

Fuel flow, kg/s Ambient pressure, kPa	Clock angle, deg	JP4 Nozzle 1		HDF-1 Nozzle 1		HDF-2 Nozzle 2		HDF-3 Nozzle 3		HDF-4 Nozzle 4	
		ϕ_L	ϕ_R	ϕ_L	ϕ_R	ϕ_L	ϕ_R	ϕ_L	ϕ_R	ϕ_L	ϕ_R
0.0021	0	45.8	50.2	48.5	52.2	53.7	50.2	44.9	47.1	53.9	51.5
101.4	90	41.1	43.2	46.2	54.4	50.8	54.4	49.2	50.1	48.9	49.9
	180	43.8	48.0	51.8	52.8	51.5	54.8	48.5	53.5	49.8	52.3
	270	35.0	45.2	52.3	48.4	52.6	52.7	44.9	49.2	51.5	48.4
0.0113	0	35.7	35.2	32.2	39.7	33.2	31.8	25.6	33.4	36.7	36.4
239.3	90	32.8	34.8	27.1	40.4	25.5	34.4	26.7	32.0	30.5	37.6
0.021	0	38.1	38.9	38.1	39.7	37.9	39.1	34.3	38.3	37.5	37.9
239.3	90	31.4	37.4	40.8	44.1	33.3	41.0	31.7	38.6	34.4	41.3
	180	29.8	40.0	34.7	45.5	32.9	41.9	33.3	39.8	31.8	42.6
	270	32.8	38.8	38.4	44.9	36.4	39.3	33.5	38.2	35.5	39.9
0.0266	0	34.3	34.9	37.6	41.7	37.3	39.6	35.6	38.7	37.4	38.8
273.7	90	36.4	40.0	35.8	44.1	34.5	41.5	33.0	39.5	34.7	42.7
0.0529	0	40.3	48.6	45.0	44.2	34.6	35.4	37.9	39.3	32.0	34.8
480.6	90	40.5	47.8	39.1	42.4	34.3	37.4	28.9	38.6	36.2	41.7

V. DATA EVALUATION

In this section, the experimental results obtained during the testing phase of the program are evaluated in regard to the effects of the high density fuels on the combustor performance. The analysis includes the fuel effects on the following terms:

- o spray characteristics
- o combustor performance
  - o gaseous emissions
  - o smoke emissions
  - o combustion efficiency
  - o temperature profile at the combustor exit
  - o combustion stability
  - o ground start and altitude restart
- o 3-D combustor performance model
- o combustor dome and liner temperature
- o carbon deposition within the combustion system
- o fouling of the fuel nozzles
- o fuel flow transient effect
- o combustor and turbine life

Description of the approach adopted in the analysis and the relevant correlations used in this effort are given in the following subsections.

5.1 SPRAY CHARACTERISTICS

The fuel injector used in the T56-A-15 production liner is an air-assist dual orifice, pressure atomizing type and is shown in Figure 14. An internal switching valve on this nozzle opens the main fuel circuit when the fuel pressure exceeds a value of about 448.2 kPa (65 psi). The flow capacities of the pilot and main orifices as given by their flow numbers are 0.00023 and 0.001 kg/s/$\sqrt{\text{kPa}}$ (4.8 and 21.2 lb/hr/$\sqrt{\text{psi}}$), respectively. Figure 15 gives the fuel flow rate at various fuel pressures for the baseline JP4. The high

29
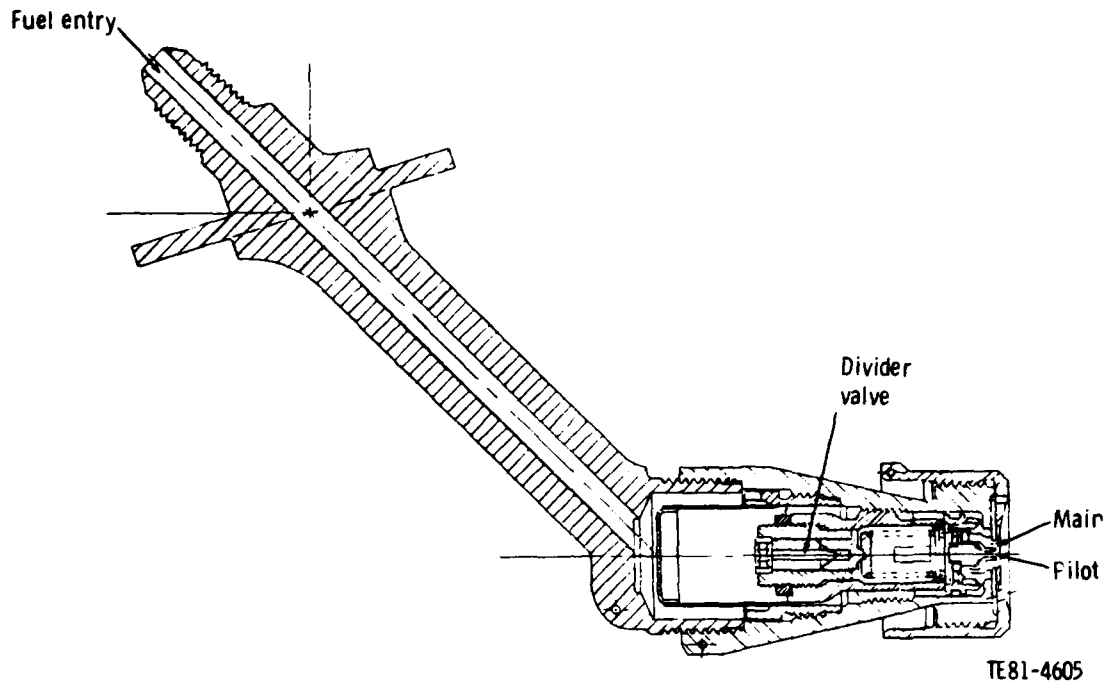
Figure 14.   Dual-orifice fuel nozzle schematic.
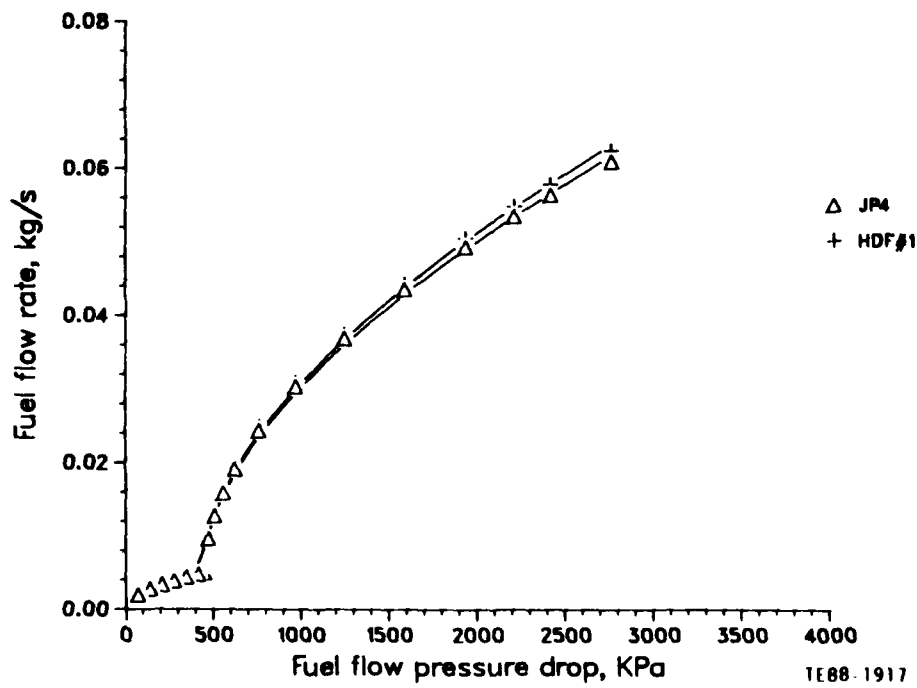
Figure 15.   Nozzle fuel flow characteristics.

density fuels show slightly higher flow rates compared to these of the JP4 type. The airflow characteristics through the atomizer are illustrated in Figure 16. An average effective airflow area calculated from this figure is about 15.03 mm^2 (0.0233 $in.^2$).

The measurements in the spray included the radial fuel distribution (radial patternation), Sauter mean diameter, and drop size distribution. The test conditions were selected to simulate the engine power levels at ground idle, cruise, maximum cruise, and sea level static (SLS) takeoff. Since the measurements are usually difficult at elevated temperature, the tests were conducted at higher levels of ambient pressure that represented the actual air density in the combustor at each power setting. The test conditions are given in TABLE 16.

A number of tests were also conducted at sea level (SL) ignition conditions.

5.1.1 Radial Fuel Distribution

The objectives of the radial patternation tests were to examine the symmetry of the spray produced by the atomizer, and to determine the effects of the high density fuels on the fuel distribution. These required taking the measurements at a number of angle increments starting from a reference nozzle position. One nozzle was used for the testing of JP4 and HDF-1, while each of the other high density fuels was run with a different nozzle. A large number of radial patternation tests were carried out. The main conclusion was that a

TABLE 16. Fuel injector test conditions.

| Engine mode	Fuel mass flow rate kg/s	Ambient pressure kPa
Ground idle	0.0113	293.3
Cruise	0.0210	239.3
Maximum cruise	0.0266	273.7
Takeoff	0.0529	480.6

31
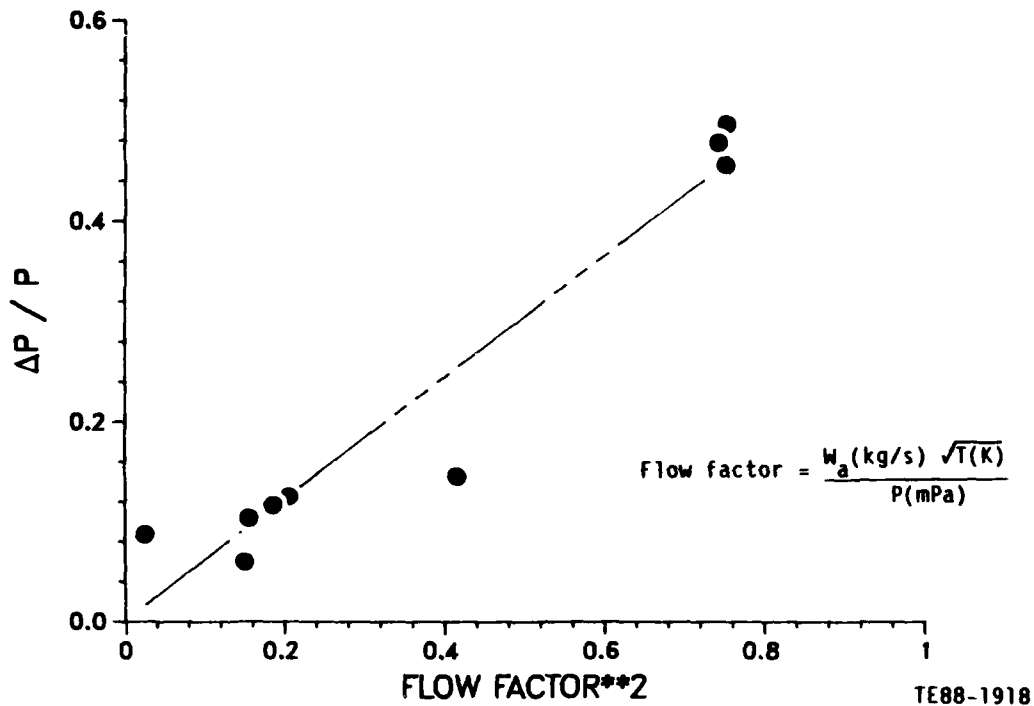
Figure 16. Nozzle airflow characteristics.

spray asymmetry was observed in several cases; however, under most conditions
the spray demonstrated a fairly symmetrical shape. Examples of the results
are given in Figures 17 through 20. The radial patternations of the four high
density fuels are compared to those of the JP4 at idle conditions in Figures
17 and 18, and takeoff in Figures 19 and 20. The hollow cone spray is evident
in all cases, with most of the drops concentrated at the periphery. In order
to enable making a direct comparison between different sprays, the radial fuel
distribution may be reduced to a single value that represents an "equivalent
spray cone angle". This angle is the sum of two angles, $\phi = \phi_L + \phi_R$,
which are calculated using the following equation (Reference 4):

$$\phi_L \text{ (or } \phi_R) = \frac{\Sigma y \theta \sin\theta}{\Sigma y \sin\theta} \tag{1}$$

L and R represent the left and right lobes of the fuel distribution curve, re-
spectively, θ is the angular location of the sampling tubes, and y is the
fuel volume measured at the corresponding tubes. The physical meaning of the
equivalent spray angle is that ϕ_L (or ϕ_R) is the value of θ which corresponds to

32

IDLE

Tank Pressure= 239.3 KPa

Fuel Flow Rate= 0.011 Kg/s

TE88-1919
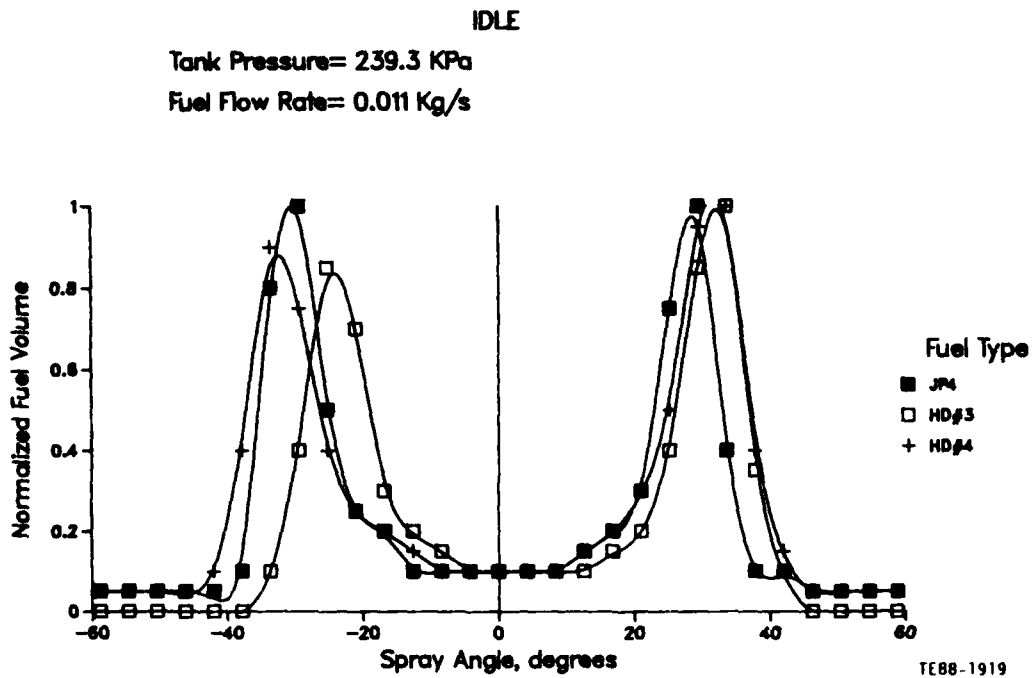
Figure 17. Radial patternation data at idle.

IDLE

Tank Pressure= 239.3 KPa

Fuel Flow Rate= 0.011 Kg/s

TE88-1920
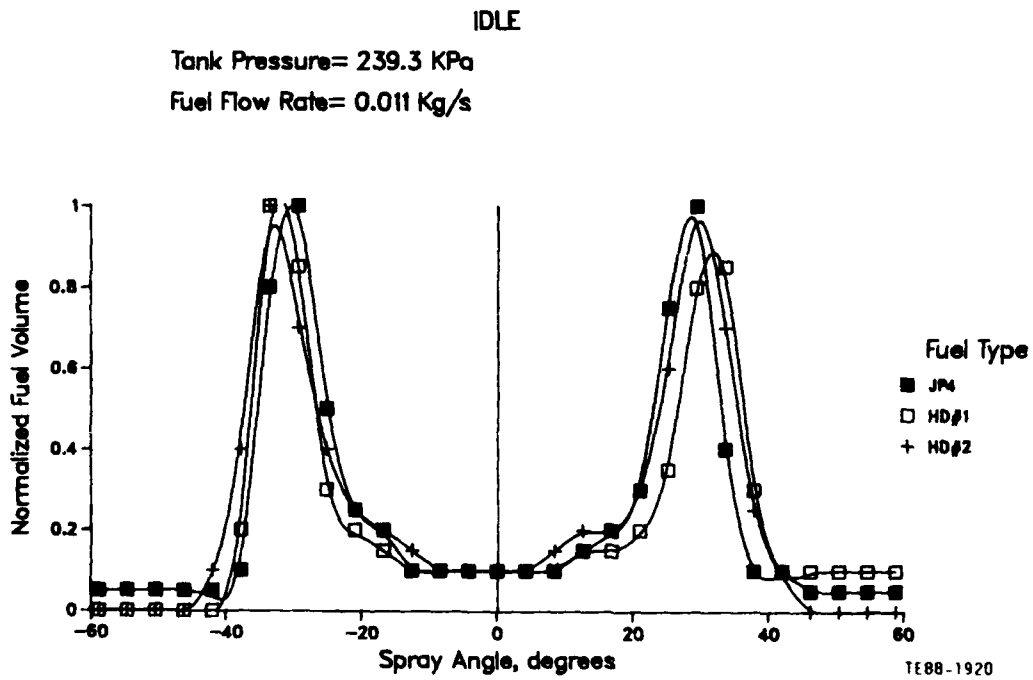
Figure 18. Radial patternation data at idle.

33

TAKEOFF

Tank Pressure= 480.6 KPa

Fuel Flow Rate= 0.053 Kg/s
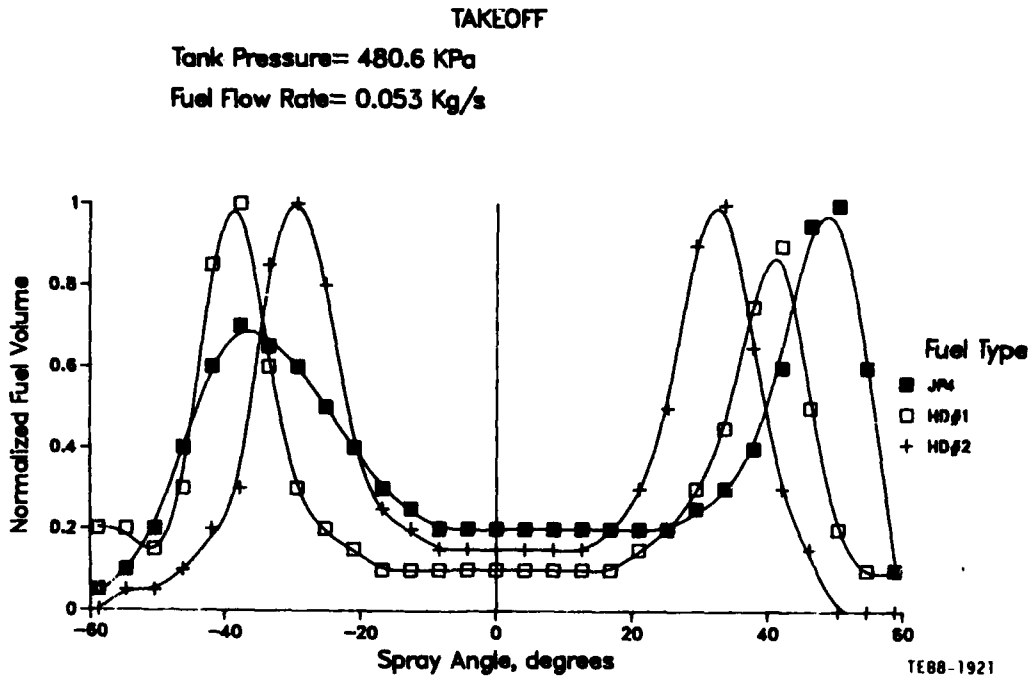
Figure 19. Radial patternation data at takeoff.

TAKEOFF

Tank Pressure= 480.6 KPa

Fuel Flow Rate= 0.053 Kg/s
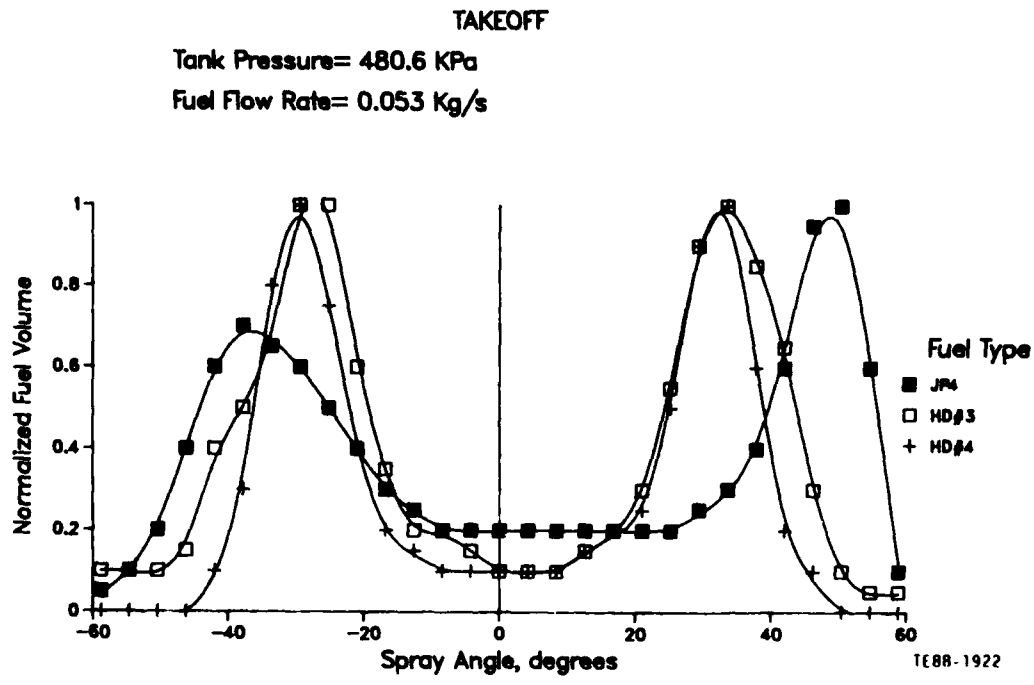
Figure 20. Radial patternation data at takeoff.

34

the position of the center of mass of material system for the left (or right) hand lobe of the curve.

The equivalent angle is plotted against fuel flow rates which represent various power levels, in Figure. 21. It is evident that, in general, the sprays produced at conditions simulating SL ignition have wide cone angles. At higher power modes the higher ambient pressure, accompanied by the increase in fuel flow and pressure, results in a reduction in the cone angle. According to Reference 5, the initial cone angle of spray produced by a pressure atomizer is determined by a number of factors including nozzle flow capacity, fuel pressure drop, and fuel properties. The ambient pressure plays a significant role in defining the spray envelope further downstream of the nozzle. Since the present atomizer is a dual orifice pressure type, the atomizer flow capacity and the effective fuel pressure vary greatly according to the flow split between the pilot and main circuits. The net effect of these variables is responsible for the trends of variation of the spray cone angle with power levels that are observed in Figure 21. At takeoff conditions, the equivalent angle of most of the high density fuel sprays is considerably narrower than that of the JP4 spray.

5.1.2 Drop Sizes

Drop size distribution in the sprays was measured by the Malvern particle size analyzer in a high pressure test facility under various simulated power conditions. Once again four identical atomizers were used in these tests. One atomizer was used for both the JP4 and HDF-1, and a separate atomizer was used for each of the other fuels.

The first set of measurements was taken at the four power modes, in addition to a SL ignition condition, for the five types of fuel. No shroud air was used in these measurements. At each test condition a minimum of six data points were taken, to ensure the consistency of the results. Several data points were rejected due to their large deviation from the majority of the points. Also, the data obtained at the SL ignition condition were not acceptable since the

35
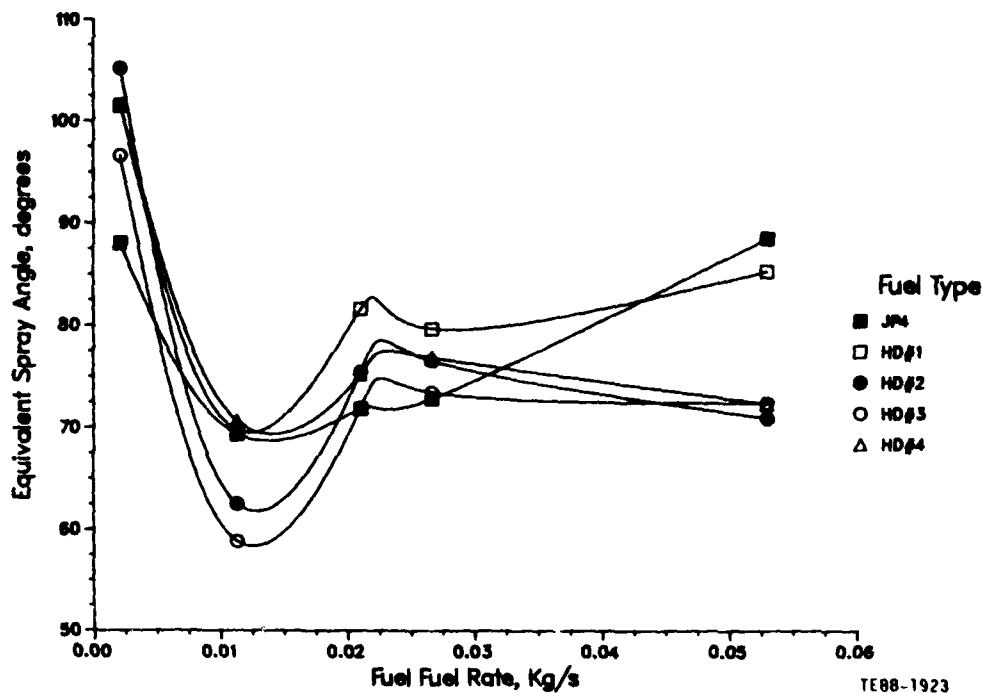
Figure 21. Equivalent spray angle of high density fuels.

very low fuel pressure drop used at these conditions (less than 69 kPa [10 psi]) resulted in large ligaments formed at the nozzle exit, which indicated an incomplete atomization process. The implication at the ignition and low power setting is that the nozzle shroud air must have a significant effect in improving the atomization quality to an acceptable level for the ease of ignition.

The data points obtained in this first set of tests are plotted in Figure 22. A direct quantitative comparison between the data at various power conditions is not an easy task since the ambient pressure varied from one test to another. However, it could be seen that, in general, the high density fuels exhibit higher Sauter mean diameters (SMD) than those obtained for the JP4 sprays, due to their higher surface tension and viscosity levels. Also, the complicated manner by which the fuel effective pressure varies when the nozzle valve starts to admit fuel into the main circuit contributes to the observed behavior of the nozzle. The atomization is expected to be at worst near these conditions due to the large jump in the fuel flow rate that is accompanied by a significant drop in effective fuel pressure.

36
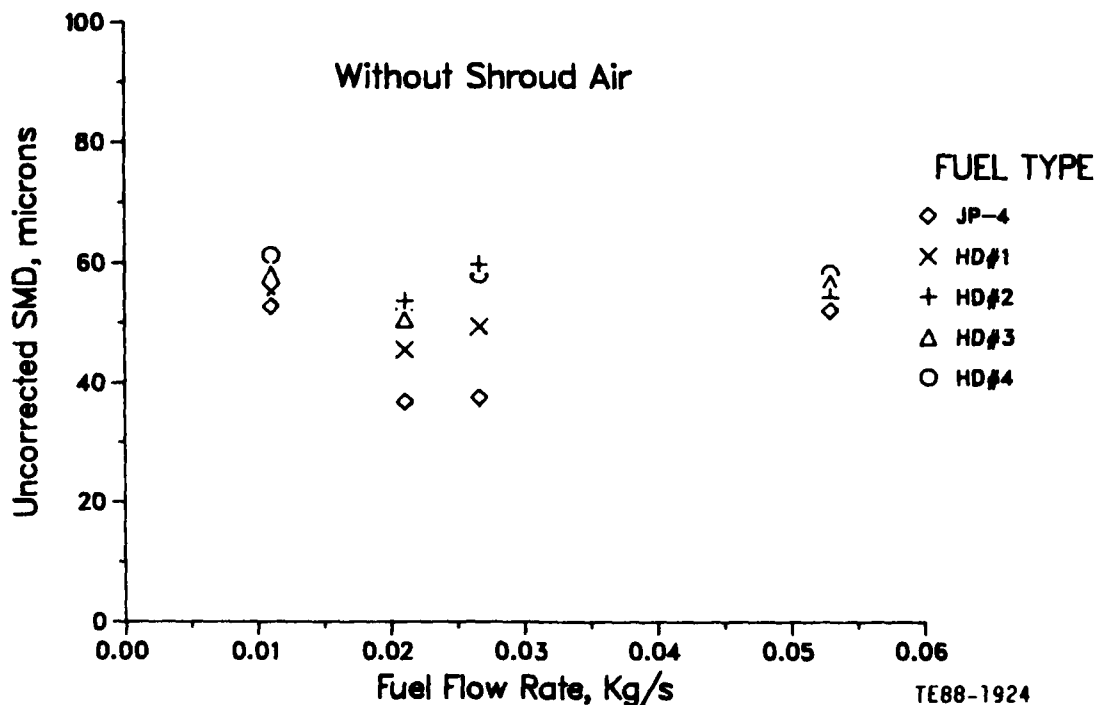
Figure 22. Spray characteristics of dual-orifice atomizer.

The obscuration parameter, which indicates the attenuation of the laser beam due to its passage in the spray and the resulting multiple scattering, showed consistently higher values above the recommended upper limit of 50% set by the Malvern manufacturer. Under these circumstances, a correction procedure must be adopted to bring up the data points to their actual size levels. Acceptable procedures are given in References 6 and 7.

The SMD values reported in Figure 22 were corrected for beam attenuation and plotted in Figure 23. The obscuration observed for the JP4 sprays was always significantly higher than that of the high density fuel sprays. This implies the existence of a larger proportion of fuel mist in the high pressure tank in the case of the JP4 spray. The correction made for the JP4 data is therefore expected to be overestimated.

The second phase of spray testing was carried out to determine the spray characteristics under the effect of the nozzle shroud air. The air pressure drop across the atomizer was calculated to give the appropriate levels of air veloc-

37

Without Shroud Air

FUEL TYPE

◇ JP-4
✕ HD#1
+ HD#2
△ HD#3
○ HD#4

Corrected SMD, microns (y-axis: 0, 20, 40, 60, 80, 100)

Fuel Flow Rate, Kg/s (x-axis: 0.00, 0.01, 0.02, 0.03, 0.04, 0.05, 0.06)

TE88-1925
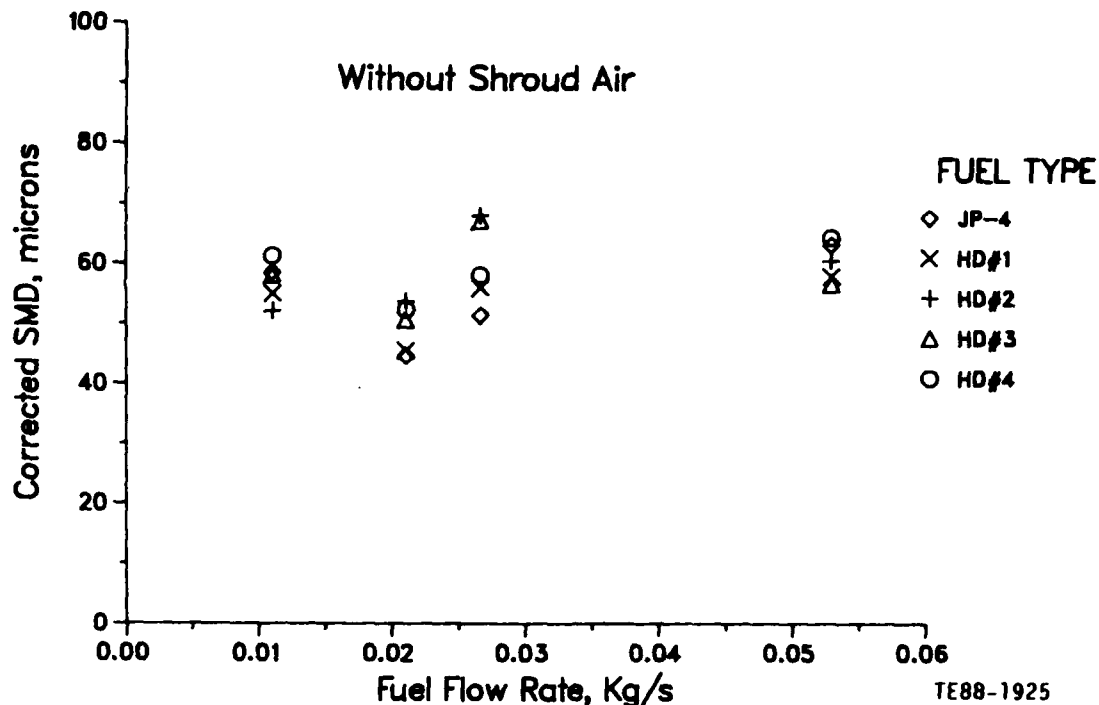
Figure 23. Spray characteristics of dual-orifice atomizer.

ity and flow rate through the atomizer at the various power modes. Due to the limited amount and high cost of nitrogen that replaced the atomizer air for safety reasons, the tests were confined to the HDF-1, with few extra points for the other fuel types. The data are plotted in Figure 24.

In order to accurately evaluate the effects of the high density fuels on the combustor performance, especially at SL ignition and altitude relight conditions, a means of estimating the values of SMD is highly needed. An empirical equation recently developed for air-assist pressure atomizers (Reference 8) was adopted in the present investigation to enable extrapolating the values of SMD at any operating conditions. The equation is given by the following:

$$\text{SMD} = \frac{0.066 \ (1/\text{AFR})^d \ (\mu_f \ \sigma_f)^{0.25} \ \rho a^{0.1}}{U_a \ (B+(AU_f/U_a)^3 - (AU_f/U_a)^2 + (AU_f/U_a))^{0.5}} \qquad (2)$$

38
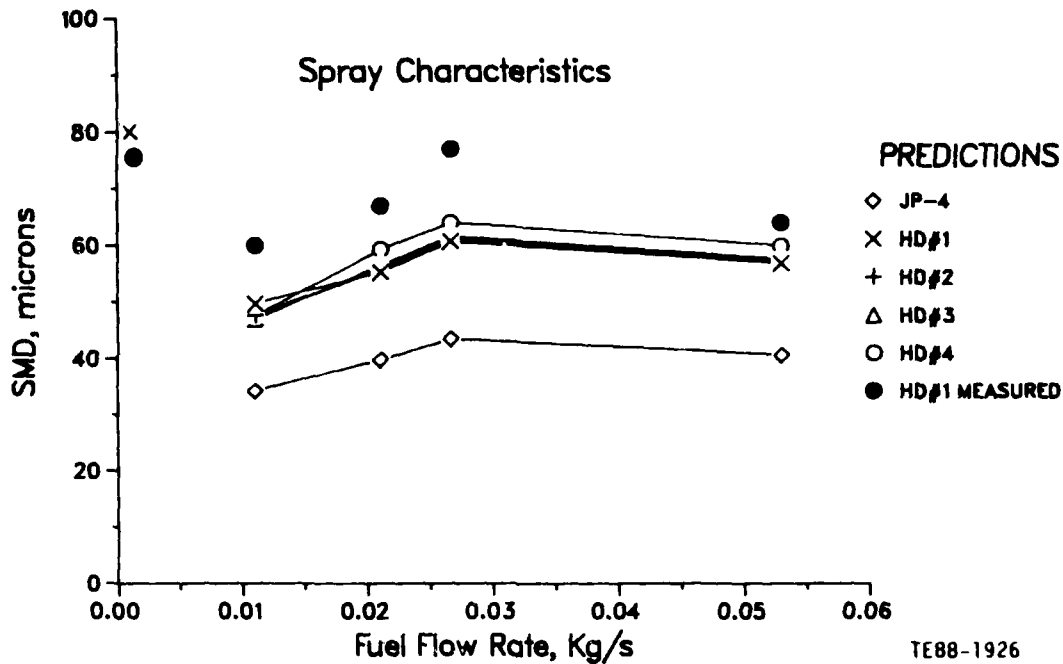
Figure 24. Effect of shroud air on spray characteristics.

The parameters A and B are given by the following:

$$A = 2^{(2.65/FN^{1.86})} \tag{3}$$

$$B = 0.875 \ (FN)^{0.254} \tag{4}$$

where FN is the atomizer flow number in $lb/hr/\sqrt{psi}$, U_f and U_a are fuel and air velocities in m/s, respectively, AFR is air/fuel ratio through the atomizer, and μ_f and σ_f are fuel viscosity and surface tension. The exponent d is given by the following:

$$d = 0.0076 \ U_a - 0.0022 \ U_a \ . \ e^{(1.122/FN^{0.4})} -0.1 \tag{5}$$

To make these equations applicable to air-assist dual-orifice atomizers it was necessary to define the effective fuel pressure of the combined pilot and main fuel flows. Once the divider valve opens the main fuel circuit, the effective pressure was calculated using the following equation (Reference 9):

39

$$\Delta P_e = \frac{4 \ \Delta P_p}{R^2} \ [(1+R)^{0.5} - 1]^2 \qquad (6)$$

where ΔP_p is the fuel pressure of the pilot circuit and R is the ratio of the main to pilot flow numbers. It is found that to give more realistic effective pressure variation in this critical operating region, the main flow number should be based on the pilot fuel pressure rather than on the net fuel pressure in the main circuit. By this means, the main flow number adopted in this equation gradually increases with flow rate. The critical region is taken to cover the flow range from the valve opening until the increasing momentum of the main flow equals that of the pilot flow. Beyond this point, the effective fuel pressure will be given by the fuel split in the two circuits as follows:

$$\Delta P_e = (F_p^{1.25}/\Delta P_p^{0.5} + F_m^{1.25}/\Delta P_m^{0.5})^{-2} \qquad (7)$$

F_p and F_m are the fuel flow fractions in the primary and main lines, respectively, and ΔP_m is the pressure in the main circuit. Finally, the overall flow number used in Equations 2 through 5 is directly determined by the ratio of the total flow rate through the atomizer to the square root of the effective pressure.

This procedure was followed to calculate the SMD at various operating parameters. Due to the fact that the spray cone angle for most cases decreased at higher ambient pressures, as reported earlier, the atomization process may actually be hindered by the higher ambient density (Reference 10). Therefore, it was found that it is more appropriate to modify the dependence of SMD on the air density term reported in Reference 8 by simply shifting this term to the numerator of Equation 2, as shown in this equation, and adjusting the empirical constant. This form of equation was adopted throughout the data analysis phase.

The calculated SMDs at various operating modes are plotted in Figure 24 to give a direct comparison with the experimental data. The trends of variation of SMD follow the experimental one at much lower levels. The fact that the measured

40

values of the SMD are higher than the calculated ones may be partly attributed to the different downstream distances adopted in the measurement and the calculations. The data were obtained at 0.15 m to minimize sampling error due to droplet ballistic arguments, while most of the empirical equations that calculate the SMD are based on data obtained at distances from 0.05 to 0.075 m where the atomization process is expected to be completed. Droplet coalescence and evaporation may significantly increase the sizes of the droplets at larger distances from the nozzle. The wide cone angle, coupled with the fairly low fuel flow rate, and large droplet sizes at ignition conditions are expected to minimize the droplet recombination and evaporation.

The shroud air effect is significant at ignition conditions, where the low fuel pressures that accompany the low fuel flow at these conditions cannot solely support good atomization. The long ligaments and blobs of fuel observed when no air was employed in the atomization have disappeared under the effect of shroud air. At higher power ratings, the effect of air on atomization is insignificant. In fact, it may even hinder the atomization due to the higher fuel discharge velocity that effectively reduces the relative velocity between the air and fuel streams.

The distribution of droplet sizes in spray is plotted in Figure 25 for the five test conditions and the HDF-1. The widest spread in drop sizes is observed at the ignition mode. On the other hand, nearly all the droplets in the spray at takeoff mode are less than about 150 microns. The sprays produced in the other three operating conditions fall somewhere in between the two extremes. The Rosin-Rammler distribution expression was used to reduce the Malvern data (Reference 11).

5.2 COMBUSTOR PERFORMANCE

In this section the experimental data obtained for the JP4 and the high density fuels are evaluated in order that the effects of the fuel type on the combustor performance and emissions characteristics may be determined. The data analysis utilizes the correlations developed by Lefebvre and reported in Reference 1.

41
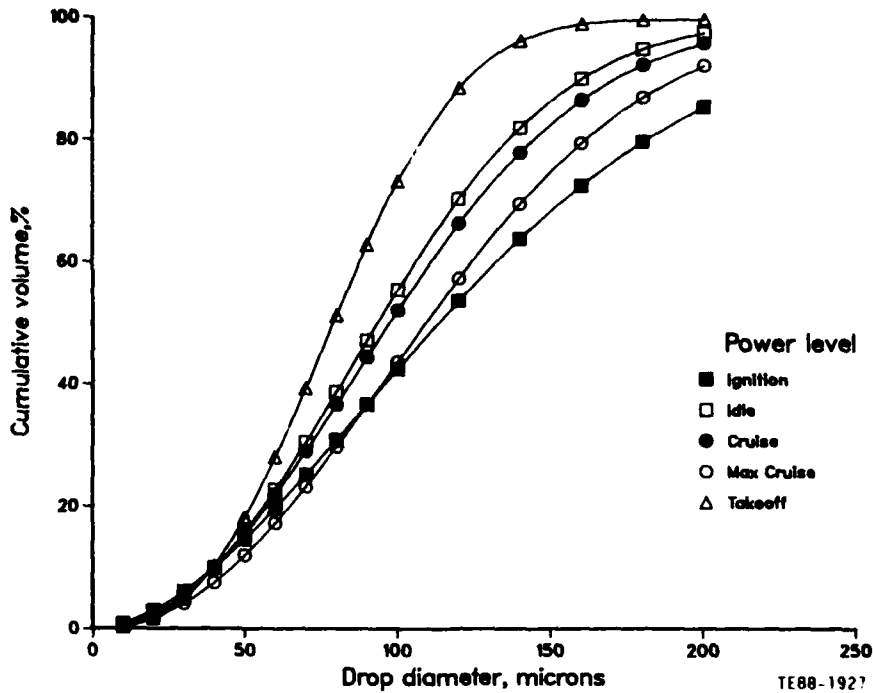
Figure 25. Drop size distribution in spray.

Modifications were performed, whenever needed, to enhance the correlation's capabilities to predict the high density fuel effects. In addition, supporting tools were developed to facilitate calculating the key parameters in the correlations, such as flame temperature and evaporation rates.

As described in Reference 1, the successful application of the correlations to a certain combustor design relies on the accurate estimation of the volume of the liner that is occupied in combustion, and the fraction of the combustor air utilized in the primary combustion. In the present investigation, a computer program was developed that takes into account these estimated parameters and performs all the necessary calculations to predict the combustor performance. The evaporation rate calculation in the program is based on the vapor concentration gradient principle that estimates the gas properties at reference film temperature using the one-third rule of the following forms (Reference 12):

$$T_r = T_s + (1/3)(T_\infty - T_s) \tag{8}$$

42

$$Y_{Fr} = Y_{Fs} + (1/3) (Y_{F\infty} - Y_{Fs}) \tag{9}$$

T is temperature, Y_F is mass fraction of fuel vapor, and subscripts r, s, and ∞ refer to reference, surface, and ambient conditions. The fuel vapor concentration is evaluated using the vapor partial pressure principle that is based on the mass transfer number (BM). For many fuels at high ambient pressures and temperatures, the heat up period constitutes the major portion of the drop evaporation time. The evaporation model takes into account both heat-up and steady state stages in addition to the forced convection effects. The rate of change of drop surface temperature during heat-up is given by the following:

$$\frac{dT_s}{dt} = \frac{m_F L}{c_{PF} m} [\frac{BT}{BM} - 1] \tag{10}$$

where m_F is rate of fuel evaporation, L is latent heat of evaporation, c_{PF} is specific heat of fuel, m is droplet mass, and BT is thermal diffusion transfer number. The evaporation constant λ is given by the following:

$$\lambda = \frac{8 \text{ kg}}{c_{pg} \rho_F} \ln (1 + BM)(1 + 0.3 R_e^{0.5} P_r^{0.33}) \tag{11}$$

R_e and P_r are the Reynolds and Prandtl numbers based on gas properties at film temperature, and instantaneous drop diameter. The relevant properties of the five fuel types considered in the present investigation were prepared for the use in the model, and the calculation followed a step-by-step procedure throughout the life of the droplet. By this means, an effective evaporation constant (λ_{ev}) that accounts for both heat-up and steady state evaporation phases, is readily determined for use in the performance correlations.

5.2.1 Gaseous Emissions

This subsection describes the data analysis performed to determine the influence of utilizing the high density fuels in the gas turbine combustor on the pollutant emissions. The pollutants of importance considered in this investigation are carbon monoxide (CO), unburned hydrocarbons (UHC), and the oxides

43

of nitrogen (NO_x). The exhaust concentrations of these pollutants were assumed in Reference 1 to be proportional to the product of mean residence time in the combustion zone, the chemical reaction rates, and the mixing rates. Based on this concept and considering the various mechanisms involved, a number of expressions were derived and reported in that reference. Descriptions of the expression forms used in the present effort along with any modifications made to improve the levels of agreement with the data are given in the following paragraphs.

The formation of much of the CO arises from the incomplete combustion of the fuel. This condition may be caused by inadequate burning rates in the primary zone due to a low fuel/air ratio, inadequate mixing of fuel and air, and/or insufficient residence time. High levels of CO could also be formed due to the quenching of the post-flame products by entrainment with the liner wall cooling air. The expression for calculating the CO emissions is given by the following:

$$CO(g/kg) = \frac{18.17 \ W_{a3} \ \cdot \ T_{Pz} \ \cdot \ e^{-.0023 \ T_{Pz}}}{P_3^{1.5} \ (V_c - V_{ev})(\frac{\Delta P_L}{P_3})^{0.5}} \qquad (12)$$

where the volume occupied in fuel evaporation (V_{ev}) is defined as

$$V_{ev} = \frac{0.55 \ F \ \cdot \ W_{a3} \ \cdot \ SMD^2}{\rho_{Pz} \ \lambda_{ev}} \qquad (13)$$

The combustion volume, V_c, and fraction of air to primary zone, F, are estimated to give the best fit to the data and are based on the combustor configuration. The effective evaporation constant, λ_{ev}, and the Sauter mean diameter of the spray, SMD, are determined from the procedures given in the previous subsections. T_{Pz} and ρ_{Pz} are gas temperature and density in the primary zone, P_3 is inlet air pressure, W_{a3} is total combustor air, and ΔP_L is the liner pressure drop.

The results of the calculations of CO at the four power modes and for the five fuel types are plotted in Figures 26 through 30. In the same figures, the

44
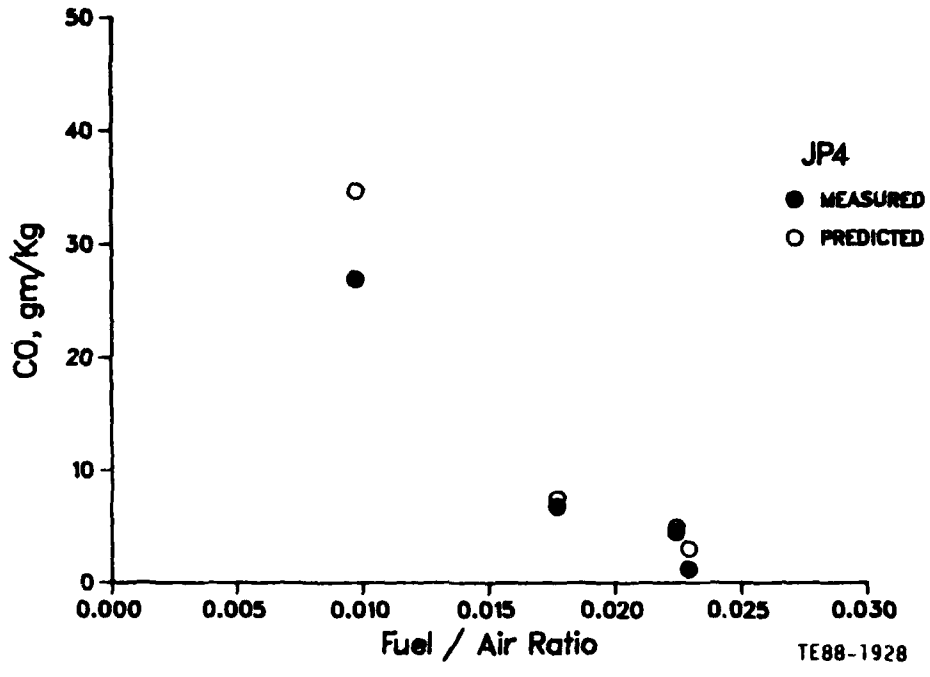
Figure 26. CO emissions for JP4.
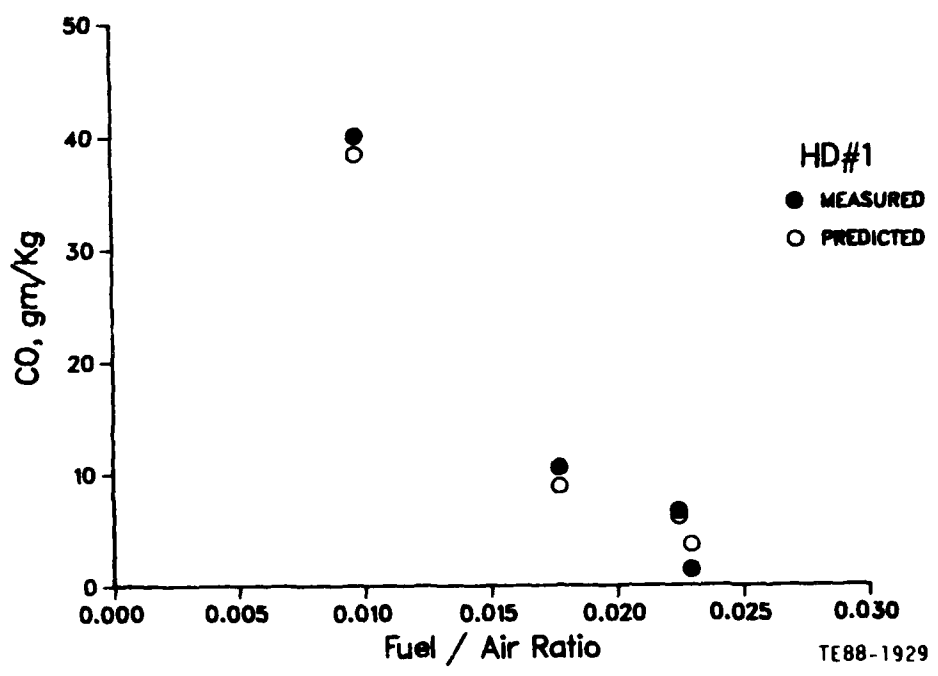

Figure 27. CO emissions for HDF-1.

45
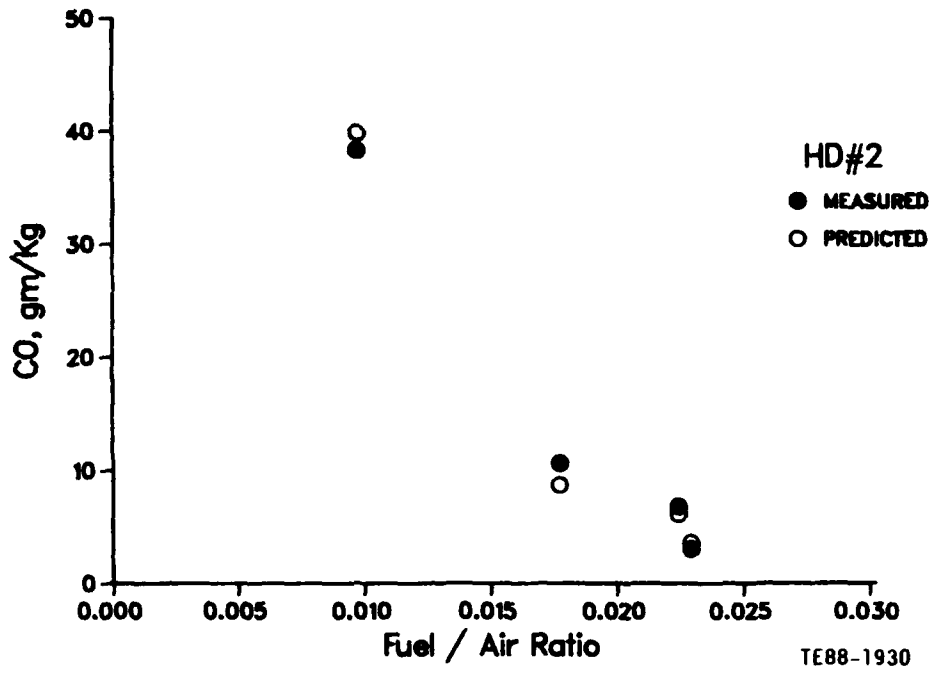
Figure 28. CO emissions for HDF-2.
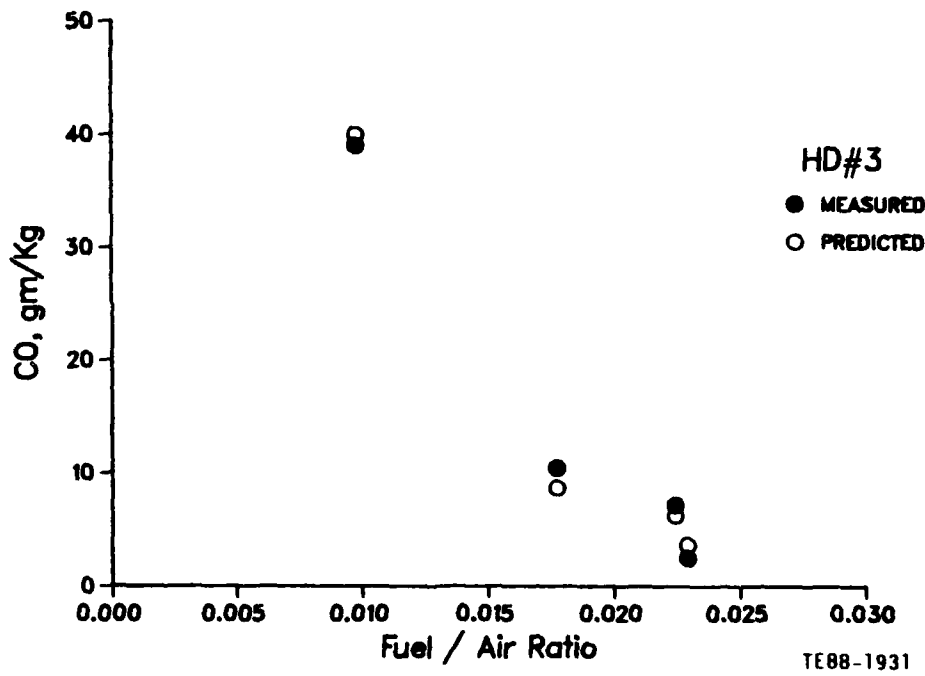
Figure 29. CO emissions for HDF-3.
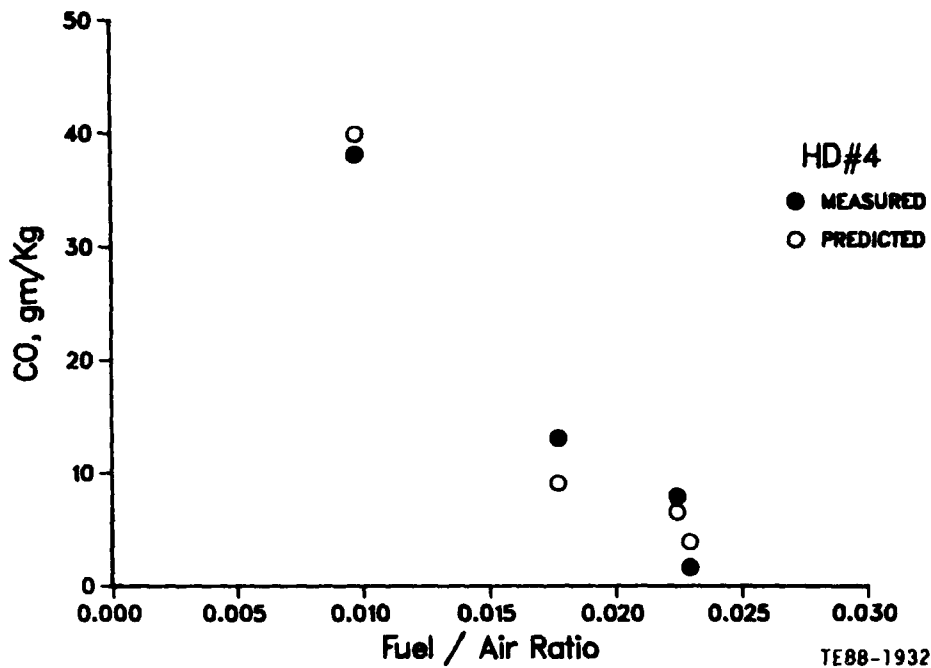
Figure 30. CO emissions for HDF-4.

experimental data are shown for the comparison. As expected, the concentration of CO is highest at low power conditions and diminishes with increases in power. Also, the CO levels for the JP4 fuel are generally lower than those of the high density fuels. The lower evaporation rates achieved for these fuels, due to the higher SMD and lower evaporation constant, are the main causes for the higher CO observed.

The good agreement between the experimental data and the calculations is evident in these figures. All the points are replotted in Figure 31 to give an overall view of the level of agreement for all fuels.

The presence of the unburned hydrocarbons in the combustor exhaust is an indication of incomplete combustion due to poor atomization, inadequate burning rates, or the chilling effects of liner coolant. The similarity between the CO and UHC emissions in regard to the effects of operating parameters on their formation leads to the following expression for the UHC:

47
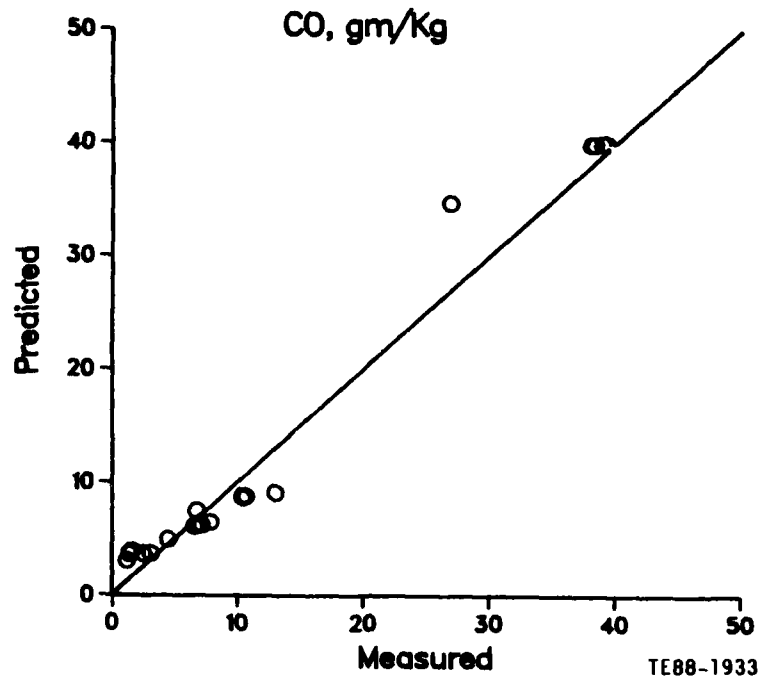
Figure 31.   Comparison of measured and predicted values of CO.

$$\text{UHC (g/kg)} = \frac{5288 \ W_{a3} \cdot T_{Pz} \cdot e^{-.0025 \ T_{Pz}}}{P_3^{2.5} \ (V_c - V_{ev}) \ (\frac{\Delta P_L}{P_3})} \qquad (14)$$

The corresponding predictions of the UHC for the JP4 and the four high density fuels are plotted in Figures 32 through 36 together with the measurements at the four power conditions. Figure 37 shows all the predicted points plotted against the experimental data. The variations of the UHC with power mode and fuel type are similar to those observed for the CO emissions. Once again, very satisfactory correlation of data is provided by Equation 14.

The oxides of nitrogen are produced in the central hot region of the combustor by the oxidation of the atmospheric nitrogen, and most of the NO_x emitted in the exhaust is nitric oxide (NO). Thermal, prompt, and fuel nitric oxides are three different mechanisms that can produce NO_x. The formation of NO_x depends upon the temperature of the flame, and significant quantities are only produced at temperatures higher than 1800 K.

48
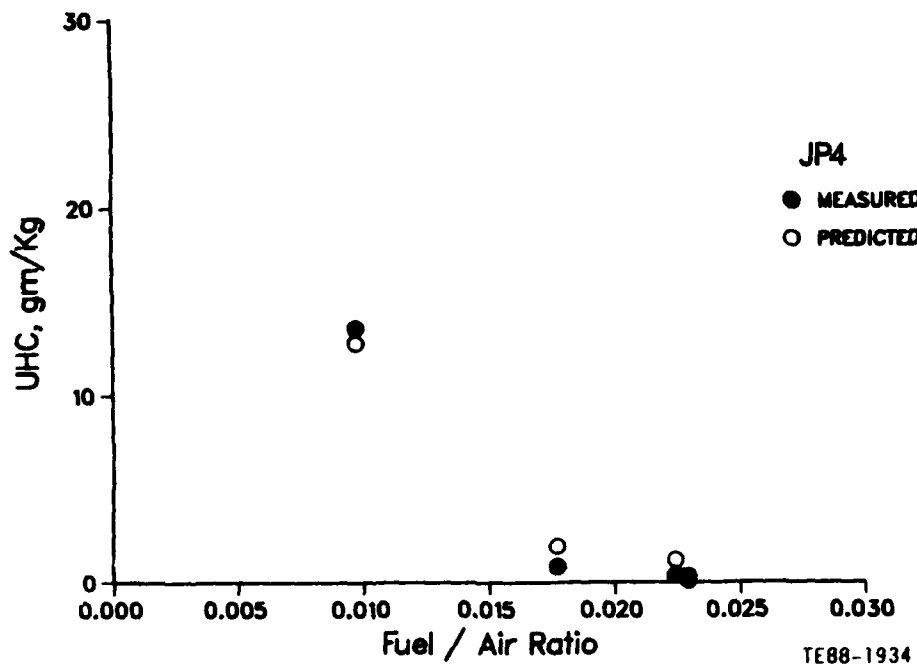
Figure 32.   UHC emissions for JP4.
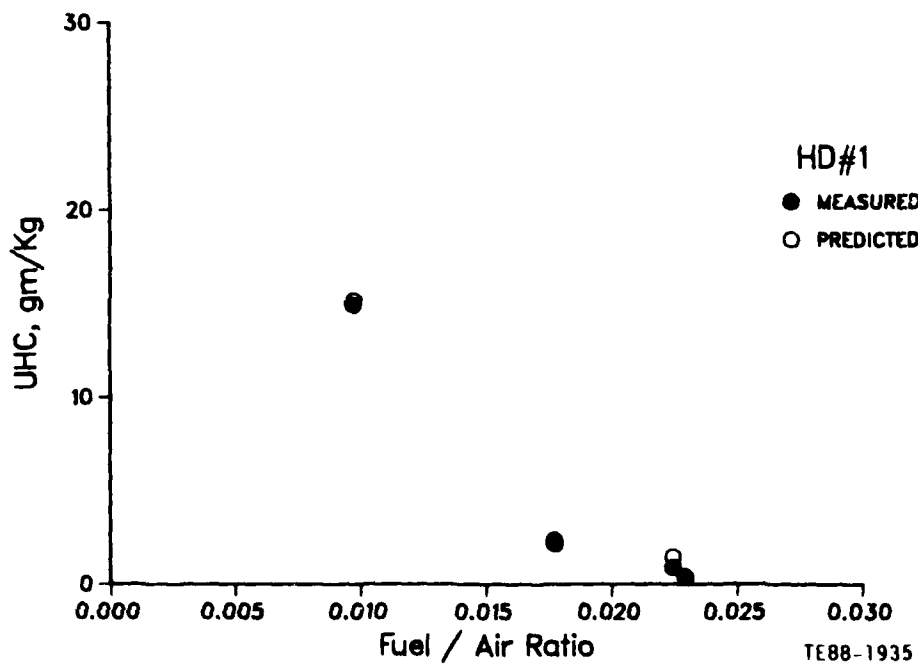
Figure 33.   UHC emissions for HDF-1.
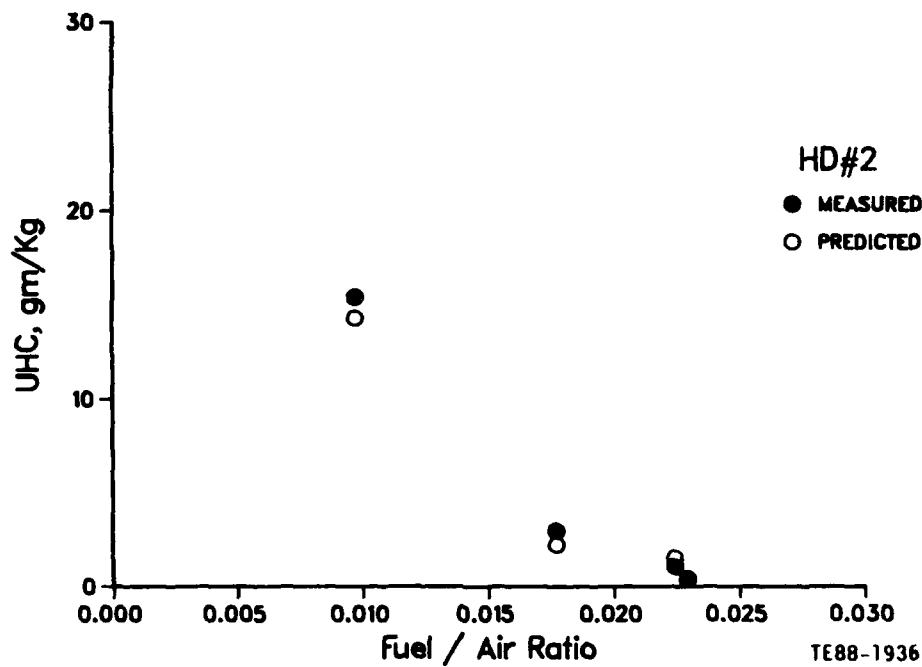
Figure 34. UHC emissions for HDF-2.
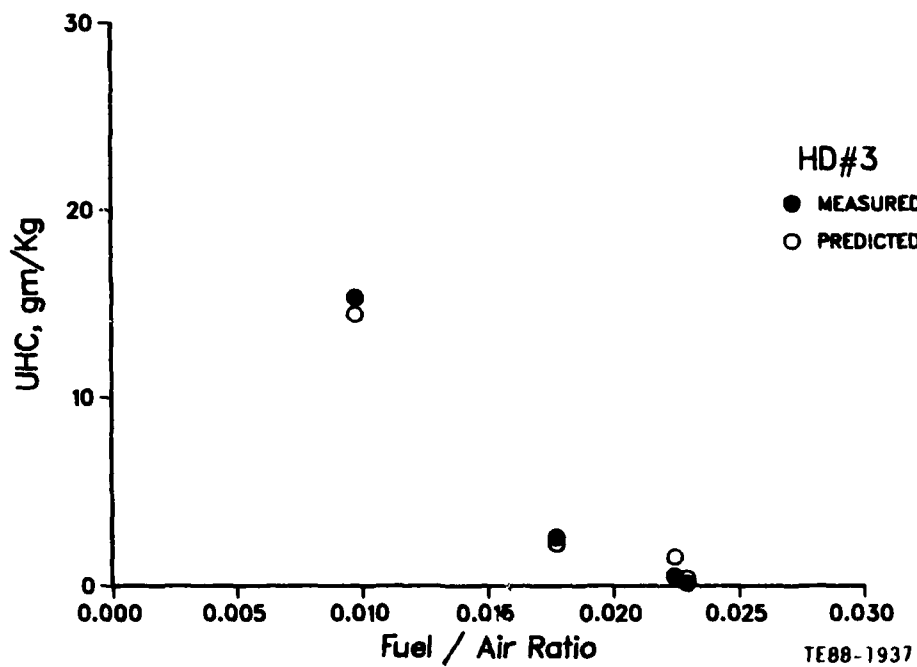
Figure 35. UHC emissions for HDF-3.
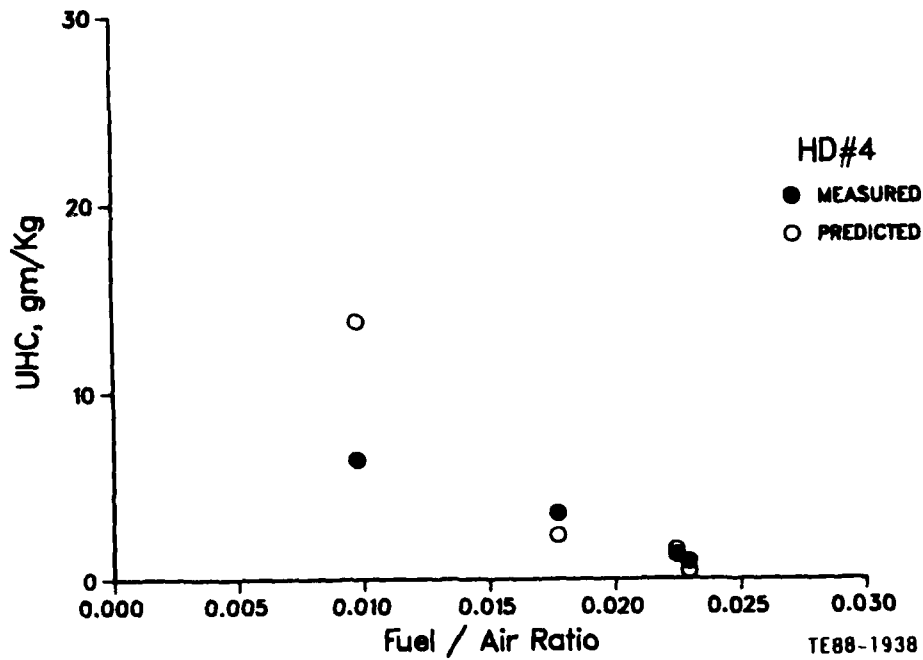
Figure 36. UHC emissions for HDF-4.
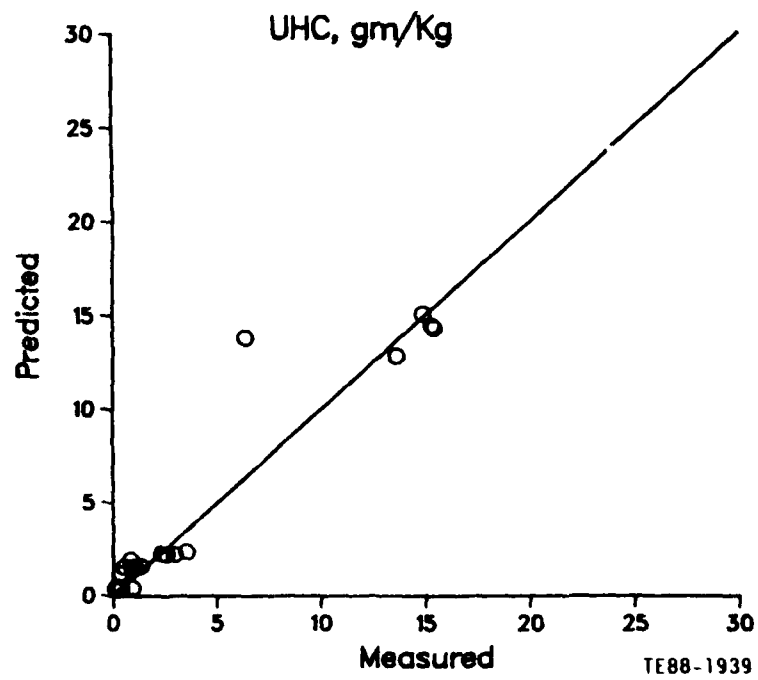

Figure 37. Comparison of measured and predicted values of UHC.

51

The expression used to calculate NO_x is given by the following:

$$NO_x \ (g/kg) = \frac{9 \times 10^{-8} \ P_3^{1.25} . \ V_c \ . \ e^{0.01 \ T_{st}}}{W_{a3} \ T_{Pz}} \qquad (15)$$

T_{st} is the stoichiometric flame temperature corresponding to the combustor inlet temperature.

Highest NO_x levels occur at takeoff operating conditions as shown in Figures 38 through 42 for the five types of fuel. Excellent agreement between the data and the predictions are achieved using the above equation. Figure 43 indicates that when the predicted values are plotted against the measurements, most of the points fall on or very close to the line that represents the perfect correlation.

5.2.2 Smoke Emissions

Smoke or soot in the combustor exhaust consists mostly of carbon and a mixture of hydrogen, oxygen, and other species. Soot is produced in the flames in quantities in excess of the equilibrium concentration, in fuel-rich regions, and may be generated in any part of the combustion zone where mixing is inadequate. In practice, the rate of soot formation tends to be governed more by the physical processes of atomization and fuel/air mixing rather than by kinetics. This gives airblast atomizers advantages over pressure atomizers in their application to gas turbine combustors. The airblast atomization process ensures thorough mixing of air and fuel, resulting in low soot formation in the combustion zone.

If high temperature and sufficient air are available in the intermediate zone (and dilution zone in advanced high temperature engines), most of the soot produced in the main combustion zone will be consumed before exiting from the combustor. The soot concentration is known to rapidly increase with increase in system pressure and is diminished by the reduction in fuel/air ratio. Fuel
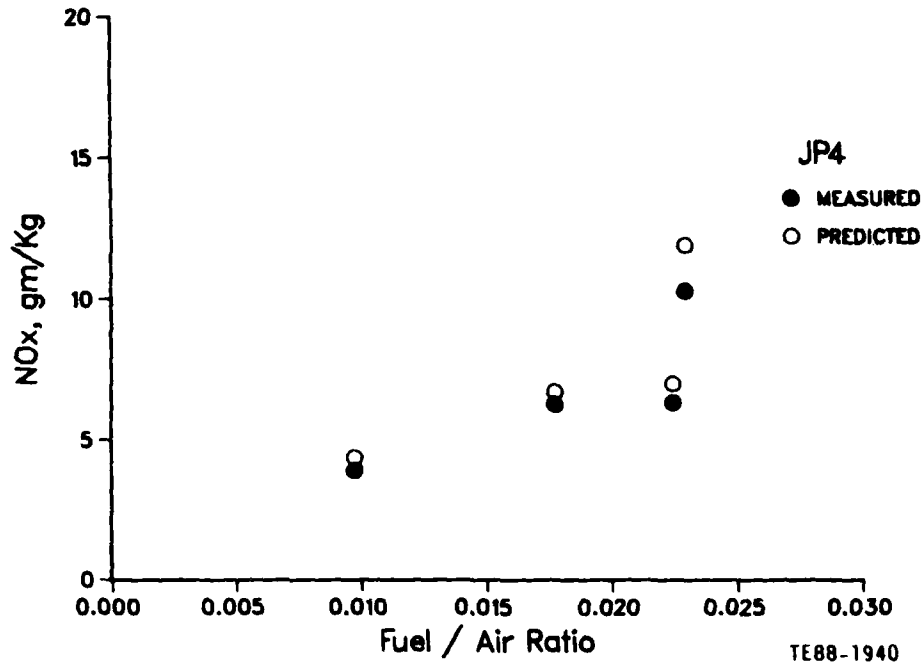
Figure 38. NO$_x$ emissions for JP4.
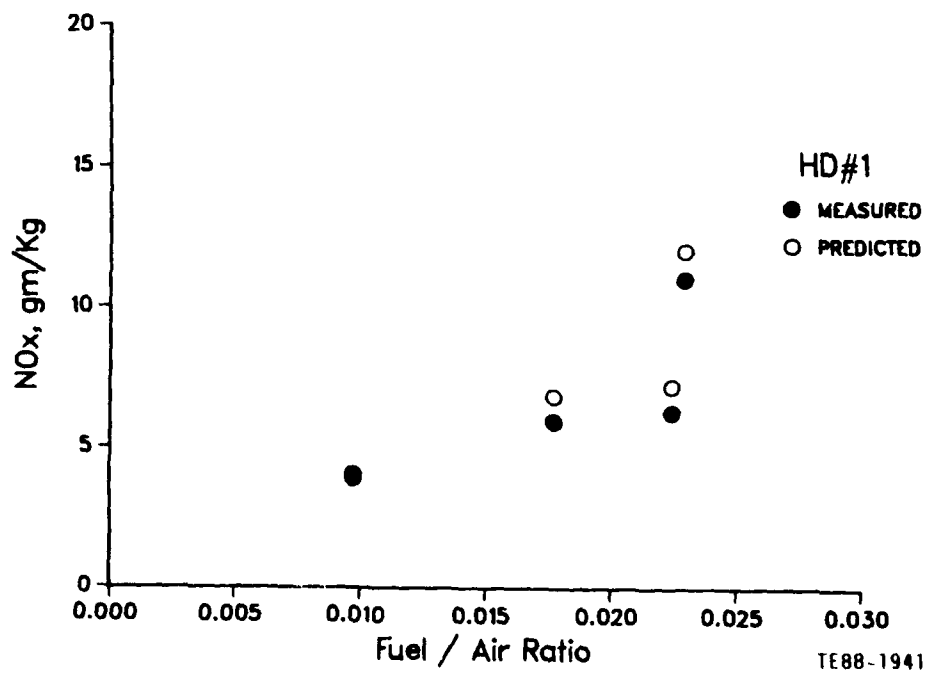

Figure 39. NO$_x$ emissions for HDF-1.
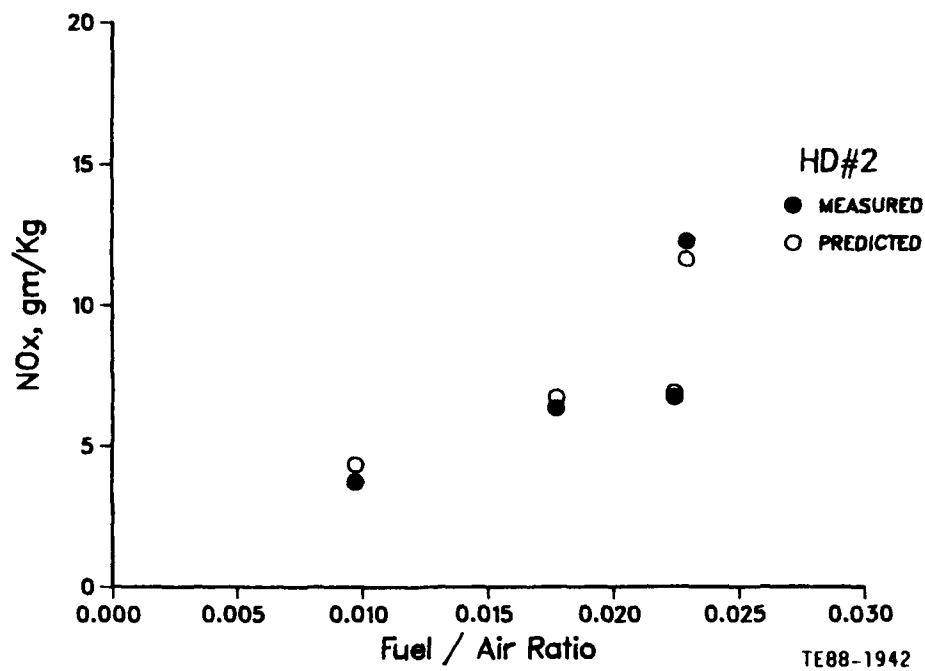
Figure 40. NO$_x$ emissions for HDF-2.
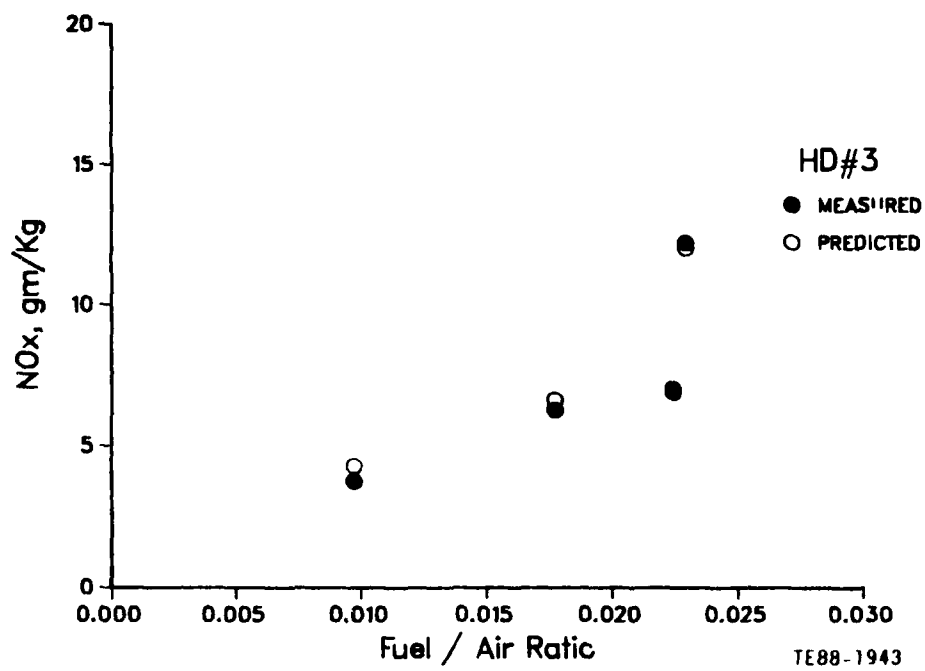
Figure 41. NO$_x$ emissions for HDF-3.

54
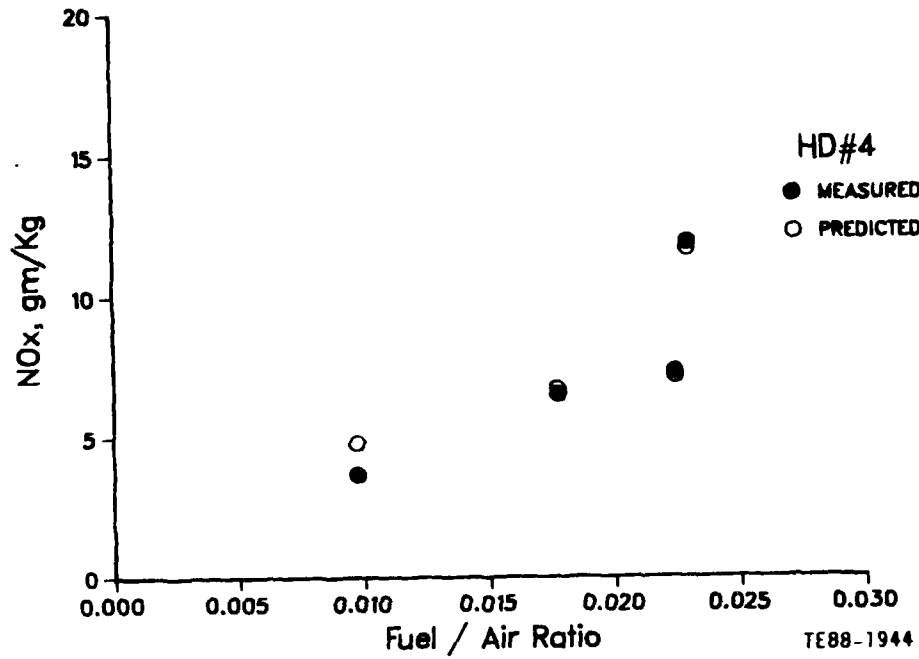
Figure 42. NO_x emissions for HDF-4.
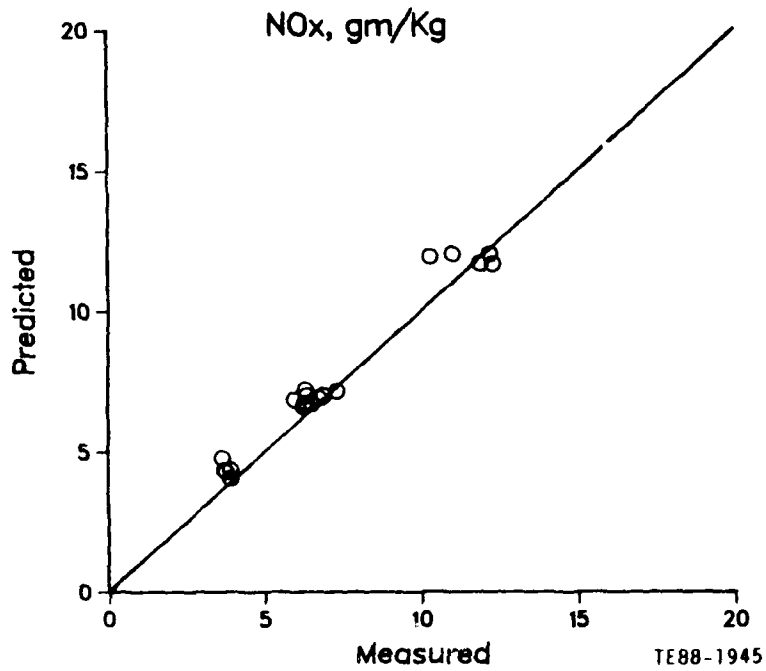
Figure 43. Comparison of measured and predicted NO_x.

properties, such as hydrogen content, smoke point, and aromatic content, have great influence on the soot formation mechanism.

In order to determine the most appropriate chemical fuel properties that can describe the trends of soot variation with fuel type, the experimental data were plotted against several common terms. In Figure 44, the smoke number is plotted against a parameter that is uniquely a function of hydrogen content at various power conditions. Alternatively, the same data points were plotted against a term that contains the smoke point and naphthalene content proposed in Reference 13 and in Figure 45. Comparing the two approaches indicates that the variation of the smoke number with the latter parameter follows a more consistent trend at the four power conditions than that of the former parameter. Better correlation with the data was also obtained when the second parameter was incorporated in the expression for smoke in place of the hydrogen content term.

A parameter developed during the present effort that includes the smoke point and the aromatic content was also used to correlate the smoke data, as illustrated in Figure 46. This parameter offers further improvement in the analytical correlation, especially at high power modes. This suggested that the following expression would give good fit to the data:

$$S(mg/kg) = \frac{73 \cdot P_3^2}{W_{a3}} (\frac{FAR}{FT})_{pz}(1-0.00423 \ (\frac{e^{0.0011T}}{FAR})_{sz})(SP - \frac{AR}{10})^{-1.2} \tag{16}$$

SP is fuel smoke point, AR is aromatic content, and the subscripts pz and sz refer to primary and intermediate combustion zones, respectively. The parameters related to the intermediate zone require the estimation of the fraction of the combustor air that is utilized in both primary and intermediate zones. The other parameters in this equation were defined earlier.

The calculated smoke number values are plotted against the fuel/air ratio levels that represent the four main power modes in Figure 47 for the JP4 and Figures 48 through 51 for high density fuels. The soot concentration was con-
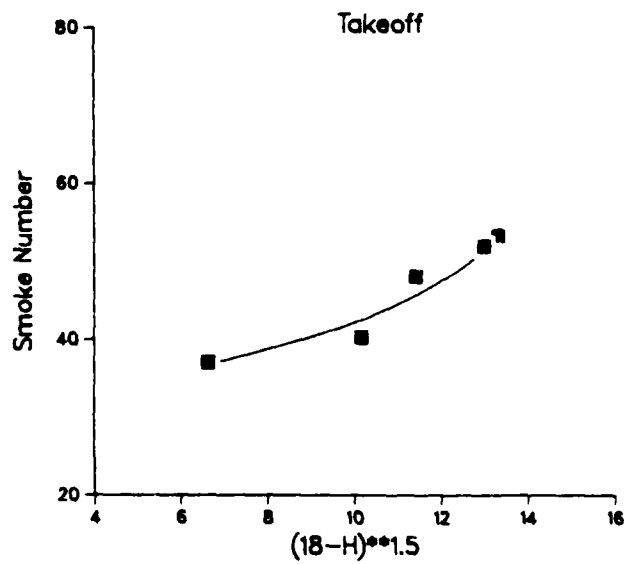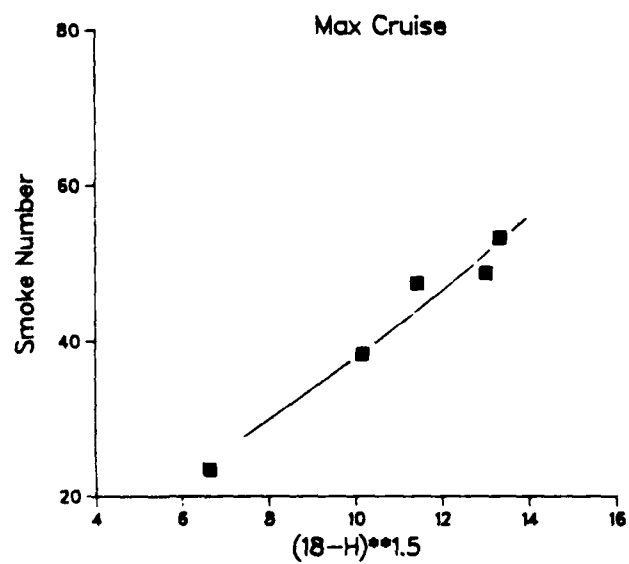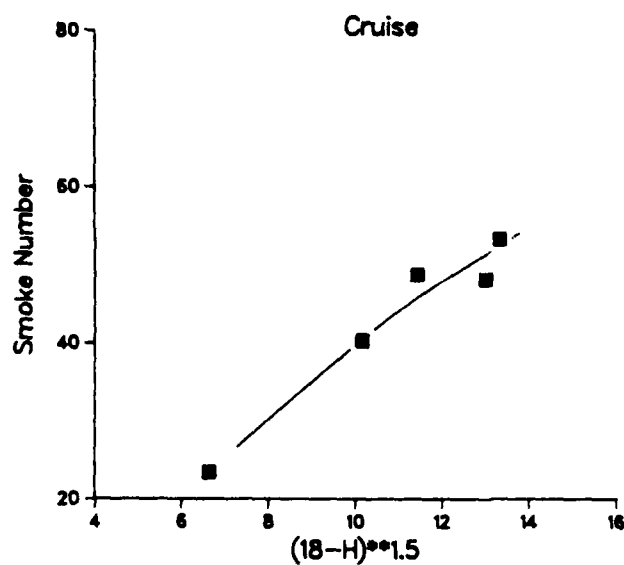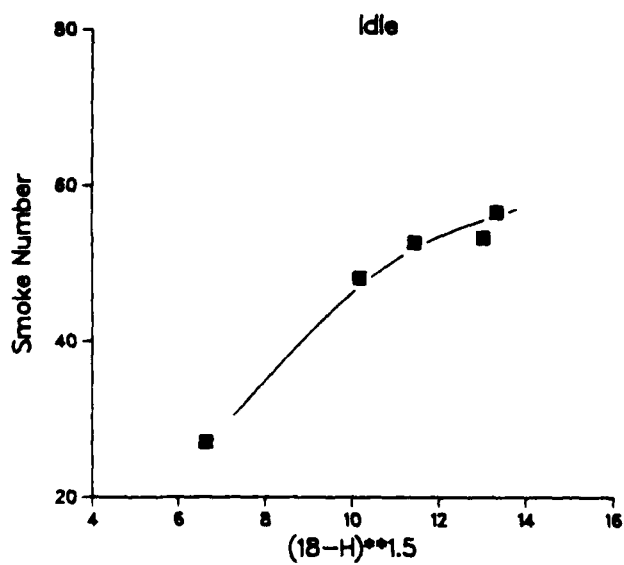
Figure 44. Effect of hydrogen content on smoke.
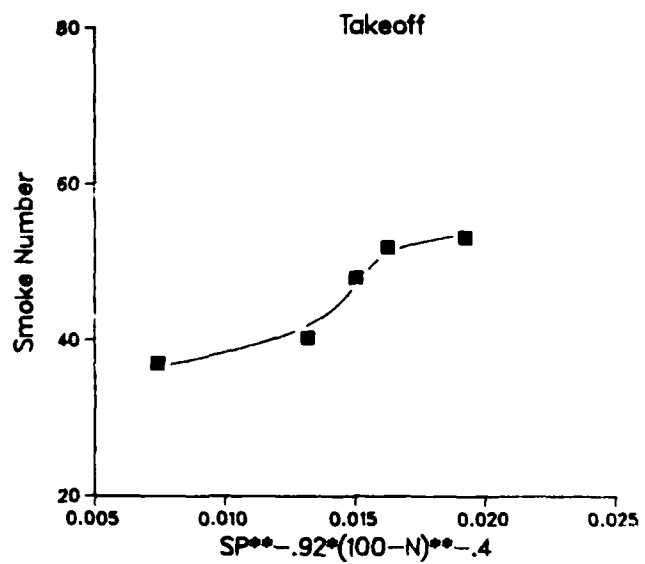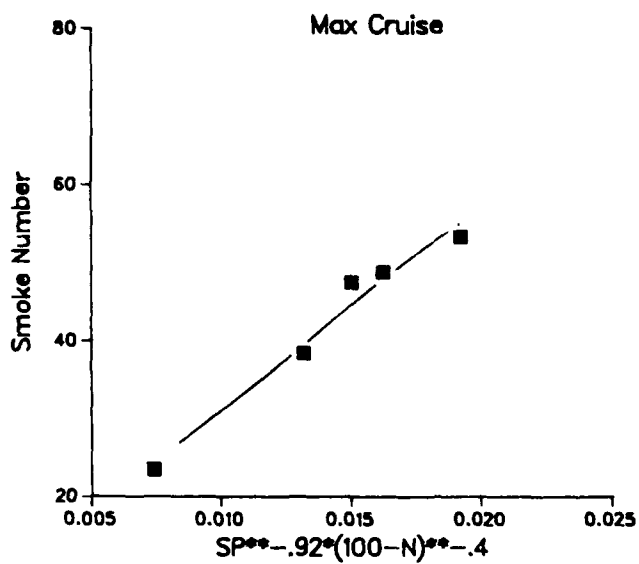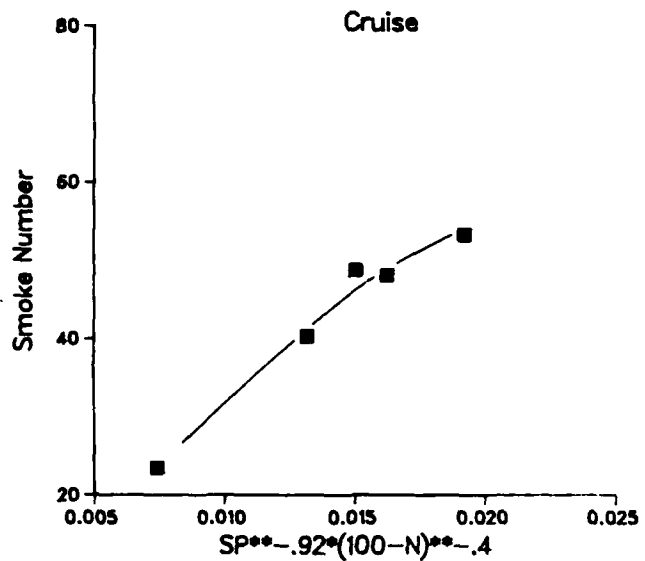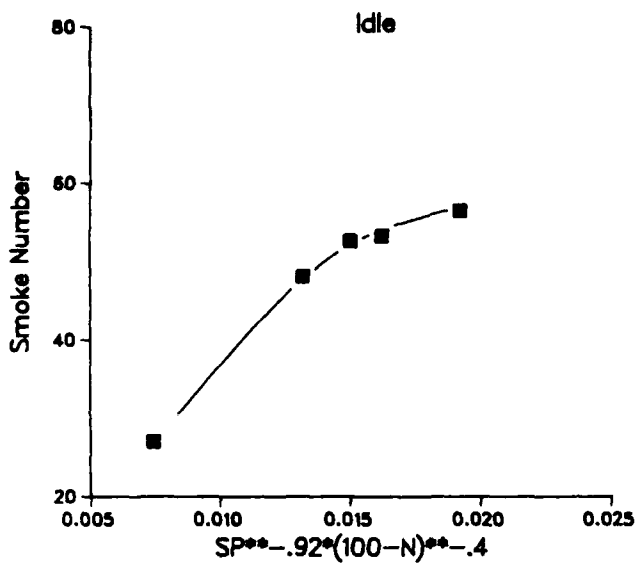
TE88-1946

Figure 45. Effect of smoke point and napthalene on smoke.

TE88-1947

TE88-1948

Figure 46.   Effect of smoke point and aromatic content on smoke.
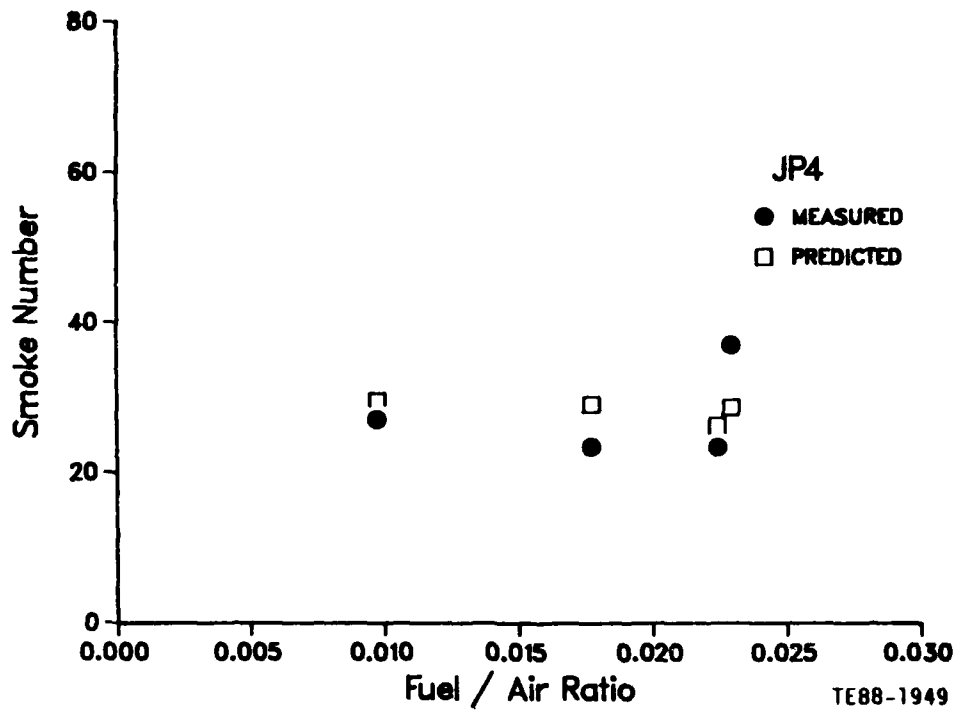
Figure 47.   Smoke emissions for JP4.
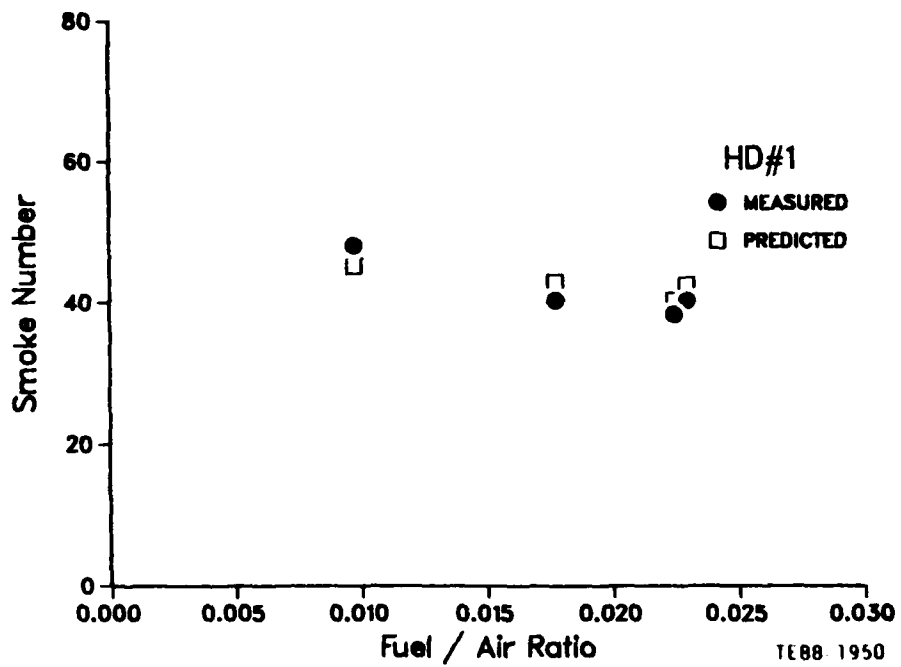
Figure 48.   Smoke emissions for HDF-1.
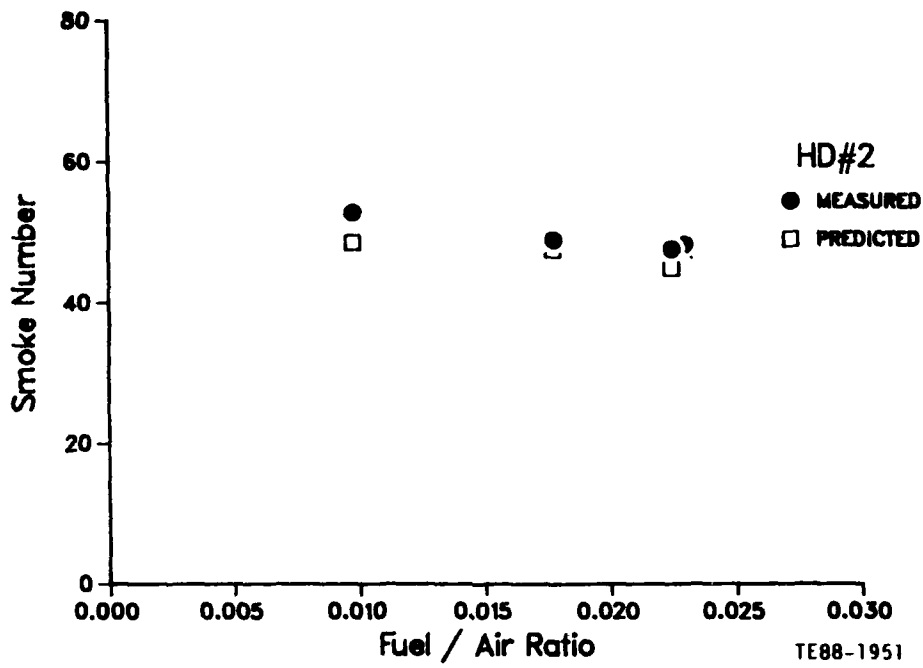
Figure 49. Smoke emissions for HDF-2.
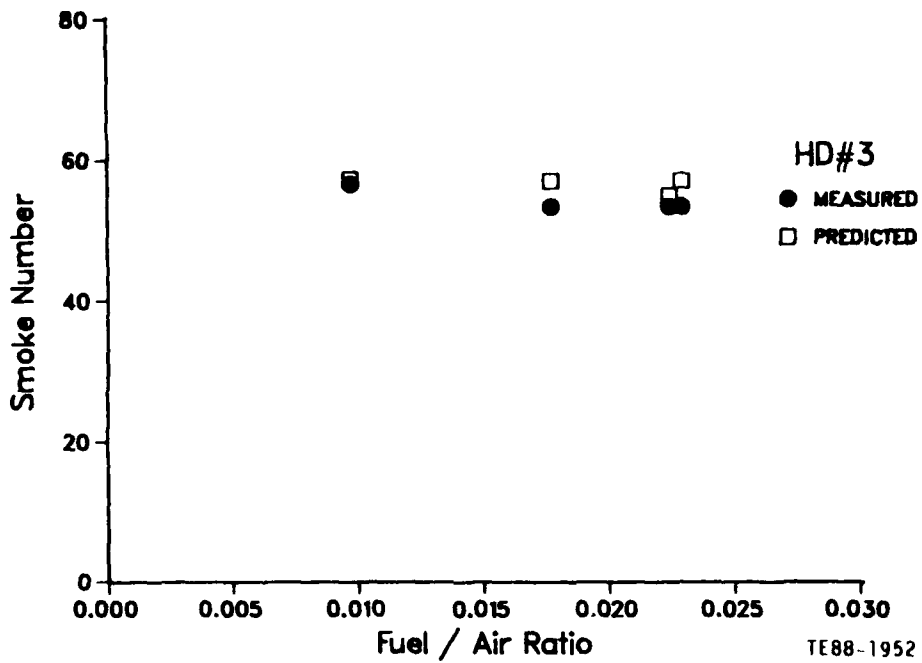
Figure 50. Smoke emissions for HDF-3.

61
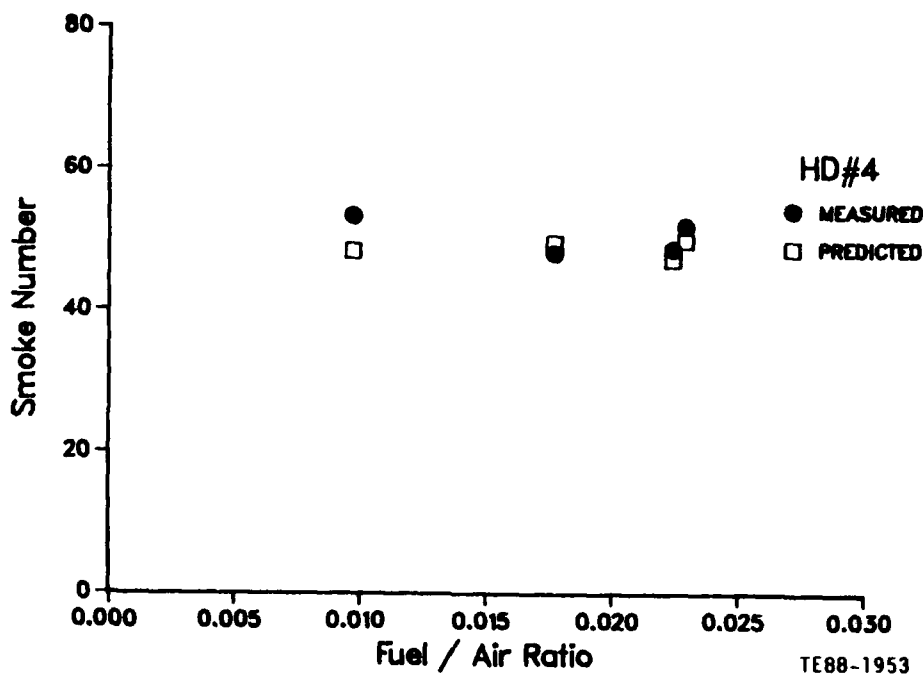
Figure 51. Smoke emissions for HDF-4.

verted to smoke number according to the relationship given in Reference 14.
In the same figures, the experimental data obtained at the four power modes
are shown. It is clear that relatively high levels of smoke are produced for
JP4 even at idle conditions. Higher smoke number values are observed for the
high density fuels, with the HDF-3 showing the highest tendency to smoke. The
HDF-3 is the fuel with the lowest hydrogen content, smoke point, and highest
aromatic content. The implication is that the fuel nozzle type used and the
dome configuration of the combustor are creating very rich regions, with
inadequate mixing, in the primary zone.

Once again, very satisfactory agreement is observed between the calculated
smoke number and the data in these figures. The agreement is also evident in
Figure 52 where all the points are plotted in the prediction versus measure-
ment form.
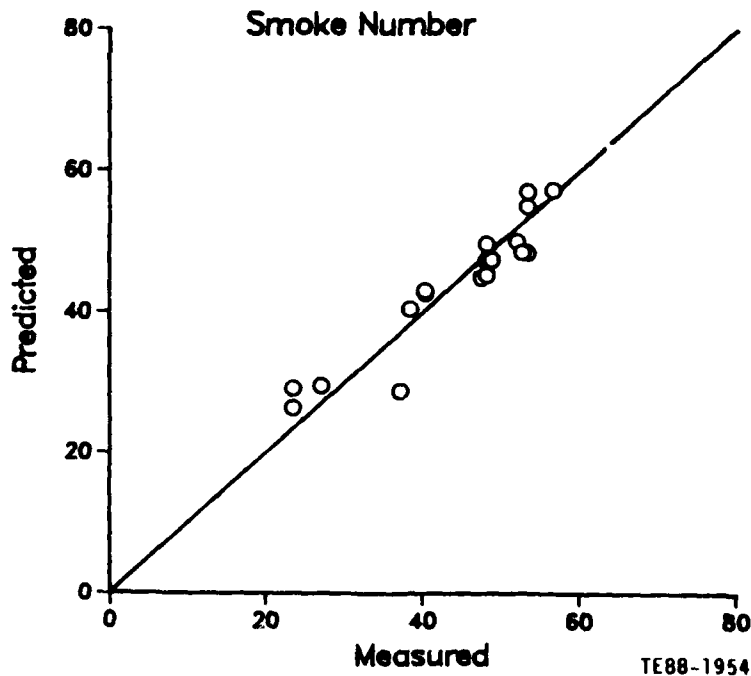
Figure 52. Comparison of measured and predicted smoke number.

5.2.3 Combustion Efficiency

Combustion efficiency is of paramount importance for combustion systems, since it is an indication of the amount of fuel wasted. Combustor inefficiency is manifested in the form of undesirable pollutant emissions, notably unburned hydrocarbons and carbon monoxide. It is influenced by the various processes taking place in the combustion zone including fuel atomization, evaporation, and subsequent mixing with air and products, all occurring simultaneously with chemical reaction and heat transfer.

When the overall rate of heat release is limited by chemical kinetics, the burning velocity or the stirred reactor models are most widely used to describe efficiency (Reference 15). Both models yield similar correlating parameters that are based on temperature, pressure, and combustor geometry, with the fuel effects accounted for in the determination of flame temperature. The equation used in the present effort is given by the following:

63

$$\eta_r = 1 - \exp\left(-.022 \; P_3^{1.3} \; \frac{V_c}{F_c \; W_{a3}} \; e^{T_c/400}\right) \tag{17}$$

T_c is the adiabatic flame temperature in the combustion zone as given by the appropriate values of P_3, T_3 and the fraction of air to the combustion zone F_c.

The fraction of fuel that is fully vaporized within the combustion zone could set a limit on the combustion efficiency under certain operating conditions. The inefficiency due to evaporation is controlled by combustor geometry, operating parameters, fuel nozzle characteristics, and fuel type. The expression used in this analysis is given by the following:

$$\eta_{ev} = 1 - \exp\left(-17 \; . \; \frac{P_3 \; . \; V_c \; . \; \lambda_{ev}}{T_c \; . \; SMD^2 \; . \; W_{a3} \; . \; F_c}\right) \tag{18}$$

Since it is difficult to assess the importance of the mixing rates to combustion efficiency, the final equation is based on the reaction and evaporation terms as follows:

$$\eta_c = \eta_r \; . \; \eta_{ev} \tag{19}$$

The results of the detailed calculations using this equation are presented in Figures 53 through 57 for the five fuels under investigation. Both the experimental data and the predictions plotted in these figures show an increase in the combustion efficiency with the increase in power rating to reach a near complete combustion at maximum cruise and takeoff. The good agreement obtained between the calculated and the measured efficiencies indicates that Equation 19 contains the appropriate elements required to predict the combustion efficiency. Figure 58 is another form of plotting the data that gives a direct assessment of the prediction capabilities of the equation. It can be seen that most of the points fall within a narrow envelope that surrounds the perfect correlation line.
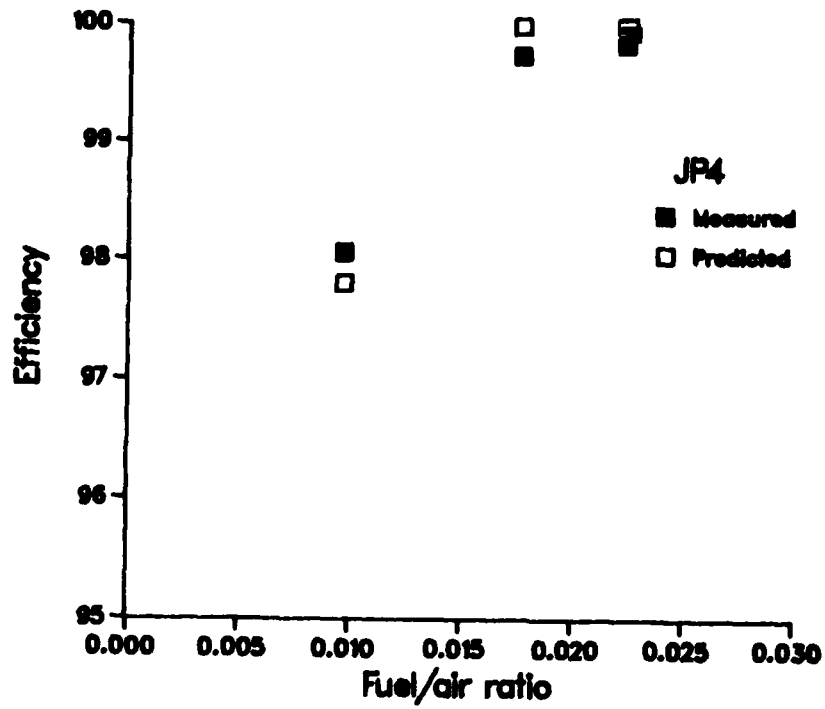
Figure 53.   Combustion efficiency for JP4.
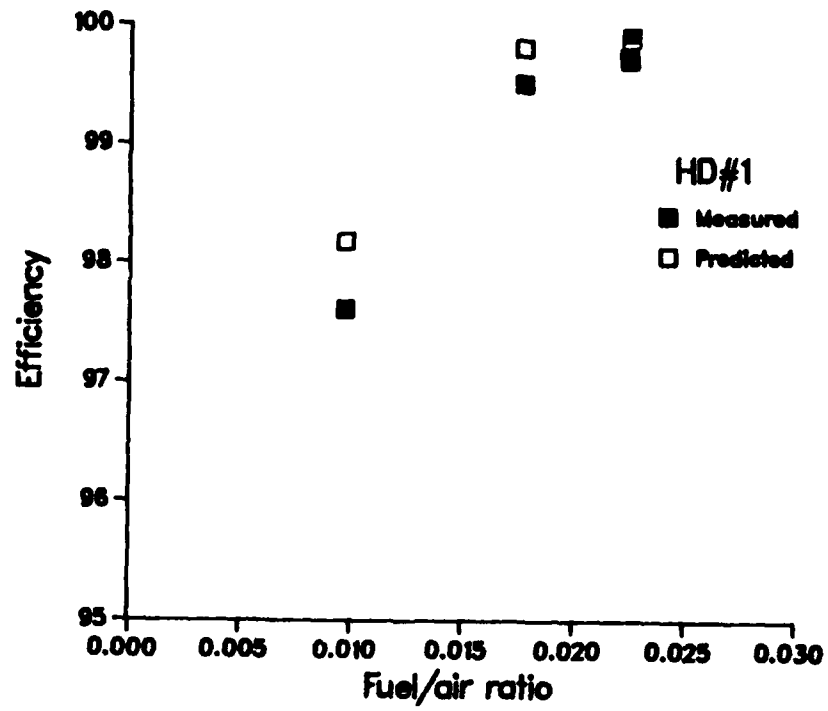
Figure 54.   Combustion efficiency for HDF-1.

65
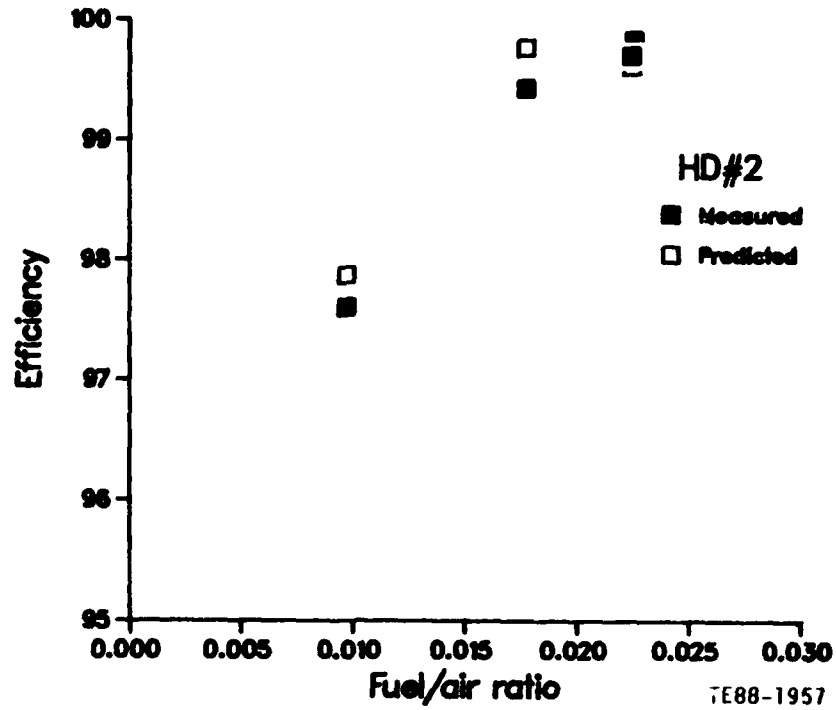
Figure 55. Combustion efficiency for HDF-2.
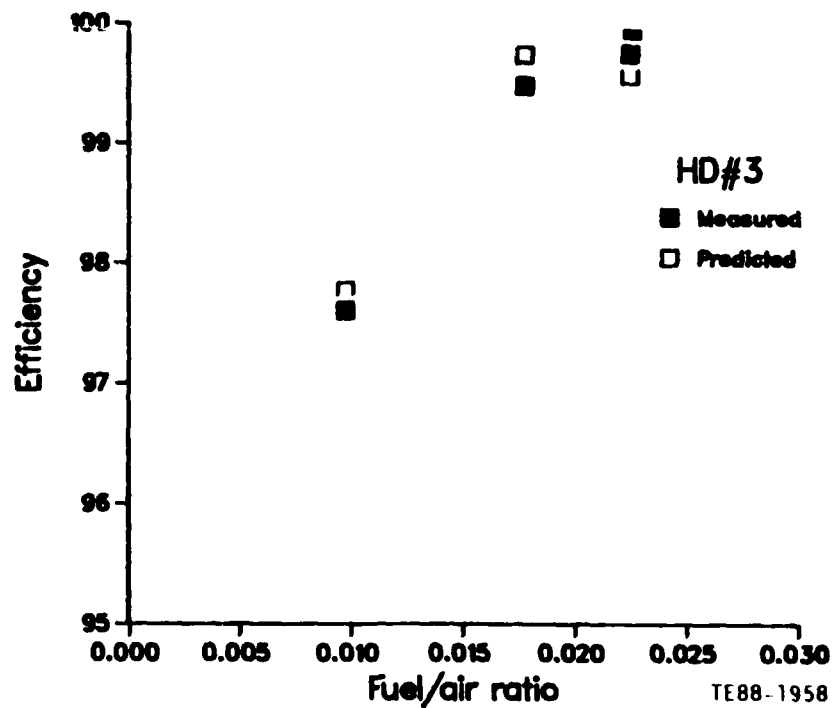
Figure 56. Combustion efficiency for HDF-3.

66
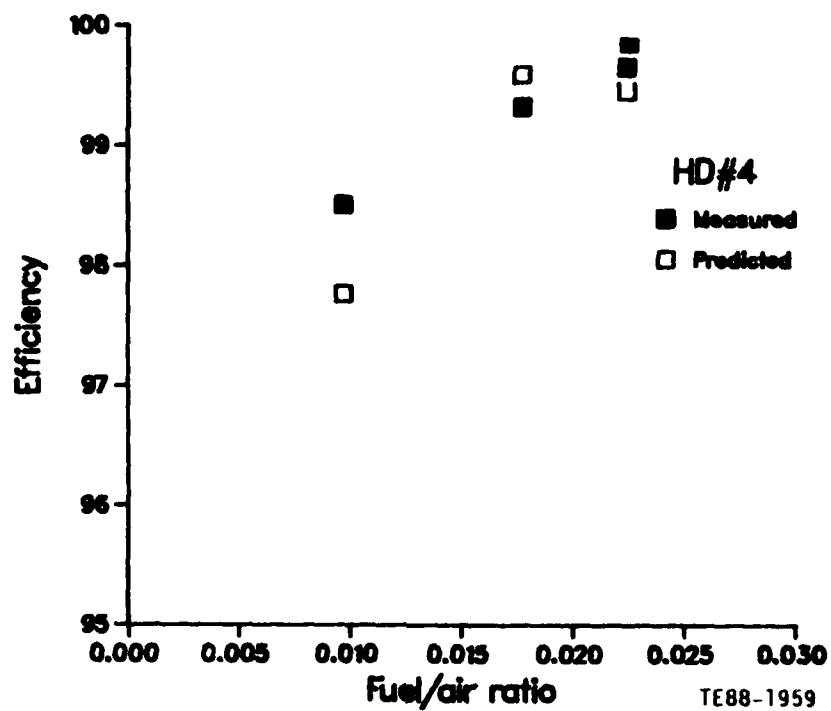
Figure 57. Combustion efficiency for HDF-4.
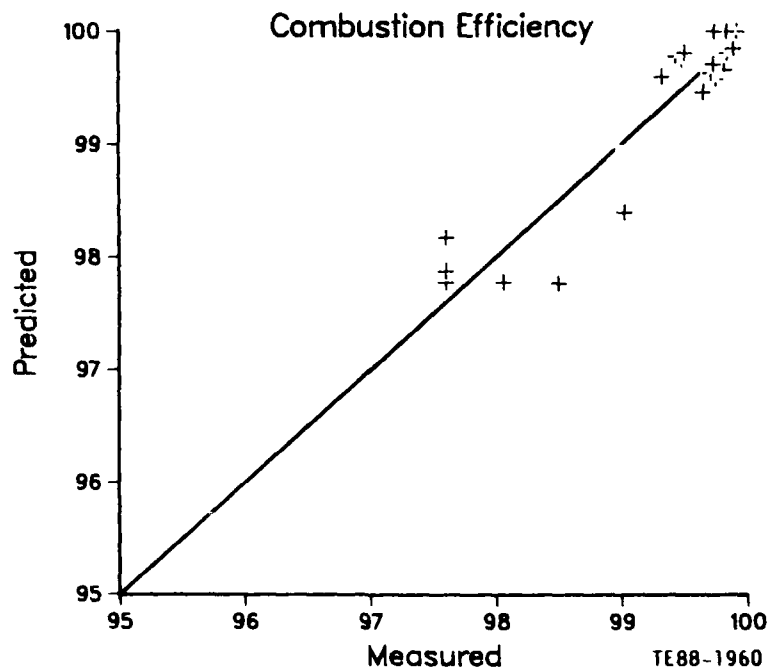
Figure 58. Comparison of measured and predicted combustion efficiency.

5.2.4 Temperature Profile at Combustor Exit

The nozzle guide vanes and turbine blades lives are most affected by the tem-
perature profile in the efflux gases discharging from the combustor. In the
design and development phases of a combustor, one of the most important prob-
lems is to achieve satisfactory temperature profiles set by the durability
goals of the hot sections downstream of the combustor. The two common parame-
ters used to describe the temperature traverse quality at combustor exit are
the radial profile and pattern factors. Both are dependent on the front end
design of the combustor that controls the temperature distribution of gases
entering the dilution zone, and the subsequent mixing of these gases with the
dilution jets.

The radial temperature profile is obtained by averaging the temperature around
each radius at the exit of the combustor. Figures 59 to 62 illustrate the ex-
perimental data that were obtained using 10 rakes of thermocouples mounted at
the combustor exit. Three thermocouples per rake gave the gas temperature at
hub, mid-point, and tip.

Highest radial profile factor is observed for the JP4 and HDF-1. It is also
noticed in these figures that as the power increases, the levels of the normal-
ized gas temperature at mid-point are decreased, and the gas temperatures at
the hub and tip shift slightly toward the average temperatures. The experi-
mental data were also used to calculate the pattern factor (PF) in each case.
It is the value that indicates the deviation of the maximum recorded tempera-
ture in the exhaust gases from the average burner outlet temperature (BOT).

The expression adopted in this investigation for calculating the PF takes into
account the combustor length occupied by the evaporation process L_{ev}, and is
given by the following:

$$PF = 1 - exp - 20 \ D_L / (\frac{\Delta P_L}{q_{ref}} (L_L - L_{ev})) \tag{20}$$
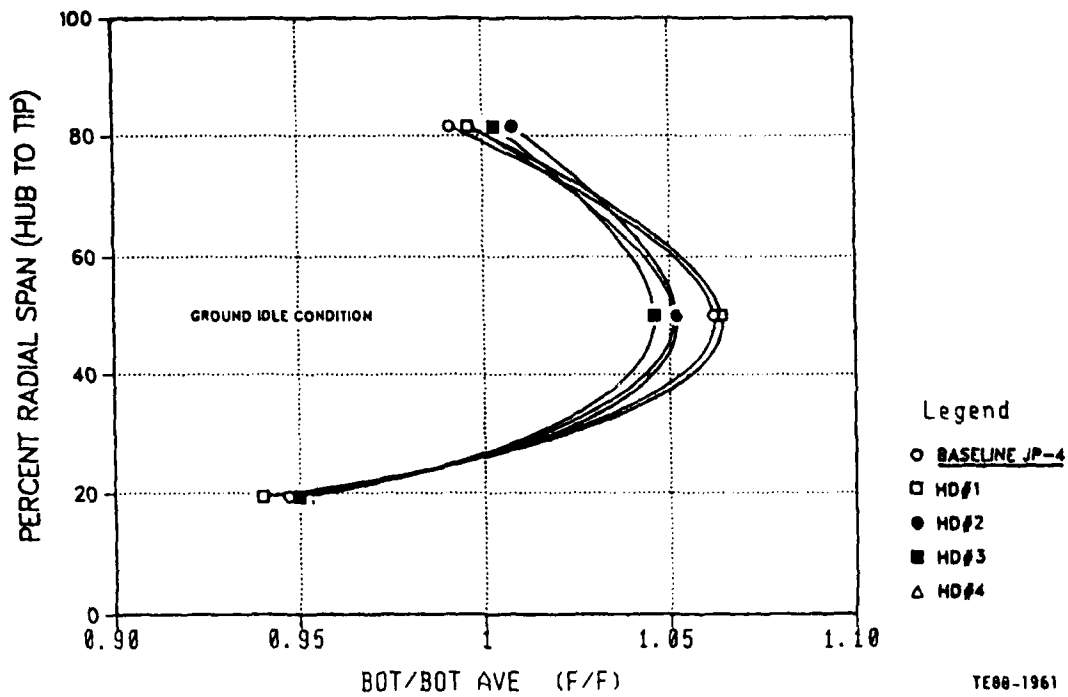
Figure 59. Radial exit temperature profile at idle.
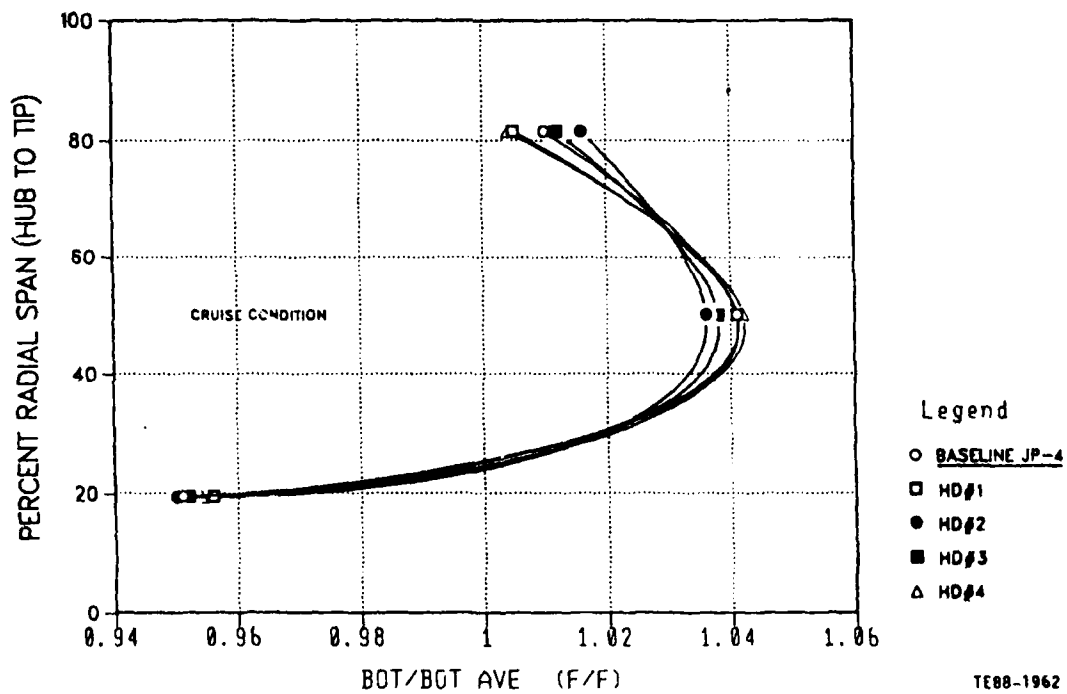
Figure 60. Radial exit temperature profile at cruise.

69
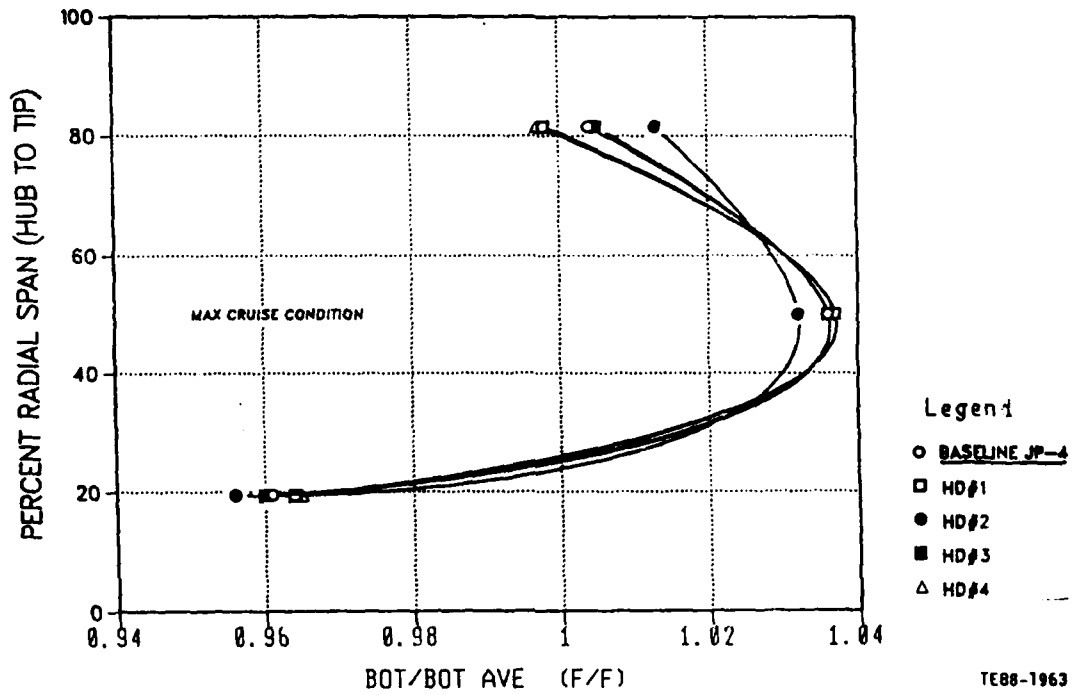
Figure 61. Radial exit temperature profile at maximum cruise.
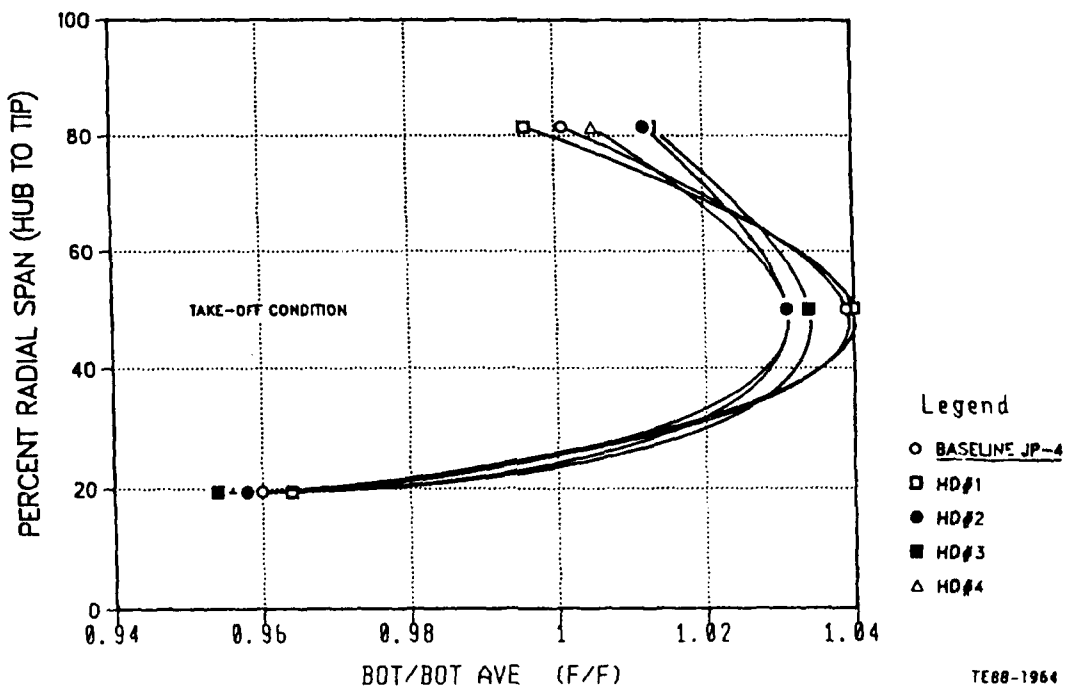
Figure 62. Radial exit temperature profile at takeoff.

70

D_L and L_L are liner diameter and length, and q_{ref} is the reference dynamic head based on the combustor casing area. The evaporation length is given by the following:

$$L_{ev} = 0.33 \left(\frac{W_{a3} \; SMD^2}{\rho_g \; A_L \; \lambda_{ev}} \right) \tag{21}$$

A_L is the cross-sectional area of the liner and ρ_g is the average gas density upstream of the dilution zone.

The calculated values of the PF are plotted against the measured ones in Figure 63. All the measured values are found to be within a range that extends from 0.17 to 0.23. Considering the usual BOT quality variability, it may be concluded that the overall effect of the fuel properties on the PF and radial profiles is small.
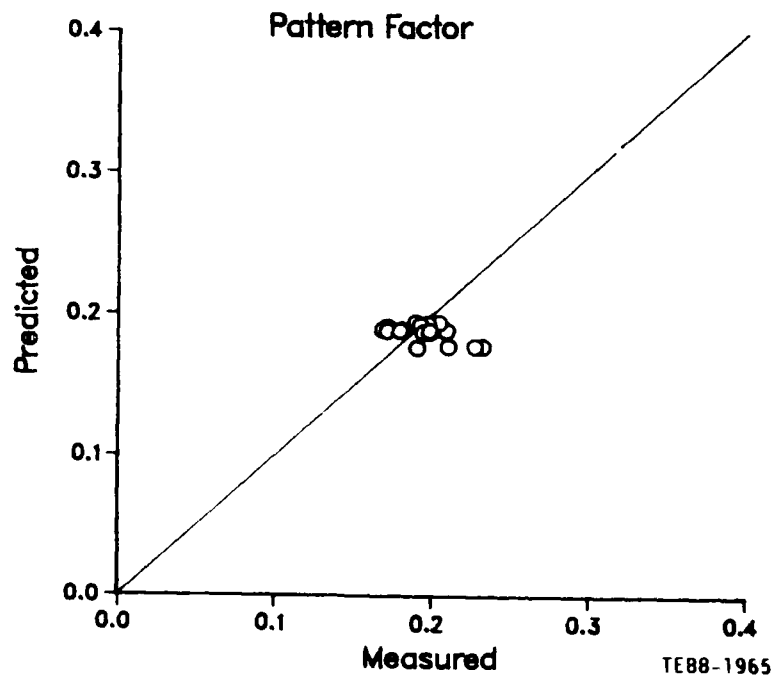
Figure 63. Comparison of measured and predicted pattern factor.

71

5.2.5 Combustion Stability

One of the main requirements of most practical combustion systems is for the flame to stay alight over a wide range of operating conditions. Combustion must be initiated and maintained in highly turbulent air streams flowing at speeds many times greater than the normal burning velocity of the fuel/air mixture employed. Flame blowout occurs when the rate of heat liberation in the combustion zone becomes insufficient to heat the incoming fresh mixture up to the required reaction temperature. For fuel sprays of low volatility and large mean drop size, the time required for fuel evaporation is relatively long and is often the main factor limiting the overall rate of heat release.

The lean blowout fuel/air ratio is calculated in the present effort using the following equation:

$$FAR_{LBO} = 850 \ (\frac{FW_{a3}}{V_c P_3^{1.3} \ e^{T3/300}}) \ (\frac{SMD^2}{\lambda_{ev} \ LHV})$$ (22)

LHV is the lower heating value of the fuel.

Figure 64 shows the capability of Equation 22 to correlate the experimental data. In this figure, it is obvious that HDF-4 has the highest lean blowout limit, while the JP4 shows the capability of burning down to the weakest mixture strength compared to the other fuels. The fact that HDF-4 possesses the highest viscosity and surface tension, and the JP4 has the lowest values of the two properties among the five fuels, indicates that the spray quality has a significant influence on the flame stability. To support this conclusion, the values of the spray SMD calculated at the test conditions and used in the lean blowout predictions, were plotted against the fuel/air ratio in Figure 65.

5.2.6 Ground Start and Altitude Restart

The process of igniting a combustible mixture is envisioned to occur i the

72
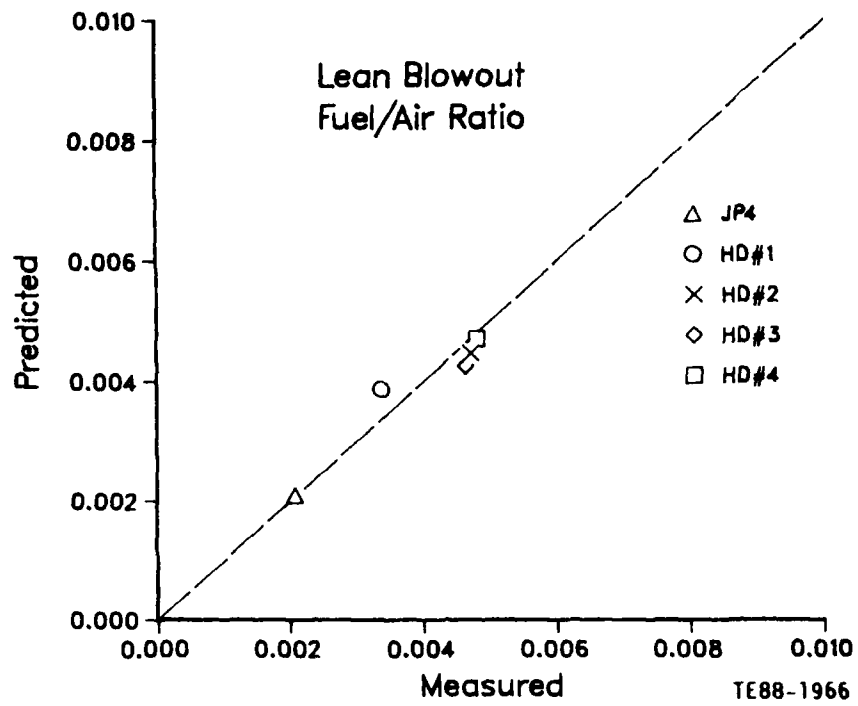
Figure 64. Comparison of measured and predicted lean blowout fuel/air ratio.
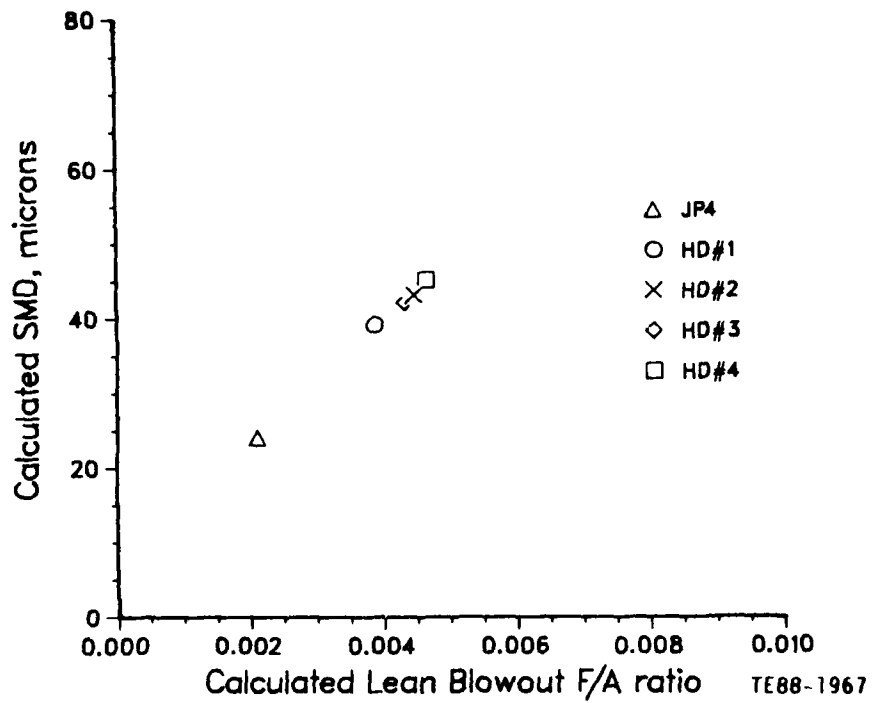
Figure 65. Predicted SMD for lean blowout calculation.

following manner. The transient ignition source, usually an electrical spark, supplies to the mixture sufficient energy to create a critically small volume of hot gases that just satisfies the necessary condition for propagation. That is, the rate of heat generation is sufficient to initiate rapid evaporation of fuel drops contained within the volume, and to compensate for the heat loss to the outer zone of unburned gas.

The analysis of the processes governing the rate of heat generation by combustion in the spark kernel, and the rate of heat loss by thermal conduction and turbulent diffusion shows that for the kernel to survive and propagate unaided throughout the mixture, its minimum dimension should always exceed the quenching distance (Reference 9). Based on this concept, the equation used in the present investigation is given by the following:

$$FAR_I = 10,800 \ (\frac{F \ W_{a3}}{P_3^{1.5} V_c \ e^{T3/400}}) \ (\frac{SMD^2}{\lambda_{ev} \ LHV}) \qquad (23)$$

In order to accurately predict the large number of ground start and relight ignition points measured in the tests, an iterative procedure was adopted in the calculation. By this means, values of SMD and evaporation constant are calculated at an assumed level of fuel/air ratio and used in Equation 23 to predict the ignition fuel/air ratio. The assumed fuel/air ratio is gradually changed until the two ratios coincide or converge to a certain limit.

The results of this procedure are plotted in Figure 66 for JP4 and Figures 67 through 70 for the high density fuels. In these figures, the ignition mixture strength is plotted against the corrected reference velocity, which is derived from liner velocity, inlet pressure, and inlet temperature. The experimental data are also included in the figures to demonstrate the capabilities of the present approach to predict ignition characteristics at various operating conditions. The good agreement with the data is also shown in Figure 71 where all the calculated points are plotted against the measurements.
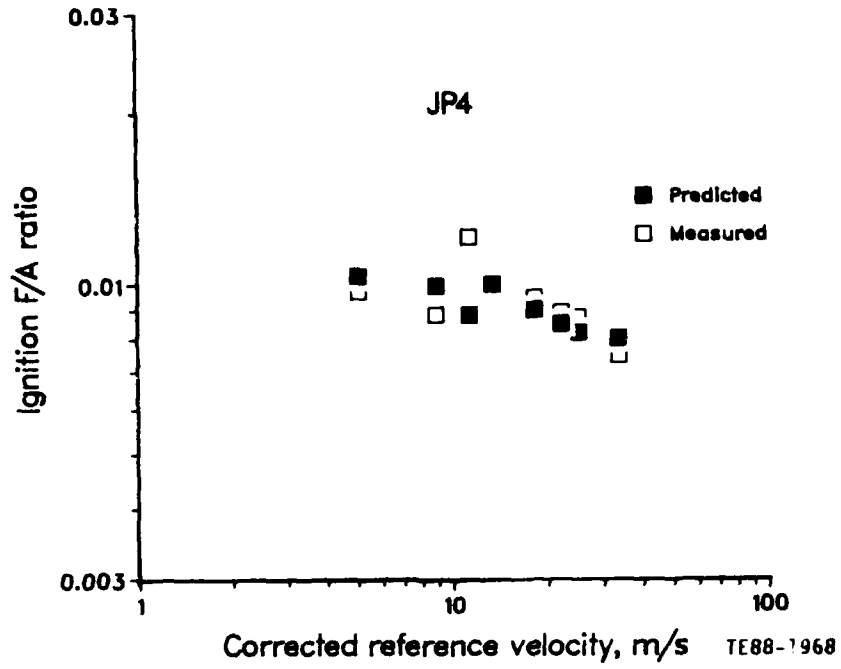
Figure 66.   Ignition fuel/air ratio for JP4.
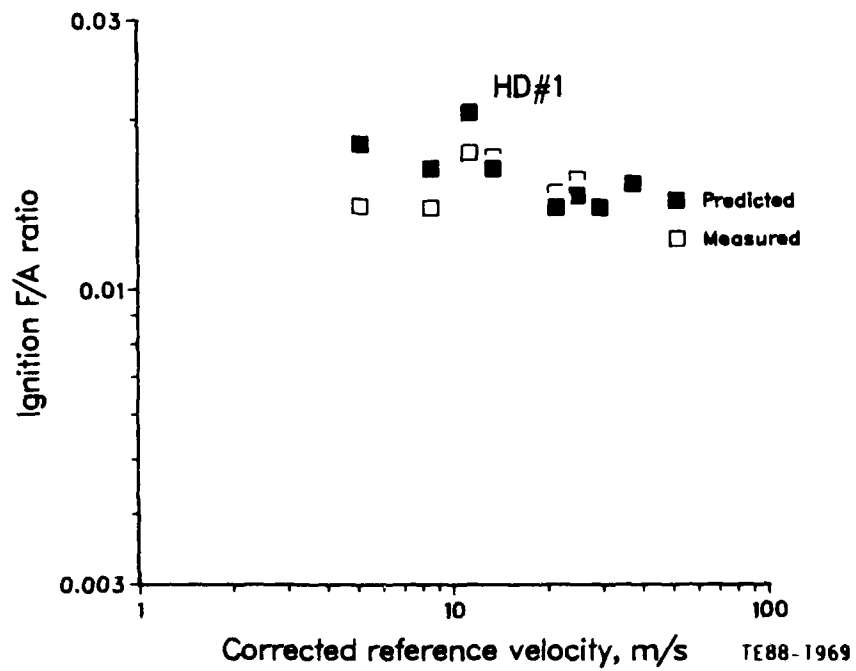
Figure 67.   Ignition fuel/air ratio for HDF-1.
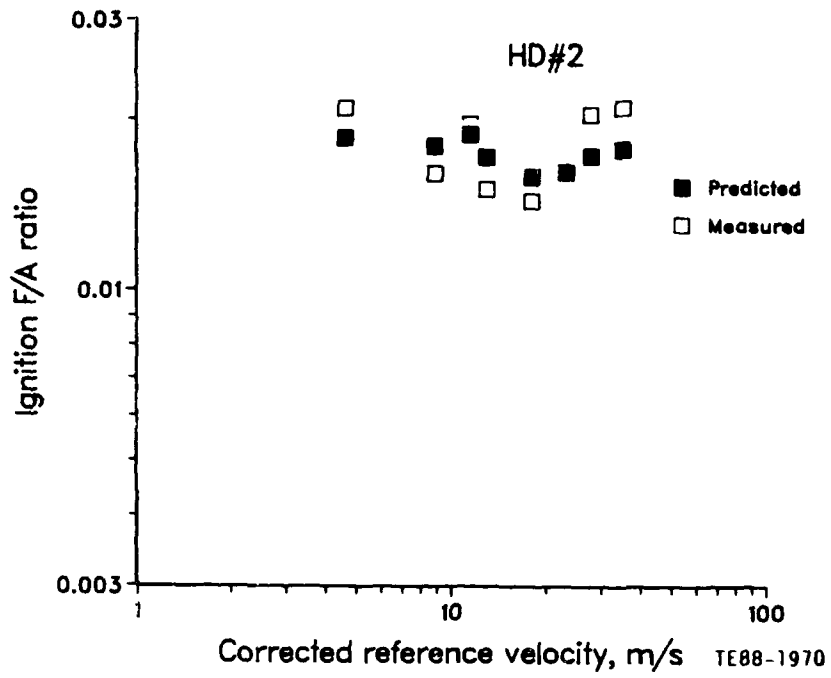
Figure 68.   Ignition fuel/air ratio for HDF-2.
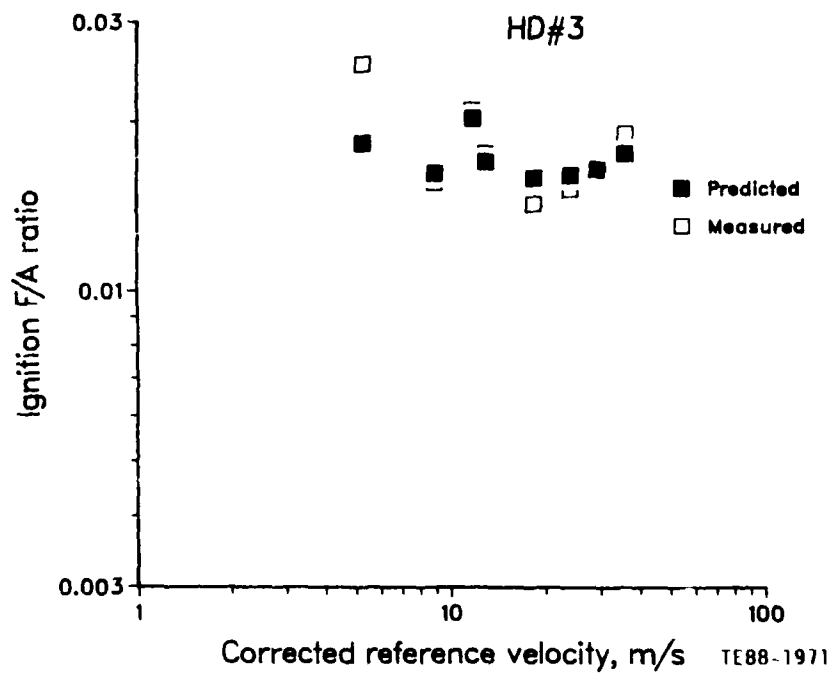
Figure 69.   Ignition fuel/air ratio for HDF-3.
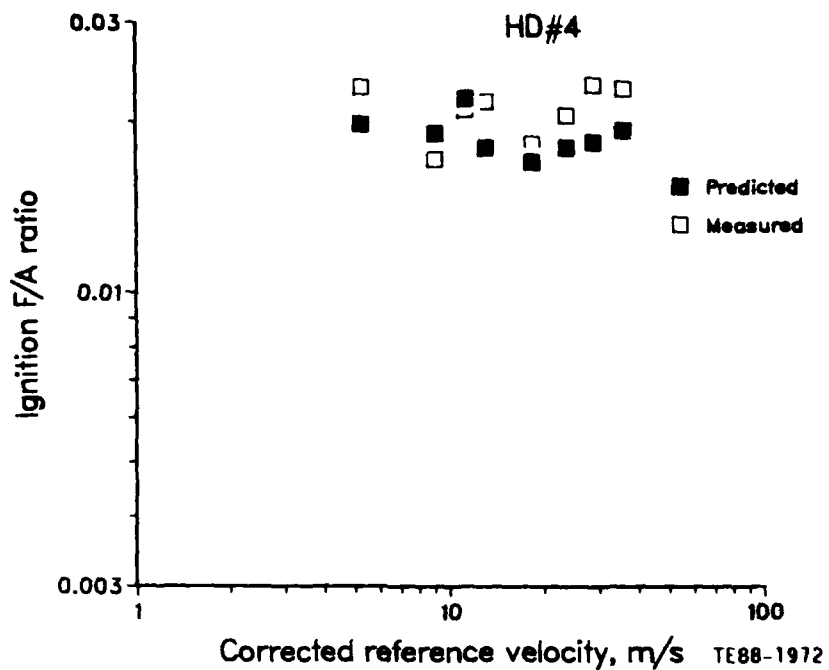
Figure 70. Ignition fuel/air ratio for HDF-4.
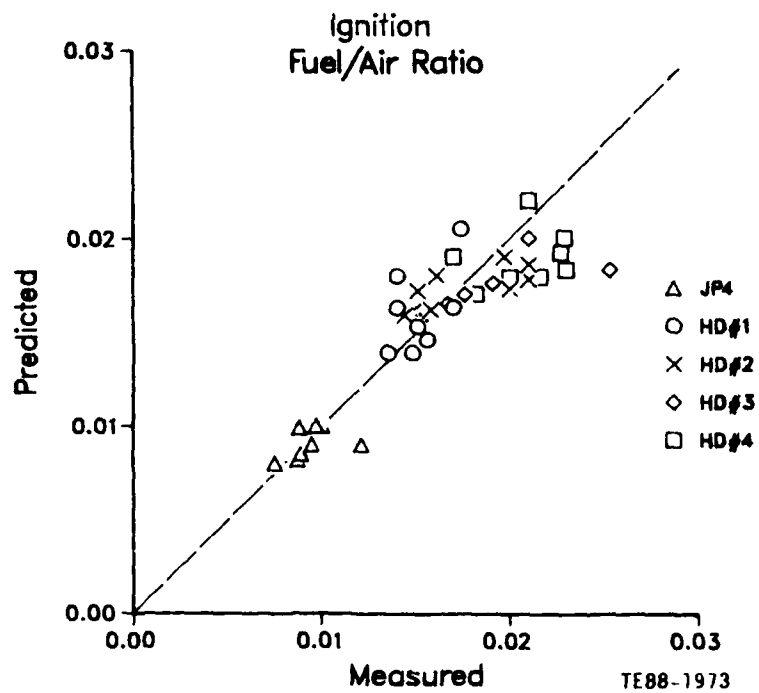
Figure 71. Comparison of measured and predicted ignition fuel/air ratio.

Due to the lack of experimental data available for the effect of subatmospheric conditions on the performance of dual-orifice atomizers, it was most appropriate to examine this effect in light of the ignition and altitude restart data. The reported data indicate stronger dependence on the ambient conditions in this range of operation, when all relevant parameters are accounted for. The best fit to the data was obtained when the exponent of the air density in Equation 2 of SMD was increased from 0.1 to 0.4 with the proper adjustment of the empirical constant. The calculated values of SMD used to predict the ignition fuel/air ratio are plotted in Figure 72 against the corresponding ignition points.

5.3 3-D COMBUSTOR PERFORMANCE MODEL

An essential requirement of the combustor modeling activity is to predict the performance of the combustor with reasonable accuracy. Due to the complexity of the combustor geometry, often it is difficult to adopt a typical empirical design and development approach to achieve significant advances in technology.
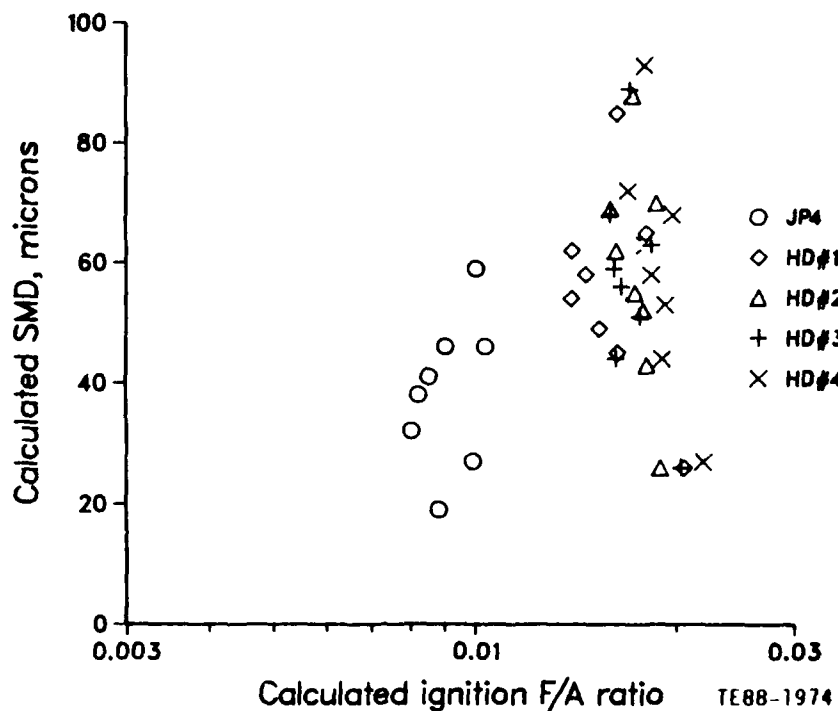
Figure 72. Predicted SMD for ignition calculation.

78

Also, the applicability of empirical methods developed for certain conventional design concepts may not always be suitable to novel or revolutionary combustor concepts. Moreover, the evaluation of performance parameters such as ignition, lean blowout, and pattern factor requires the accurate calculation of the combustor flow field, spray dynamics, and evaporation. Likewise, improved models are needed for combustion efficiency and emission predictions.

To use the detailed representation of the flow and combustion processes made available through the analytical 3-D codes, and the predictive tool of the proven empirical correlations, a combustor performance model was formulated (Reference 16). The success of the correlations, developed in Reference 1 and applied to the high density fuel effects in the present effort to predict the combustor performance certainly makes them most appropriate for inclusion in the model. With this approach, the impact of a systematic modification to the details of the burner is easily determined.

A 3-D, primitive variable, finite-difference code that solves the Navier-Stokes equations for a reacting flow field is adopted in the combustor performance model. The program simulates turbulence by a two-equation k-ε model, and combustion following vaporization is determined by a two-step chemical reaction model based on Arrhenius and eddy breakup concepts (Reference 17).

The following variables are computed by the 3-D code:

- o axial, radial, and swirl velocity components
- o specific enthalpy and temperature
- o turbulence kinetic energy and dissipation rate
- o unburned fuel, CO, and composite fuel fraction
- o fuel spray trajectory and evaporation rate

The transport equations for all dependent variables are of the following form:

$$\text{div} \left(\rho\, u\, \phi - \frac{\mu_{eff}}{P_r}\, \text{grad}\, \phi \right) = S_\phi \tag{24}$$

where ρ is mixture density, u is velocity vector, μ_{eff} is effective turbulence viscosity, P_r is effective Prandtl/Schmidt number, and S_ϕ is source term for variable ϕ.

An iterative finite-difference solution procedure is used to solve the resulting system of nonlinear, partial-differential equations. Extensive improvements in the code included the development of a more flexible grid system and the incorporation of an advanced evaporation model that addresses the critical properties of the high density fuels.

The developed performance model was verified by applying the method to a number of production combustors that varied significantly in design and concept. They represented various classes of can-annular, and both through, and reverse flow annular combustors. Satisfactory agreement between the model predictions and the experimental data was obtained under various operating conditions (References 18, 19).

To use the output data of the 3-D code fully, a feature is introduced into the code that allows the modeled combustor sector to be divided into a large number of subvolumes. The relevant combustion and flow characteristics within each subvolume are evaluated and prepared for use as an input to the performance correlations.

The combustor performance model was utilized in the high density fuel effects investigation in order to verify its capability to handle these fuels, and to support the effort required to define the combustor modifications needed to improve performance. The calculation of the air distribution to various combustion zones and cooling requirements was made using an air management program that accounts for the flow losses in various elements. The combustor air flow split was given earlier in Figure 3.

A 60-degree sector of the combustor was selected for modeling and was divided into 40 x 28 x 21 finite difference nodes along axial, radial, and circumferential directions, respectively. The grid network used in the analysis is shown
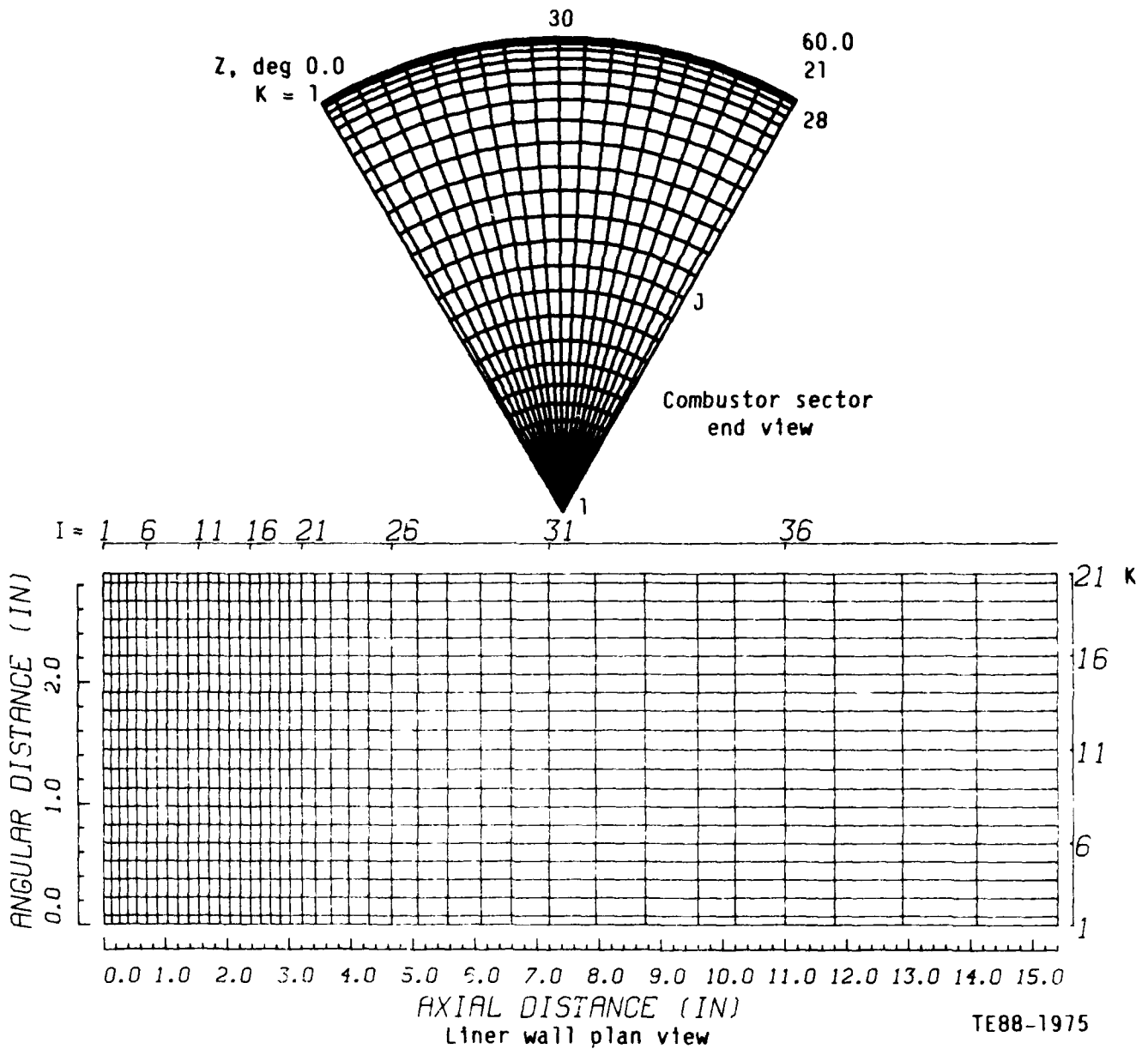
Figure 73.   Grid network used for 3-D modeling.

in Figure 73.   The flow pattern and combustion characteristics predicted by the 3-D code can be visualized by examining computer drawn plots of selected longitudinal section (x–y) and cross-sections (y–z) of the combustor sector.

For JP4, Figure 74 shows the velocity field, fuel/air ratio, and temperature

Velocity vectors

JP4

Fuel/air ratio

A	0.13533
B	0.10150
C	0.08120
D	0.06767
E	0.05413
F	0.04060
G	0.02093
H	0.01569
I	0.01046

Fuel/air ratio

Temperature--°F

A	4000
B	3600
C	3200
D	2800
E	2500
F	2300
G	2100
H	1900

Temperature contours

TE88-1976
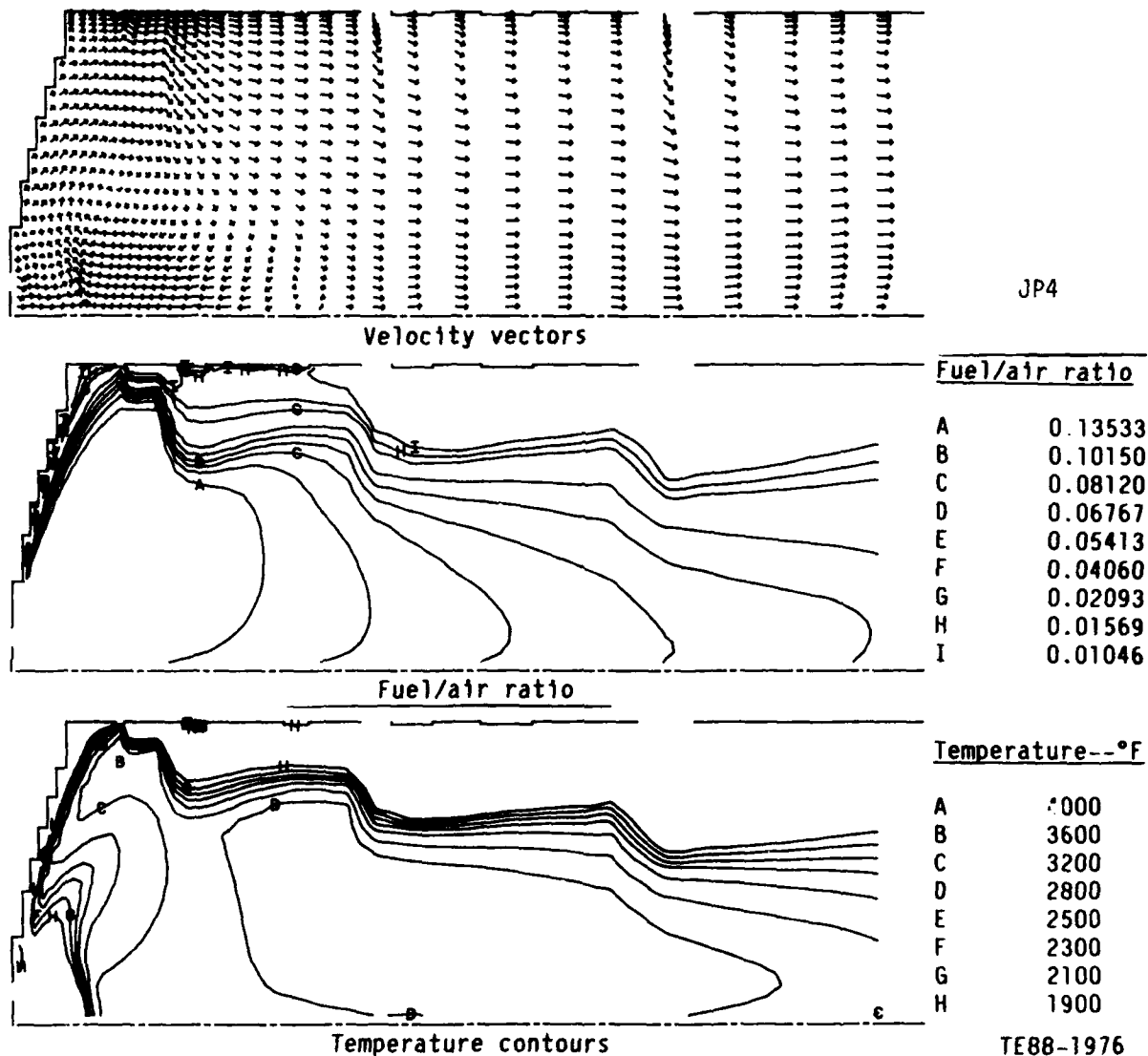
Figure 74. Flow field characterisics in x-y plane for JP4.

contours for x-y plane at takeoff conditions. Figure 75 gives the corresponding plots at two y-z planes located midway in the combustor primary zone, and at the plane of the first row of the primary holes. Similar plots obtained for HDF-3 are shown in Figures 76 and 77. The other three high density fuels were also included in the 3-D analysis.
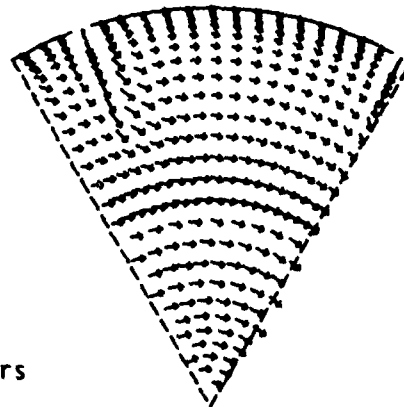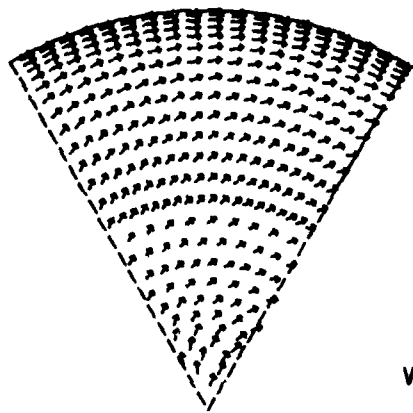
Velocity vectors
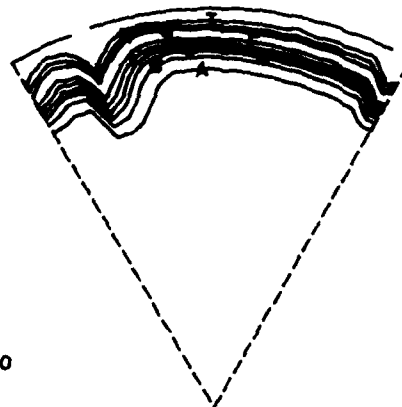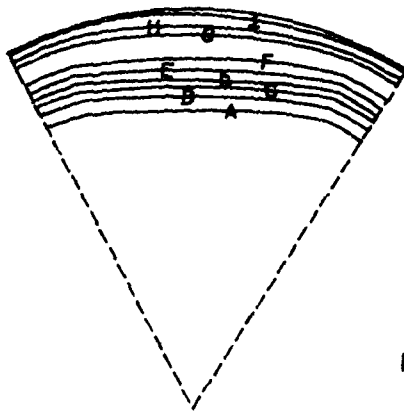
Fuel/air ratio
contours

Temperature contours

X = 1.372 in.

X = 2.654 in.

JP4

Fuel/air ratio

A	0.13533
B	0.10150
C	0.08120
D	0.06767
E	0.05413
F	0.04060
G	0.02093
H	0.01569
I	0.01046

Temperature--°F

A	4000
B	3600
C	3200
D	2800
E	2500
F	2300
G	2100
H	1900

TE88-1977

Figure 75.   Flow field characterisics in y-z plane for JP4.

83

Velocity vectors

Fuel/air ratio

Temperature contours

HDF-3

Fuel/air ratio

A	0.13963
B	0.10472
C	0.08378
D	0.06982
E	0.05585
F	0.04189
G	0.02097
H	0.01573
I	0.01049

Temperature--°F

A	4000
B	3600
C	3200
D	2800
E	2500
F	2300
G	2100
H	1900

TE88-1978
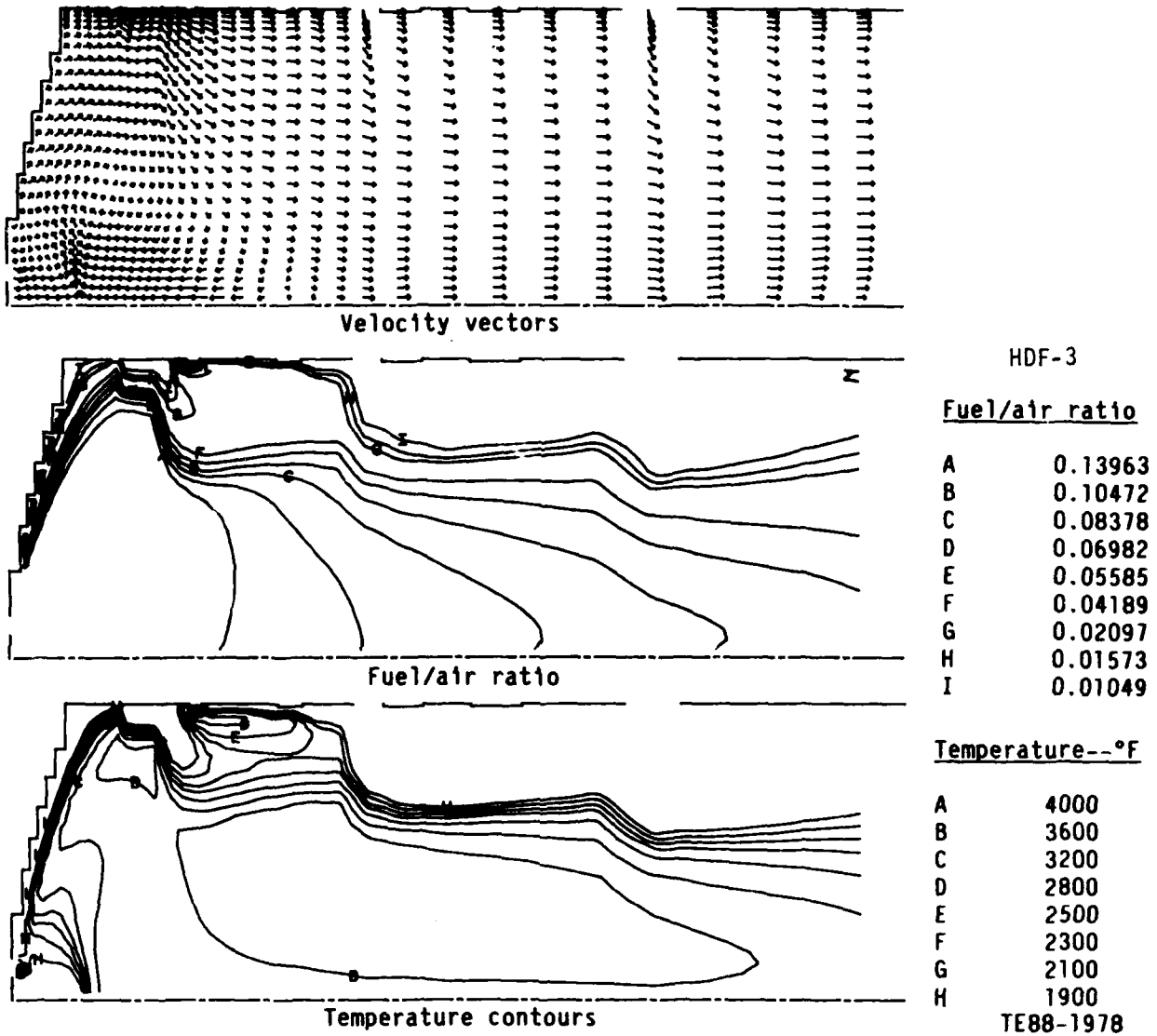
Figure 76.   Flow field characteristics in x-y plane for HDF-3.

The properties of these fuels that affect the atomization, evaporation, and combustion processes are quite different from those of JP4. The impact of these properties on performance could be noticed in the fuel/air ratio and temperature contours. Both fuels demonstrate very rich regions that occupy large
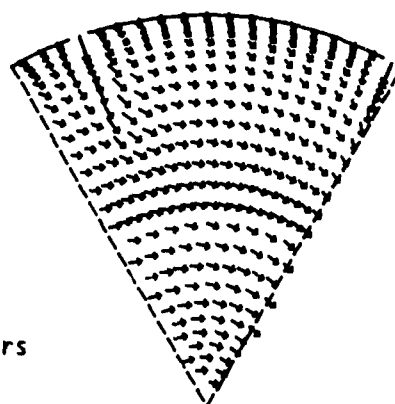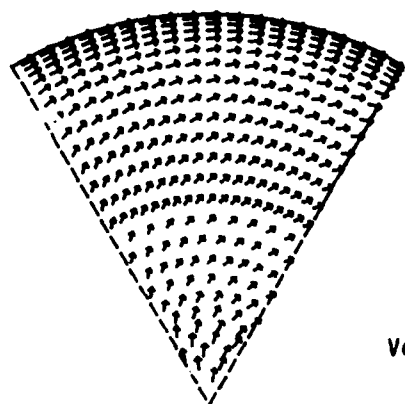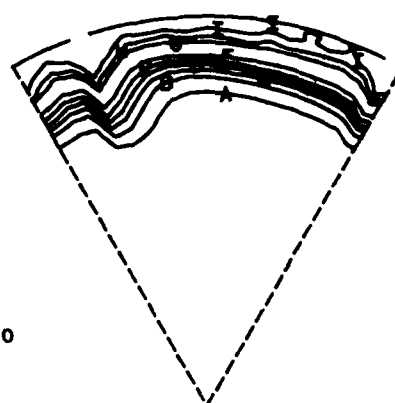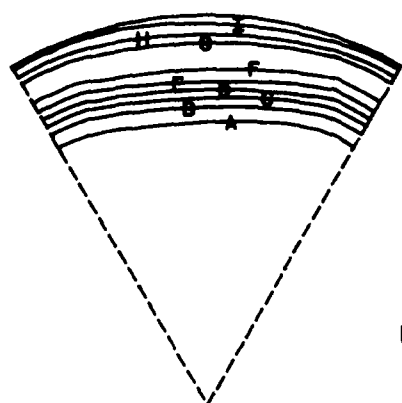
84

Velocity vectors

Fuel/air ratio
contours

Temperature contours

HDF-3

Fuel/air ratio

A	0.13963
B	0.10472
C	0.08378
D	0.06982
E	0.05585
F	0.04189
G	0.02097
H	0.01573
I	0.01049
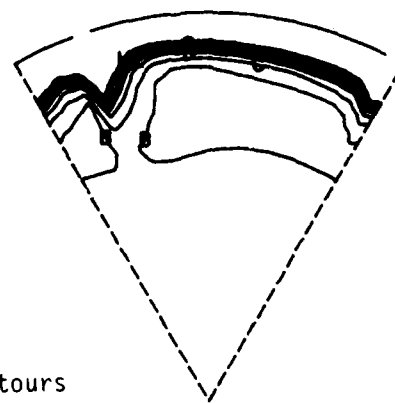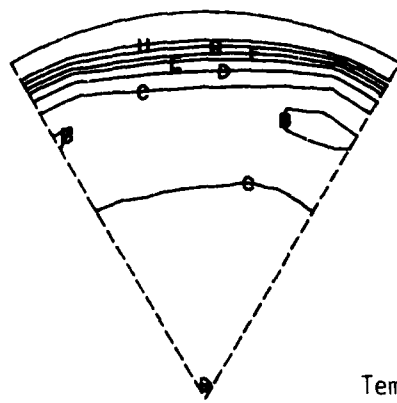
Temperature--°F

A	4000
B	3600
C	3200
D	2800
E	2500
F	2300
G	2100
H	1900

X = 1.372 in.   X 2.654 in.

TE88-1979

Figure 77.   Flow field characteristics in y-z plane for HDF-3.

portions of the combustor front end. The effect of larger SMD and harder to evaporate spray of the HDF-3 compared to the JP4 fuel is not showing in this region since the fuel/air ratio in these locations is much higher than the highest contour value used in the figures. In fact, the lower evaporation rate expected with the HDF-3 may result in some increase in gas temperature in this region since a reduction in the fuel/air mixture, that is already on the rich side of the temperature rise curve, will result in higher temperature.

The effects of fuel properties on atomization and evaporation are more obvious near the wall in the primary zone. The fuel/air ratios in these regions are much higher for the HDF-3 case. The resulting temperature levels shown in these figures correspond with these observations. To put the information given by the 3-D code in a form that can be utilized in the performance correlations, the macro-volume model described earlier was used. The various parameters calculated in the subvolumes, such as fuel/air ratio, temperature, and fraction of fuel burned, are plotted in Figure 78 for JP4, and Figure 79 for HDF-3 for an x-y slice through the combustor sector. The obvious difference between the two figures is the significantly larger amount of fuel burned near the wall of the primary zone with the HDF-3. This indicates that the high density fuel spray of larger SMD and lower evaporation rate had a better chance to penetrate the recirculation zone and reach these regions.

5.3.1 Emissions Predictions

As described earlier, the 3-D code output was combined with the performance correlations to form a combustor performance model. The model was applied to the T56-A-15 combustor in order to predict the various performance parameters for the high density fuels. The correlations used to predict CO, UHC, and NO_x emissions are given by the following:

$$CO \ (g/kg) = \frac{0.0093}{P_3^{1.5}} \left[\frac{m_A \ m_B \ T \ e^{-0.0023T}}{V(1 - m_{ev}/m_F) \ T_u^{0.5}} \right]_{ijk} \tag{25}$$
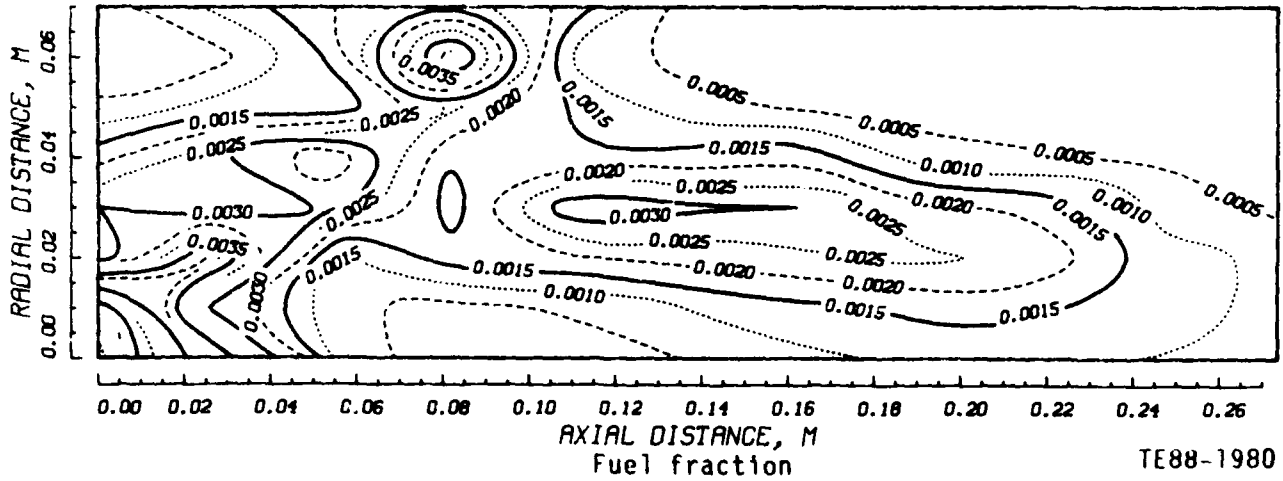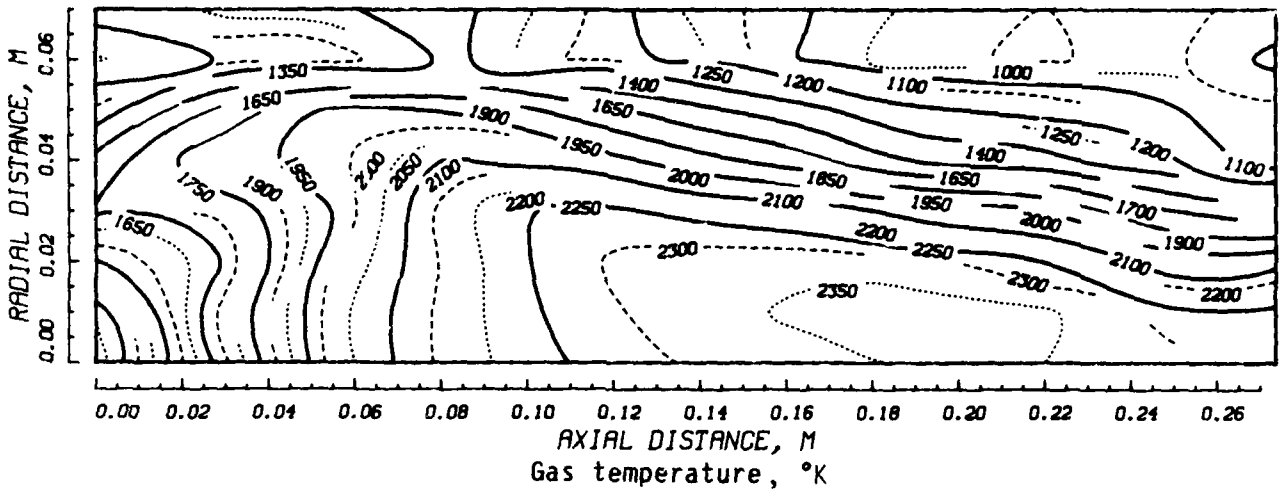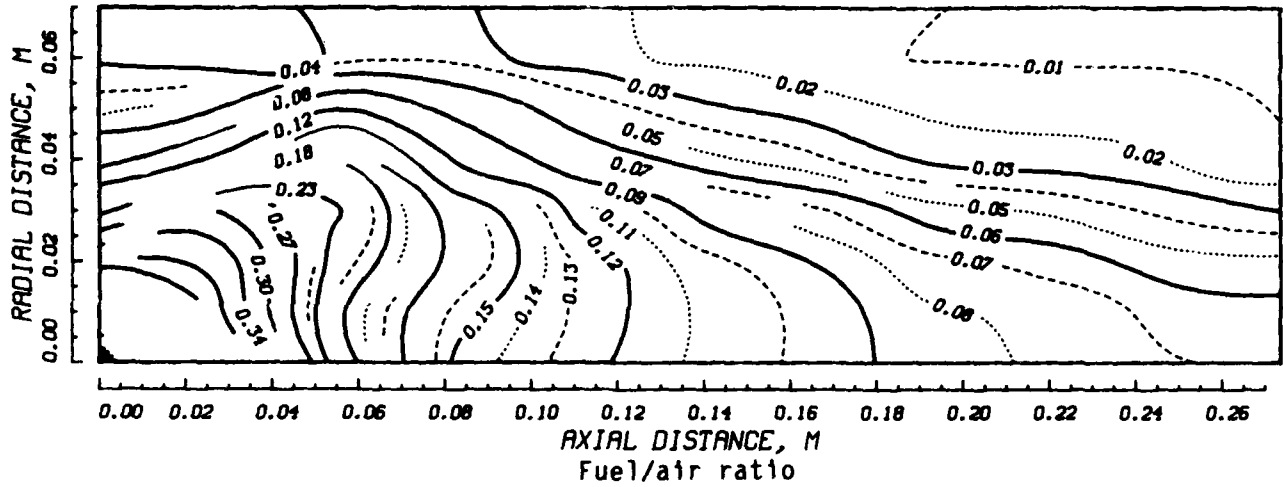
Figure 78.   Macro-volume model output for JP4.

X-Y SLICE AT Z-20-30DEG
HD#3

RADIAL DISTANCE, M

AXIAL DISTANCE, M
Fuel/air ratio

AXIAL DISTANCE, M
Gas temperature, °K

AXIAL DISTANCE, M
Fuel fraction

TE88-1981

Figure 79. Macro-volume model output for HDF-3.

$$UHC \ (g/kg) = \frac{3.85}{P_3^{2.5}} \left[\frac{m_A \, m_B \, T \, e^{-0.0025T}}{V(1-m_{ev}/m_F) \, T_u^{0.5}} \right]_{ijk} \tag{26}$$

and

$$NO_x \ (g/kg) = 15.0 \, P_3^{1.25} \left[\frac{V \, m_B \, e^{0.003T}}{T \, m_A} \right]_{ijk} \tag{27}$$

The expressions within the square brackets, as predicted by the 3-D code, are summed over each of the control volume units. T is gas temperature, m_A is airflow rate, V is volume, and m_f is fuel flow rate. Fuel mass fractions evaporated and burned within each subvolume are represented by m_{ev} and m_B, respectively. T_u is a parameter to describe mixing rate and is based on turbulence characteristics within each subvolume and airflow rate.

The equations used to predict the soot formation and oxidation are given by the following:

$$S_F = 0.1773 \, P_3^2 \, (18-H)^{1.5} \left[\frac{(F/A) \, m_B}{T \, m_A \, T_u^{0.25}} \right]_{ijk} \tag{28}$$

$$S_O = 0.042 \, (18-H)^{1.5} \, \frac{P_3^2}{V} \left(\frac{F/A}{T} \right)_{pz} \left[\frac{V \, e^{0.0011 \, T}}{m_A \, (F/A)} \right]_{ijk} \tag{29}$$

V is the combustor volume, the subscript pz indicates average values in the primary zone, and H is hydrogen content in fuel. These two equations were successfully applied to a large number of combustor designs and fuel types. These forms of equations were used in the present effort, since the inclusion of a term based on the smoke point and aromatic content, similar to the one reported in the previous section, in place of the hydrogen content term would require an extensive effort. This effort is required to define the smoke point of various fuels used in the model validation phase and the simultaneous adjustment of the two empirical constants in the two equations to fit all the data of various cases.

89

The application of the combustor performance model to a certain combustor design has shown a great potential to predict the impacts of systematic modifications to the details of the combustor, fuel type, and power mode on the combustor performance. Each case required a full analysis using the 3-D code. In the present investigation, to limit the use of the 3-D code, it was thought most appropriate to run the code at takeoff conditions for the five fuels under investigation. Since the effects of the operating parameters on the combustor performance are well established, as illustrated in the previous section, conversion parameters were devised to predict the performance at other operating modes. These parameters utilize the predictions at takeoff and carefully account for the operating conditions, evaporation constant, and spray quality as compared to those obtained at maximum power.

The combustor performance model predictions of CO, UHC, and NO_x are plotted against the measured data in Figures 80, 81, and 82, respectively. Good agreement is shown in these figures. In order to define the regions that are responsible for the high soot levels observed for this combustor, contours of soot concentration formed in various zones are plotted in Figures 83 and 84 for JP4 and HDF-3. It is seen that soot is formed in the very rich zone near the fuel injector for both fuels, and the formation region extends for the HDF-3 to reach the liner wall. Inadequate mixing in the primary zone, coupled with low quality atomization, are contributing to the high soot concentration observed in these figures. Figure 85 shows the satisfactory agreement between the predicted and measured values of the smoke number.

5.3.2 Performance Predictions

The 3-D code output was also combined with the performance correlations to predict parameters such as combustion efficiency, pattern factor, lean blowout, and ignition characteristics. The following expression is used to predict the efficiency:

$$\eta_c = \eta_r \, \eta_{ev} \, \eta_{mix} \tag{30}$$
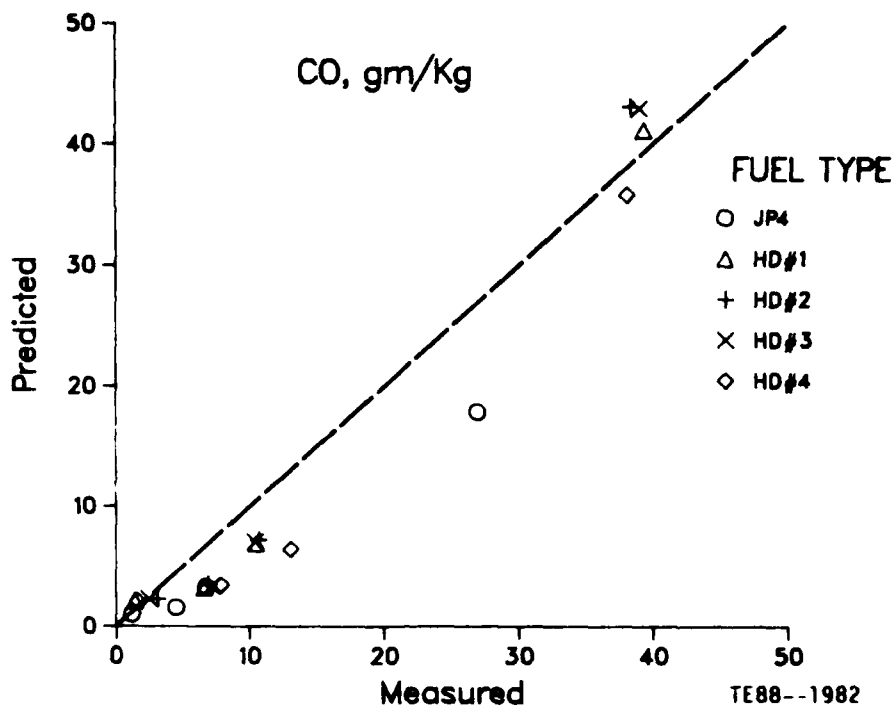
Figure 80. Performance model predictions of CO.
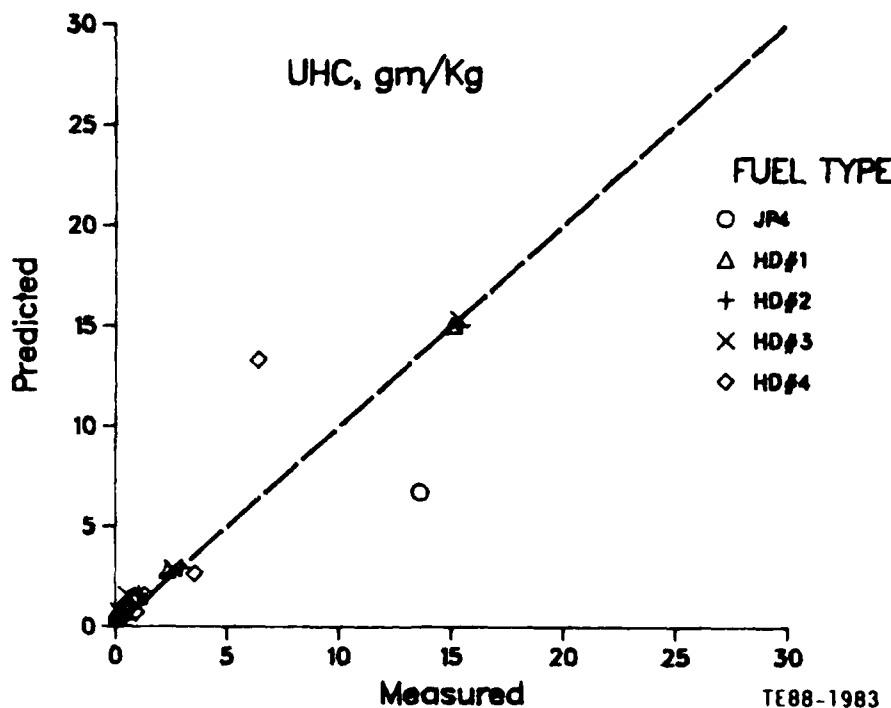
Figure 81. Performance model predictions of UHC.

91
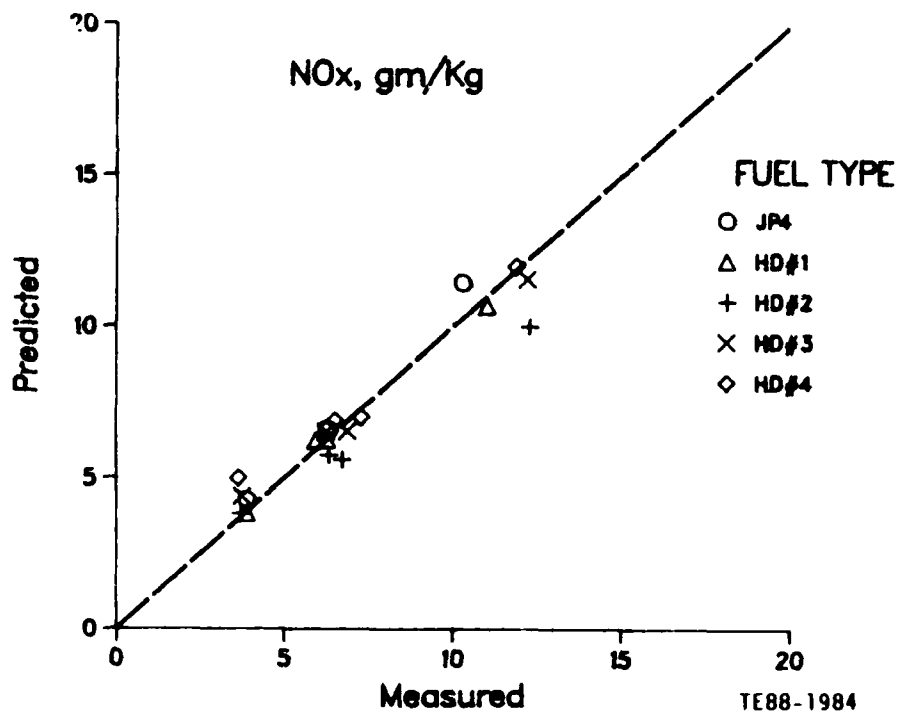
Figure 82. Performance model predictions of NO_x.

X-Y SLICE AT Z-20-30 DEG -SOOT FORMED IN EACH ZONE
JP4
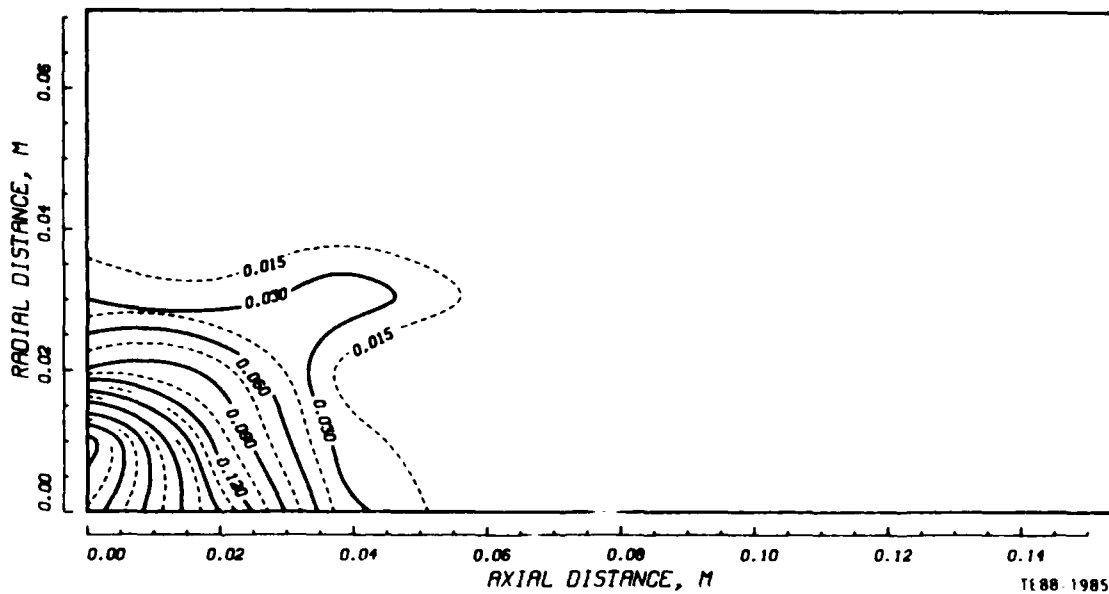
Figure 83. Contours of soot formation in combustor x-y slice for JP4.
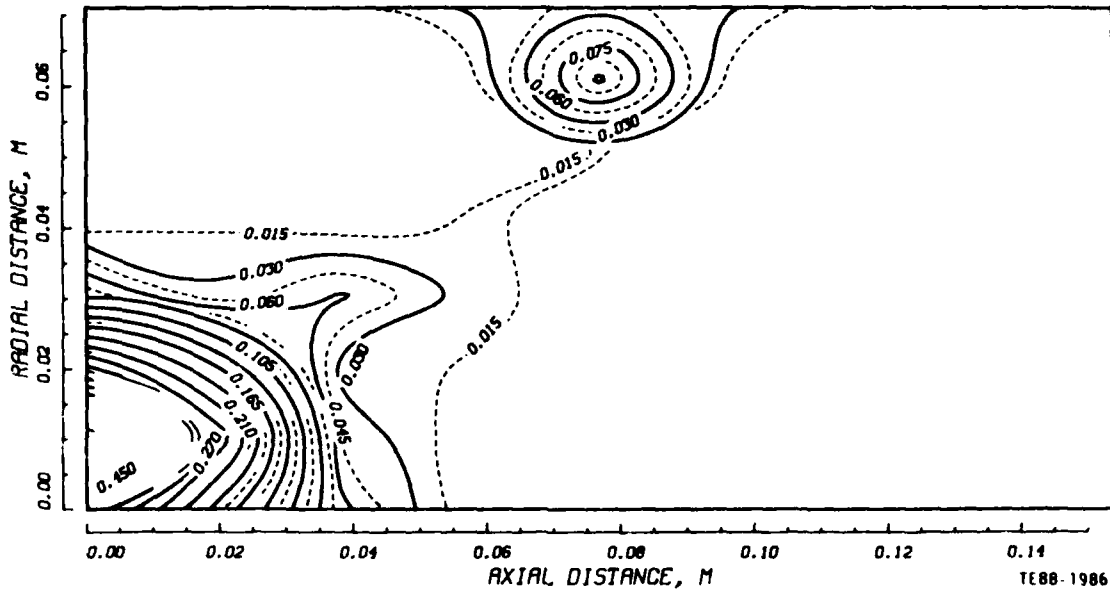
Figure 84.   Contours of soot formation in combustor x-y slice for HDF-3.
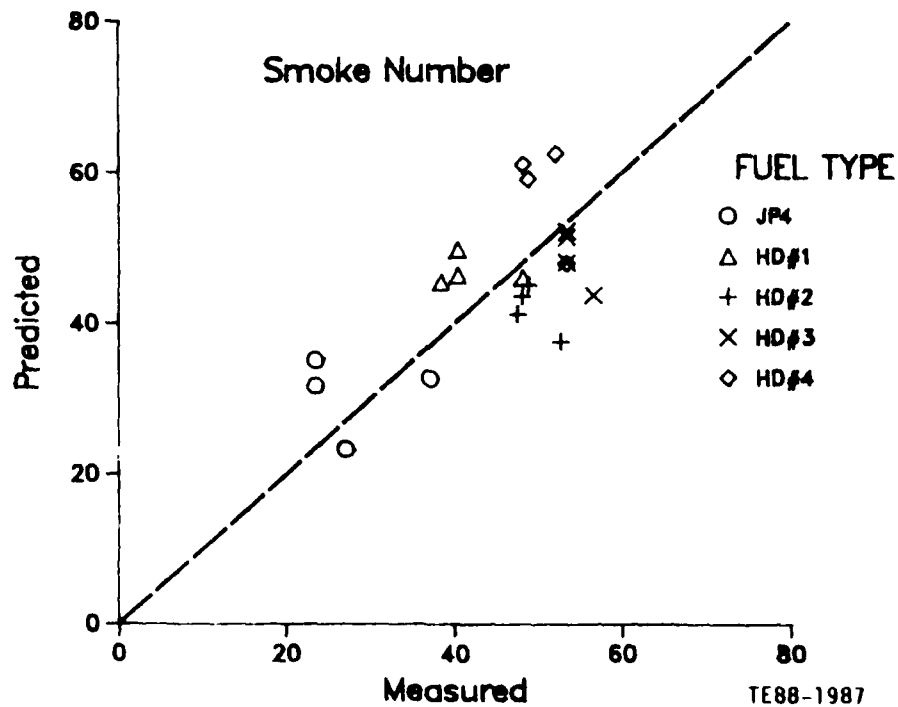
Figure 85.   Performance model predictions of smoke.

93

where the reaction term is given by the following:

$$\eta_r = 1 - \exp\left(-0.07 \; P_3^{1.3} \; [\frac{V \; m_B \; e^{T/400}}{m_A}]_{ijk}\right) \qquad (31)$$

the evaporation term is

$$\eta_{ev} = 1 - \exp\left(-1.71 \; [\frac{m_F \; m_B}{m_A}]_{ijk}\right) \qquad (32)$$

and the mixing rate contribution to combustion efficiency is

$$\eta_{mix} = 1 - \exp\left(- \frac{1500}{V} \; [Tu^{0.5}V]_{ijk}\right) \qquad (33)$$

The definitions of all terms are as given before. The predictions of the combustion efficiency are plotted against the measured values in Figure 86. Good agreement is observed in this figure.
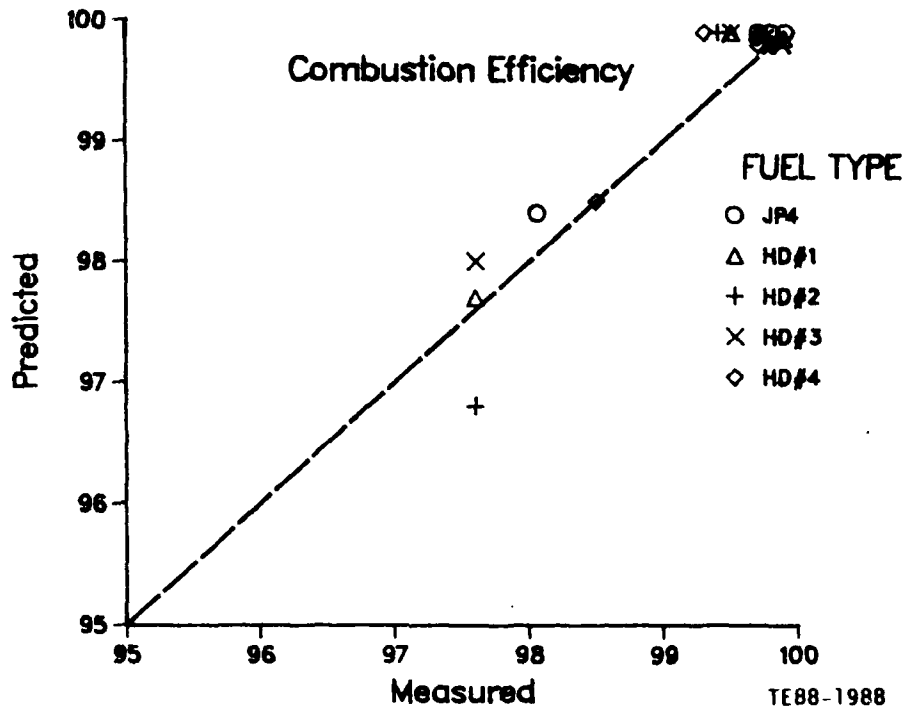
Figure 86. Performance model predictions of combustion efficiency.

94

The combustor exhaust gases pattern factor was calculated using the following equation:

$$PF = 1 - \exp - 0.0095/(\frac{L_L - L_{ev}}{D_L \ V \ F_D} \cdot [Tu^{0.5}V]_{ijk}) \tag{34}$$

L_L is the combustor length, D_L is combustor diameter, L_{ev} is length occupied in fuel evaporation, and F_D is a factor that defines the temperature profile in the dilution zone. The terms in the square brackets are subvolume values that are summed over the sector volume. The predictions of this equation are plotted in Figure 87 against the data.

Lean blowout (LBO) fuel/air ratio is calculated using the flow field given by the 3-D code through an iterative procedure. The SMD calculation is based on the liner pressure drop at the operating conditions under consideration and selected fuel/air ratio using the procedure given earlier. Also, an evaporation constant is determined and employed in the lean blowout equation that
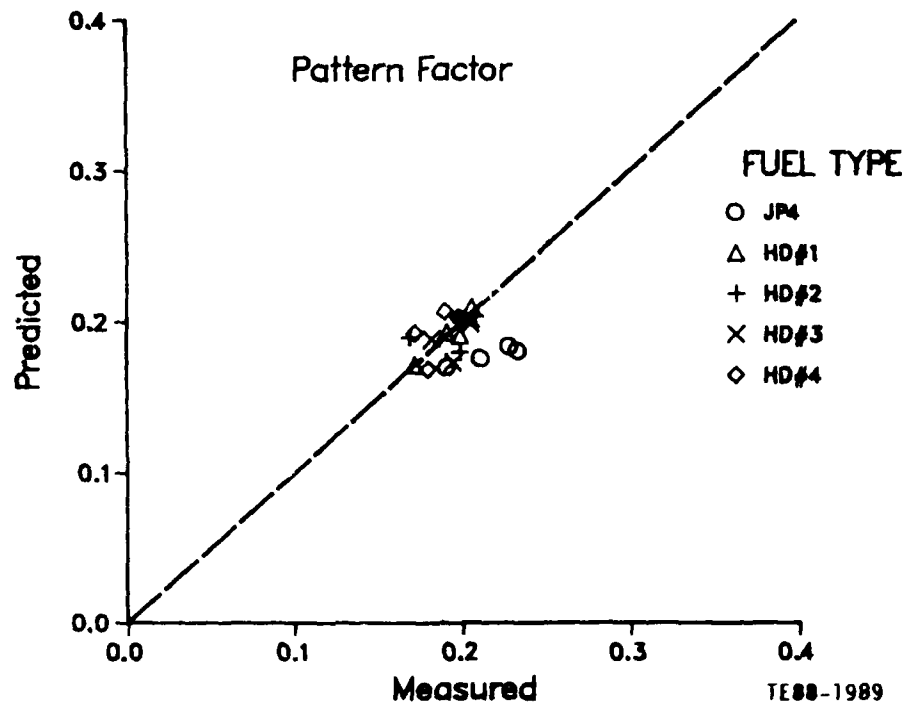
Figure 87. Performance model predictions of pattern factor.

95

predicts fuel/air ratio. The procedure is repeated until the difference in the two fuel/air ratios is less than a prescribed value. The expression used for lean blowout fuel/air ratio is given by the following:

$$\text{LBO F/A} = \frac{98,000}{\text{LHV}} \, P_{3\text{des}} \, \left(\frac{F\,W_{a3}\,t_r}{P_3^{1.3}\,e^{T/300}}\right) \cdot \left[\frac{m_{ev}\,m_B}{Tm_A\,m_F}\right]_{ijk} \qquad (35)$$

where t_r is ratio of evaporation time at LBO conditions to evaporation time at design conditions, F is the fraction of air based on average fuel/air ratio in primary zone, and $P_{3\text{des}}$ is the pressure at design mode. The good agreement between the predictions of Equation 35 and the data is evident in Figure 88.

The calculations of the ground ignition and altitude relight fuel/air ratio follow similar procedures to that used for the lean blowout ratio. The equation used in this effort is given by the following:

$$\text{Ignition F/A} = \frac{16.5 \times 10^5}{\text{LHV}} \, P_{3\,des} \, \left(\frac{F\,Wa_3\,t_r}{P_3^{1.5}\,e^{T/300}}\right)\left[\frac{m_{ev}\,m_B}{Tm_A\,m_F}\right]_{ijk} \qquad (36)$$
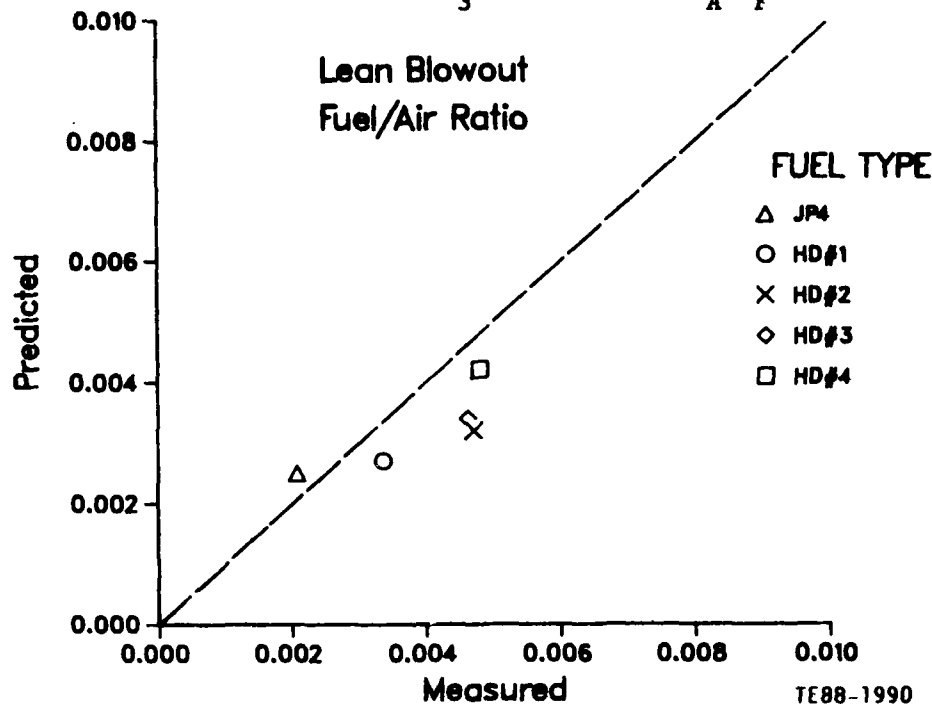
Figure 88. Performance model predictions of lean blowout limit.

96

LHV is the lower heating value of the fuel, m_{ev} and m_B are the fractions of fuel evaporated and burned within a subvolume, and m_F is fuel flow rate. The predictions of Equation 36 for the five fuels under consideration are plotted against the measurements in Figures 89 through 93, respectively. Once again fairly satisfactory agreement is obtained between the predictions and the data.

It has been seen in this section that the application of the combustor perfor-mance model to predict the performance of the T56-A-15 combustor when operating on the high density fuels is very encouraging. This model combines the analy-tical capabilities of the 3-D combustor codes to define the flow field with the proven empirical correlations. The model validation effort, therefore, was taken a step further ahead to include the effects of alternate fuels, in addition to the extensive application to various combustor designs. The advan-tage offered by the performance model is the capability to sense the impact of minor modification to the details of the dome or liner designs. Moreover, the model can be easily employed to detect the regions in the combustor responsible for any observed trends in performance.
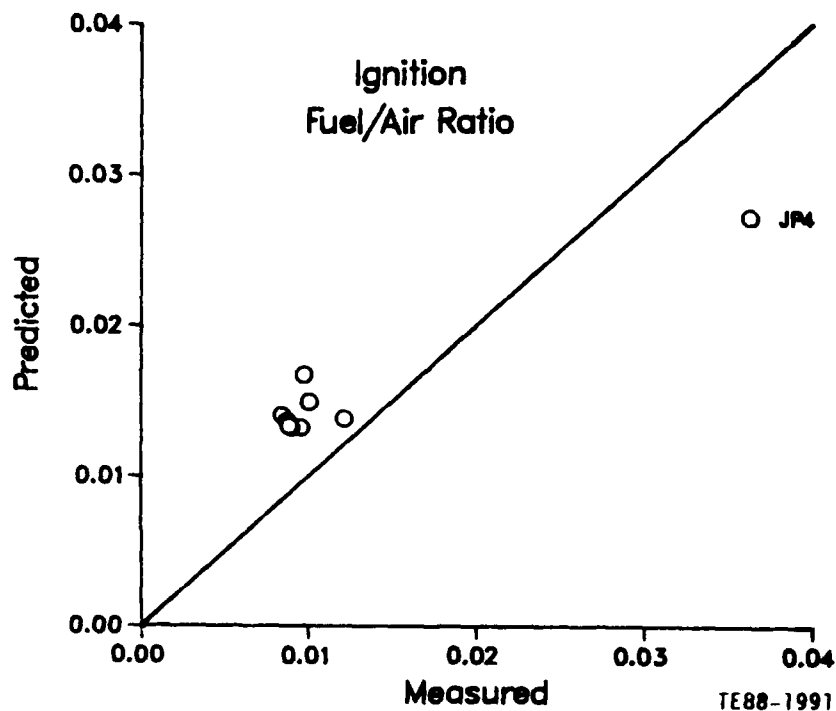
Figure 89. Performance model predictions of ignition for JP4.

97
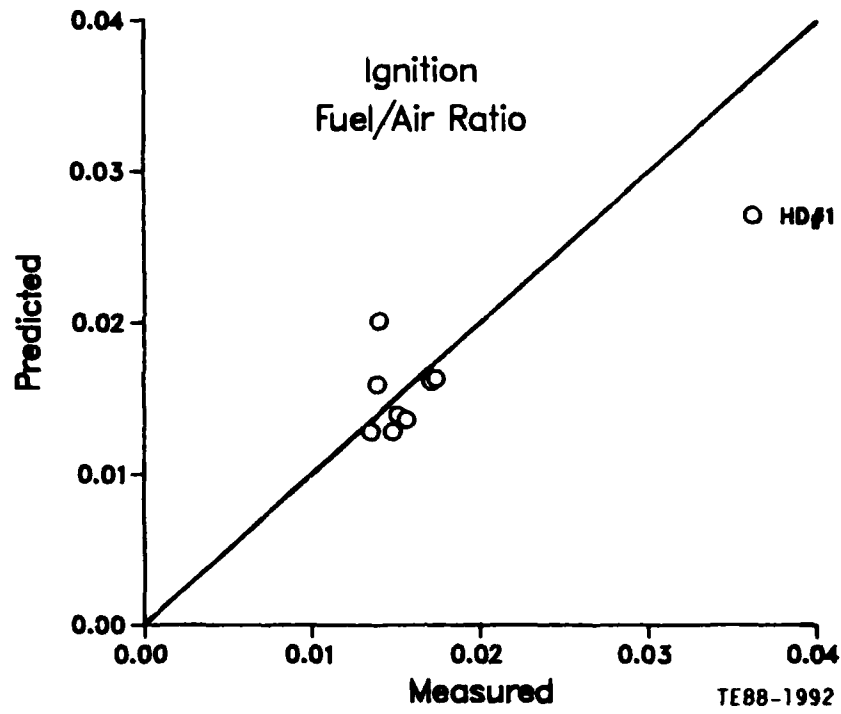
Figure 90. Performance model predictions of ignition for HDF-1.
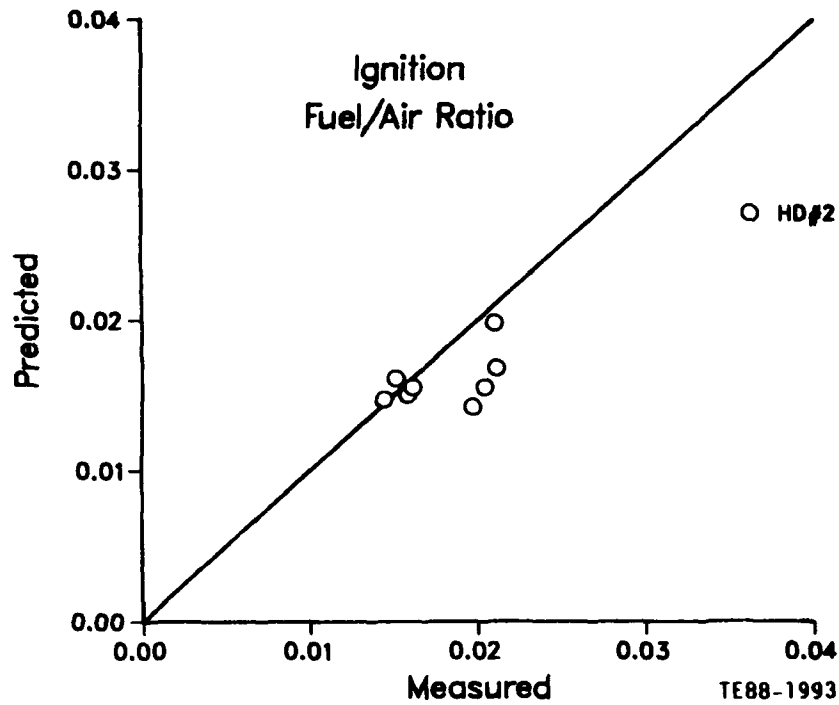
Figure 91. Performance model predictions of ignition for HDF-2.
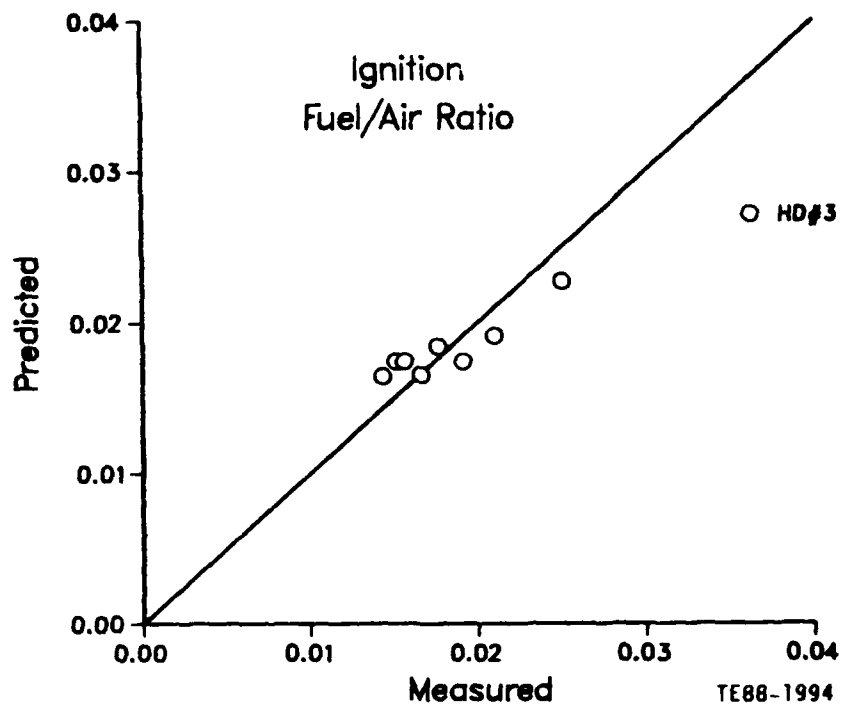
Figure 92.   Performance model predictions of ignition for HDF-3.
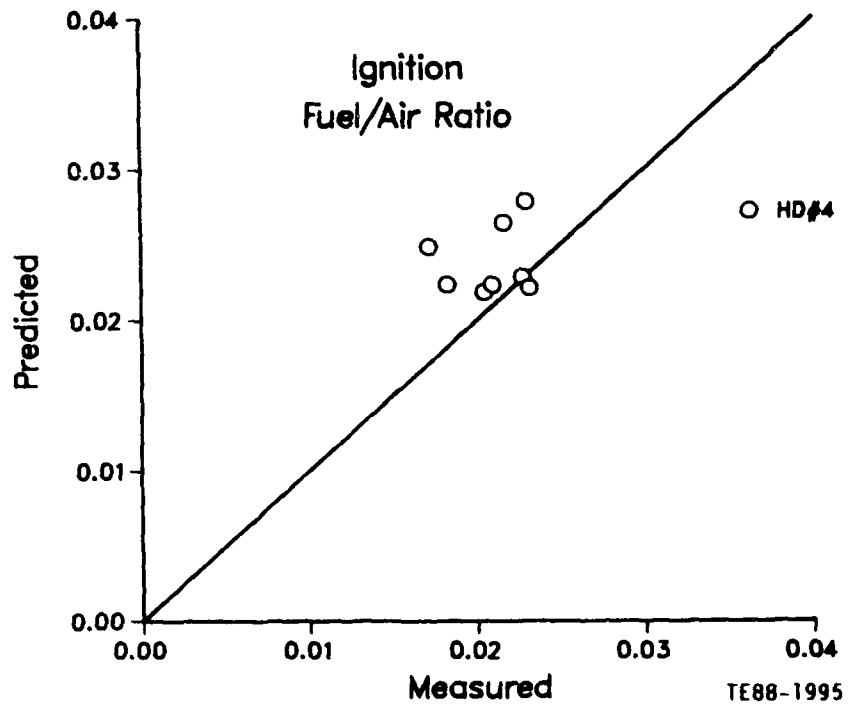
Figure 93.   Performance model predictions of ignition for HDF-4.

99

5.4 COMBUSTOR DOME AND LINER TEMPERATURES

In this section, the effects of burning the high density fuels on the T56-A-15 liner wall temperature are evaluated. A heat transfer calculation approach that was followed in this investigation is described, and its predictions are compared with the wall temperature measurements.

Thermal paint testing of the combustor was performed at takeoff power conditions using the baseline JP4 fuel. This gave an overall picture of the ranges of wall temperature in each zone. The highest temperatures observed on the outer surface of the dome are about 1000 K and occur in regions between baffles, near the outer radius of the liner. The transition section demonstrated high temperature levels in the range of 1060 - 1200 K in most locations. The highest temperatures of the liner wall are in the order of 1100 K in locations near the end of each cooling zone where the film cooling effectiveness is at the lowest.

The flame radiation measurements are reported in the previous chapter and plotted in Figure 94 for the JP4 and the high density fuels. The figure indicates that the radiation emittance varies with power level and fuel type. The highest radiation is measured at takeoff and maximum cruise conditions. In general, HDF-3 and -4 demonstrate the highest radiation loads compared with other fuels. It is a combination of fuel composition and actual flame temperature that determine the emittance level.

After the liner paint test, the combustor was instrumented with 30 C/A type thermocouples distributed on dome, liner, and transition sections. The locations of the thermocouples and the details of the measurements are given in the previous chapter. The data were obtained at idle, cruise, maximum cruise, and takeoff conditions for the JP4 and the high density fuels.

In the heat transfer analysis, the liner is heated by the radiation from the flame and hot gases, and convection from the gas flow within the chamber. The removal of heat from the burner walls occurs through radiation to the outer
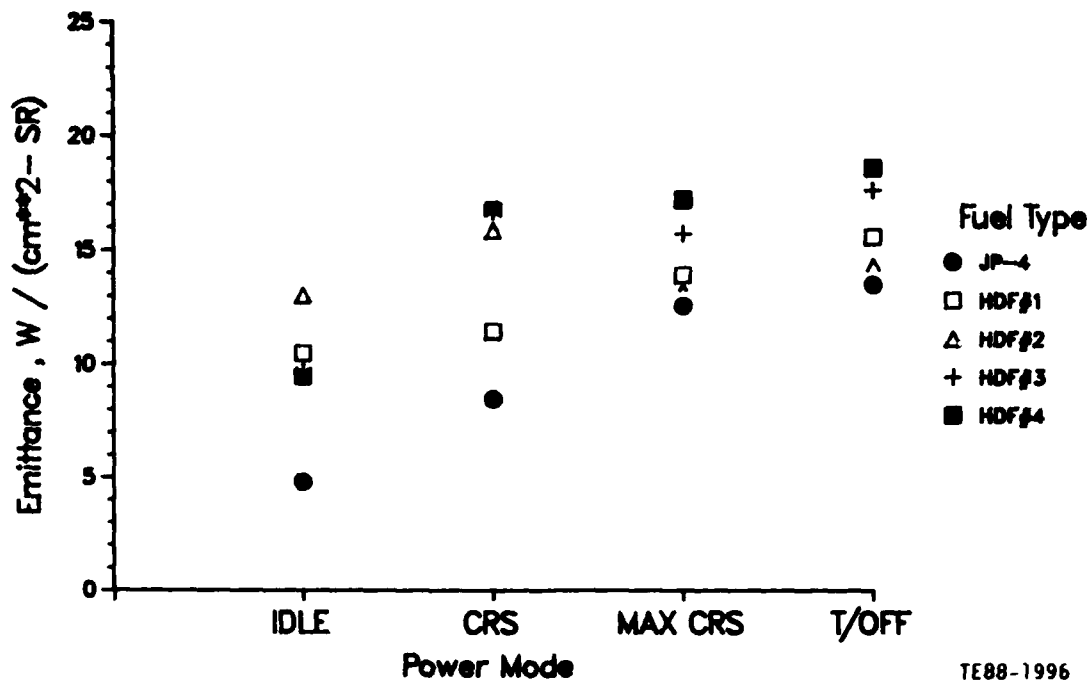
Figure 94. Primary zone emittance.

casing, and convection to the annulus air, and is supplemented by the film cooling concept adopted in the combustor design.

Due to the complexity involved in estimating the luminous emissivity from the knowledge of the size, mass concentration, and optical properties of the soot particles in the flame, a luminosity factor (L_u) is introduced into the empirical expression of nonluminous flame as follows (Reference 9):

$$\varepsilon g = 1 - \exp \left(-290 \ P_3 \ L_u \ (F/A \ . \ 1_b)^{0.5} \ . \ Tg^{-1.5}\right) \tag{37}$$

The factor L_u depends largely on such parameters as carbon/hydrogen mass ratio and fuel hydrogen content. Widely used equations are given by the following:

$$L_u = 0.0691 \ (C/H - 1.82)^{2.71} \tag{38}$$

or

$$L_u = 336/H^2 \tag{39}$$

However, an expression that was found to fit a wide data base and was used
extensively in different applications was employed in the present effort, and
is given by the following:

$$L_u = 5.964 \times 10^8/H^{7.365} \tag{40}$$

The beam length l_b in Equation 37 is determined by the size and shape of the
gas volume. The internal radiation is calculated from the following equation:

$$R = 0.5 \, \sigma \, (1+\varepsilon_w) \, \varepsilon g \, Tg^{1.5} \, (Tg^{2.5} - Tw^{2.5}) \tag{41}$$

where ε_w is wall emissivity that depends on material, temperature, and degree
of oxidation of the wall, and σ is the Stefen Boltzmann constant.

The internal convection component calculation is based on the adiabatic gas
temperature that is obtained from the definition of the film cooling effective-
ness $T_{w,ad}$ (Reference 20). The convection term is given by the following:

$$C = 0.1 \, (\frac{ka}{X^{1.36}}) \, R_e^{0.8} \, t^{0.36} \, (T_{w,ad} - T_w) \tag{42}$$

where X is downstream distance from cooling slot, t is depth of film cooling
slot, and R_e is Reynolds number based on flow conditions at slot exit and
distance X. Similar equations are available for external components of radia-
tion and convection. The calculation of the wall temperature T_w is performed
by balancing the heat fluxes on a wall segment through an iterative procedure,
and a wall conduction component is used to determine the temperature gradient
across the segment.

The overall flow and combustion characteristics in the combustion system are
given by an Allison air management program (CJ2). As will be discussed later
in this section, the 3-D combustor code is used to provide a more detailed flow

field to the heat transfer model. It should also be mentioned that the model handles various film configurations such as convection/film, extended/etched surfaces, and impingement/film schemes in addition to advanced techniques such as Lamilloy®*, effusion, and composite matrix system. This provides a useful tool that can be used to define the most suitable cooling technique for a certain application, and to suggest modifications to an existing design.

The calculations of the wall temperature at a number of axial locations carefully selected to represent various zones in the combustor liner were performed, and the results are plotted in Figures 95 through 98 for the four power modes. The wall temperature predictions for the JP4 are plotted with those of the HDF-3 since it has the lowest hydrogen content among the fuels tested and is expected to give the highest wall temperature. The results of the other three high density fuels fall somewhere in between the two extremes. The thermocouple measurements are also shown in these figures. It is noted that the predicted temperature profiles follow the measured ones with good agreement in regard to the temperature levels. The differences between the predictions and measurements observed in some locations are attributed to local cooling effect provided by small slots in these regions. Also, adopting global flow and combustion characteristics within the chamber may add to these differences.

The figures also show that the highest temperatures, whether calculated or measured, occur toward the end of the transition section. Also, the HDF-3 demonstrates higher temperatures compared to the JP4 case, and the difference in most instances is well predicted by the heat transfer model.

Combustor liner durability is affected by liner wall temperature levels and gradients and attendant thermally induced stresses. Therefore, it is important to take a further step in the heat transfer analysis to accurately predict liner hot streaks. To obtain more accurate estimates of liner wall tempe ture, it is essential to include the radiation flux contribution from various

---

*Lamilloy is a registered trademark of GM.

103
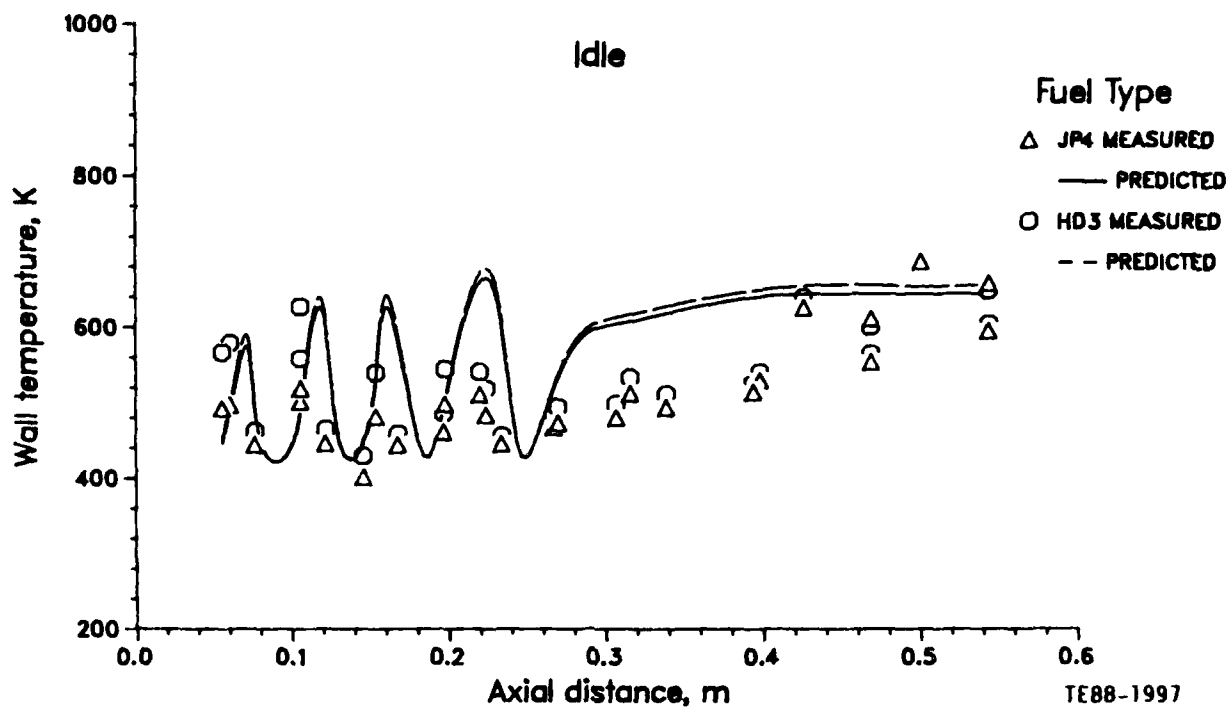
Figure 95. Wall temperature predictions at idle.
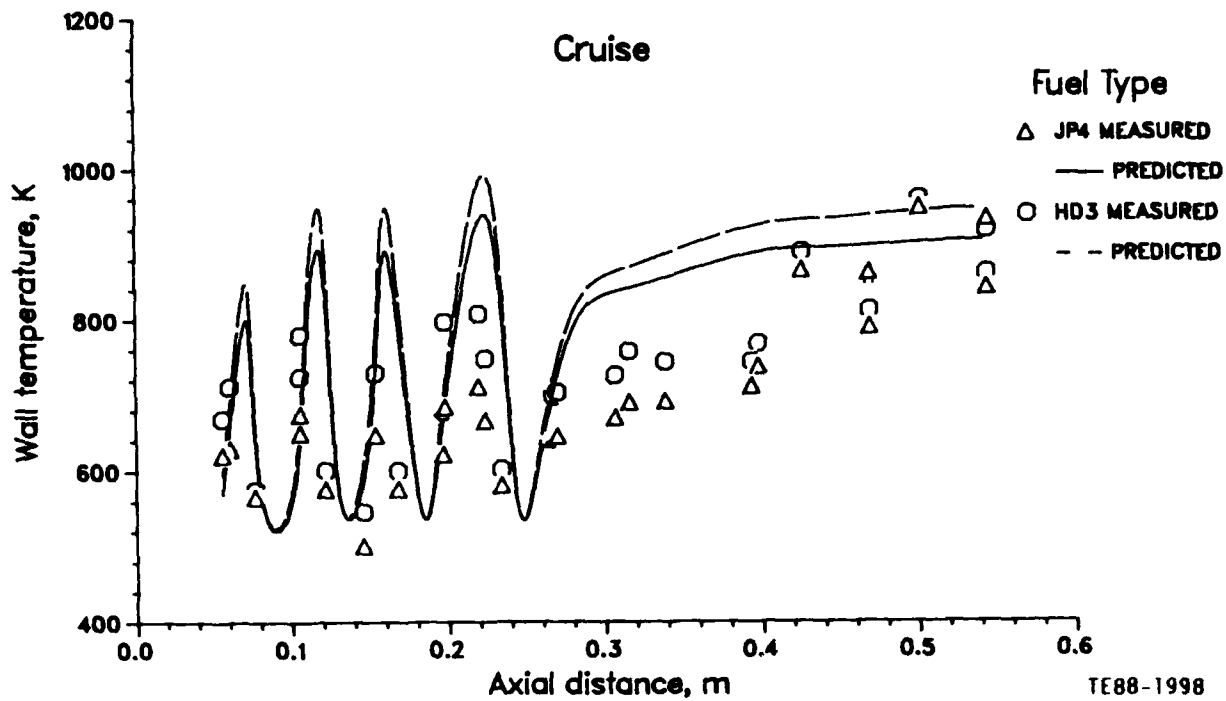
Figure 96. Wall temperature predictions at cruise.

104
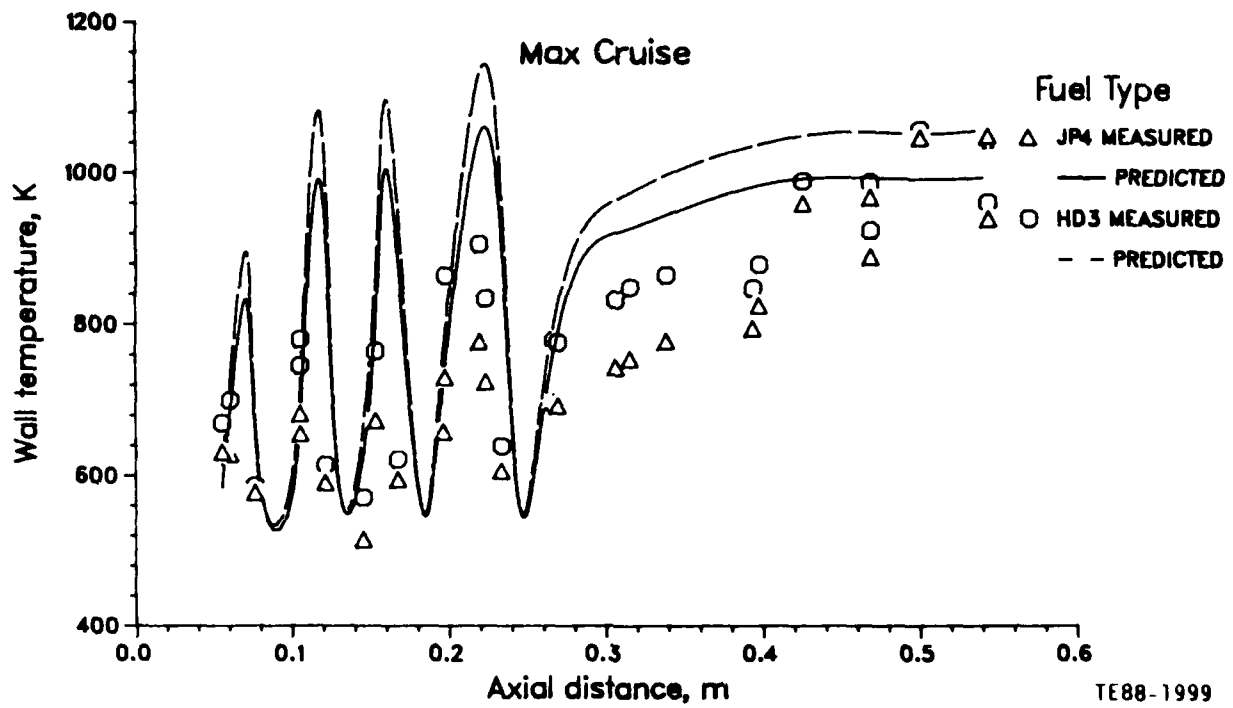
Figure 97.   Wall temperature predictions at maximum cruise.
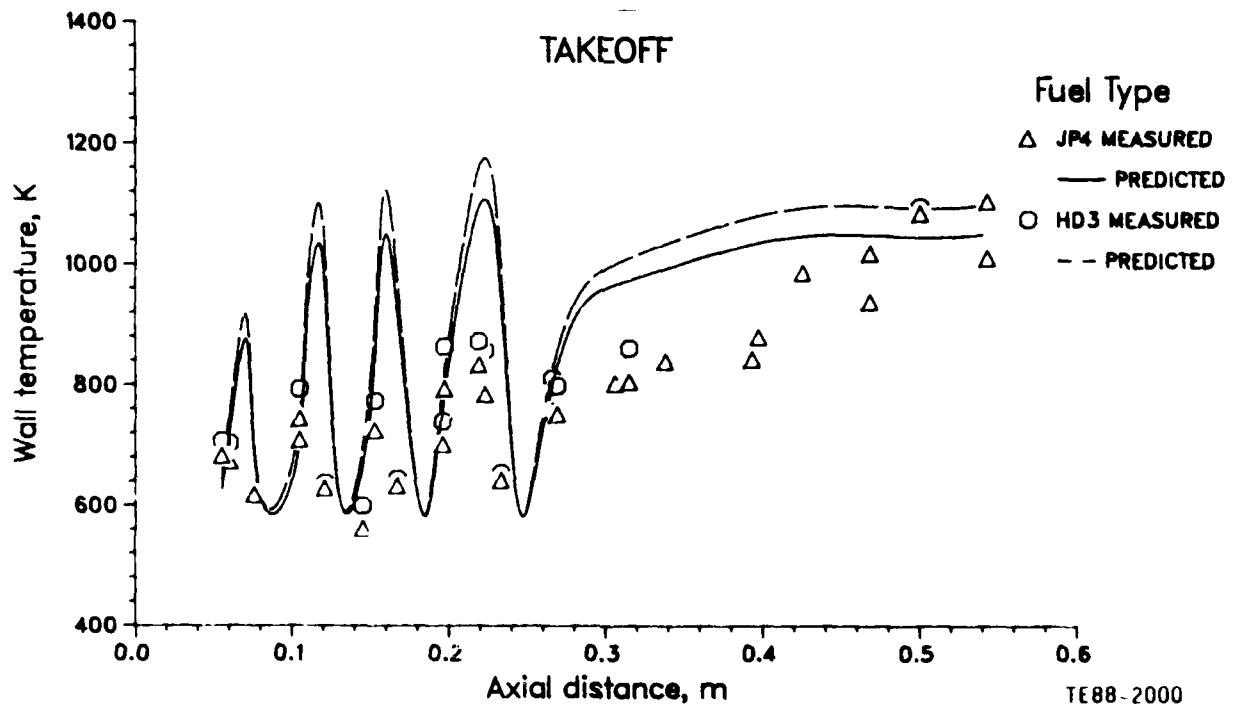
Figure 98.   Wall temperature predictions at takeoff.

105

combustor zones onto each wall segment. This step calls for the knowledge of the detailed 3-D combustor flow field, in addition to an accurate means of defining a radiation view factor F_v.

Adopting this concept, the radiation flux to a wall segment can be calculated using the following equation:

$$R = 0.5 \, \sigma \, (1 + \epsilon_w) \, \Sigma \, [F_v \, \epsilon g \, T^{1.5} \, (T^{2.5} - T_w^{2.5})]_{ijk} \qquad (43)$$

where the terms within the square brackets are based on local properties within each combustor zone, as given by the 3-D code. The same arrangement of dividing a combustor sector into large number of subvolumes used for the combustor performance model, is adopted for the 3-D heat analysis effort.

The wall temperature at three axial planes of the combustor sector is given in Figure 99 for JP4 at takeoff conditions. The thermocouple measurements are also plotted in the figure. It is obvious that the utilization of the 3-D variation in combustor internal parameters leads to better correlation with the data, especially in the prediction of hot spots on the liner and transition section. Examples of the results obtained for high density fuels are given in Figures 100, 101, and 102. Once again, good agreement with the measurements are shown in these figures.

To obtain a detailed picture of the temperature variation in both the axial and circumferential directions, the temperature contours of unwrapped sectors are plotted in Figure 103 to 105 for the JP4 and two high density fuels. From these figures, one can see the locations of hot and cold regions, and the higher temperature levels obtained with the HDF-3. The dome temperature distribution plotted against the distance from the exit plane of a dome baffle is shown in Figure 106 for a number of radii, and for JP4 and HDF-4. The measurements are also included in the figure. Contours of dome temperatures as given by the heat transfer model for both fuels are shown in Figure 107.
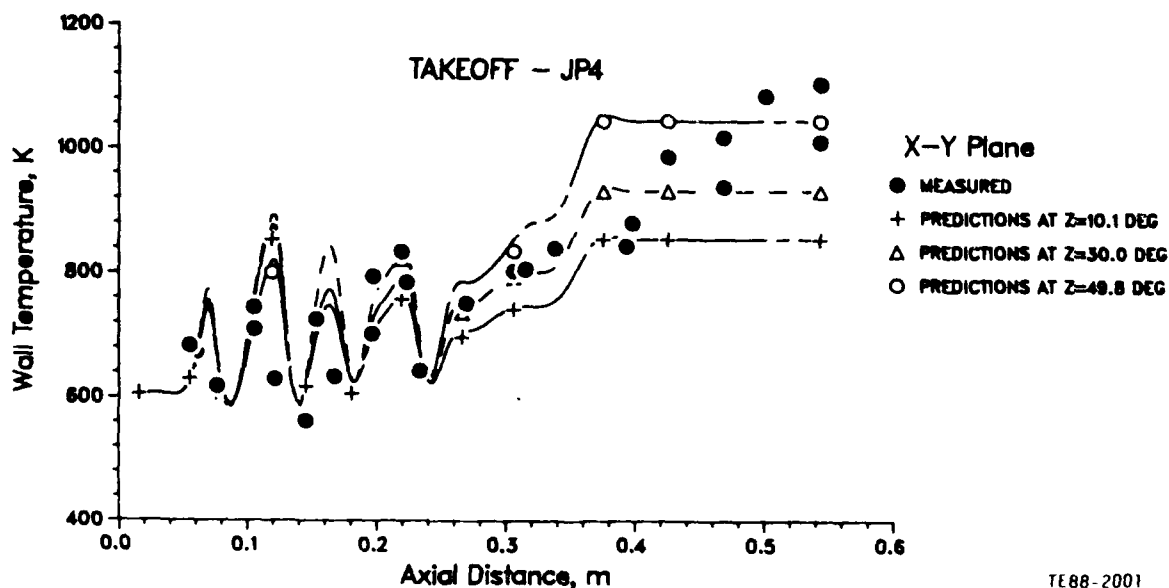
Figure 99. Heat transfer model predictions for JP4.
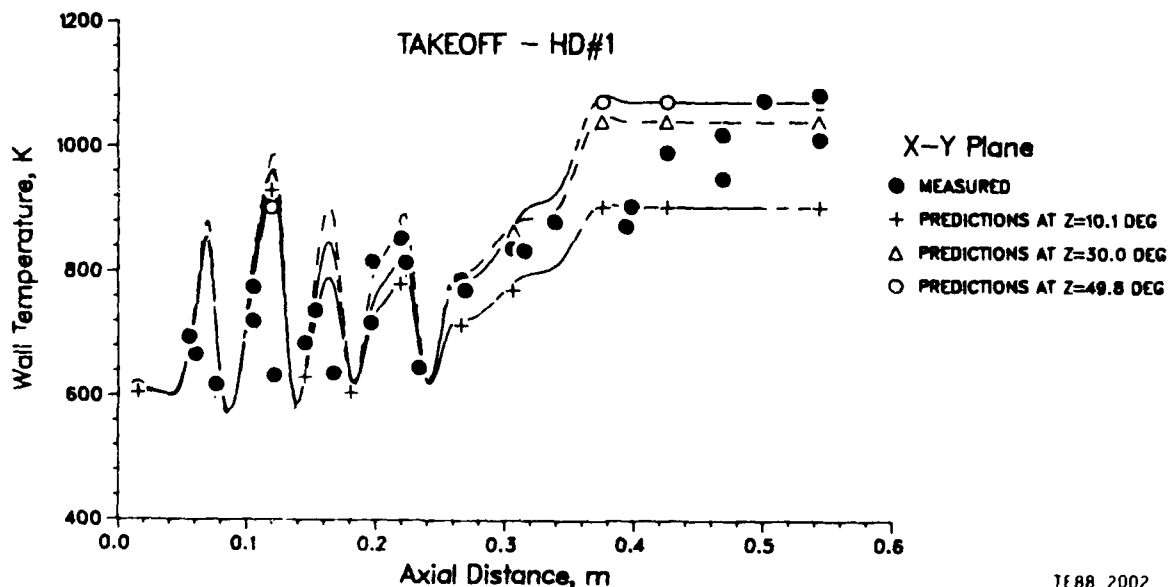
Figure 100. Heat transfer model predictions for HDF-1.

5.5 FUEL FLOW TRANSIENT EFFECT

The response of the T56-A-15 combustion system to transient throttle movements was evaluated on the combustor test rig. The response was measured by observing the burner outlet temperature as a function of time while varying the fuel

107
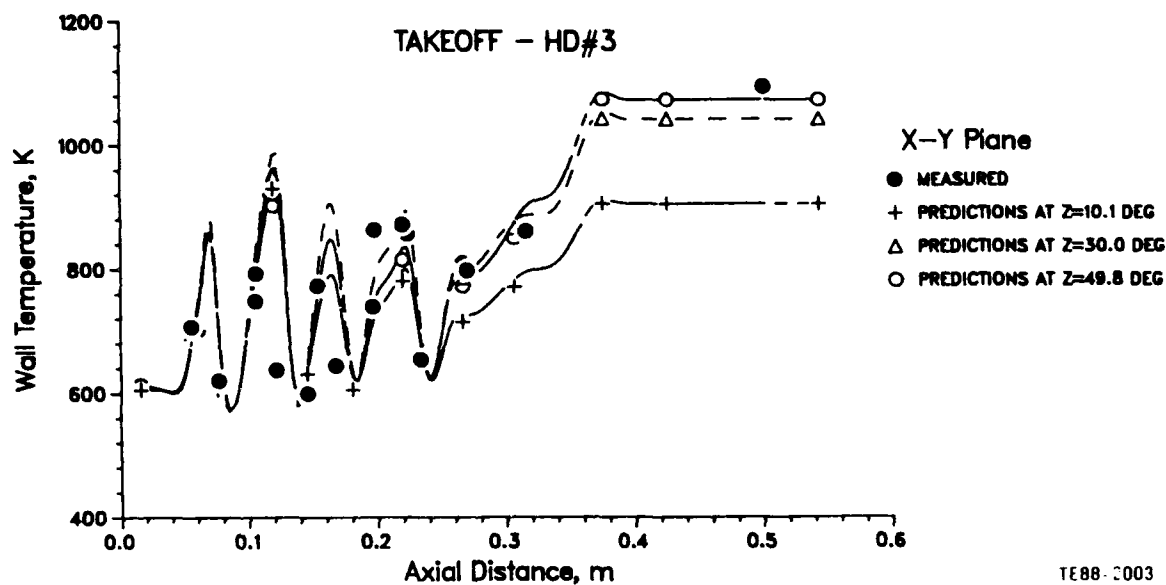
Figure 101. Heat transfer model predictions for HDF-3.
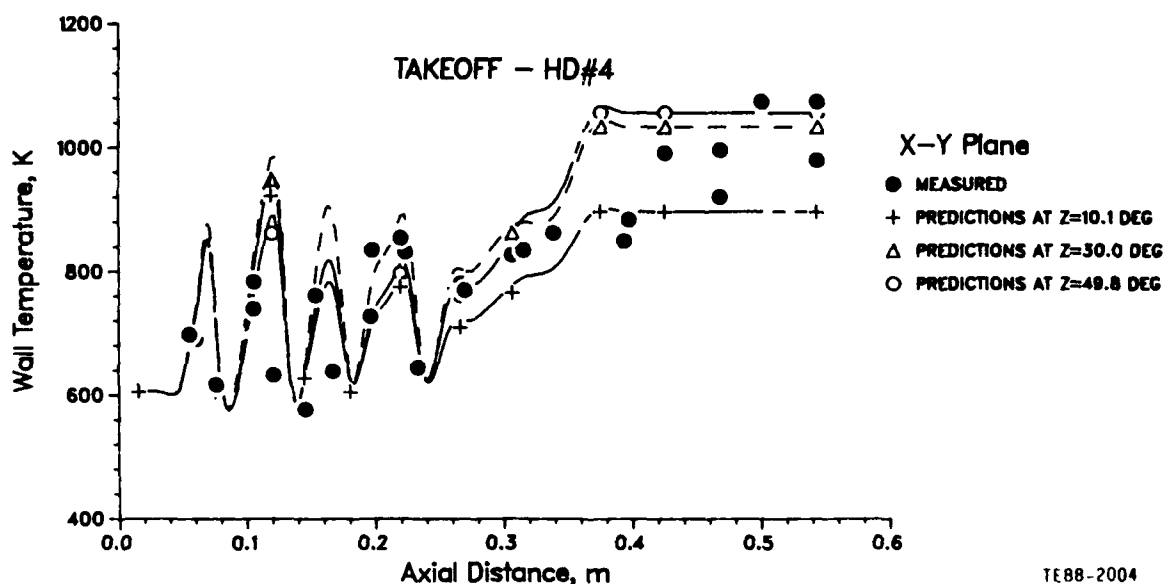
Figure 102. Heat transfer model predictions for HDF-4.

flow in step functions. The test procedure was initiated by setting off the combustion system at maximum cruise power conditions. The fuel flow step function was then applied to reduce the fuel flow to idle conditions (i.e. from 0.026 to 0.011 kg/s). The BOT was measured until the system stabilized. Finally the throttle was advanced to set off the fuel back to maximum cruise.

TEMPERATURE—DEG K, JP4, TAKEOFF

ANGULAR DISTANCE, M

AXIAL DISTANCE, M

TE88-2005
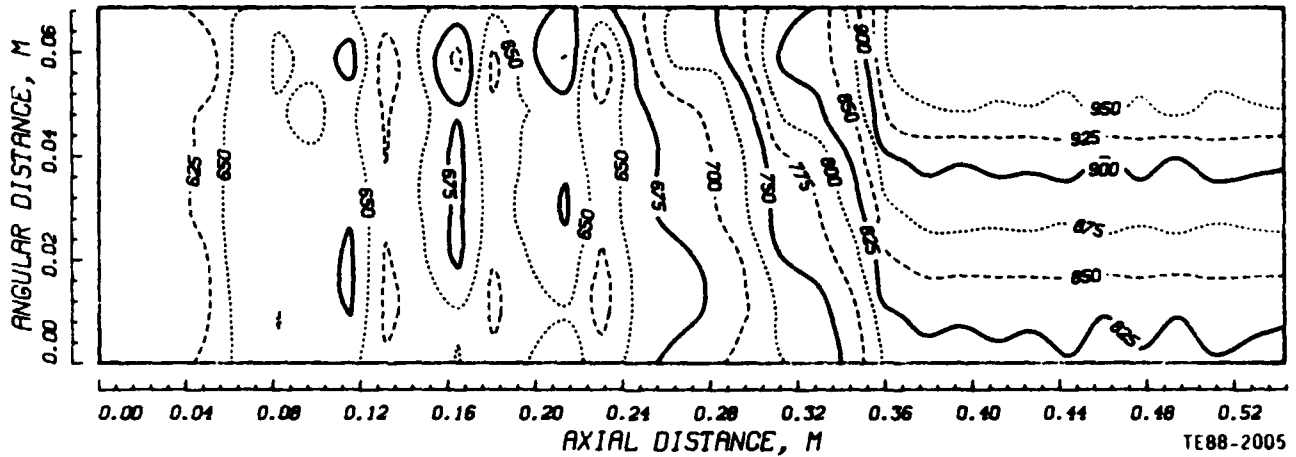
Figure 103. Contours of wall temperatures for JP4.

TEMPERATURE—DEG K, HD#1, TAKEOFF

ANGULAR DISTANCE, M

AXIAL DISTANCE, M

TE88-2006
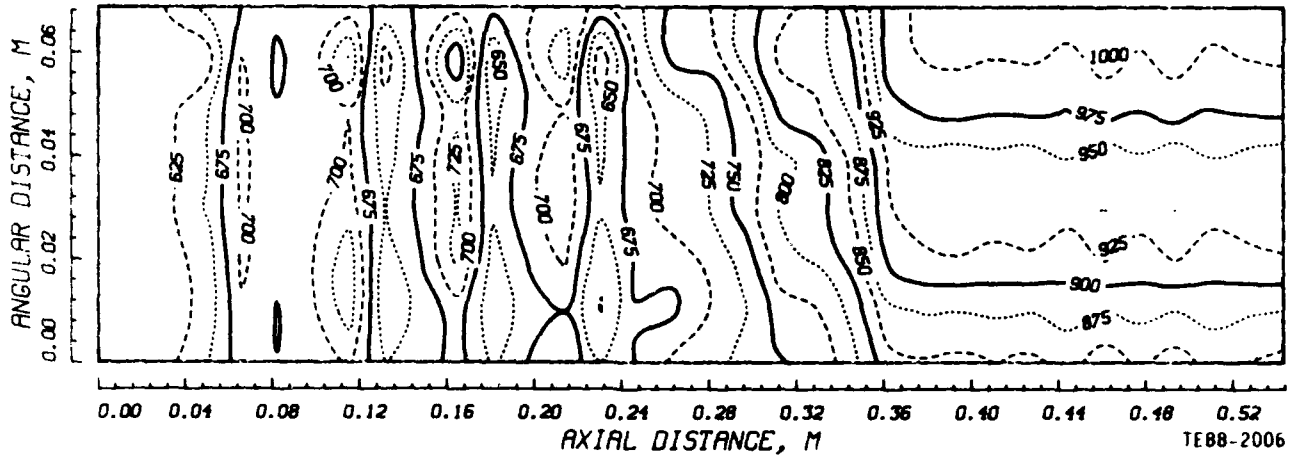
Figure 104. Contours of wall temperatures for HDF-1.

To facilitate the fuel flow step function, a three-way valve and a control
valve were added to the fuel system setup. The fuel flow transient testing
failed to produce a single flameout.

109
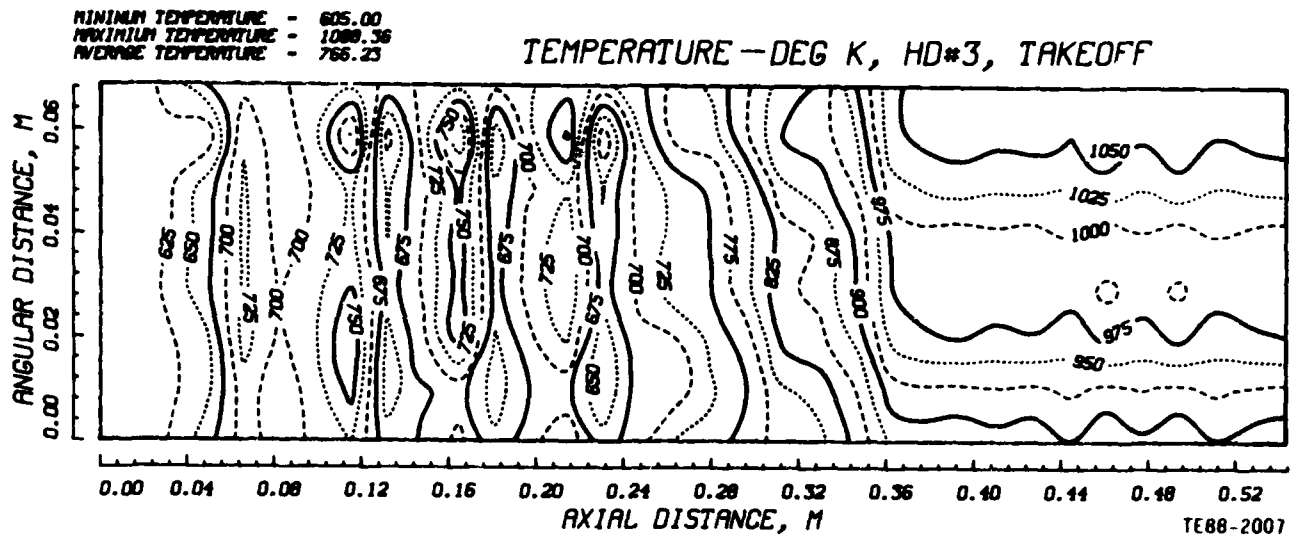
Figure 105. Contours of wall temperatures for HDF-3.

The test procedure was repeated several times for each fuel type. The fuel flow rate and the corresponding average burner outlet temperature were plotted against the elapsed time. Examples of these plots are given in Figures 108 through 112 for the five fuels under consideration. The average time needed for the BOT to stabilize following the step down in fuel flow (T_1), and the time elapsed until the BOT stabilized at the maximum cruise fuel flow (T_2) are given in each figure. The general trend observed in these figures is that the shortest response time occurs for the JP4. The high density fuels demonstrate slightly longer response time, with the longest time occurs when operating on HDF-4. The higher surface tension and viscosity of the high density fuels compared to the JP4 result in larger spray mean drop size. This, coupled with the unfavorable evaporation characteristics of these fuels, result in the longer delay time observed in these cases. The HDF-4 has the highest surface tension and viscosity compared to the other high density fuels.

5.6 CARBON DEPOSITION WITHIN THE COMBUSTION SYSTEM

Carbon deposition in a combustor generally is cyclic in nature since a sudden change in combustion zone flow or temperature causes carbon deposits to break

110
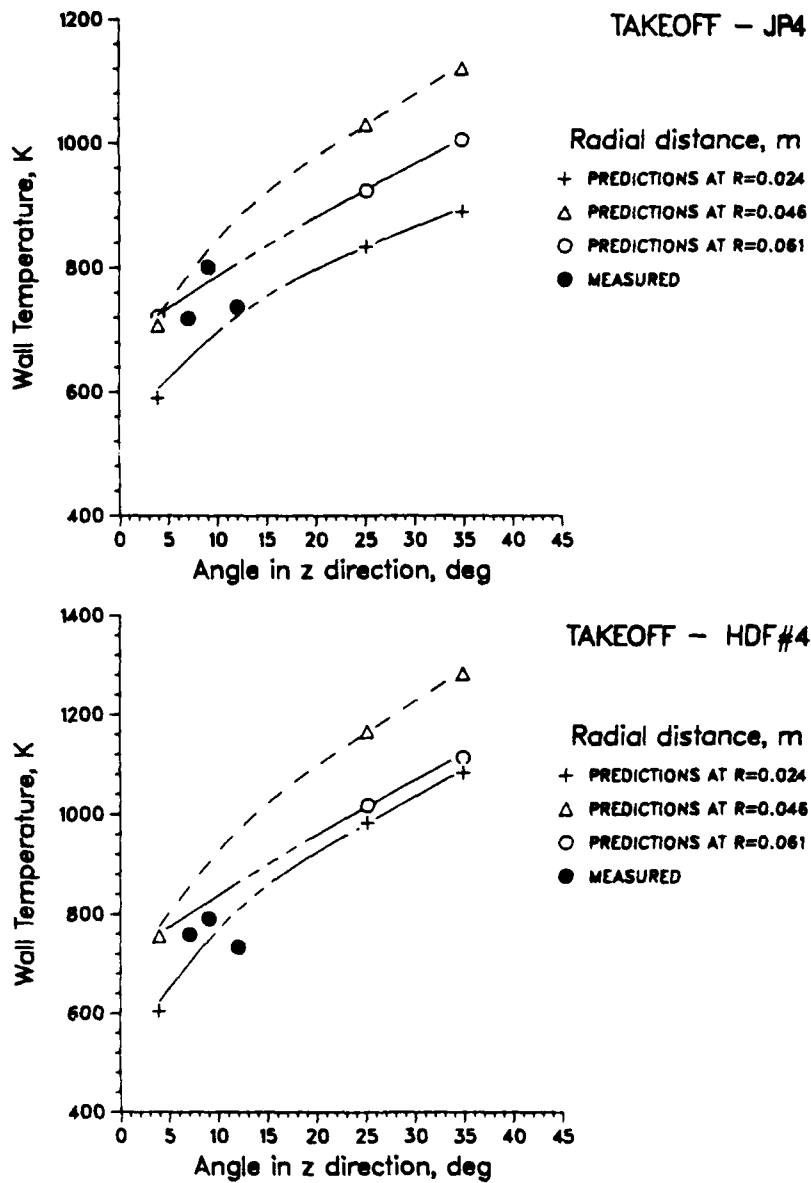
Figure 106.   Predictions of dome temperatures.

off or shed.   The governing factor in this phenomenon is the loss of combustion temperature rise when the fuel is shut off.   A technique of maintaining combustor temperature rise constant while the combustor flow is reduced down to a point where the fuel flow and airflow are shut off almost simultaneously (fuel flow slightly before airflow) has been highly successful in preserving carbon

111

TE88-2009
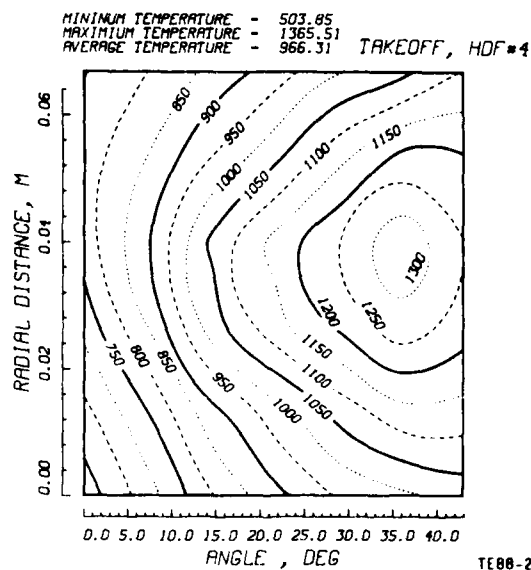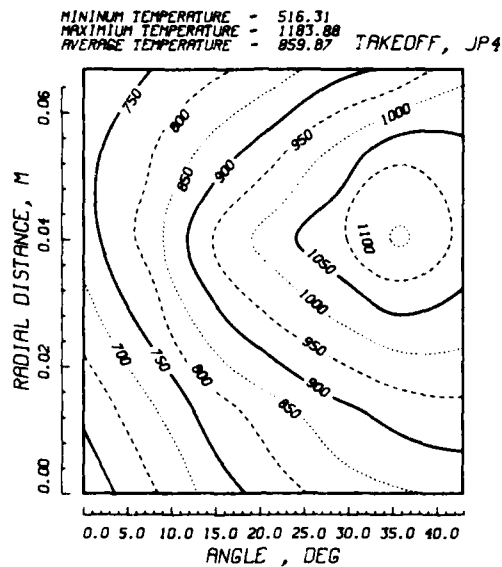
Figure 107.   Contours of dome temperatures.

deposits in the combustor for inspection purposes. This technique can deter-
mine carbon deposition location and relative amount. This "hot shutdown" tech-
nique was used to compare the carboning tendencies of the various test fuels
in this program.

112
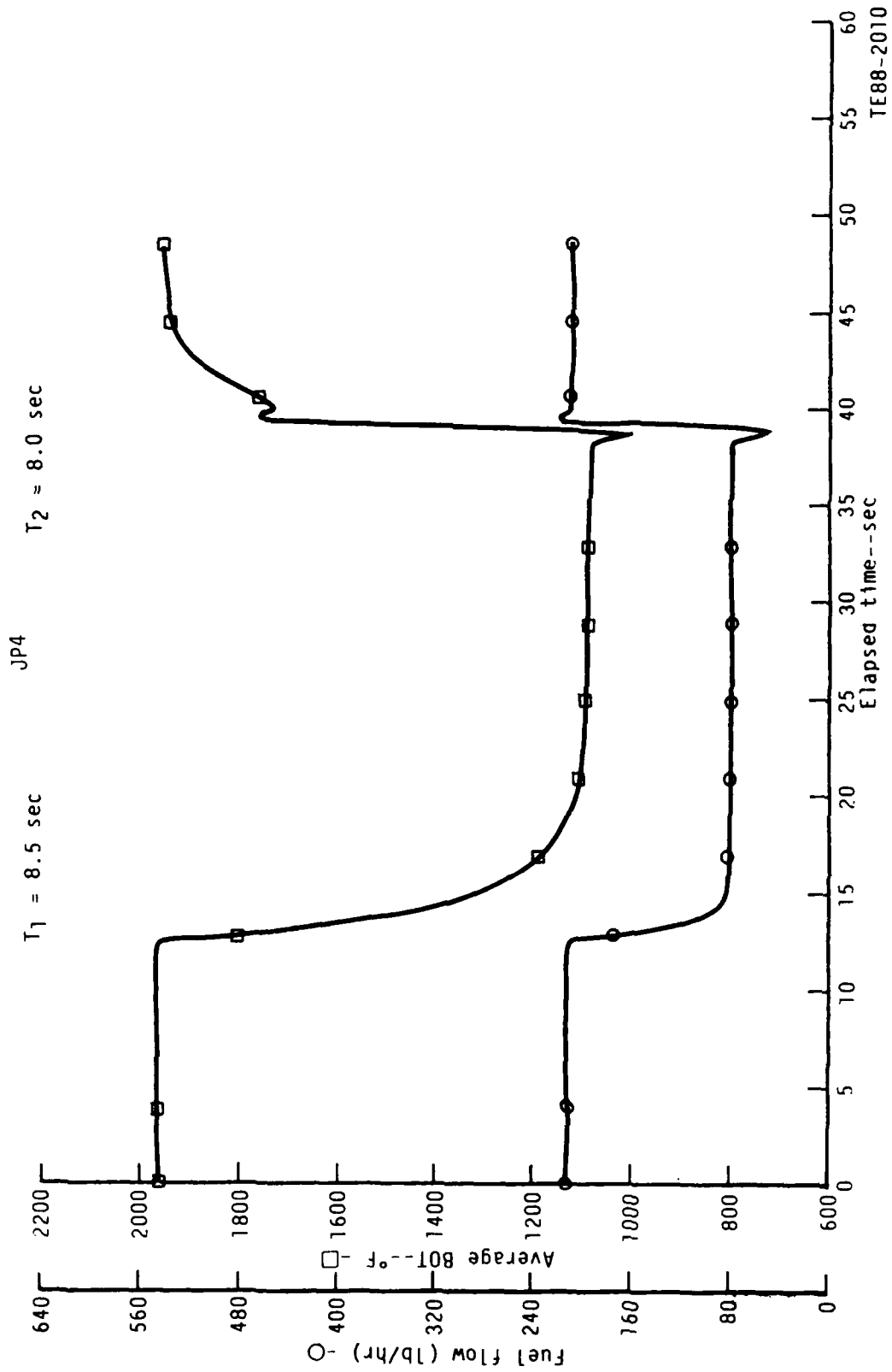
Figure 108. Fuel flow transient effect of JP4.

113
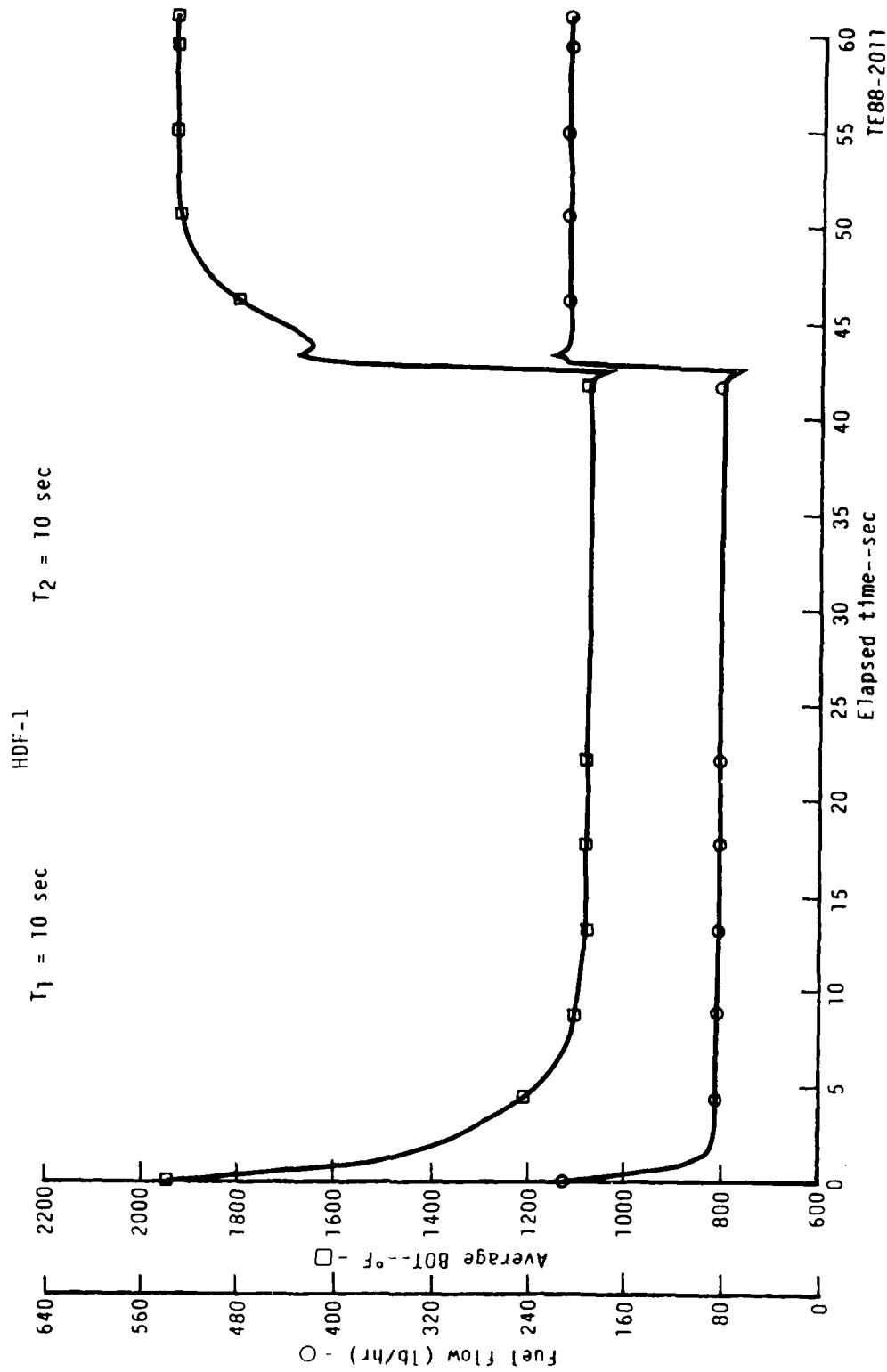
Figure 109. Fuel flow transient effect of HDF-1.

114
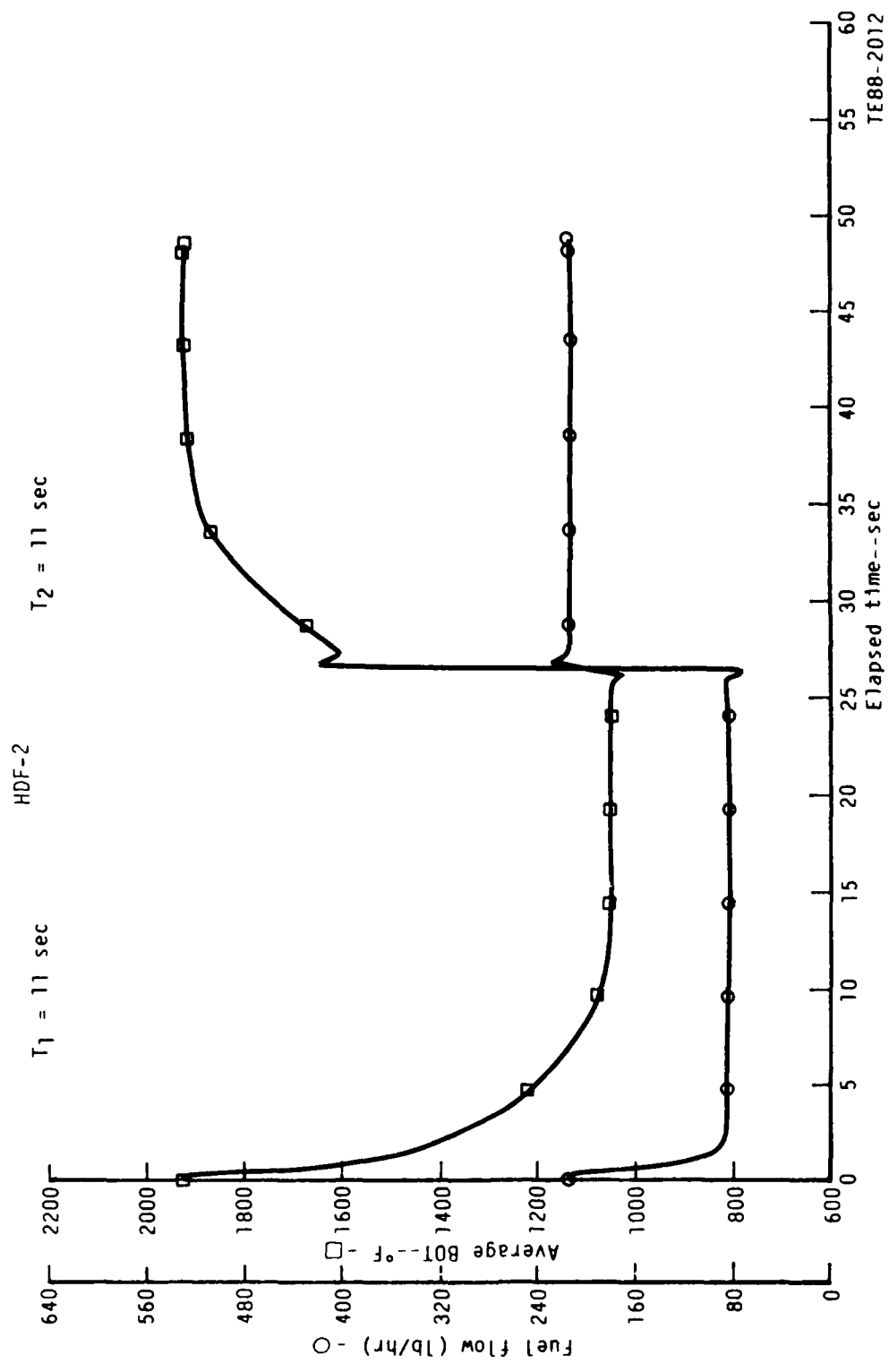
Figure 110. Fuel flow transient effect of HDF-2.

115
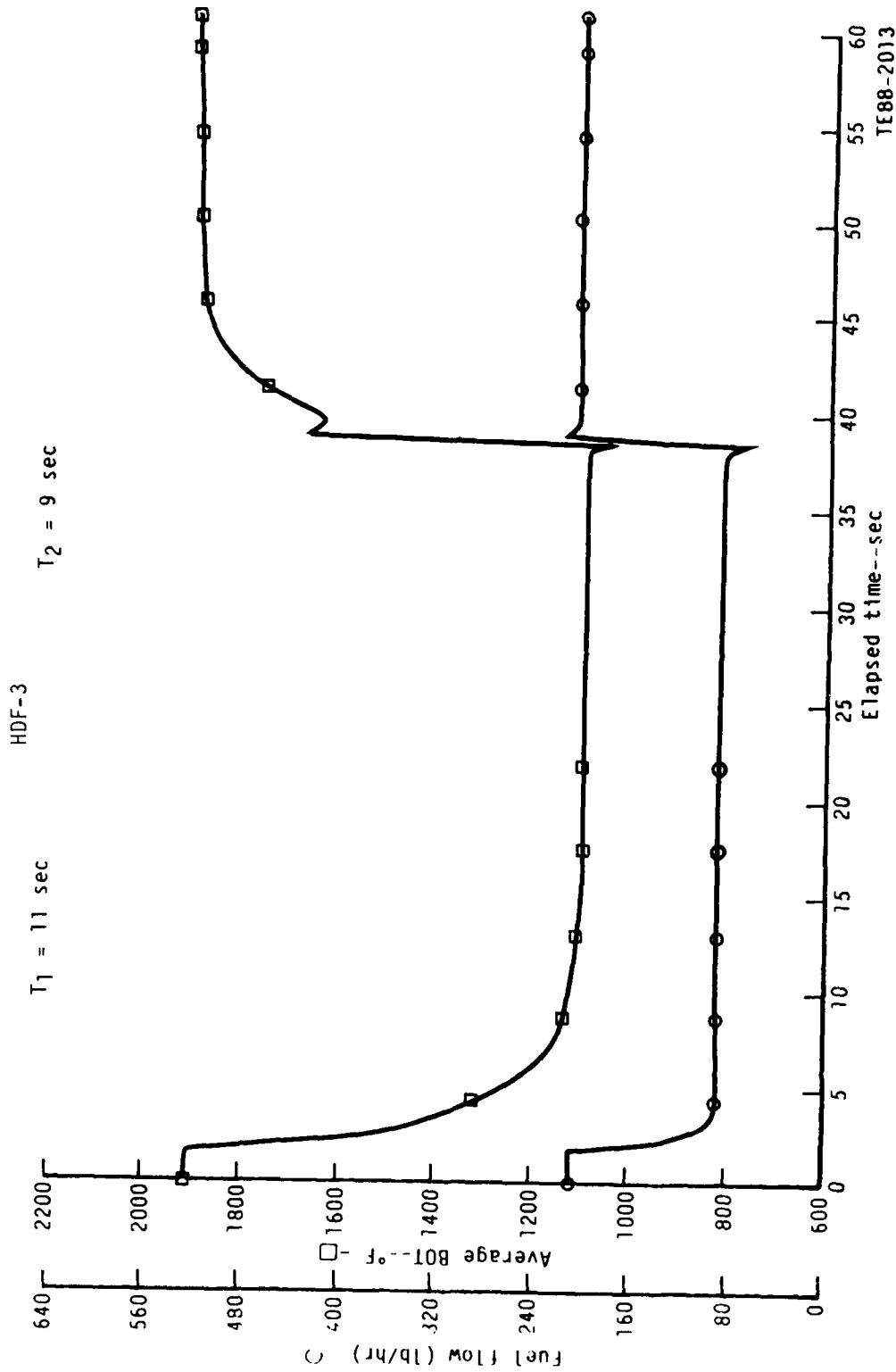
Figure 111. Fuel flow transient effect of HDF-3.

116
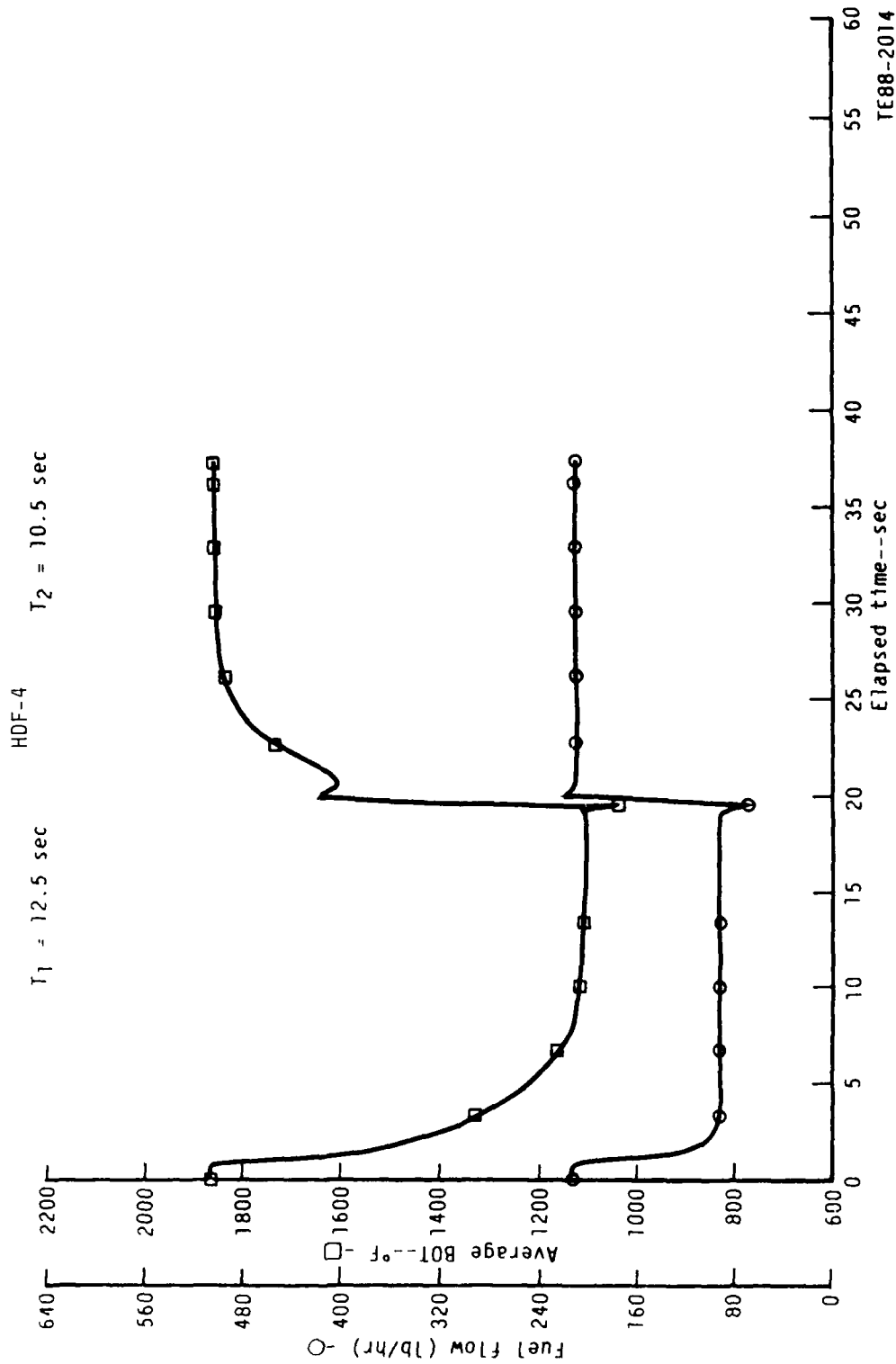
Figure 112. Fuel flow transient effect of HDF-4.

117

The coking test involved running the combustor rig at maximum cruise power continuously for two hours. The liner was removed after each test in order to photograph the liner's interior. A borescope was used to illuminate the dome during photographing. Before the start of each coking test, the liner's interior was grit blasted in order to remove any existing carbon buildup.

The results of the coking test are shown in Figures 113 through 117 for the JP4 and the four high density fuels, respectively. One fuel nozzle was used for both JP4 and HDF-1. A separate nozzle was used for each of the other fuels. The results show that the carbon buildup was limited to the nozzle face and the liner dome. Baseline JP4 appeared to have the least amount of carbon buildup at the end of the two-hour test. Any difference in coking behavior may be attributed to the differences in the chemical properties of the fuels, namely aromatic content, hydrogen content, etc, and physical properties relevant to atomization and evaporation characteristics. Twelve sets of data were taken during each two-hour coking test.

5.7 FOULING OF THE FUEL NOZZLES

When an aviation fuel is thermally stressed, degradation can occur resulting in a variety of the end products. Some of these products are insoluble and can either adhere to surfaces or remain suspended in the fuel. The suspended solubles can restrict orifices and filters, while their adherence to surfaces can result in restrictions of movement ultimately leading to fuel system malfunction.

The thermal stability of aviation fuels is influenced by a variety of factors other than time at temperature, namely fuel quality, composition, and catalytic influences. For quality control purposes, aviation fuel specifications include a measurement of the thermal stability within the specific requirements for the fuels. The two current tests are the ASTM-CRC Fuel Coker and the Jet Fuel Thermal Oxidation Tester (JFTOT).

JP4

Fuel nozzle
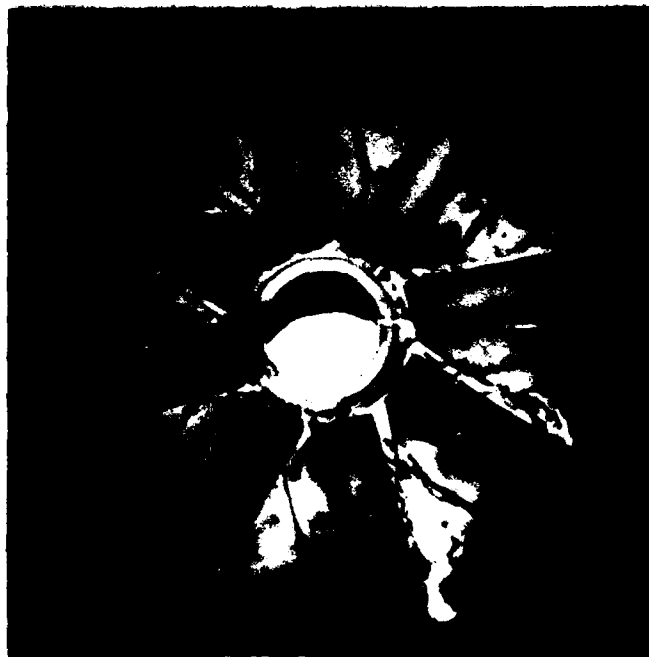
Combustor dome

TE88-2015

Figure 113. Carboning deposition for JP4.

119
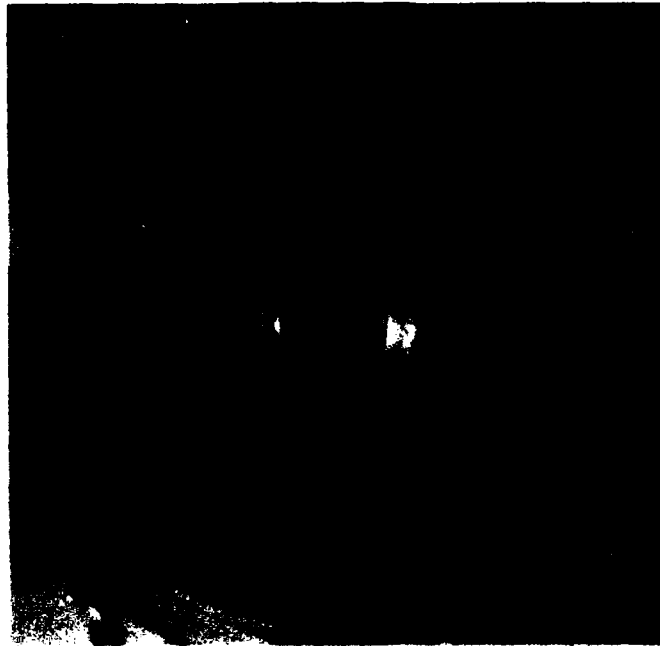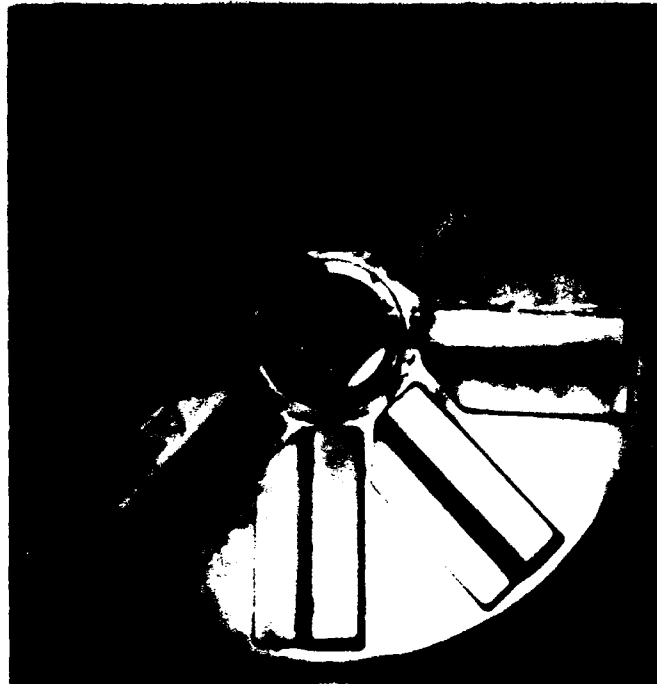
Fuel nozzle

Combustor dome

TE88-2016

Figure 114.   Carboning deposition for HDF-1.

120
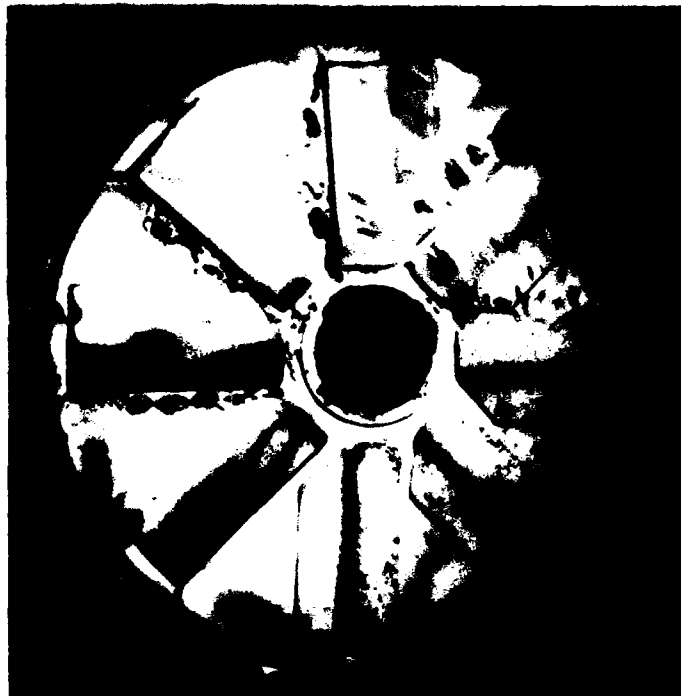
fuel nozzle

Combustor dome

TE88 2017

Figure 115. Carboning deposition for HDF-2.

Fuel nozzle
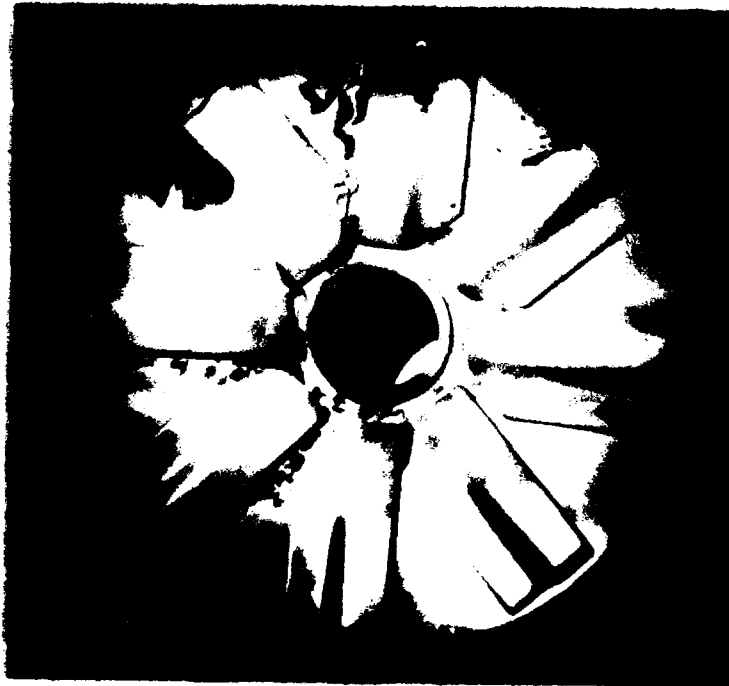
Combustor dome

TE89-2018

Figure 116. Carboning deposition for HDF-3.

122
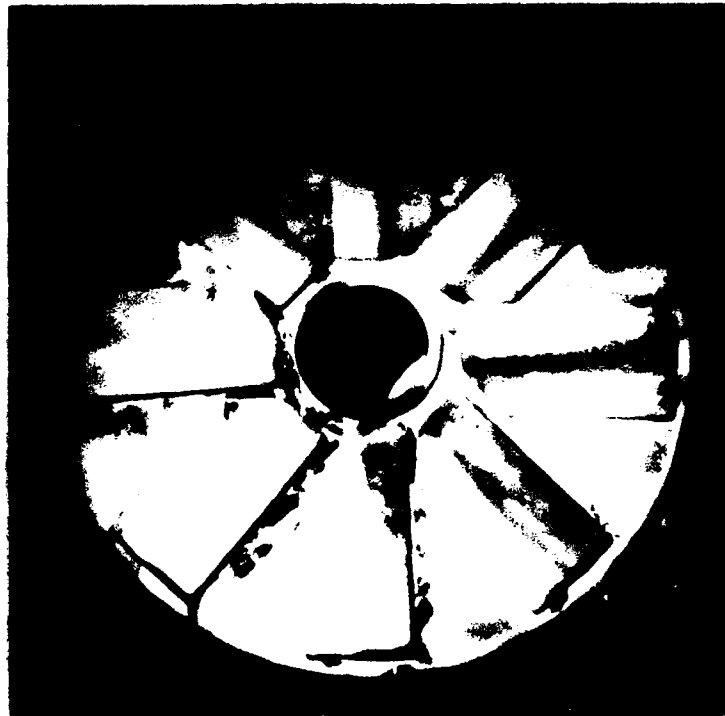
Fuel nozzle

Combustor dome

TE88 2019

Figure 117. Carboning deposition for HDF-4.

The effects of the high density fuel usage on the potential fuel nozzle plug-
ging were investigated by operating the combustor test rig at maximum cruise
power conditions continuously for two hours. The fuel nozzles were flow cali-
brated after each test, and the circumferential patternation measurements were
taken over the whole range of operation. The fuel flow through the atomizer
was recorded as the fuel pressure was increased in increments until it matched
the takeoff conditions, and then was reduced again. One atomizer was used in
the combustion tests of the JP4 and HDF-1, while a nozzle for each of the other
high density fuels was used in these tests. A standard test fluid (MIL-C-7024
Stoddard solvent) was used in all the flow calibration tests.

The flow results show small reduction in flow capacity of nozzles due to nozzle
fouling, and the largest drop in flow occurs after HDF-4 testing. The data
obtained after the nozzle fouling tests are plotted in Figure 118 along with
the baseline flow characteristics before the tests.
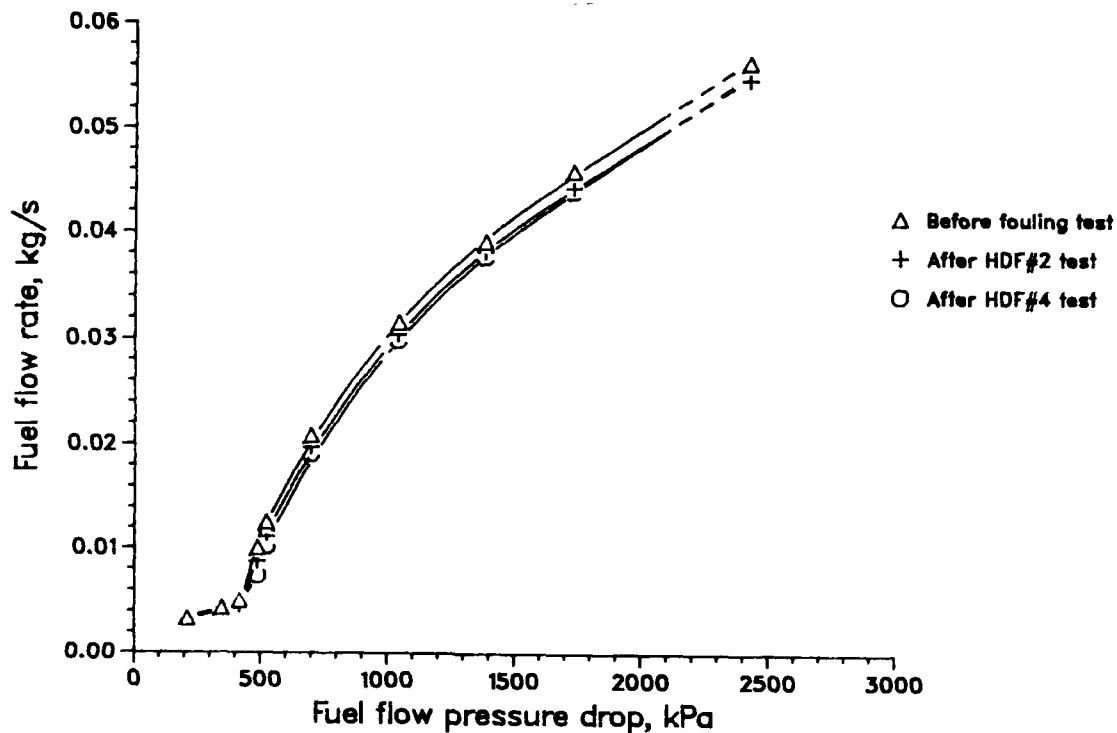
Figure 118. Nozzle fouling results.

124

The circumferential patternation results indicate some changes in the pattern after conducting the fouling tests. Figure 119 shows a comparison between the patternations before and after the fouling tests for the HDF-1. The maximum percentage difference in the fuel accumulation in the 12 segments of the patternator is 37.5 before the fouling tests and 44.2 after the testing. The results obtained for the HDF-3 after the fouling tests are plotted in Figure 120 for a number of flow conditions. The figure shows that more uniform distribution of fuel concentration in spray is obtained at higher fuel pressure and flow rate. It is also observed in the figure that the nozzle used for this particular high density fuel produces more uniform circumferential patternation as compared to the nozzle used for testing JP4 and HDF-1. TABLES 17 and 18 summarize the patternation results for all fuels.

5.8 COMBUSTOR AND TURBINE LIFE

5.8.1 Combustor Life

Fuel properties have a direct effect on combustion liner metal temperatures. Combustor metal temperatures are dependent upon flame luminosity during reaction in the combustor primary zone. Increased luminosity relates to the fuel chemical composition, i.e. hydrogen content, carbon/hydrogen ratio, and quantity and type of aromatic compounds. Low cycle fatigue (LCF) is the dominant failure mode and life dependent consideration for a combustor. Increased localized metal temperatures and thermal gradients can both be expected to reduce combustor fatigue life. A higher temperature reduces the fatigue strength of the material, while a larger gradient increases the strain excursion and causes higher stresses.

5.8.1.1 Combustor Liner Section. The combustor liner was studied in terms of LCF life using the computer program STRATA, which accurately determines deflections and elastic stresses in structures subjected to loads due to thermal gradients, pressures, centrifugal effects (if any), and externally applied forces and boundary conditions. Any linear elastic analysis assumes that

125

TABLE 17. Maximum percent difference in circumferential patternation for JP4 and HDF-1.

Fuel pressure, kPa Fuel flows, kg/s	Before fouling Nozzle No. 1 No. of sectors 6	12	JP4 Nozzle No. 1 No. of sectors 6	12	HDF-1 Nozzle No. 1 No. of sectors 6	12
206.6 0.0033	39.9	47.5			39	45.7
520.8 0.0125	23.1	37.5	33.5	45.8	40.6	44.2
692.9 0.0208	26.4	47.6			29.8	49.1
1379.0 0.039	19.9	28.1	26.4	33.2	25.2	33.4
2413.3 0.0562	17.7	23.0	22.8	25.8	21.8	23.8

TABLE 18. Maximum percent difference in circumferential patternation for HDF-2, HDF-3, and HDF-4.

Fuel pressure, kPa Fuel flows, kg/s	HDF-2 Nozzle No. 2 No. of sectors 6	12	HDF-3 Nozzle No. 3 No. of sectors 6	12	HDF-4 Nozzle No. 4 No. of sectors 6	12
206.6 0.0033	34.0	46.6	22.5	33.0	26.3	34.1
520.8 0.01-0.011	20.6	36.8	18.5	37.4	19.8	31.5
692.9 0.0196	24.1	73.7	24.0	53.9	25.1	54.8
1379.0 0.038	26.2	58.9	13.1	31.2	13.7	30.6
2413.3 0.055	16.5	22.8	11.9	20.0	11.6	17.9

Wf = 0.0125 kg/s , ΔPf= 521 KPa
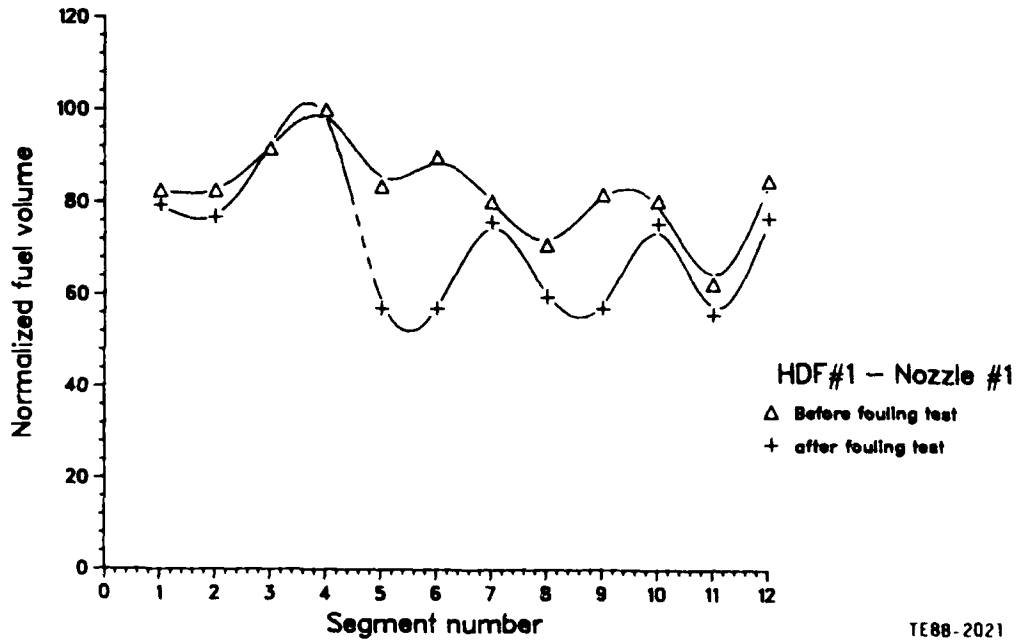
Figure 119.   Circumferential patternation after fouling test of HDF-1.

HDF#3 — Nozzle #3
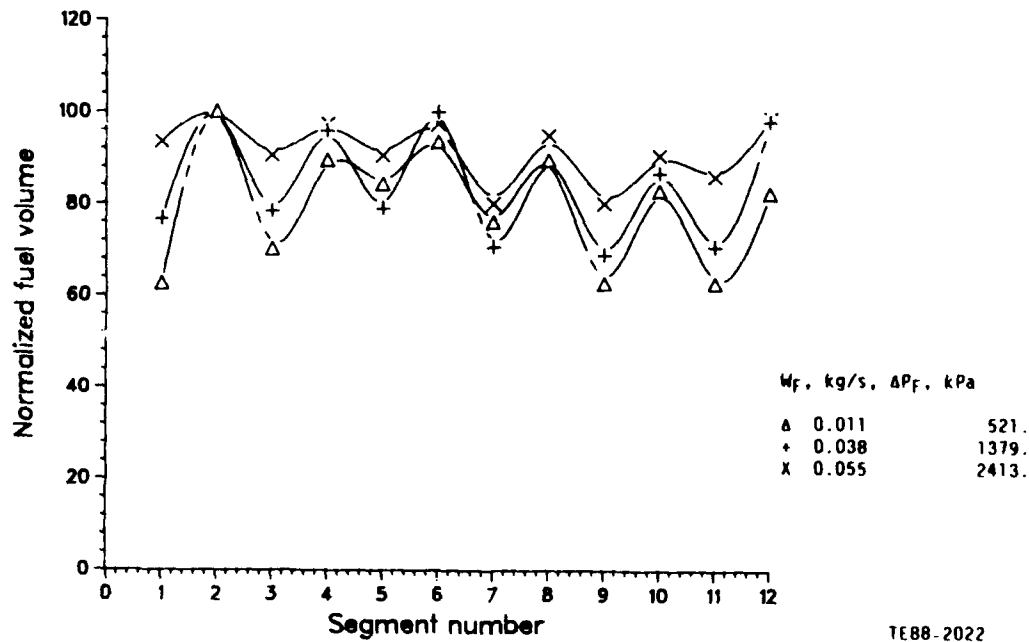
Figure 120.   Circumferential patternation after fouling test of HDF-3.

127

stress induced is a direct function of strains even if the predicted stress is beyond the yield strength of the material. A plastic analysis assumes that between the yield and ultimate strengths, a necking phenomenon occurs. In this region, true stress depends on the plastic deformation. According to the Maximum Distortion Energy theory, this plastic deformation begins when the equivalent stress equals the yield strength times the square root of 2. Thus, as the material yields, it deforms to relative stress at the yielded area, and load is carried by surrounding material. Equivalent stress in this STRATA analysis is high enough to cause plastic deformation. However, these stresses are not seen in actual operation, and should be used only in relative terms (Reference 21).

Figure 121 shows the finite element model used to determine relative stresses of the worst case high density fuel versus the baseline JP-4. This 3-D model depicts an 8.2 deg wedge of the combustor can circumference. It is built of 12-noded meanline shell elements. The layering and spot-welding of the various parts are accounted for by allowing increased shell thickness at the overlaped sections. Any further work on this model should include reducing the areas of the increased thickness to those of the respective welds alone. This would lower the constraints and reduce the apparent stress on the model.

Another improvement to the model, that would offer more accurate results, would be the inclusion of the fillets and rounds of the corrugated section (see Figure 121). Due to the sharp edges, stresses at the area of concern are abnormally high. To reduce this stress concentrating effect, a stress linearization technique was applied to the highest stress point in the model. This method consists of linearly extrapolating component stresses near that point to approximate those components at that point. Since meanline shell elements support no through-wall stress components, only those stresses supported in a given element can be estimated using nodes of that element. Therefore, nodes of several elements are used to arrive at the equivalent stresses at the low-life point.

The geometry of the model approximates one-half of a single cooling slot of the T56-A-15 combustor at the point of the highest axial thermal gradient,

128
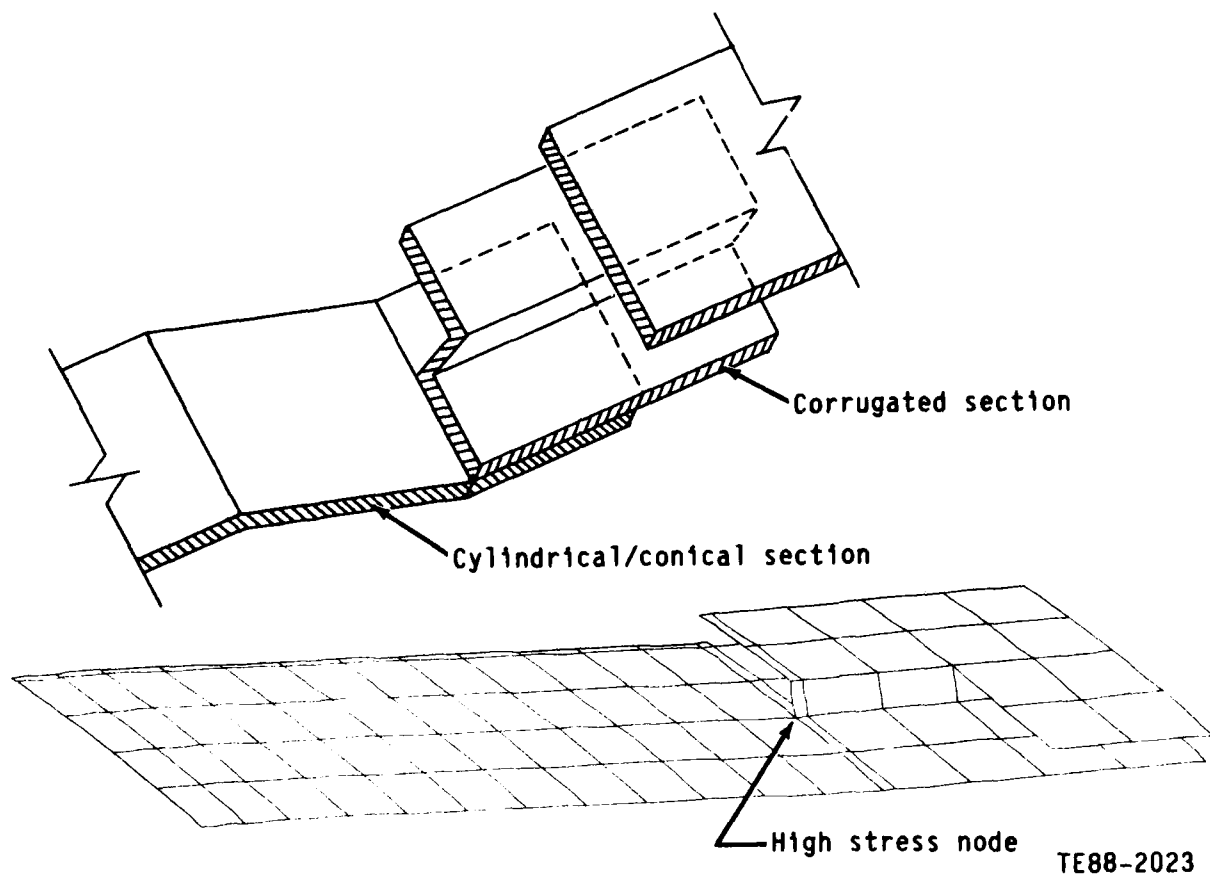
Figure 121. Finite element model for cooling slot.

which was determined from test temperatures. Temperature data was obtained by correcting all high density fuel temperatures to the baseline JP4 burner outlet temperatures. Linear axial temperature gradients were next superimposed on the nodes of the inboard and outboard sides of the model (hot side and cold side).

The model is constrained from deflection and rotation across the planes of symmetry extending from the lengthwise edges to the combustor centerline. It is held axially along the forward edge, simulating the parts weldment to the forward structure. The model is then free to grow under the influence of axial temperature differences. Besides temperature, a pressure differential of 35 kPa was the only applied load on the combustor can.

LCF data for Hastelloy X was obtained from Reference 22. Since the calculated
lives are relative numbers, this bar data can be used for sheet applications.
A least-squares fit of the plastic and elastic data (with cyclic life being the
dependent variable) was input into the DH4C computer program to obtain ful-
ly reversed SN curves. The combustor life calculation assumes a zero to maxi-
mum (R = 0) cycle, so DH4C was used to obtain SN curves for this cycle. These
curves were cross-plotted to obtain a plot of stress range versus temperature
for R = 0, as shown in Figure 122. The low life locations with the baseline
JP4, and the HDF-3, which provided the worst axial gradient in the combustor
can, are plotted on this graph to show the range of differences among the fuels.
Based on the maximum axial thermal gradients for each fuel, one can conclude
that all other high density fuels would produce lives between those of the
baseline JP4 and the HDF-3 over the same mission. According to this plot, the
use of the high density fuel-3 would reduce the LCF life of the T56-A-15 com-
bustor by a relative factor of about 6 compared to JP4.
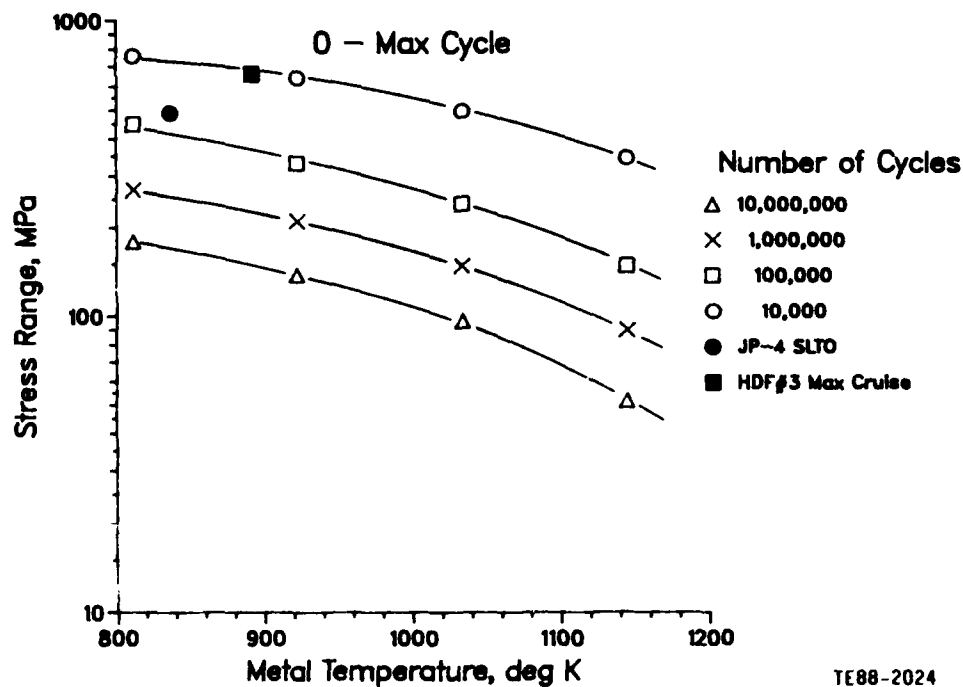
Figure 122. Liner cooling slot stresses.

130

5.8.1.2 Combustor Transition Section. To assure that the stress analysis found the worst LCF differences among the fuels tested, a check on the combustor transition section was also performed. A finite element model of this part was modified from previous work on the 501-KH 1KB5 combustor. The transition section model is of a single burner cut at its centerline by a radial plane. The full section is then approximated by boundary conditions at the cut edges. No motion is allowed across that plane nor about the axes it makes with the model edges. Also, the model is restrained from axial movement at its forward edge, which becomes its base for thermal growth aft. An outside-in pressure of 35 kPa simulates coolant air pressure to the transition section. The transition section finite element model is shown in Figure 123.

As with the liner cooling slot analysis, metal temperatures throughout the section were obtained for each fuel under each condition. The high density fuel that provided the maximum axial gradient was run against the baseline JP4 fuel. As corrected, the high density fuel temperatures showed lower axial gradients than did JP4.

Results from the model showed that stresses from the baseline fuel were slightly higher than those of the high density fuels. However, no stress even approached the level found in the cooling slot of the cylindrical section. LCF is thus not a limiting failure mode for the transition section of this combustor, and the liner cooling slot analysis is deemed sufficient.

5.8.2 Vane and Blade Life

In this section, the effects of high density fuels on first stage turbine vanes and blades are studied in terms of oxidation penetration and stress rupture, respectively. These life criteria were related to the measured combustor exit temperature pattern, based on existing correlations relating vane and blade metal temperatures to local gas temperature.
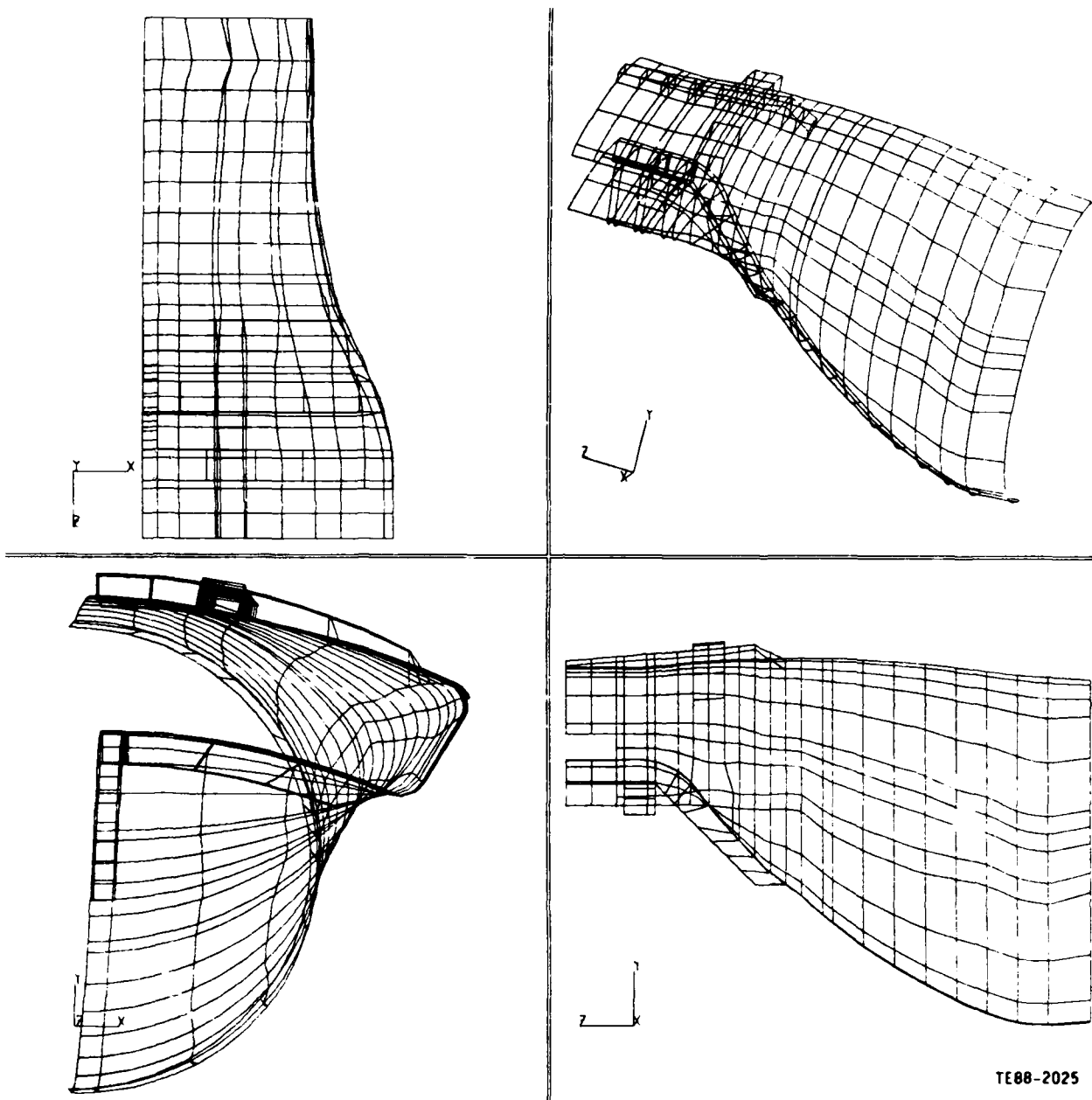
Figure 123.   Finite element model for transition section.

At high metal temperatures, oxidation occurs in materials. Blade airfoils are constantly moving through the burner outlet hot spot, thus averaging the circumferential burner pattern and producing lower metal temperatures. Oxidation is therefore of less importance to the blade than the vane. Since the vane

sits in the burner hot spot, oxidation is often an important damage mechanism on this component. The rate of material loss is a direct function of metal temperature.

The vane, cast from X-40 material, is fed with cooling air that travels radially from the hub through an impingement tube. The cooling air is discharged onto the vane inner surface through a row of holes along the leading edge of the tube. The air cools the pressure and suction surfaces prior to being discharged into the gas path through slots near the trailing edge. The internal cooling configuration for the INCO 738 blade consists of a single channel/single pass-type with radial fins to augment the internal surface area. The T56-A-15 first stage vane and blade are shown in Figure 124.

First stage vane--mean section

First stage blade--mean section
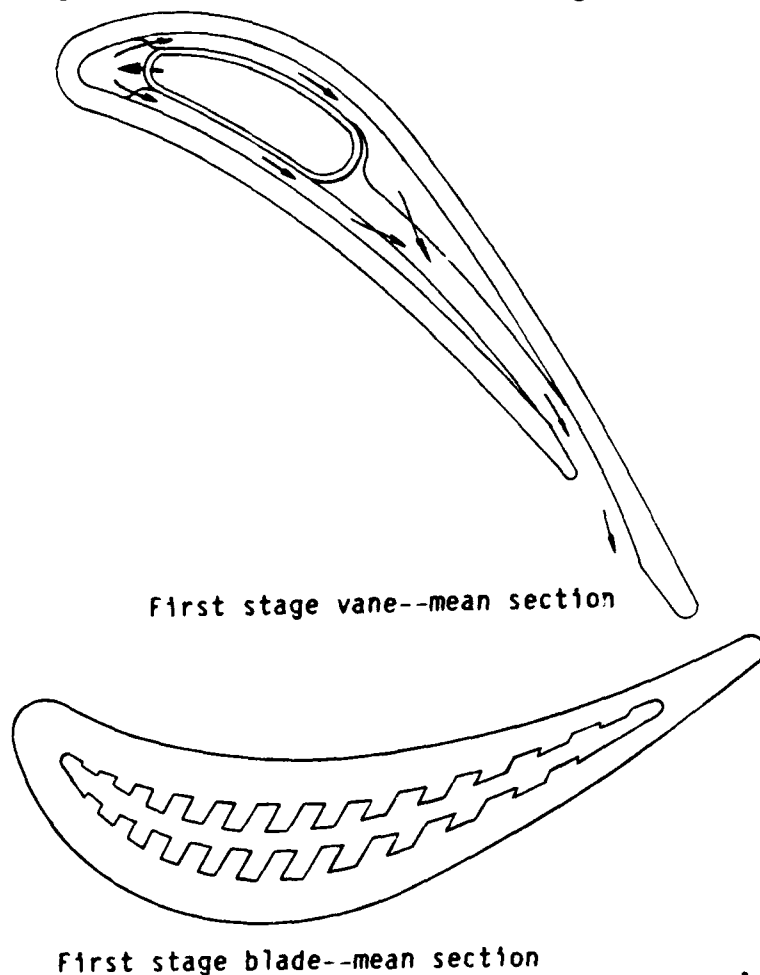
TE88-2026

Figure 124. Sections in first stage vane and blade.

133

The life of the first stage vane was evaluated using the oxidation penetration versus temperature curve shown in Figure 125. This curve was generated by the Allison materials department from observed data. The method to determine maximum metal temperature for each of the four fuels relies on an experimental cooling effectiveness parameter ϕ that is primarily a function of relative internal/external boundary layer thermal resistance. It is largely independent of gas temperature level, and is therefore useful in estimating the influence of combustor exit conditions on turbine airfoil temperature levels. The wall metal temperature T_w is thus given by the following:

$$T = \frac{T_g + \phi \, T_c}{1 + \phi} \tag{44}$$

where T_g is gas temperature at critical section, and T_c is average coolant inlet temperature. The results of the oxidation penetration for each of the test fuels are listed in TABLE 19.

The high density fuels of this analysis pose 60-70 percent less oxidation threat than JP4, or 8-13 percent higher vane coating life.

In the case of turbine rotor first stage blades, cross-sectional thermal gradients induce the mechanical and thermal strains controlling LCF and stress/

TABLE 19. Oxidation penetration of the high density fuels.

Fuel type	Pattern factor	Max gas temp K	Max vane airfoil temp K	Oxidation penetration in 100 hr		Percent of baseline vane coating life
				mm	% of base	
JP4	0.232	1519	1310	0.737×10^{-3}	100	100
HDF-1	0.209	1502	1297	0.508×10^{-3}	69	108
HDF-2	0.207	1501	1296	0.508×10^{-3}	69	108
HDF-3	0.204	1498	1294	0.495×10^{-3}	67	109
HDF-4	0.197	1493	1291	0.457×10^{-3}	62	113
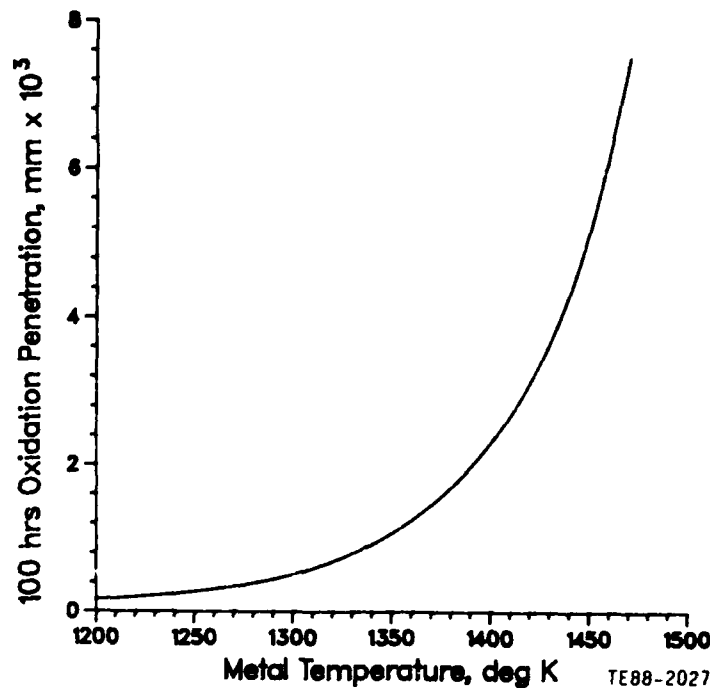
Figure 125. Turbine vane oxidation penetration.

rupture life. Past experience, though, indicates that these gradients would
not change appreciably using alternate fuels. Stress/rupture life is a func-
tion of average temperature and stress as shown on the typical Larsen-Miller
stress/rupture curve. The relative effect of measured change in radial gas
temperature profile on blade life was evaluated at midspan because the maximum
gas temperature occurred at that location.

The overall approach adopted for stress/rupture life calculations is described
in the following paragraphs. The gas temperature adjacent to the first stage
turbine blade was determined using the rig burner outlet and radial temperature
profile data for each fuel. The cooling parameter ϕ was then established for
each mission condition, from which the analytical metal temperature (T_m) was
calculated. The Larsen-Miller parameter, K, was then determined from a previ-
ously established stress distribution and the following equation:

$$K = 41.51 + 19.82 \text{ (log (stress))} - 10.98 \text{ (log (stress))}^2 \tag{45}$$

135

The stress/rupture life (t) was found from K and T_m for each fuel and condition at blade midspan using the following expression:

$$t \ (hrs) = \frac{1}{5} \log^{-1} [(\frac{1000 \ K}{T_m + 35 + 460}) - 20 - Z\sigma] \tag{46}$$

In this equation, degradation due to engine-to-engine variation, thin wall properties, and material property scatter (σ), is accounted for. Z is the number of standard deviations from the mean of the probability of failure chart. The mean blade set lives were then determined and the results were included in TABLE 20. As all characteristic temperatures of the high density fuels were lower than that of the baseline, their stress/rupture lives were higher. Lives with the high density fuel ranged from 110 to 156 percent of the baseline. Figure 126 shows the relationship between percent of the base baseline stress/rupture life versus percent of the baseline temperature. The graph indicates that a nearly linear function exists between the two.

It should be mentioned that, considering the usual burner outlet temperature quality variability in addition to the great sensitivity of the vane and blade lives to changes in this temperature, the variation of lives for high density cases compared to the base JP4 might actually be smaller than predicted.

TABLE 20. Stress rupture life of first stage turbine blade.

| | Baseline JP4 | High density fuel | | | |
		HDF-1	HDF-2	HDF-3	HDF-4
Blade set, average % of base	100	110	156	135	131
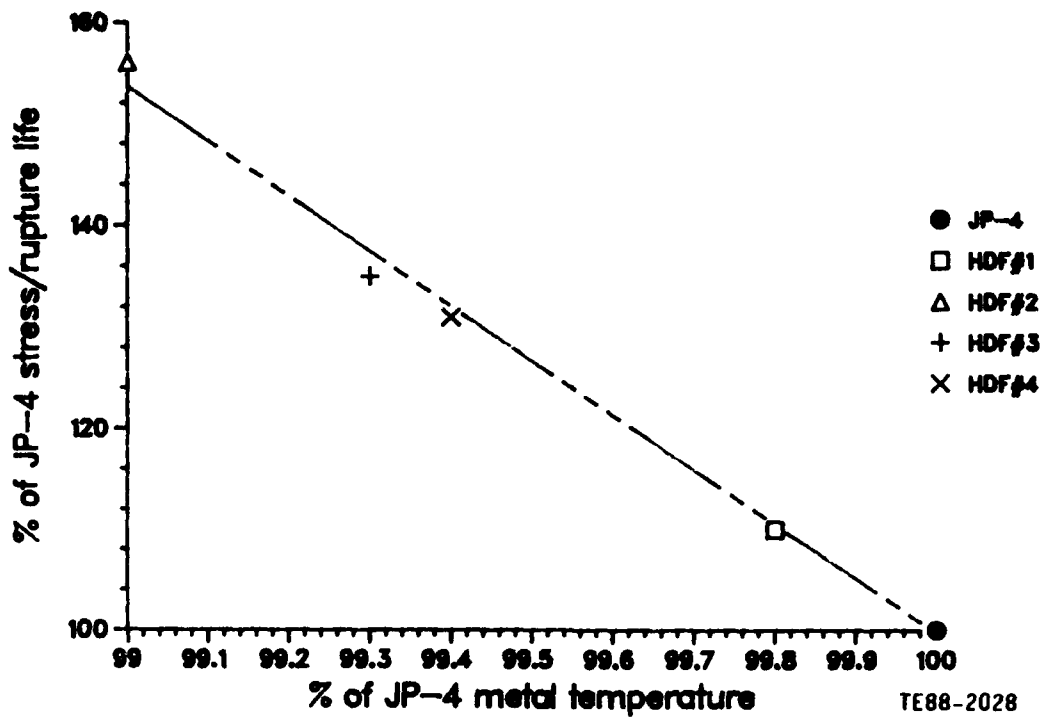
Figure 126.   Stress rupture life of high density fuels.

VI. COMBUSTION SYSTEM MODIFICATION

According to the data evaluation phase of the present program, the T56-A-15 combustor produced excessively high levels of smoke, demonstrated increased levels of flame stability and altitude relight fuel/air ratios, and experienced hotter wall temperatures in the primary zone when operating on the high density fuels.

An effective approach to these performance problems posed by the high density fuels would aim at improving the atomization quality and the fuel/air mixing in the combustor primary zone. This would eliminate the locally fuel-rich regions in this critical zone. The direct effect would be a significant reduction in soot formation with a simultaneous control of wall temperature problems. The improved primary zone aerodynamics, coupled with a rapid evaporation rate of the finer spray, would result in better flame stability, starting, and altitude relight performance.

Improved cooling techniques with enhanced effectiveness could maintain acceptable wall temperatures over the hydrogen content range of the high density fuels. Examples of potential candidates for the T56-A-15 liner include convection/film extended etched surface concept, with and without thermal barrier coat to the hot surface, and transpiration cooling such as effusion or Lamilloy®. The selection of one of these advanced concepts coupled with appropriate cooling air distribution to various combustor zones would certainly achieve the liner life goal when utilizing the high density fuels.

Based on the above consideration, it is recommended that an airblast atomizer should replace the existing dual-orifice type. The internal passages will be designed to handle the proper amount of air required to produce fine sprays over the whole operating range. A pressure atomizing pilot tip may be needed to provide good atomization in the low fuel flow starting range, if the available liner pressure drop at these conditions is too low. The recommended atomizer design is of the type shown in Figure 127. This design will ensure a

138
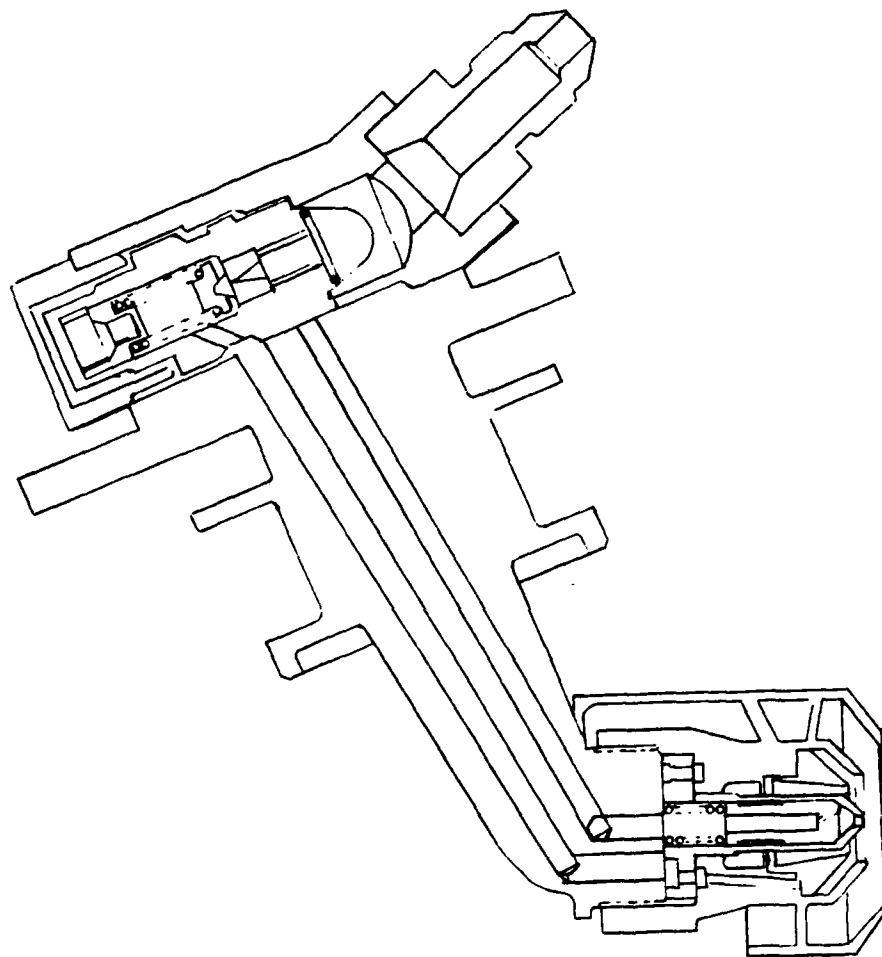
TE84-7297

Figure 127. Airblast fuel injector.

degree of fuel/air premixing occurring immediately upon discharging into the combustor.

The larger fuel passages of airblast atomizers will result in less filtration problems due to the extensive use of high density fuels, and no contamination of the fuel circuit is expected. The details of the internal passages of the atomizer could be determined by using the available analytical tools at Allison to ensure that the issuing spray conforms to the requirements in the primary zone. These tools are described in Reference 23.

In order to achieve improved overall fuel/air mixing in the primary zone, a
dome swirler that encloses the fuel atomizer is suggested in the modified com-
bustor design. The recent experience with the dome swirler configuration in
the T406 and K34 Allison combustors indicates improved performance over the
nonswirler designs. In addition to the swirler, an air shroud of the configu-
ration given in Figure 128 is proposed in the modified combustor to further
enhance the fuel/air mixing.

In order to maintain a proper stoichiometry in the primary zone, enlarged holes
of the first row are proposed in the design. Also, a ring that surrounds the
atomizer/swirler combination may be used to admit cooling air to the dome in
radially outwards direction. Keeping the present dome baffle configuration is
another option.

A convection/film cooling concept with redistributed cooling air to different
combustor zones is adopted in the new design. An extra cooling slot is re-
quired towards the end of the cylindrical portion of the liner to provide a
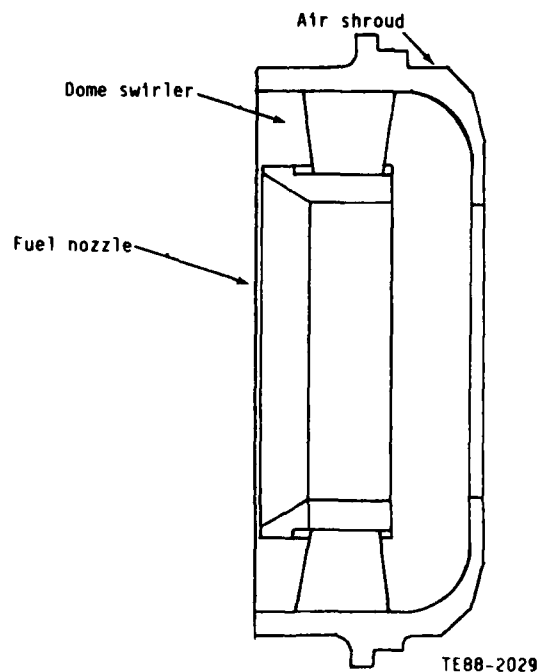
Figure 128. Swirler air shroud.

140

protecting film to the transition section. The recommended combustor air distribution for all combustor zones is shown in Figure 129.

The new configuration was used in the analytical/empirical combustor performance model to demonstrate the extent of performance improvement over the current T56-A-15. The SMD values needed for the model were calculated using well established empirical expressions for this type of atomizer. The flow field characteristics as given by the 3-D codes and reduced by the macro-volume model are shown in Figure 130 for the baseline JP4 and in Figure 131 for the HDF-3. These figures give the predicted contours of fuel/air ratio, gas temperature, and fraction of fuel burned in each subvolume of the combustor sector, respectively. When these plots are compared with the corresponding plots of the original design, as reported earlier, one can conclude that reduction in the levels of fuel/air ratio downstream of the atomizer is observed with the modified design, which indicates better mixing. Higher gas temperatures in this region can be seen in these plots. The other important effect of better atomization and mixing is the considerable reduction in the fraction of fuel burned near the wall specifically for HDF-3, as compared with the predictions of the flow field of the production liner. The direct results of all these factors are a significant reduction in the soot formation in the combustor. This is obvious in Figures 132 and 133 that depict the soot formation contours for JP4 and HDF-3 when the modified combustor is used.

The improved atomization and evaporation characteristics are reflected in the enhanced combustor performance predictions as given by the performance model and included in TABLE 21.

The wall temperature predictions utilizing 3-D combustor code output are given in Figure 134 for the HDF-3, which has the lowest hydrogen content. Reduction in the peak temperatures is predicted by using the modified cooling configuration. This will result in a considerable increase in the low cycle fatigue life which, according to the stress analysis, was expected to decrease due to the use of high density fuels.

141

TABLE 21. Predictions of performance of modified combustor.

	JP4			HDF-3		
	T56-A-15		Proposed liner	T56-A-15		Proposed liner
	measured	predicted	predicted	measured	predicted	predicted
Sea level takeoff						
CO g/kg	1.16	0.97	1.15	2.46	2.25	1.9
UHC g/kg	0.09	0.33	0.36	0.12	0.74	0.62
NO_x g/kg	10.28	11.45	15.9	12.19	11.57	15.6
Smoke SAE No.	37.0	32.6	<5.0	53.3	51.4	<5.0
Combustion efficiency	0.999	0.999	0.999	0.999	0.999	0.997
Pattern factor	0.23	0.18	0.13	0.204	0.20	0.14
Lean blowout F/A	0.0021	0.0025	0.0012	0.0047	0.0034	0.0015
Altitude relight F/A	0.0097	0.0167	0.0061	0.025	0.0227	0.0102
	0.0088	0.0133	0.0034	0.0156	0.0174	0.0057
	0.0121	0.0138	0.0045	0.021	0.0191	0.0048
Sea level ignition F/A	0.010	0.0149	0.006	0.0176	0.0184	0.0102
	0.0089	0.0132	0.0042	0.0143	0.0164	0.0074
	0.0095	0.0132	0.0033	0.0151	0.0174	0.0056
	0.0087	0.0136	0.0025	0.0166	0.0165	0.0047
	0.014	0.0084	0.0022	0.0191	0.0174	0.0040
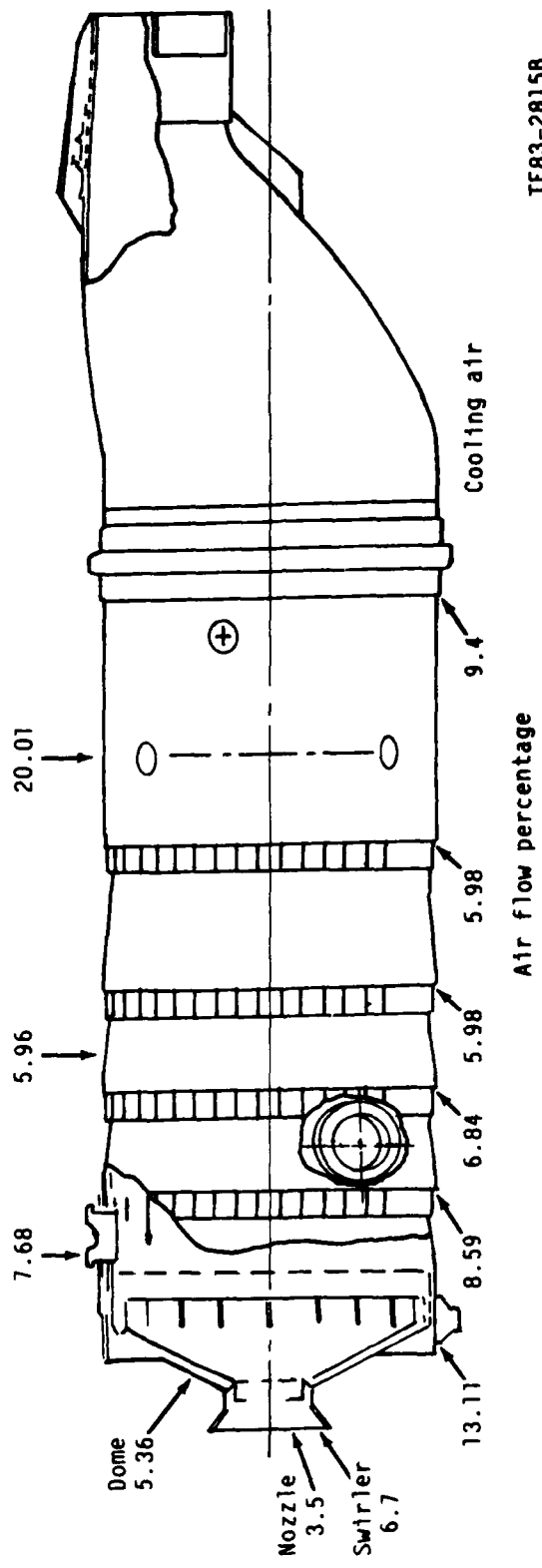
Figure 129. Air distribution of proposed combustor.

143
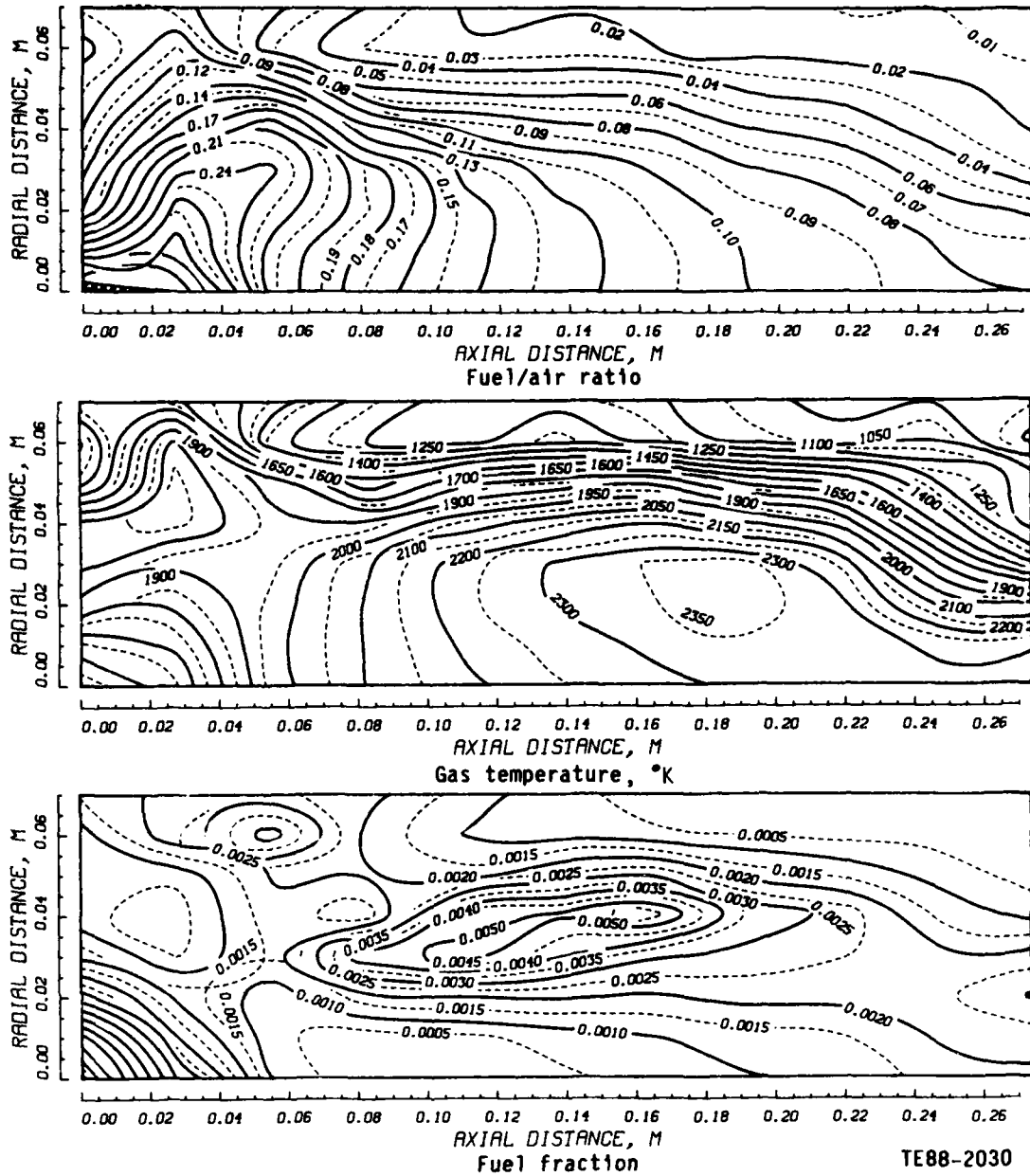
Figure 130. Macro-volume model output of proposed combustor for JP4.

144
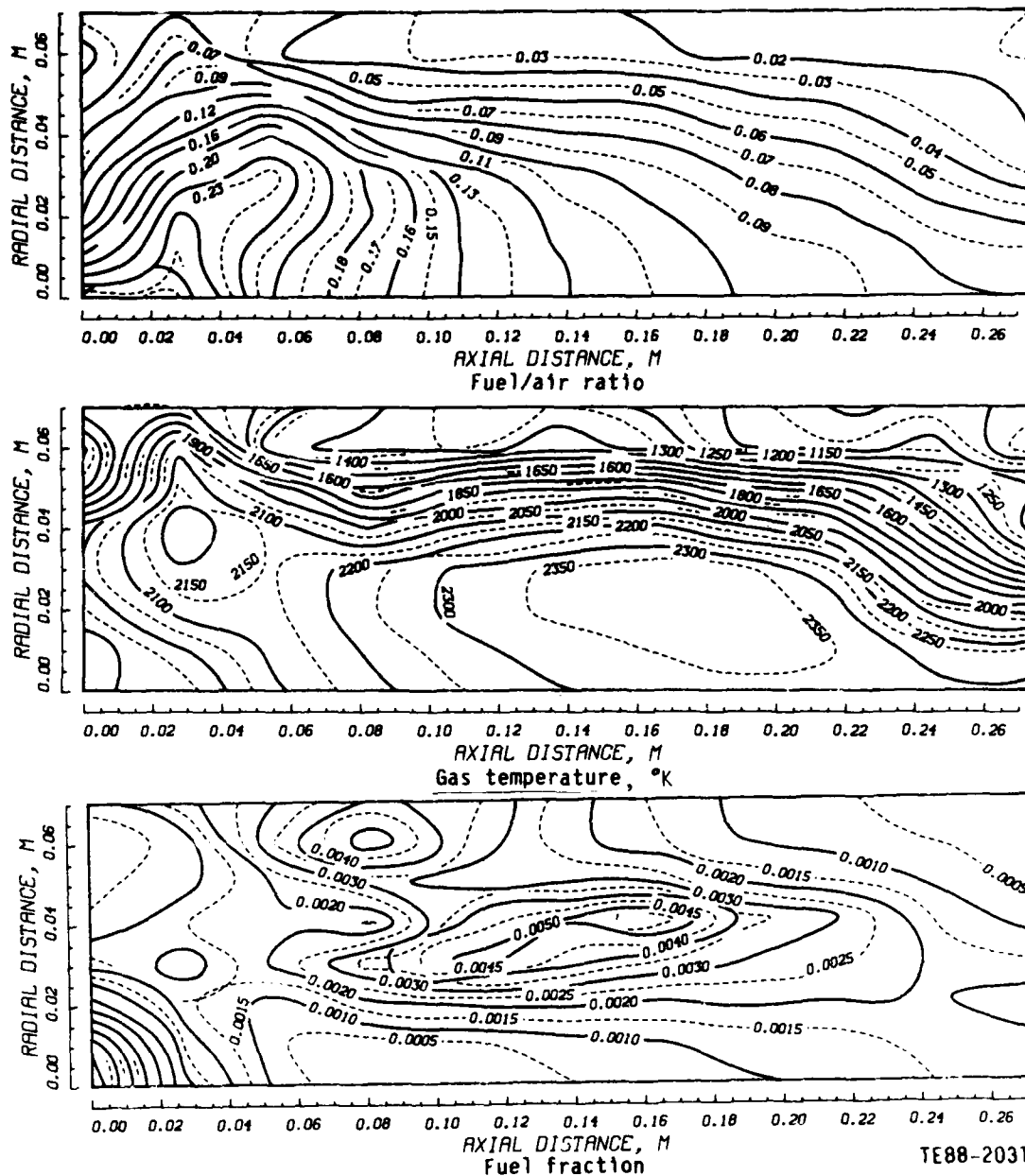
Figure 131. Macro-volume model output of proposed combustor for HDF-3.

145

X-Y SLICE AT Z-20-30 DEG -SOOT FORMED IN EACH ZONE
JP4 -MODIFIED LINER
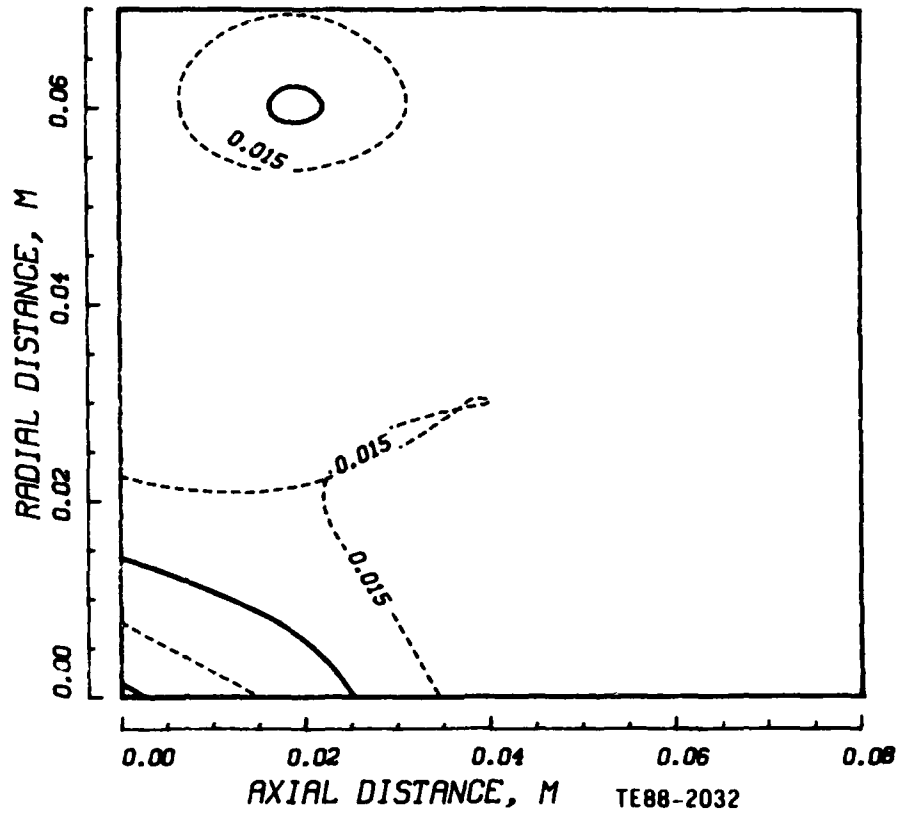
Figure 132.   Contours of soot formation of proposed combustor.   JP4.

X-Y SLICE AT Z-20-30 DEG   SOOT FORMED IN EACH ZONE
HDF*3 MODIFIED LINER
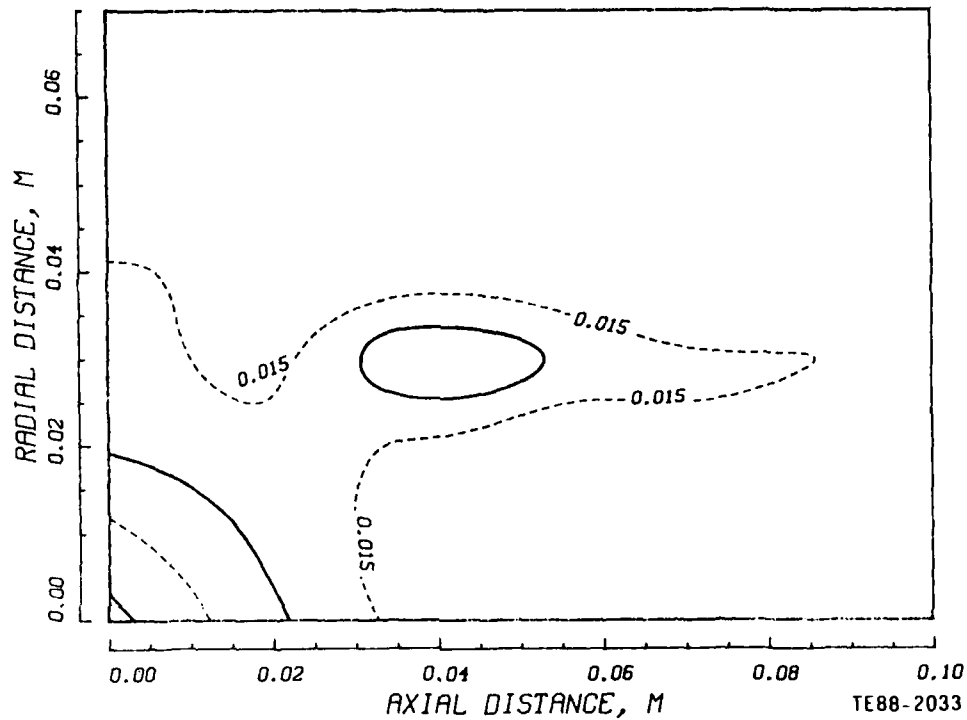
Figure 133.   Contours of soot formation of proposed combustor.   HDF-3.

TAKEOFF – HD#3

X–Y Plane

+ PREDICTIONS AT Z=10.1 DEG
△ PREDICTIONS AT Z=30.0 DEG
○ PREDICTIONS AT Z=49.8 DEG
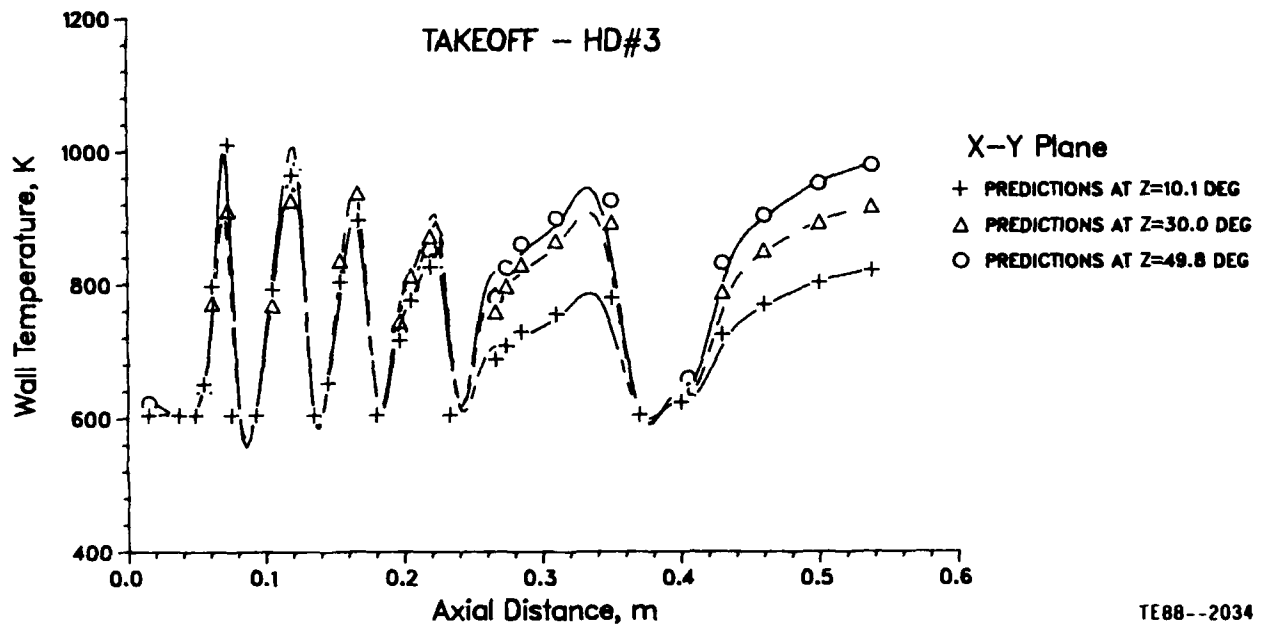
TE88--2034

Figure 134. Wall temperature predictions of proposed combustor.

148

VII. CONCLUSIONS

Based on the experimental data obtained for the baseline JP4, the four high density fuels, and the data evaluation effort, the following conclusions are offered.

7.1 SPRAY CHARACTERISTICS

The radial fuel distribution tests indicate that most of the fuel mass is contained within a wide angle at sea level ignition conditions. The angle, in general, is decreased at higher power mode conditions, and the JP4 spray demonstrates larger angles than the high density fuels.

The drop size measurements show that larger Sauter mean diameters are obtained for high density fuel sprays as compared to JP4. It is also found that the spray quality varies in a complicated manner due to the presence of the nozzle valve that admits the fuel into the main circuit of the dual orifice pressure atomizer. The nozzle shroud air significantly improves the atomization at ignition conditions. In fact, large ligaments were formed at the nozzle exit when no shroud air was used. At higher fuel flow rates, which is accompanied by high fuel pressure drop, the effect of shroud air is insignificant, or it may even hinder the atomization.

An expression has been used to predict the SMD of the air-assist dual orifice atomizer. This expression was essential for the evaluation of the combustion performance data since a means of defining an SMD with reasonable accuracy at various ignition and lean blowout conditions was needed.

The widest spread in droplet sizes in the spray is observed at ignition conditions, and, conversely, the takeoff conditions result in the least spread in sizes. The other power mode conditions produce sprays that fall in between these two distributions.

7.2 COMBUSTION EMISSIONS

The results of carbon monoxide and unburned hydrocarbon emissions show that
the maximum concentration of these pollutants occurs at low power conditions
with the high density fuels producing the largest levels compared to the JP4.
The fuel properties that are relevant to atomization and evaporation are
responsible for the increase in emissions over the JP4 case. The nitrogen
oxide data indicate less influence of fuel properties on the pollutants.

The smoke presence in the exhaust gases is strongly dependent on fuel chemical
properties such as smoke point, aromatic, naphthalene, and hydrogen content.
The HDF-3 produced the highest smoke levels among all fuels tested. In gen-
eral, the level of smoke observed for this combustor is high even at idle con-
ditions. The implication is that the fuel nozzle type used, and dome configu-
ration of the combustor are creating a very rich zone in the primary zone down-
stream of the nozzle, that enhances soot formation.

7.3 COMBUSTION PERFORMANCE

The fuel properties produced an insignificant effect on combustion efficiency
and combustor exit temperature distribution (pattern factor and radial pro-
file). However, it is observed that generally the pattern factor measured for
this combustor is high, indicating a low quality spray and inadequate mixing
in the combustor primary zone that control the temperature distribution of
gases entering the dilution zone.

The flame stability data show that the JP4 has the capability of burning at a
weaker mixture strength than any of the high density fuels. The HDF-4, which
has the highest viscosity and surface tension, demonstrates the highest lean
blow out fuel/air ratio limit. This indicates that the spray quality has a
significant influence on flame stability, together with the properties affect-
ing evaporation.

150

Sea level and altitude ignition results show great dependence on fuel proper-
ties such as vapor pressure and boiling temperatures that control evaporation
history of the fuel spray, and physical properties relevant to atomization.
High density fuels ignite, in some instances, at nearly double the fuel/air
ratio required for the JP4 ignition.

7.4 PREDICTIONS OF COMBUSTOR EMISSIONS AND PERFORMANCE

The correlations reported in report AFWAL-TR-84-2104, were used to evaluate
the experimental data of the combustor. Some modifications to the correlations
were necessary to enhance their prediction capabilities with the high density
fuel results. The correlations were coupled with methods to calculate SMD and
evaporation history. Very satisfactory correlations with the data were ob-
tained by estimating the volume occupied in combustion, and fraction of air
utilized in primary combustion.

The use of the detailed representation of the flow and combustion processes
made available through the analytical codes in the correlation effort, proved
to be very encouraging. It provides an insight to the combustor zones respon-
sible for observed performance trends and aids in the effort to enhance them.
The method also senses the impact of a systematic modification to the details
of the combustor on its performance. It eliminates the need for engineering
estimates of certain combustor parameters.

7.5 COMBUSTOR LINER TEMPERATURE

The highest temperatures measured on the liner wall are in locations near the
end of each cooling zone where the film cooling effectiveness is at the lowest,
and on the transition section especially toward its end. The HDF-3, which has
the lowest hydrogen content among all fuels tested, demonstrated the highest
measured wall temperature in the combustion zone where the flame radiation is
the dominant heat transfer mode. The differences in wall temperatures observed
for all the fuels in the transition section are fairly small.

The highest temperatures measured on the outer surface of the combustor dome occur in regions between the baffles, near the outer radius of the dome. HDF-3 results in the hottest dome when compared with the other fuels.

Wall temperatures measured at takeoff conditions are the highest levels observed, followed closely by those measured at maximum cruise. Idle conditions result in lowest temperature levels.

Primary zone radiation measurements show that the radiative heat loadings are higher for the high density fuels than JP4. The results indicate that the flame emittance is a function of the various physical processes and fuel composition. Takeoff conditions result in the highest radiation components, followed by maximum cruise.

Wall temperature predictions using a heat transfer model are in close agreement with the experimental data. The flame emissivity in the calculations is based on the hydrogen content of the fuel. The radiation flux components are based on the detailed flow field as given by the 3-D combustor code and the accurate definition of a view factor. The heat transfer model provides a very useful tool in selecting the optimum cooling configuration for a developed combustor.

7.6 FUEL FLOW TRANSIENT EFFECT

Following a fuel flow step function that reduces the flow from maximum cruise to idle conditions, the JP4 demonstrates the shortest response time. The high density fuels have slightly longer response times, with the longest time occurring for the HDF-4.

7.7 CARBON DEPOSITION WITHIN THE COMBUSTION SYSTEM

After running the combustor for two hours at maximum cruise conditions, carbon buildup was observed only on the nozzle face and liner dome. Baseline JP4 appeared to have the least amount of carbon buildup. Differences in coking behavior are attributed to differences in chemical properties of fuels, namely

aromatic and hydrogen content, anc physical properties relevant to atomization and evaporation.

7.8 NOZZLE FOULING

The flow calibration of fuel nozzles after two hours of continuous combustion at maximum cruise conditions indicated a small reduction in flow capacity due to nozzle fouling. The largest drop in flow occurred after the HDF-4 fouling test.

Changes in the circumferential patternation were reported after the nozzle fouling test. The maximum percentage difference in fuel volume collected in the patternator sectors was greater following the test at low flow rate, but typical fuel distribution was observed at higher fuel pressure and flow rates.

7.9 COMBUSTOR AND TURBINE LIFE

Based on the maximum axial thermal gradients observed on the liner wall for each fuel, the use of the high density fuel No. 3 would reduce the low cycle fatigue life of the combustor liner by a relative factor of about 6 compared to JP4, according to the finite element stress model.

In the transition section, the stresses from the baseline JP4 are slightly higher than those of the high density fuels. However, the stress levels in this section are much less than the levels found in the cooling slots of the liner.

The high density fuels are found to pose between 60 to 70 percent less oxidation threat than the JP4, or 8 to 13 percent higher vane coating life. Stress/rupture lives of the first stage turbine blades are between 110 and 156 percent higher when running the high density fuels versus the JP4.

153

7.10 RECOMMENDATIONS FOR COMBUSTOR MODIFICATIONS

Improved fuel injection by adopting an air-blast atomizer design, and improved primary zone mixing by modifying the dome design to include a swirler, are the main modifications required to achieve acceptable performance when using the high density fuels in the T56-A-15 combustor. Increased airflow through the primary zone holes is also needed to optimize primary zone stoichiometry.

A convection/film cooling concept is recommended for the liner with redistributed cooling air to various zones to maintain more uniform wall temperature distribution. Additional cooling slots are required toward the end of the cylindrical part to give enough protection to the transition section.

Based on the above recommendations, the modified combustor features were determined, and a demonstration run using the combustor performance model was performed. The predictions show that satisfactory levels of performance and liner wall temperature can be achieved for the modified liner when operating on the high density fuels.

154

REFERENCES

1. Lefebvre, A. H., _Influence of Fuel Properties on Gas Turbine Combustion Performance_, AFWAL-TR-84-2104, January 1985.

2. Mongia, H. C., Reynolds, R. S., and Srinivasan, R., "Multidimensional Gas Turbine Combustion Modeling: Applications and Limitations," _Journal of the AIAA_, Vol 24, No. 6, pp. 890-904, June 1986.

3. Oechsle, V. L., Ross, P. T., and Mongia, H. C., "High Density Fuel Effects on Gas Turbine Engines," AIAA paper No. 87-1829, 1987.

4. Ortman, J., and Lefebvre, A. H., "Fuel Distribution from Pressure-Swirl Atomizers," _Journal of Propulsion and Power_, Vol 1, No. 1, pp. 11-15, January/Feburary 1985.

5. Rizk, N. K., and Lefebvre, A. H., "Influence of Liquid Properties on the Internal Flow Characteristics of Simplex Swirl Atomizers," _Atomization and Spray Technology_, Vol 2, No. 3, pp. 219-233, 1986.

6. Felton, P. G., Hamidi, A. A., and Aigal, A. K., "Measurement of Drop Size Distribution in Dense Sprays by Laser Diffraction," Proceedings of the 3rd International Conference on Liquid Atomization and Spray Systems, No. AVA/4/1-11, London, 1985.

7. Dodge, L. G., "Change of Calibration of Diffraction-Based Particle Sizers in Dense Sprays," _Optical Engineering_, Vol 23, No. 5, pp. 626-630, September/October 1984.

8. Rizk, N. K., and Mongia, H. C., "Spray Characteristics of Air-Assist Atomizers," Proceedings of the 2nd Conference of the Institute for Liquid Atomization and Spray Systems--ILASS-Americas, Pittsburg, PA, May 1988.

9. Lefebvre, A. H., _Gas Turbine Combustion_, McGraw Hill, 1983.

10. Rizk, N. K., and Lefebvre, A. H., "Spray Characteristics of Spill-Return Atomizers," _Journal of Propulsion and Power_, Vol 1, No. 3, pp. 200-204, May/June 1985.

11. Rosin, P., and Rammler, E., "The Laws Governing the Fineness of Powdered Coal," _The Institute of Fuel_, Vol 7, pp. 29-36, October 1933.

12. Faeth, G. M., "Current Status of Droplet and Liquid Combustion," _Progress in Energy and Combustion Science_, Vol 3, pp. 191-224, 1977.

13. Chin, J. S., and Lefebvre, A. H., Technical material to be published, Purdue University, School of Mechanical Engineering, West Lafayette, IN, 1988.

14. Shaffernocker, W. M., and Stanforth, C. M., "Smoke Measurement Techniques," SAE paper C80346, April 1968.

15. Essenhigh, R. H., An Introduction to Stirred Reactor Theory Applied to Design of Combustion Chambers, Combustion Technology: Some Modern Developments, edited by H. B. Palmer and J. M. Beer, Academic Press, pp. 374-415, 1974.

16. Rizk, N. K, and Mongia, H. C., "Gas Turbine Combustion Design Methodology," AIAA paper No. 86-1531, 1986.

17. Mongia, H. C., and Reynolds, R. S., "Combustor Design Criteria Validation," Vol III USARTL-TR-78-SSC, February 1979.

18. Mongia, H. C., "A Status Report on Gas Turbine Combustion Modeling," AGARD Conference Proceedings, No. 422, October 1987.

19. Rizk, N. K, and Mongia, H. C., "The Application of Gas Turbine Combustor Design Method," Proceedings of Central States Meeting, The Combustion Institute, Indianapolis, IN, May 1988.

20. Ballal, D. R., and Lefebvre, A. H., "A Proposed Method for Calculating Film-Cooled Wall Temperatures in Gas Turbine Combustion Chambers," ASME paper No. 72-WA/HT-24, 1972.

21. Luke, D. J., T56-A-15 Hot Section Life Under the Effects of High Density Fuels, Allison Technical Data Report No. AR0301-004, February 1988.

22. Reider, S. B., Vogel, R. E., and Weaver, W. E., Effect of Fuel Composition on Navy T56 Aircraft Engine Hot Section, Final Report for NAPC Contract No. N00140-78-C-0027, November 1983.

23. Rizk, N. K., Mostafa, A. A., and Mongia, H. C., "Modeling of Gas Turbine Fuel Nozzles," to appear in Atomization and Spray Technology, Vol 4, 1988.

NOMENCLATURE

A	area, m^2
AFR	air/fuel ratio
BM	mass transfer number
BOT	burner outlet temperature, K
BT	heat transfer number
C_p	specific heat of gas, kJ/kg K
D	combustor liner diameter, m
F	fraction of combustor air to primary zone
F/A	fuel/air ratio
FN	nozzle flow number
F_v	view factor in radiation
kg	gas thermal conductivity, kJ/(ms K)
L	length, m
l_b	beam length in gas emissivity Eq., m
LHV	lower heating value of fuel kJ/kg
L_u	luminosity factor in gas emissivity Eq.
m_B	fuel fraction burned in subvolume
m_{ev}	fuel fraction evaporated in subvolume
P_3	liner inlet air pressure, kPa
ΔP_a	air pressure drop, kPa
ΔP_f	fuel pressure drop, kPa
ΔP_L	liner air pressure drop, kPa
PF	pattern factor
P_r	Prandtl number
q_{ref}	reference dynamic head, kPa
R_e	Reynolds number
SMD	Sauter mean diameter, m
S_ϕ	source term in transport equation
T_3	liner inlet air temperature, K
T_4	liner exit air temperature, K

T_r	reference gas temperature, K
T_s	fuel drop surface temperature, K
T_u	turbulence characteristics term
T_∞	main stream gas temperature in evaporation, K
U_a	air velocity, m/s
U_f	fuel velocity, m/s
V	volume, m^3
$W_{a3.1}$	liner airflow rate, kg/s
W_f	fuel flow rate, kg/s
Y_F	fuel vapor concentration
εg	gas emissivity
σ_f	surface tension of fuel, N/m
μ_f	fuel viscosity, kg/ms
ϕ	equivalent spray angle, deg
η_c	combustion efficiency
ρ_a	air density, kg/m^3
ρ_f	fuel density, kg/m^3